UNIVERSITY OF CALIFORNIA
RIVERSIDE

Controlling the Exsolution of Nanoparticles in Defect Engineered Perovskites to Enable the Rational Design of Sustainable Catalysts

A Dissertation submitted in partial satisfaction
of the requirements for the degree of

Doctor of Philosophy

in

Chemical and Environmental Engineering

by

Soham Emil Shah

December 2022

Dissertation Committee:
Dr. Kandis Leslie Gilliard Abdul-Aziz
Dr. Francisco Zaera
Dr. Michael Zachariah

The Dissertation of Soham Emil Shah is approved:

Committee Chairperson

University of California, Riverside

ABSTRACT OF THE DISSERTATION

Controlling the Exsolution of Nanoparticles in Defect Engineered Perovskites to Enable the Rational Design of Sustainable Catalysts

by

Soham Emil Shah

Doctorate in Philosophy, Graduate Program in Chemical and Environmental Engineering
University of California, Riverside, December 2022
Dr. Kandis Leslie Abdul-Aziz, Chairperson

The conversion of C1 molecules such as carbon dioxide and methane into syngas, hydrocarbons and other valuable chemicals requires catalysts that are resistant to deactivation by coking and sintering. Furthermore, the cost-effectiveness and sustainability necessitate minimizing or eliminating the use of precious metal catalysts. The in-situ synthesis of metallic nanoparticles via in-situ exsolution in reducing environments is an emerging strategy for developing sustainable catalysts. Exsolved catalysts are anchored strongly on parent perovskite support, can be tailored for optimized activity and stability and are regenerable through redox cycling.

In this dissertation, the exsolution of nickel containing catalytic nanoparticles in ABO_3-type simple perovskites is studied. Various strategies to manipulate the dynamics

of exsolution are employed and their effects on the catalyst performance are evaluated. The introduction of vacancies on the A-site creates oxygen vacancies which favors the exsolution of reducible metals on the B-site. Substituting multiple-metals on the B-site resulted in the formation of alloyed nanoparticles that enable synergistic effects and enhance catalyst activity and stability. Conditions of perovskite synthesis and reduction also affect material characteristics and the nucleation and growth dynamics of the nanoparticles. Each of these strategies has an impact on the size, dispersion and composition of the resulting exsolved nanoparticle and thus on catalyst performance. The experiments conducted in this study elaborate the implications of each strategy by evaluating and comparing catalyst activity and stability for reactions such as dry methane reforming. A combination of in-situ and ex-situ characterization techniques capture the kinetics of the exsolution and shed light on the dynamic nature of exsolving metals subject to different redox conditions.

This dissertation lays the foundation of rationally designed catalysts developed from the perovskite platform. The characteristics of exsolved nanoparticles are controllable and thus desirable properties such as selectivity and stability can be exacted from these materials. The stability and regenerability of these materials can also enable a sustainable use of earth-abundant metals as catalysts.

ACKNOWLEDGEMENT

This research would not have happened if not for my wonderful advisor, Dr. Kandis Leslie Abdul Aziz. She put faith in me to be the first student of her new lab and supported me through every crest and trough of the adventure that has been graduate school. She has been a guide in the truest sense of the word and an advisor well beyond the scope of research.

The Sustainable Lab at UCR also introduced me to amazing colleagues – Mark Gale, Tu Nguyen, Somchate Wasantwisut, Seogbin Jo, Luz Cruz, Barnali Sutradhar and Naharin Jannath. Their help, feedback and inputs were immeasurably valuable to me as I grew as a researcher. I would also like to thank my undergraduate mentees Samuel Sayono, Jenna Ynzunza, Ryan Pan and Jacob Graves. To watch them grow as researchers in their own right was a very fulfilling part of my PhD and made significant contributions to my research. I have learned to be a better mentor and teacher because of them.

Over the course of my PhD, I also learned from and collaborated with incredible scientists who also contributed to the work in this dissertation. Dr. Mingjie Xu and Dr. Xiaoqing Pan conducted important work with Transmission Electron Microscopy and Scanning Transmission Electron Microscopy to our research. Dr. Simon Bare and Dr. Jiyun Hong collaborated with the X-ray Absorption Spectroscopy for the in-situ catalysis study. Dr. Adam Hoffman and Dr. Griffin Canning supported the beamline study. Dr. Luz Cruz besides was also a contributor to the study. Dr. Christopher Hahn and Dr.

Huiyun Jeong have been gracious hosts and insightful mentors for the reactive capture of carbon dioxide project that is ongoing as of writing this dissertation. Each of these collaborations were an opportunity to learn and grow as a scientist, a professional and a person.

I am thankful to the University of California, Riverside to have given me this opportunity and the opportunities that will follow because of this. I am proud to call this institution my alma mater.

Most of all, I could not have done this without of my family – my aunts, my uncles, my cousins, and of course my parents and grandparents. I am who I am and where I am because of their support.

A portion of the research presented in this dissertation has been previously published in:

1) Shah, S.; Sayono, S.; Ynzunza, J.; Pan, R.; Xu, M.; Pan, X.; Gilliard-Abdulaziz, K. L. The Effects of Stoichiometry on the Properties of Exsolved Ni-Fe Alloy Nanoparticles for Dry Methane Reforming .*AIChE J.* **2020**, *66* (12), e17078. https://doi.org/10.1002/aic.17078.

2) Shah, S.; Xu, M.; Pan, X.; Gilliard-Abdulaziz, K. L. Exsolution of Embedded Ni–Fe–Co Nanoparticles: Implications for Dry Reforming of Methane. *ACS Appl. Nano Mater.* **2021**, *4* (8), 8626–8636. https://doi.org/10.1021/acsanm.1c02268

3) Shah, S; Xu, M.; Pan, X.; Gilliard-Abdulaziz, K. L.; Complex Alloy and Heterostructure Nanoparticles Derived from Perovskite Oxide Precursors for Catalytic Dry Methane Reforming. ACS App. Nano Mater. **2022**. https://doi.org/10.1021/acsanm.2c03857

Dedication

To family and friends, mentors and colleagues.

Table of Contents

List of Figures

List of Tables

CHAPTER 1. INTRODUCTION AND BACKGROUND

1.1 Introduction

Synthesis gas is a mixture of carbon monoxide and hydrogen and is used in the production of ammonia, methanol and a number petrochemicals and synthetic fuels and in steel making. The global market for synthesis gas was $43.6 billion in 2019, expected to grow at 6% per year to $66.6 billion in 2027[1]. Syngas, another name for it, is the building block of the petrochemical industry and an input to the production of an array of objects, from fuels and plastics to detergents and textiles, that we use daily. The primary methods of production of syngas are gasification of coal and steam reforming of methane. Reforming of methane with carbon dioxide (see reaction (1)) or Dry Methane Reforming (DMR) can help reduce the overall carbon footprint of the process by utilizing CO_2 in the process. Thus, two potent greenhouse gases can be turned into a valuable commodity[2].

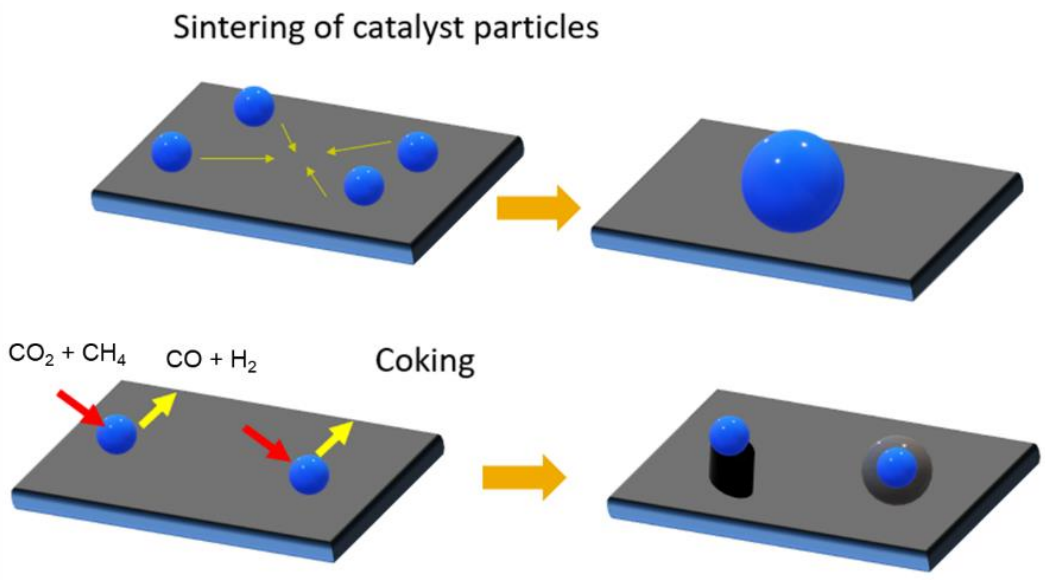

Figure 1.1 A schematic for the deactivation of catalyst nanoparticles by sintering and coking.

$$CH_4 + CO_2 \rightarrow 2CO + 2H_2 \qquad \Delta H_{298K} = +247 \frac{kJ}{mol} \quad (1)$$

Precious metals such as palladium and rhodium and platinum are highly active for the activation of methane in DMR by coking and sintering but are challenged by their prohibitive cost and limited supply[3]. Nickel is seen as an industrially viable metal of choice for DRM[4] due to its earth-abundance and significantly lower cost compared to Pd, Pt and Rh. The challenge however is that nickel is vulnerable to deposition of carbonaceous materials and loss of surface area due to sintering[5].

Catalysts, in general, also show a decline in activity due to decreasing active area and change in surface structure, narrowing of pores or the vanishing of surface defects. These surface changes are referred to as sintering. Sintering and coking (**Figure 1.1**) are issues faced across the entire heterogenous catalyst industry – a $20 billion market. Coupled with the need to reduce dependency on precious metals there is an urge to develop novel catalysts that have similar performance metrics. As a result, a lot of catalysis research has focused on strategies to combat deactivation by sintering or coking, while still primarily using sustainable and economic metals such as Ni, Co or Fe.

One strategy to produce more resilient and highly active catalysts has been the combination of a primary catalytic metal with another metal. Bimetallic catalysts have been studied for various applications given their enhanced properties due to their synergetic effects. The conventional choice of catalyst for methane dry reforming reaction, nickel, has been paired with other transition metals such as Co, Fe and Cu for enhanced stability[6–8]. Nickel has also been coupled with noble metals such as Pd, Ru, Au, Ag for boosting activity as well as reducing or controlling coke formation[6]. Ni-Co in

particular has been widely studied as the addition of Co elevates the activity of Ni due to its affinity for oxygen groups[7,9,10]. An optimal amount of Fe in combination with Ni can also stabilize the Ni and prevent coking. The Fe^0/FeO_x redox couple supplied oxygen to any coking products formed on the catalyst thus oxidizing the carbon and stabilizing the catalyst[11,12]. A high content of Fe in fact suppressed activation of methane by Ni and thus there was an optimal content of Fe. Bimetallic and multi-metallic catalysts can display elevated catalytic performances due to variety of synergistic relationships[13]. A great deal of research is being poured into studying the interaction between different metal species within alloyed catalyst materials within themselves and with their supports to understand better how these enhancements are engendered. The superior performances of bimetallic catalysts are inspiring new developments in judiciously fabricating catalysts that are performing significantly better than either metal being used individually.

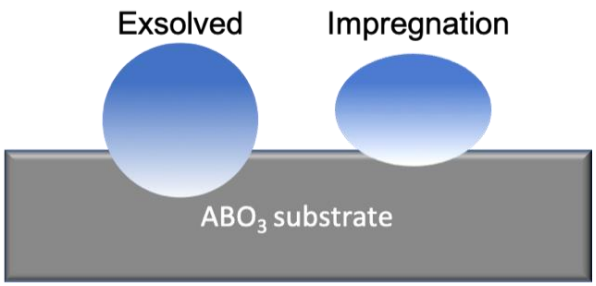

Figure 1.2. Comparison catalyst-support systems in exsolved and impregnated catalysts.

The phenomenon of exsolution as seen in perovskites supported catalysts has been targeted for their properties of sintering and coking resistance as well as enhanced support effects. Perovskite are a family of mixed metal oxides with a basic structure of ABX_3. Typically. 'A' is a group II or lanthanide series metal while 'B' is often a transition metal. There has been significant research done on geo-inspired perovskite oxide based catalyst supports since the discovery of the self-regeneration ability of

perovskites was first described by researchers at Daihatsu[14–16]. The phenomenon of exsolution in perovskites, involves the release of reducible cations, generally from the B-site, under reductive atmospheres at high temperatures. Subsequently, these cations form metallic nanoparticles on the surface of the perovskite. This method of growing catalysts in-situ can render nanoparticles that are smaller (~1 nm[17]) and much better dispersed and thermally stable[18] compared conventional catalysts prepared by methods such as impregnation[19,20] (**Figure 1.2**). Furthermore, because they emerge from within the support, they adhere strongly to the support surface that is the parent perovskite. The strong interaction between the catalyst and support also enhances catalytic activity and inhibits sintering and coking[21]. Additionally, any eventual agglomeration or sintering can simply be reversed through re-oxidation of the catalyst sample that causes the particles to diffuse back into the perovskite bulk[14,22]. These catalysts therefore also have a longer lifetime which is beneficial for establishing catalysts with improved industrial capabilities.

The versatility of multi-metallic catalysts along with the tunability of perovskite oxides present an opportunity to rationally design perovskite supports that exsolve multi-metallic nanoparticles that are optimized for specific applications. Therein lies the motivation for this dissertation. We refer the doping of perovskites with catalytic metals of interest and the concomitant manipulation of exsolution as Defect Engineering. The materials that we develop with defect engineering would be novel not only for catalysis, but for far ranging applications from fuel cells to thermal materials.

1.2 Background

1.2.1 Exsolution of Nanoparticles in Perovskites

Perovskites are a class of mixed metal compounds with general stoichiometry ABX_3. Perovskites were first described in the 1970s, as materials whose unique properties could make superior catalyst and electrode materials[23,24]. Further research led to the discovery of the self-regenerating property of catalytic activity due to the reversible ingress-egress of nanoparticles[14,15]. After high temperature reduction, $LaFe_{0.57}Co_{0.38}Pd_{0.38}O_3$ formed Pd-Co bimetallic nanoparticles the size of 1-3 nm. The nanoparticles were found to have no deterioration in catalytic activity over a 100-hour aging test. Moreover, when re-oxidized during the redox cycles of catalytic conversion of NO_x-CO, the particles returned to the perovskite lattice. After the discovery of reversible exsolution of nanoparticles, perovskites were now considered as the basis for the formation of catalysts whose particle sizes, dispersion and anchorage can be finely tuned. This is as opposed to the conventional method of decorating surfaces by depositing catalytic nanoparticles using methods such as impregnation onto the surface of perovskite supports, that does not offer any control over the same parameters.

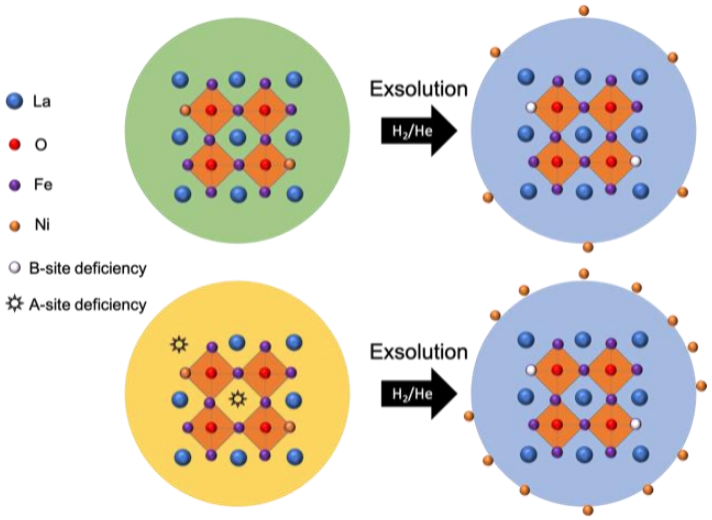

Figure 1.3. Schematic of exsolution of Ni cations from $La(FeNi)O_3$ perovskite.

Since the discovery by the scientists at Daihatsu, the phenomenon of exsolution of metal nanoparticles through perovskites. Among the advantages that perovskites offer over conventional support materials are thermal stability, valency and vacancy control[15]. The oxidation states of transition metals can change in redox conditions to compensate for charge-neutrality upon the formation or filling up of oxygen vacancies. Altering the combination of metals can be done to tweak properties such as stability under redox conditions.

1.2.2 Exsolution Trends and the Role of Defects in Perovskites

A primary factor in controlling the composition of exsolved nanoparticles is the composition of the parent perovskite itself. Kwon et.al[25] described co-segregation trends in $PrBaMnO_5$ double layered perovskites. They discussed the reduction of Mn^{+3} to Mn^{+2} and the concomitant exsolution of MnO particles. When the Pr-Ba-Mn perovskites were doped with other transition metals such as Ni, Co, Fe to replace some of the Mn sites the exsolution trends change. Based on their DFT calculations the segregation energies of the perovskites are in the order Co<Ni<Mn<Fe, i.e., Co and Ni exsolve much favorably than Mn which in turn exsolves easily compared to Fe.

The presence of vacancies in either A site and/or oxygen, is a deviation from stoichiometry. This can in turn drive exsolution of atoms from the B-site to restore stoichiometric balance. Hamada et.al.[26] showed with their DFT calculations that the introduction of oxygen deficiencies is the key to the self-regenerative property of perovskites. The oxygen deficiencies in their Pd doped $LaFeO_3$, generated during calcination at high temperatures, help form a $LaPdO_{3-y}$ layer which permits the passage of

Pd atoms in and out of the host lattice. Sun et.al.[18] demonstrated that Ni doped lanthanum-strontium chromate with A site deficiencies formed excellent fuel cells. The A site deficiency helps create oxygen vacancies that make the Ni nanoparticles easily reducible thus accelerating exsolution.

Neagu et.al.[27] demonstrated the trends in growth of nanoparticles in non-stoichiometric perovskites. They discussed a mechanism wherein A-site deficient perovskites promoted the exsolution of B cations to greater degree than stoichiometric samples.

$$ABO_{3-\delta} \rightarrow (1-\alpha)ABO_{3-\delta'} + \alpha AO + \alpha B_{(exsolved)} \quad (2)$$

$$A_{1-\alpha}BO_{3-\delta} \rightarrow (1-\alpha)ABO_{3-\delta''} + \alpha B_{(exsolved)} \quad (3)$$

The presence of A site deficiencies introduces oxygen deficiencies in the perovskite and there is a divergence from stoichiometry. There would be a greater number of point defect sites and several B sites would be uncoordinated with neighboring O sites. The vacancies on two primitive sites out of the three, destabilize the perovskite. There is a drive to restore stoichiometry in the lattices which pushes the exsolution mechanism forward. This can also be viewed as the presence of excess B metal ions that need to exit the perovskite matrix. In contrast with that, perovskites with excess of either the A-site cation or oxygen, would have fewer B cations that are uncoordinated and are not as predisposed to exsolve.

The implications of their study meant that controlling compositions of perovskites and more specifically tuning the degree of non-stoichiometry would control the extent of exsolution. Rationally engineering the perovskite's intrinsic features such as defect types,

defect concentrations and metal composition as well as adjusting external factors such as the temperature and atmospheric conditions during reduction can expedite or hinder particle nucleation and/or growth. In another publication[21,28], Neagu and co-workers discussed the features of the interface between exsolved particles and parent perovskite. Since the particle is socketed on to the support from which it emerged, the tip growth mechanism of coking is hindered as the particle cannot be lifted from the support, unlike deposited catalyst particles. The nano-socketing also precludes any agglomeration of the catalyst particles as they are held in one place and therefore cannot coalesce.

Steiger et.al.[29] obtained estimated the quantity of reducible Ni in $LaFe_{1-x}Ni_xO_3$ perovskites. The reducibility of Ni was found to increase with amount Ni doped in the $LaFeO_3$ with 35% of Ni reducing for x=0.05 going up to 50% for x=0.20 after reduction in 10% H_2/Ar for 1 hour. Moreover, upon reoxidation at 650°C in 20%O_2/N_2 for 1 hour between 80-90% of the Ni had reincorporated as Ni^{+3} species into the perovskite matrix rather than being Ni^{+2} in NiO dispersed over La-Fe-O lattice.

Sheng Dai et.al.[17] observed Rh doped $CaTiO_3$ under a TEM in *in situ* conditions. They discussed the time scales required for exsolution and found that nanoparticles can precipitate in the order of minutes. Additionally, Rh nanoparticles were visible under TEM at temperatures as low as 250°C. Lai and Manthiram[30] compared the exsolution behavior of Co-Fe nanoparticles in a (La,Sr)-Cr oxide perovskite. At 700°C, as opposed to 800°C nanoparticles were smaller and had a greater areal density. Thus, temperature at which exsolution is carried out has a profound influence on the size distribution and dispersion of the exsolved nanoparticles.

In this dissertation, these ideas are combined and the synthesis of multi-metallic alloyed catalysts, via in-situ exsolution in perovskites is discussed. The goal of this research is to develop highly stable and active catalysts for reactions that activate methane, reduce carbon dioxide, and produce syngas. I have extended the understanding of the mechanism that underly the phenomenon of exsolution of nanoparticles in perovskites. This research has also demonstrated how Defect Engineering can be used to manipulate exsolution into adjusting nanoparticle size, dispersion and composition. Catalysts that come from being defect engineered would thus be highly active, could target selective reactions and withstand detrimental factors such as sintering or agglomeration and even coking and poisoning.

In chapter 2, the phenomenon of exsolution is explored with the role of stoichiometric defects in the A site of the perovskite under investigation. Building on the work done by Neagu et al.[27] we study the implications of defect driven exsolution on the performance of the catalysts for DRM. Stoichiometric defects i.e., deficiency of A-site elements relative to B-site elements (or vice-versa) can create vacancies (or excess in the opposite case) in the oxygen sites of the perovskite. This has an effect on the degree to which B-site metals exsolve in turn affecting the size, composition and dispersion of exsolved nanoparticles[31]. The implications of this defect engineering on catalytic performance of the perovskite-based catalysts are discussed. This research moved further, as is discussed in chapter 3, the effects of changing composition and the introduction of Co to the $La(FeNi)O_3$ perovskites. The introduction of Co as a co-dopant in the B-site of the perovskite has an influence on the co-exsolution of Ni and Fe as the reducibility of

the perovskite is altered. Furthermore, the interaction of Co along with Ni and Fe affect how the nanoparticles activate methane and carbon dioxide in DRM reaction conditions. The effect of reduction temperature on exsolution, similar to Lai and Manthiram's work[30], is also studied with the objective of understanding its consequences for catalysis. Changing the reduction temperature affected the dynamics of the exsolution process, in turn controlling the size, dispersion and composition of the resultant catalyst nanoparticles[32]. In chapter 4, with X-ray absorption spectroscopy (XAS) as a tool, we study the phenomenon of exsolution in-situ observing how the materials responds to changing redox conditions. The dynamics of Ni and Fe interactions with oxidizing and reducing gases and their switching between metallic and perovskite-oxide phases are uncovered. In chapter 5, we use the perovskite material and exsolution to demonstrate the synthesis of complex concentrated alloys (CCAs) in a facile manner. CCAs are an interesting class of materials where multiple metals interact to provide stabilization due to a high entropy of mixing. This has various potential applications, the most relevant of which, for the purpose of this dissertation is catalysis. The co-exsolution of five metals – Ni, Fe, Co, Cu and Pd – resulted in the formation of heterostructural alloys such as core-shell and Janus particles. Entropic stabilization also resulted in catalysts that are extremely stable in DRM reaction conditions while also demonstrating superior activity due to synergistic interactions of the multiple metals. In chapter 6, the use of $Sr(ZrNi)O_3$ type perovskites as dual functional materials, for sorption enhanced catalytic utilization of CO_2 is explored and preliminary data on their effectiveness is discussed. Finally,

chapter 7, summarizes the key findings of this research and lays potential future paths to be explored for further development of perovskite based materials as catalysts.

1.3 References

(1) Business Wire. Global Syngas Market (2020 to 2027) - by Gasifier, Technology, Feedstock, and Application - ResearchAndMarkets.Com | Business Wire. 2021.

(2) Lavoie, J. M. Review on Dry Reforming of Methane, a Potentially More Environmentally-Friendly Approach to the Increasing Natural Gas Exploitation. *Front. Chem.* **2014**, *2*, 1–17. https://doi.org/10.3389/fchem.2014.00081.

(3) Pakhare, D.; Spivey, J. A Review of Dry (CO2) Reforming of Methane over Noble Metal Catalysts. *Chem. Soc. Rev.* **2014**, *43* (22), 7813–7837. https://doi.org/10.1039/c3cs60395d.

(4) Liu, C. J.; Ye, J.; Jiang, J.; Pan, Y. Progresses in the Preparation of Coke Resistant Ni-Based Catalyst for Steam and CO 2 Reforming of Methane. *ChemCatChem* **2011**, *3* (3), 529–541. https://doi.org/10.1002/cctc.201000358.

(5) Kim, J. H.; Suh, D. J.; Park, T. J.; Kim, K. L. Effect of Metal Particle Size on Coking during CO2 Reforming of CH4 over Ni-Alumina Aerogel Catalysts. *Appl. Catal. A Gen.* **2000**, *197* (2), 191–200. https://doi.org/10.1016/S0926-860X(99)00487-1.

(6) Bian, Z.; Das, S.; Wai, M. H.; Hongmanorom, P.; Kawi, S. A Review on Bimetallic Ni-Based Catalysts for CO2 Reforming of Methane. *ChemPhysChem* **2017**, *18* (22), 3117–3134. https://doi.org/10.1002/cphc.201700529.

(7) Zhang, J.; Wang, H.; Dalai, A. K. Development of Stable Bimetallic Catalysts for Carbon Dioxide Reforming of Methane. *J. Catal.* **2007**, *249* (2), 300–310. https://doi.org/10.1016/j.jcat.2007.05.004.

(8) Tao, F. Synthesis, Catalysis, Surface Chemistry and Structure of Bimetallic Nanocatalysts. *Chem. Soc. Rev.* **2012**, *41* (24), 7977–7979. https://doi.org/10.1039/c2cs90093a.

(9) San-José-Alonso, D.; Juan-Juan, J.; Illán-Gómez, M. J.; Román-Martínez, M. C. Ni, Co and Bimetallic Ni-Co Catalysts for the Dry Reforming of Methane. *Appl. Catal. A Gen.* **2009**, *371* (1–2), 54–59.

(10) Xu, J.; Zhou, W.; Li, Z.; Wang, J.; Ma, J. Biogas Reforming for Hydrogen Production over Nickel and Cobalt Bimetallic Catalysts. *Int. J. Hydrogen Energy* **2009**, *34* (16), 6646–6654. https://doi.org/10.1016/j.ijhydene.2009.06.038.

(11) Wang, L.; Li, D.; Koike, M.; Koso, S.; Nakagawa, Y.; Xu, Y.; Tomishige, K. Catalytic Performance and Characterization of Ni-Fe Catalysts for the Steam Reforming of Tar from Biomass Pyrolysis to Synthesis Gas. *Appl. Catal. A Gen.* **2011**, *392* (1–2), 248–255. https://doi.org/10.1016/j.apcata.2010.11.013.

(12) Theofanidis, S. A.; Galvita, V. V.; Poelman, H.; Marin, G. B. Enhanced Carbon-Resistant Dry Reforming Fe-Ni Catalyst: Role of Fe. *ACS Catal.* **2015**, *5* (5), 3028–3039. https://doi.org/10.1021/acscatal.5b00357.

(13) Sankar, M.; Dimitratos, N.; Miedziak, P. J.; Wells, P. P.; Kiely, C. J.; Hutchings, G. J. Designing Bimetallic Catalysts for a Green and Sustainable Future. *Chem. Soc. Rev.* **2012**, *41* (24), 8099–8139. https://doi.org/10.1039/c2cs35296f.

(14) Nishihata, Y.; Mizuki, J. Self-Regeneration of a Pd-Perovskite Catalyst for Automotive Emissions Control. *Nature* **2002**, *418* (x), 164–167.

(15) Tanaka, H.; Tan, I.; Uenishi, M.; Taniguchi, M.; Kimura, M.; Nishihata, Y. LaFePdO 3 Perovskite Automotive Catalyst Having a Self-Regenerative Function. *J. Alloys Compd.* **2006**, *412*, 1071–1077. https://doi.org/10.1016/j.jallcom.2004.12.138.

(16) Mizuki, J.; Akao, T.; Tanaka, H.; Uenishi, M.; Kimura, M.; Okamoto, T.; Hamada, N. Self-Regeneration of a Pd-Perovskite Catalyst for Automotive Emissions Control. *Nature* **2002**, *418*, 164–167. https://doi.org/10.1038/nature00875.1.

(17) Dai, S.; Zhang, S.; Katz, M. B.; Graham, G. W.; Pan, X. In Situ Observation of Rh-CaTiO3Catalysts during Reduction and Oxidation Treatments by Transmission Electron Microscopy. *ACS Catal.* **2017**, *7* (3), 1579–1582.

(18) Sun, Y.; Li, J.; Zeng, Y.; Amirkhiz, S.; Wang, M. A-Site Deficient Perovskite: The Parent for in Situ Exsolution of Highly Active, Regenerable Nanoparticles as SOFC Anodes Exsolution of Highly Active , Regenerable Nano-. *J. Mater. Chem. A* **2015**, *3*, 11048–11056. https://doi.org/10.1039/c5ta01733e.

(19) Delmon, B.; Thomas, J. M.; Bell, R. G.; Catlow, C. R. A.; Feijen, E. J. P.; Martens, J. A.; Jacobs, P. A.; Souverijns, W.; van Rhijn, W. 2.2.2 Formation of Final Catalyst. *Handb. Heterog. Catal.* **1997**, 264–365.

(20) Lee, D. W.; Yoo, B. R. Advanced Metal Oxide (Supported) Catalysts: Synthesis and Applications. *J. Ind. Eng. Chem.* **2014**, *20* (6), 3947–3959.

(21) Neagu, D.; Oh, T. S.; Miller, D. N.; Ménard, H.; Bukhari, S. M.; Gamble, S. R.; Gorte, R. J.; Vohs, J. M.; Irvine, J. T. S. Nano-Socketed Nickel Particles with Enhanced Coking Resistance Grown in Situ by Redox Exsolution. *Nat. Commun.* **2015**, *6* (8120). https://doi.org/10.1038/ncomms9120.

(22) Li, J.; Singh, U. G.; Bennett, J. W.; Page, K.; Weaver, J. C.; Zhang, J. P.; Proffen, T.; Rappe, A. M.; Scott, S.; Seshadri, R. BaCe1-XPdxO3-δ($0 \leq x \leq 0.1$): Redox Controlled Ingress and Egress of Palladium in a Perovskite. *Chem. Mater.* **2007**, *19* (6), 1418–1426. https://doi.org/10.1021/cm062500i.

(23) Libby, W. . Promising Catalyst for Auto Exhaust. *Science (80-.).* **1971**, *1277* (February), 6–7.

(24) MEADOWCROFT, D. B. Low-Cost Oxygen Electrode Material. *Nature* **1970**, *226* (5248), 847–849. https://doi.org/10.1038/226848a0.

(25) Kwon, O.; Sengodan, S.; Kim, K.; Kim, G.; Jeong, H. Y.; Shin, J.; Ju, Y.; Han, J. W.; Kim, G. Exsolution Trends and Co-Segregation Aspects of Self-Grown Catalyst Nanoparticles in Perovskites. *Nat. Commun.* **2017**, *8* (May), 1–7.

(26) Hamada, I.; Uozumi, A.; Morikawa, Y.; Yanase, A.; Katayama-yoshida, H. A Density Functional Theory Study of Self-Regenerating Catalysts. *J. Am. Chem. Soc.* **2011**, *133* (001), 18506–18509. https://doi.org/10.1021/ja110302t.

(27) Neagu, D.; Tsekouras, G.; Miller, D. N.; Ménard, H.; Irvine, J. T. S. In Situ Growth of Nanoparticles through Control of Non-Stoichiometry. *Nat. Chem.* **2013**, *5* (11), 916–923. https://doi.org/10.1038/nchem.1773.

(28) Oh, T.; Rahani, E. K.; Neagu, D.; Irvine, J. T. S.; Shenoy, V. B.; Gorte, R. J.; Vohs, J. M. Evidence and Model for Strain-Driven Release of Metal Nanocatalysts from Perovskites during Exsolution. **2015**, 5106–5110. https://doi.org/10.1021/acs.jpclett.5b02292.

(29) Steiger, P.; Delmelle, R.; Foppiano, D.; Holzer, L.; Heel, A. Structural Reversibility and Nickel Particle Stability in Lanthanum Iron Nickel Perovskite-Type Catalysts. **2017**, 2505–2517. https://doi.org/10.1002/cssc.201700358.

(30) Lai, K. Y.; Manthiram, A. Evolution of Exsolved Nanoparticles on a Perovskite Oxide Surface during a Redox Process. *Chem. Mater.* **2018**, *30* (8), 2838–2847.

(31) Shah, S.; Sayono, S.; Ynzunza, J.; Pan, R.; Xu, M.; Pan, X.; Gilliard-AbdulAziz, K. L. The Effects of Stoichiometry on the Properties of Exsolved Ni-Fe Alloy Nanoparticles for Dry Methane Reforming. *AIChE J.* **2020**, *e17078* (June), 1–12.

(32) Shah, S.; Xu, M.; Pan, X.; Gilliard-Abdulaziz, K. L. Exsolution of Embedded Ni–Fe–Co Nanoparticles: Implications for Dry Reforming of Methane. *ACS Appl. Nano Mater.* **2021**, *4* (8), 8626–8636. https://doi.org/10.1021/acsanm.1c02268.

CHAPTER 2. THE EFFECTS OF STOICHIOMETRY ON THE PROPERTIES OF EXSOLVED NI-FE ALLOY NANOPARTICLES FOR DRY METHANE REFORMING

The text of this dissertation chapter, in full, is a reprint of the material as it appears in "The effect of stoichiometry on the properties of exsolved Ni-Fe Alloy Nanoparticles for Dry Methane Reforming" published in AIChE Journal, 2020. The text has been modified to fit the dissertation guidelines. The co-author Dr. Kandis Leslie Gilliard-Abdul-Aziz listed in that publication directed and supervised the research which forms the basis for this dissertation chapter.

2.1 Abstract

The dry reforming of methane has received notable attention as a chemical process to convert natural gas into value-added chemicals and fuels. Ni-based exsolution catalysts using perovskite oxides supports have been used for their attractive sinter-resistance and coke-resistance properties. The perovskite oxide in itself has unique defect chemistry that can be used to manipulate and control the properties of the catalyst nanoparticles exsolved on the surface, therefore influencing both the nanoparticle and support characteristics. In this study, the La:Fe ratio of Ni-doped $LaFeO_3$ was used to manipulate and control the properties of exsolved Ni-Fe alloy nanoparticles. The Ni-Fe nanoparticles consisted of different sizes ranging from 10 – 380 nm. Temperature programmed surface reaction studies along with materials characterization with SEM, STEM-HAADF, XRD and BET showed that the Ni-Fe nanoparticles from different solid precursors have the same active sites for methane activation but differ in performance and stability because of size effects, metal-support strength, composition and support basicity. A mechanism is proposed to decipher the merits of the Ni-Fe nanoparticles with the best activity, selectivity, and stability in this study.

2.2 Introduction

Dry methane reforming (DRM) reaction is an endothermic process used for the production of synthesis gas, H_2 and CO, from the conversion of two greenhouse gases, CH_4 and CO_2[1]. The ideal ratio for the production of H_2:CO is unity or above, which is suitable for further valorization to methanol[2] and other liquid fuels via the Fischer-

Tropsch process[3,4] (Reaction 1). Reverse water gas shift (RWGS) is a competitive side reaction that hinders the attainment of the optimal H_2:CO ratio through consumption of CO_2 (Reaction 2).

Dry methane reforming

$$CH_4 + CO_2 \leftrightarrow 2CO + 2H_2 \qquad \Delta H^{\circ}_{298K} = 247.3 \text{ kJ/mol} \qquad (1)$$

Reverse water-gas shift reaction

$$H_2 + CO_2 \leftrightarrow CO + H_2O \qquad \Delta H^{\circ}_{298K} = 41.1 \text{ kJ/mol} \qquad (2)$$

DRM has received notable attention as a green chemical reaction to convert greenhouse gases, biogas[5,6,] or natural gas[7] into value-added chemicals and fuels. The practical industrial implementation of DRM has limitations due to the high temperatures needed to produce synthesis gas. The common deactivation mechanism for DRM heterogeneous catalysts is sintering and coke formation[8] through the Bouduard reaction and methane cracking (Reaction 3 and 4).

Boudouard reaction

$$C + CO_2 \leftrightarrow 2CO \qquad \Delta H^{\circ}_{298K} = 159.9 \text{ kJ/mol} \qquad (3)$$

Methane cracking

$$CH_4 \leftrightarrow C + 2H_2 \qquad \Delta H^{\circ}_{298K} = 86.3 \text{ kJ/mol} \qquad (4)$$

Ni is an economical and active catalyst for the scission of C—H and C—C bonds for the production of H_2 and CO[9,10]. Despite their advantages, the use of supported Ni catalysts tends to deactivate through sintering and accumulation of coke, limiting their stability and catalyst lifetime. Catalyst development efforts to extend their longevity takes

advantage of support effects[11] or alloying of metals[12–14] to alleviate common deactivation mechanisms for DRM.

One strategy to prolong the performance for Ni catalysts includes forming bimetallic alloys with another metal[13–17]. In addition to possible synergistic interactions that may promote the activity and selectivity, in some cases, the nanoparticle exhibits increased stability with changes in the sintering rate and coke formed. For example, the synergistic effects between Ni and Co in Ni-Co bimetallic nanoparticles improved the stability and activity with the proliferation of coke that did not deactivate the catalysts[16]. Ni-Fe bimetallic catalysts supported on alumina decomposed into pseudo-Ni@FeO_x phases due to oxidation of Fe by CO_2[15]. The lattice oxygen from the FeO_x species promoted the gasification of carbon deposits using a Mars-van Krevelen mechanism. The pairing of Ni with other transition and precious metals such as Mn[18] and Cu[19], Au[20,21], Ag[22], and Pt[10,28,] have been studied for enhancement of performance and activity[13].

Another frequently used catalyst synthesis strategy is the utilization of select supports that decrease the occurrence of sintering or coking by increasing the catalyst metal-support strength, changing the primary coke structure, or gasification of deposited carbon. In the case of supports for Ni, many are oxides that have been used, including CeO_2[11], ZrO_2[23], SiO_2[24,25], Al_2O_3[26], La_2O_3[27–30], and activated carbon[31]. A select group of mixed oxides used as smart or intelligent supports can promote the stability and activity of Ni for DRM[32–41]. The exsolved nanoparticles are highly dispersed, and nucleation involves strong adherence to the oxide surface[33,42–44]. This improved metal-support interaction has been coined as “socketed” with marked stability that is impervious to

sintering and coke formation[33]. The use of $LaFeO_3$ as an exsolution catalyst support has excellent properties for DRM, where the perovskite oxide can activate the methane molecule, promoting the reaction and exhibiting bifunctionality[45].

Prior studies have explored how the bulk point defects of the smart catalyst precursors can change the size of exsolved Ni catalysts[46,47]. For example, introducing bulk oxygen vacancies and A-site cation vacancies in the bulk of perovskite oxide catalysts can induce a higher density of exsolved nanoparticles with sizes ranging from 100 – 300 nm[46,47]. A theory was developed that postulated a high concentration of A-site vacancies could cause a perturbance of the unit cell, which promotes the exsolution of B-site cations onto the surface. However, the large nanoparticle sizes minimize the number of Ni active sites, which are not sufficient for thermocatalytic applications. However, this finding that connects the bulk defect chemistry of the perovskite oxide catalyst precursor to the properties of the exsolved catalyst nanoparticles can be extended to the rational design of Ni-based catalysts. We surmise that careful manipulation of bulk defects can tailor the size, shape, and composition of nanoparticles to potentially tune the activity, selectivity, and stability of Ni-based catalysts for DRM.

In the present study, we report the preparation of Ni-doped $LaFeO_3$ samples, where the changes in the La:Fe stoichiometric ratio was used to manipulate the size, shape, and composition of exsolved Ni-based bimetallic catalysts. Changes in the La:Fe ratio qualitatively either increased vacancies and interstitials in the bulk of the solid catalyst precursor producing a dynamic response that influences the nucleation and growth of nanoparticles. The use of changing the A:B cation ratio can tailor the dynamic

response of perovskite catalyst solid precursors in a reducing environment and control the distribution and chemical composition of exsolved nanoparticles. This study serves to elucidate the structural implications for the exsolved nanoparticle properties, namely how these nuanced changes in the bulk defects of the catalyst precursor can change the size, shape, and composition of Ni-Fe catalysts for DRM. Essentially, using defect engineering to control the catalyst nanoparticle and support properties.

2.3 Experimental Section

2.3.1 Catalyst Preparation

The solid catalyst precursors were synthesized using a modified citric acid sol-gel Pechini method[48]. Stoichiometric quantities of $La(NO_3)_3 \bullet 6H_2O$, $Fe(NO_3)_3 \bullet 9H_2O$, $Ni(NO_3)_2.6H_2O$ were dissolved in deionized water to reflect either a La:Fe molar ratio of 1:1, 0.9:1 and 1:0.9. The citric acid (3 mols/ 1 mol of perovskite) and ethylene glycol (1 mol/1 mol of perovskite) were subsequently added dropwise to the solution at a temperature heated between 50 – 60°C. The citrate solution was dried overnight at 110°C. The resultant xerogel was ground finely in a mortar & pestle and calcined at 700°C in the air for four hours with a heating ramp rate of 5°C/min. The compositions of the precursor catalysts for this study followed the stoichiometry of either $La_{0.9}FeNi_{0.1}O_{3-\delta}$ (LFNO 0.9:1), $LaFe_{0.9}Ni_{0.1}O_{3-\delta}$ (LFNO 1:0.9) and $LaFeNi_{0.1}O_{3-\delta}$ (LFNO 1:1). The samples were reduced in a furnace under an environment of 5 vol% H_2 and 95 vol % He at 700°C for two hours to promote the exsolution of nanoparticles from the bulk of the materials before catalyst testing (**Figure S2.1**).

2.3.2 Catalyst Characterization

The surface areas were determined from N_2 isotherms using Brunauer-Emmett-Teller (BET) at 78 K, after the evacuation of the sample at 453 K for 8 hours. Temperature Programmed Reduction (TPR) was conducted in a quartz tube microreactor (Hiden Analytical CATLAB) to 700°C at 10°C/min ramp rate and then held for another two hours. Crystalline phases of the samples as-prepared and after reduction, were analyzed with X-ray Diffraction (XRD) on a PANalytical Empyrean Series 2 with a step-size of 0.026° and dwell time of 30 seconds. Rietveld refinement calculations were done using the FullProf suite[49]. Scanning Electron Microscopy (SEM) was done on an SEM FEI NNS450 to check for macroscopic nanoparticle dispersion, size, and surface morphology. Analysis of the SEM images for particle size distribution was done using the ImageJ software[50]. The atomic resolution images of the samples were acquired using Scanning Transmission Electron Microscopy (STEM) on a JEOL Grand ARM300CF TEM/STEM with double spherical aberration-correctors operated at 300kV STEM High-angle annular dark-field (HAADF) imaging mode. Simultaneously, the elemental mapping via energy-dispersive X-ray spectroscopy (EDS) was collected by the large angle dual dry solid-state 100 mm^2 detectors.

2.3.3 Methane Reforming Catalytic Testing

Dry methane reforming was conducted in a fixed-bed reactor at atmospheric pressure. The steady-state conversion of CH_4 and CO_2, respectively, as a function of reaction temperature, was carried out using 100 mg of catalyst supported by silica wool. Before catalytic testing, the catalysts were reduced at 700°C in 5%H_2/95%He, 60 ml/min

of gas flow rate, to promote exsolution of the catalysts to form Ni-Fe nanoparticles. After reduction, the sample was cooled to room temperature under He flow. The catalytic feed mixture of 5% CH_4, 5% CO_2, and balance He and a total flow rate of 60 mL/min. Stability tests were done for 24 hours at 700°C. The concentrations of CO and H_2 in the reactor effluent was analyzed by a Hiden Quantitative Gas Analyzer (QGA) mass spectrometer. Prior to conversion testing, the mass spectral response for CH_4, CO_2, H_2 and CO was calibrated by calculating relative sensitivity factors for known concentrations of each gas diluted with helium. As measured using STEM and SEM, the particle sizes for the powders were between 3 – 5 μm. Calibration tests monitoring the mass spectral response, with and without the catalyst bed, determined that there was minimal pressure drop in the reactor. The quantification of the conversion values from subsequent experiments was calculated from the mass spectral response and measured gas flow rates from the outlet.

2.3.4 CO_2 Temperature Programmed Desorption

CO_2 Temperature Programmed Desorption experiments were carried out in the same Hiden Analytical CATLAB setup. Catalysts were reduced in the same conditions as described in the TPR. After reduction, 50 ml/min CO_2 (10%/He) was flown over the catalyst for 1 hour at 50°C, following which temperature was increased at 10°C/min in He flow. Mass spectral responses were used to calculate molar flow rates of desorbing gases, which were then integrated over time to calculate total moles desorbed.

2.3.5 Temperature-Programmed Surface Reaction Experiments

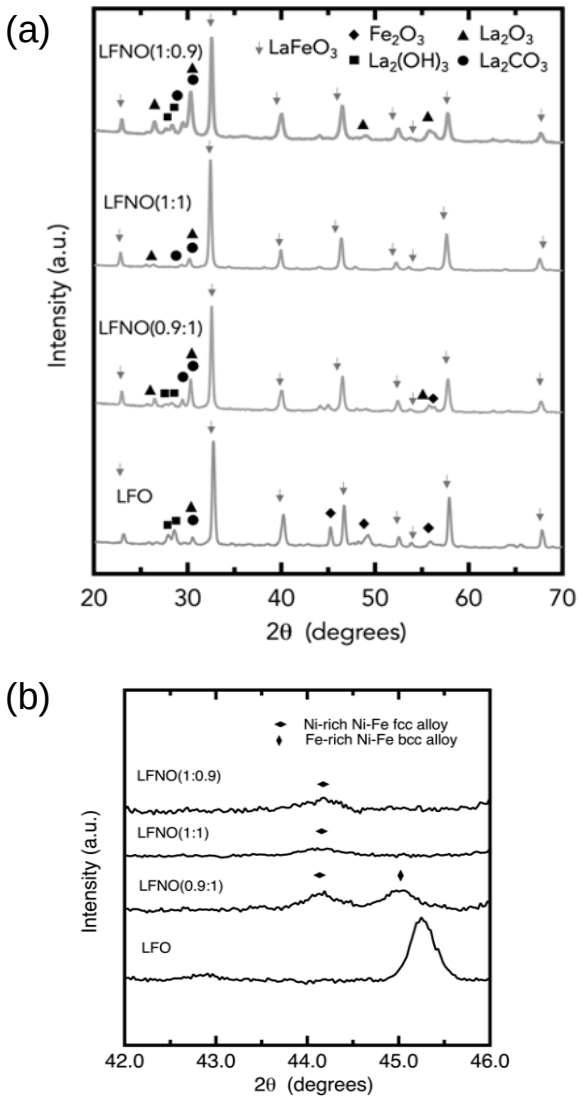

Figure 2.1: (a) XRD of LFO, LFNO(0.9:1), LFNO (1:1) and LFNO(1:0.9) after reduction at 700 °C (b) XRD of LFO, LFNO(0.9:1), LFNO (1:1) and LFNO(1:0.9) showing the formation of Ni-Fe alloy nanoparticles.

DRM Temperature-programed surface reaction helps delineate the difference in the reactivity of the Ni-based catalysts for methane activation[51,52]. For temperature-programmed surface reaction (TPSR) experiments, 100 mg of the catalyst was loaded into the reactor. Before measurement, the catalyst was reduced at 700°C in 5%H_2/95%He for 2 hours. The sample was cooled to room temperature under He flow of 40 mL/min. Once cooled to room temperature, the temperature was increased to 700°C in an environment analogous to catalytic testing at a rate of 10°C/min. The reactor effluent and desorbed gases were analyzed by Hiden Quantitative Gas Analyzer (QGA) mass spectrometer.

2.4. Results and Discussion

2.4.1 Structural Characterization of Solid Catalyst Precursors

XRD with Rietveld refinement was used to determine the crystallinity of the materials before and after the exsolution of the catalyst nanoparticles. The XRD of the as-prepared catalyst precursors and undoped $LaFeO_3$ (LFO), shows the formation of the orthorhombic structure of $LaFeO_3$ (**Figure 2.1**, **Table S1.1**). A similar XRD diffraction pattern was observed for LFNO(0.9:1), LFNO(1:1), and LFNO(1:0.9) samples with no impurity peaks or apparent segregation of the oxide phases. The XRD patterns show that the Ni dopant has full solubility in the perovskite oxide lattice in all instances where it may reside as either substitutional sites or possibly as interstitials in the lattice or grain boundaries[53]. After reduction at 700 °C for 2-hours, there is partial segregation of Fe_2O_3, La_2O_3, and $La_2(OH)_3$ from LFO (**Figure 2.1a**). LFNO(0.9:1), LFNO(1:1), and LFNO(1:0.9) after reduction also shows varying degrees of segregation of La_2O_3, $La_2(OH)_3$ and Fe_2O_3 from the perovskite lattice. In comparison to LFO, the LFNO(0.9:1), LFNO(1:0.9), and LFNO(1:1) samples had minimal exsolution of the Fe_2O_3 phases. The dissolution behavior of the catalysts is corroborated by prior studies where exsolution for near stoichiometric systems (those with a low concentration of vacancies) promotes the exsolution of AO species while A-site deficient materials preferably exsolve B-cations[33,46]. New reflections at 44.2° and 45.1° 2θ (**Figure 2.1b**) shows the formation of predominantly Ni-Fe alloy nanoparticles for all catalyst materials[54].

Rietveld refinement measurements were used to compare the lattice constants and unit cell volume for the as-prepared and reduced catalyst precursors (**Table S1.1**).

Compared to as-prepared LFO, the as-prepared LFNO(0.9:1) and LFNO(1:0.9) decreased in unit cell volume by 0.12% and 0.44%, respectively. The reduction in the unit cell volume is most likely attributed to the engineered vacancies and the smaller radii of Ni^{3+} substitution of Fe^{3+} in the lattice. The as-prepared LFNO(1:1) catalyst, when compared to LFO, expanded in volume by 0.44%, which is attributed to the chemical expansion of the dopant of Ni either occupying lattice and interstitial sites[55]. After reduction at 700 ºC, LFNO(0.9:1), LFNO(1:1) and LFNO(1:0.9) unit cell volume increase due to the thermo-chemical expansion caused by the reduction of the B-cations, Fe^{3+} to Fe^{2+} or Fe^{0} and Ni^{3+}/Ni^{2+} to $Ni^{0,}$ that generally have larger ionic radii. The increase in oxygen vacancies and small changes in the symmetry could also contribute to the volume expansion of the unit cell[55].

STEM-HAADF with EDX mapping confirmed the alloying of Ni and Fe after exsolution (**Figure 2.2**, **S2.3**, **S2.4**, and **S2.5**). Elemental analysis of the exsolved nanoparticles showed that the stoichiometric deficiencies resulted in nanoparticle compositions that vary based on the stoichiometric ratio. **Table S2.2** shows the measured Ni:Fe ratio for LFNO(0.9:1) is 0.99 while the Ni:Fe ratio for LFNO(1:0.9) is 0.36 and LFNO(1:1) is 0.15. The images confirm the alloying of Ni and Fe to form bimetallic nanoparticles. It is presumed that the composition of these nanoparticles is dictated by the bulk concentration of defects as well as the diffusivity of the dopant catalyst atoms[33]. The textural parameters of the catalysts were measured with BET and are

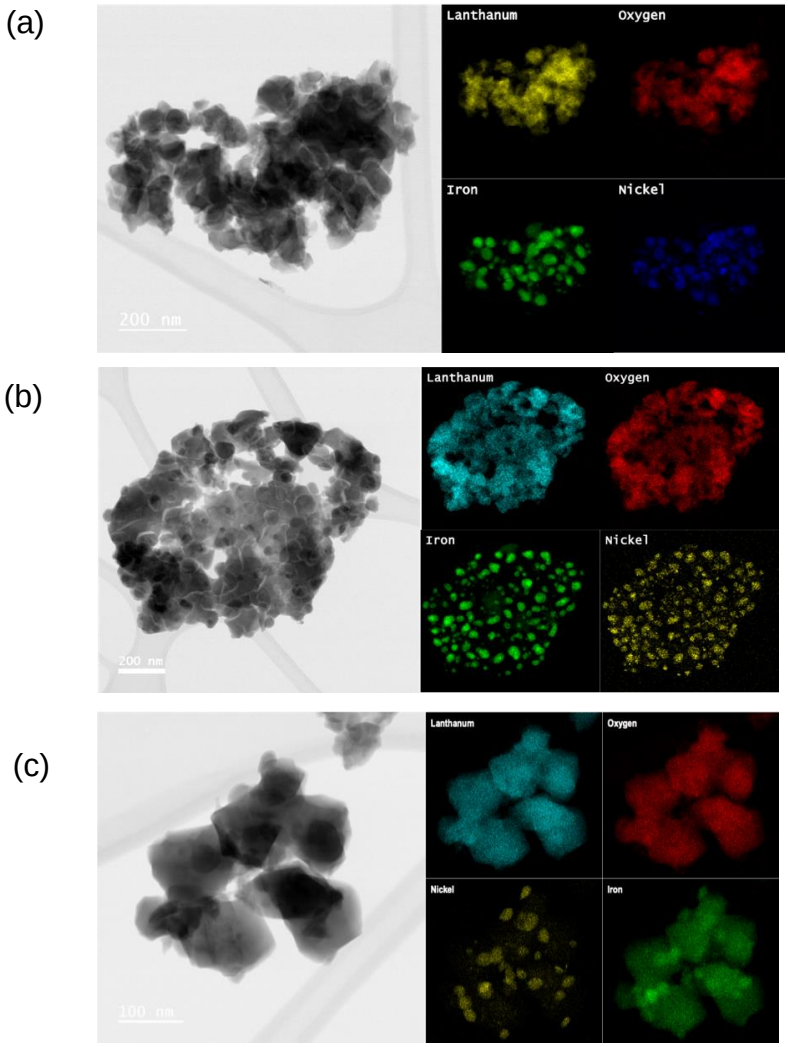

Figure 2.2: STEM-HAADF and EDS mapping of the catalysts (a) LFNO(0.9:1), (b) LFNO (1:1) and (c) LFNO(1:0.9) after reduction at 700°C.

Table 2.1: The surface area, pore size, and hydrogen consumption of the developed catalysts.

Catalyst	BET surface area (m^2/g)	BJH pore size (nm)	Hydrogen Consumption (mmol/100mg)
LFNO(0.9:1)	6.27	13.1	0.076
LFNO(1:0.9)	14.0	52.5	0.177
LFNO(1:1)	10.8	24.2	0.177
Ni/α-Al_2O_3	17.0	16.5	----------

compared in **Table 2.1**. The pore size and pore volume are shown in **Table S2.3**. Among the three catalysts, LFNO(0.9:1) had the smallest surface area of 6.3 m^2/g with a pore volume of 0.059 cm^3/g. The sample with the largest surface area was LFNO (1:0.9), with a surface area of 14 m^2/g and a pore volume of 0.19 cm^3/g. The LFNO (1:1) has a BET surface area of 10.8 m^2/g and a pore volume of 0.062 cm^3/g, comparable to the LFNO (0.9:1) sample. The differences in the surface area and pore volume are attributed to the different sizes of the exsolved nanoparticles and morphology.

The morphology of the samples after exsolution was determined using scanning electron microscopy (**Figure S6**). The SEM images show the exsolution of large spherical nanoparticles ranging in size for LFNO(0.9:1) from 100 – 380 nm after 700°C in 2 hours of 5%H_2/He. The presence of large Ni-Fe nanoparticles confirms the influence of A-site vacancies on lowering the barrier for Ni and Fe exsolution on the surface of the catalyst precursor. In the case of LFNO(1:0.9), the sizes of the nanoparticles are much smaller, with the appearance of nanoparticles between 12 – 61 nm on the surface. The LFNO(1:1) nanoparticles are semi-spherical, with a slightly elliptical shape indicative of strong interaction with the support. The exsolved nanoparticles from LFNO(1:0.9) are smaller, ranging in size from 18 – 60 nm. The dispersion for the catalysts was calculated from the mean diameter size of the nanoparticles, as shown in Table S2.2. The LFNO(0.9:1) dispersion was 0.45% while that of LFNO(1:1) and LFNO(0.9:1) was 3.0%. The differences in the dispersion are attributed to the marked size differences of the exsolved nanoparticles. The presence of bulk A-site vacancies in LFO(0.9:1) lowers the barrier for the exsolution of the B-cations as a way to form predominantly pristine

bulk $LaFeO_3$[46]. This results in a larger concentration of Ni and Fe exsolution on the surface of LFNO(0.9:1) while there is minimal exsolution from both LFNO(1:0.9) and LFNO(1:1).

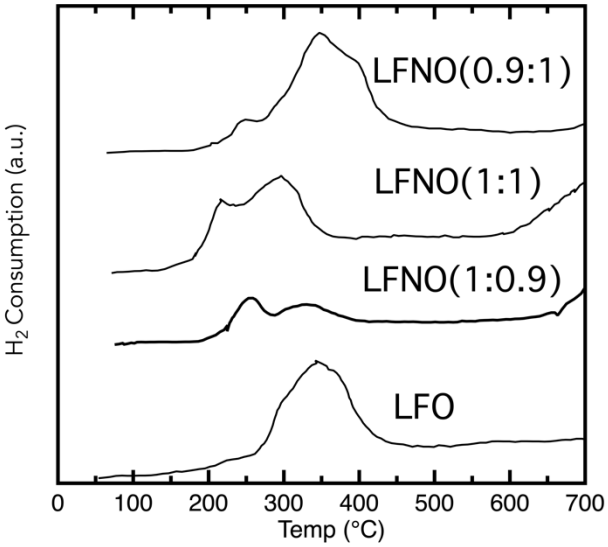

Figure 2.3: TPR of LFNO(0.9:1), LFNO (1:1) and LFNO(1:0.9). The reduction behavior of the catalyst precursors shows the reduction of the B-cations, Fe and Ni, respectively, as a function of temperature.

To measure the change in the reducibility behavior of the prepared solid catalysts, we employed TPR. The TPR reduction profiles for LFO, LFNO(0.9:1), LFNO(1:0.9), and LFNO(1:1) are shown in **Figure 2.3**. The hydrogen consumption is listed in Table 2.1. The broad peak at ~350 °C for LFO is contributed to the reduction of Fe^{3+} to Fe^{2+} and Fe^{2+} to Fe^{1+} in the lattice of LFO. In LFNO(1:0.9), there are two discernible peaks. The first peak at 252 °C most likely arises from the reduction of bulk substitutional Ni^{3+} to Ni^{2+}. The broad, shallow peak at 341 °C is attributed to the reduction of bulk Fe^{3+} to Fe^{2+} and Ni^{2+} to Ni^{1+} or Ni^{2+} to Ni^{0}. The lower temperature for the reduction of the Fe^{3+} reduction peak is due to the interactions between Ni and Fe. For LFNO(1:1), the first peak shifts to 227 °C and is attributed to the reduction of Ni^{3+} to $Ni^{2+,}$ and the peak at 275 °C is associated with Fe^{3+} to Fe^{2+} and Ni^{2+} to Ni^{0}. For LFNO(0.9:1), the small peak at 252 °C is attributed to the reduction of Ni^{3+} to Ni^{2+} in the

lattice. The noticeably smaller peak may indicate the lower concentration of Ni in the bulk as substitutional sites. It could be that the Ni resides as interstitials or in grain boundaries. The peak at 352 °C is the reduction of Fe^{3+} to Fe^{2+} and the reduction of Ni^{3+} to Ni^{2+}. The shoulder at 405 °C could be the reduction of Fe^{3+} to Fe^{2+} in the grain boundaries or Fe^{2+} to Fe^{0}. The difference in the reduction behavior and hydrogen consumption (Table 2.1) indicates a sensitivity of the perovskite structure to the inherent defects present in the catalyst precursors. The reduction profile of LFNO(0.9:1) is much closer to that of LFO, showing that the Ni interaction in the lattice is possibly weaker than the other samples. We surmise that it could be that during reduction, NiO particles are formed and are reduced with the Fe in the lattice. The concentration of which will influence the size and composition of the Ni and Fe alloy nanoparticles exsolved on the surface of the catalyst.

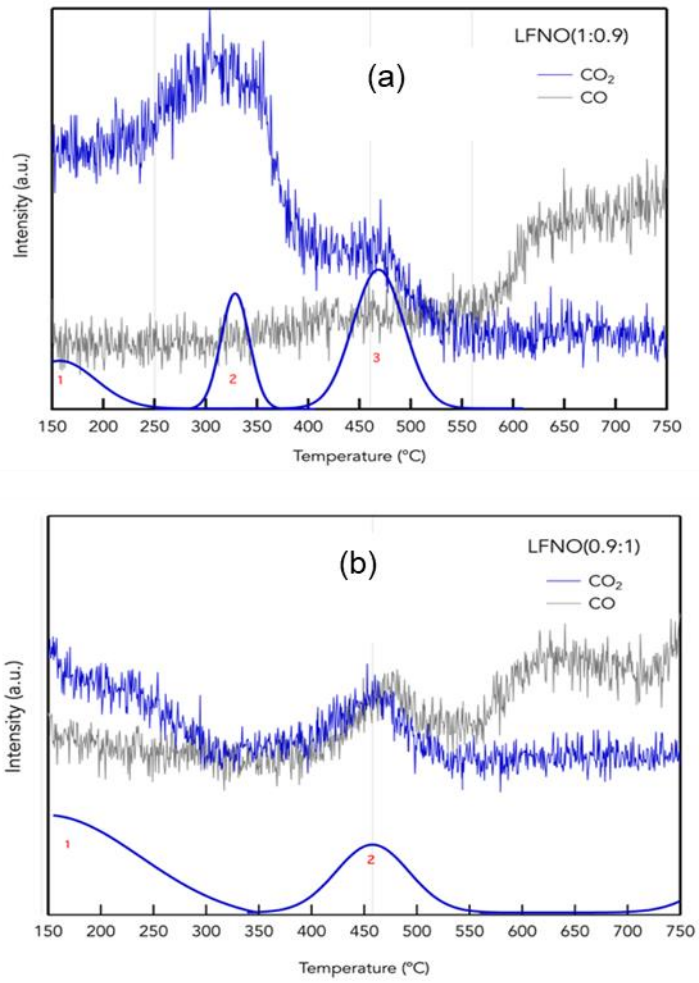

Figure 2.4: CO_2 TPD of (a) LFNO(1:0.9) and (b) LFNO (0.9:1). The CO_2 profiles were deconvoluted into Gaussian peaks. The numbered peaks represent the Gaussian used. The deconvolution was performed using Igor Pro 7 software. It was determined that (a) should be represented by the sum of 3 peaks while (b) is represented by 2 peaks.

CO_2 TPD was used to determine the strength of the basic sites for LFNO(1:0.9) and (0.9:1), who have different morphological responses after reduction at 700 °C. The desorption of both CO_2 and CO was monitored between 150 – 750 °C (**Figure 2.4**). The

CO_2 profile curves were deconvoluted into Gaussians using Igor Pro 7. The quantities of gases desorbed are tabulated in Table S2.4. For the LFNO (0.9:1), most of the CO_2 is desorbed as CO, while with LFNO (1:0.9), CO_2 is desorbed almost entirely as CO_2. In LFNO(1:0.9), three basic sites can be determined, a weak binding site at ~150°C while the peaks at 325°C and 460°C correspond to binding sites with medium strengths. The CO signal gradually increased with a rapid increase at ~600°C. This increase in CO is attributed to the reduction of the CO_2, which oxidizes the reduced perovskite and fills up O-vacancies[56]. For LFNO(0.9:1), there are two basic sites, one characterized as weak at ~150°C and another at ~460°C that has medium strength. Unlike LFNO(1:0.9), the CO signal for LFNO(0.9:1) almost overlaps that of CO_2, which may indicate a different type of active site for adsorption. Comparing the quantity of CO_2 evolved, the sample with La:Fe (1:0.9) had greater basicity than La:Fe (0.9:1). We surmise that the increased basicity of the LFNO(1:0.9) improves the activation of CO_2 for DRM, improving performance.

2.4.2 Catalytic Performance for Methane Dry Reforming

The DRM catalytic activity, selectivity, and stability were probed for a reaction temperature up to 700°C for LFNO(0.9:1), LFNO(1:1), and LFNO(0.9:1) to investigate the catalytic performance of the different Ni-Fe alloy nanoparticles properties. The catalytic activity of the catalysts is shown in **Figure 2.5**. The DRM conversions are compared to $LaFeO_3$ and 10 wt.% Ni/a-Al_2O_3 in **Table S2.5**. The catalysts were tested for their conversion between 100 - 700°C of CH_4 and CO_2 as well as the H_2:CO product ratio. The TPR indicates a correlation between the reduction behavior and the exsolution

mechanism of alloy nanoparticles where Ni-Fe alloying occurs during the reduction and exsolution process. Based on the conversion rates and activity measurements, the catalytic activity of the three catalysts is ranked as LFNO(1:0.9)>LFNO(1:1)>LFNO(0.9:1). The LFNO(1:0.9) catalyst achieved the best catalytic activity with the highest methane conversion of 79% and a CH_4 rate of 5.6 μmoles/s. g at 700°C. LFNO(1:1) shows comparable performance with 72% conversion and a methane rate of 4.73 μmoles/s. g. While that of LFNO(0.9:1) performed the worst for CH_4 conversion, with the highest conversion reaching 40% and a methane rate of 2.62 μmoles/s. g. The LFNO (1:0.9) performed the best in suppressing the reverse water gas shift reaction, which acts to lower the H_2:CO ratio below unity by reacting the hydrogen formed from DRM with CO_2 to form water.

The rates of reaction for various catalysts are tabulated in **Table S2.5**. Pristine $LaFeO_3$ and 10 wt% Ni/a-Al_2O_3 were used as control samples. The LFNO catalysts all performed better than pristine $LaFeO_3$ but were not as active as 10 wt% Ni/a-Al_2O_3. In the absence of Ni catalyst nanoparticles, CH_4 activation on pristine LFO proceeds through partial oxidation with labile lattice oxygen[57]. Given that 10 wt% Ni/a-Al_2O_3 has a comparable

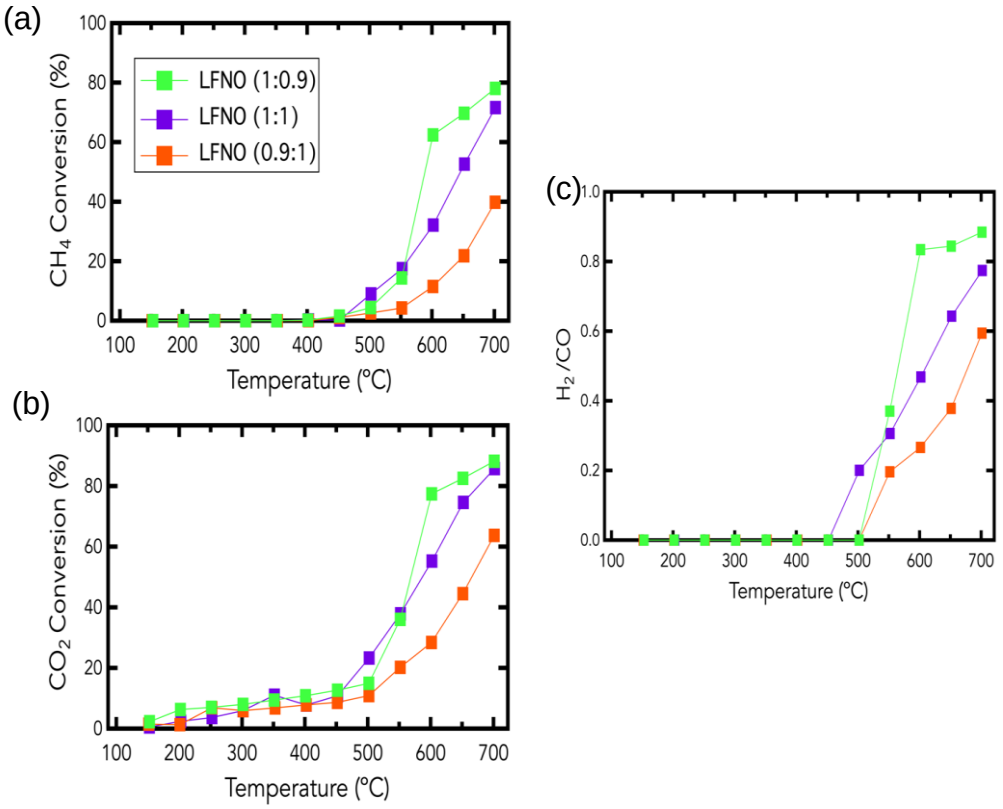

Figure 2.5: Catalytic activity of LFNO(0.9:1), LFNO (1:0.9) and LFNO (1:1). (a) CH_4 conversion and (b) CO_2 conversion. The H_2/CO ratio of LFNO(0.9:1), LFNO (1:0.9) and LFNO (1:1) are shown in part (c).

surface area (17 m^2/g) with the LFNO catalysts, we suspect that slight differences in the activity are due to the alloying of Ni with Fe. The alloying of Ni-Fe decreases the activity that can be achieved with Ni monometallic catalysts but improves the overall stability. The primary differentiating factors for the LFNO catalysts' performance are the size and composition of the exsolved Ni-Fe nanoparticles. LFNO(1:0.9) and LFNO(1:1) samples have similar Ni-Fe particle sizes and lower Ni content than that of LFNO(0.9:1). The lower Ni content will usually result in lower activity because large concentration of Fe promotes RWGS. A high Fe content in Ni-Fe catalysts can promote the gasification of coke but also suppress activity due to the reduced number of Ni surface concentration[15,58]. However, the alloying effects is not nearly as significant as the large performance difference caused by considerable particle growth and lower dispersion of Ni-Fe catalysts from LFNO(0.9:1) compared to LFNO(1:0.9) and

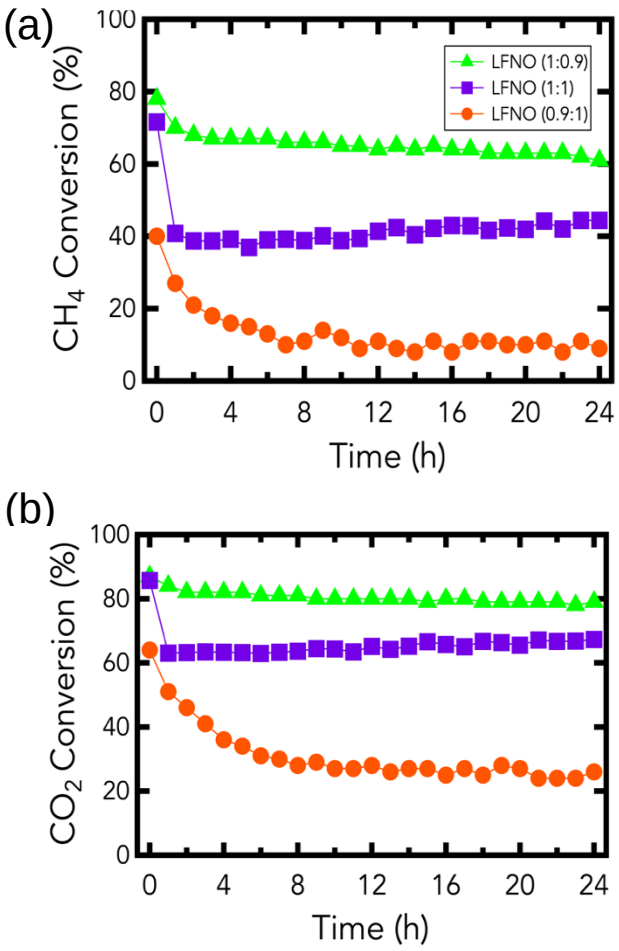

Figure 2.6: Stability of LFNO(0.9:1), LFNO (1:0.9) and LFNO (1:1) up to 24 hours on stream. (a) CH_4 conversion and (b) CO_2 conversion.

LFNO(1:1). Given the differences in the LFNO catalysts, it is difficult to parse the influence of the composition and size effects; however, it is essential to note that the composition seems to be governed by bulk defects and exsolution kinetics.

2.4.3 Stability of the Catalysts

The catalysts were aged up to 24 hours on stream to determine catalyst stability (**Figure 2.6**) and the surface was analyzed after aging using STEM-HAADF (**Figure 2.7**). **Figure 2.6** shows that LFNO(0.9:1) has a rapid decay in activity for both the CO_2 and CH_4 conversions while the LFNO(1:0.9) and LFNO(1:1) have comparatively improved stability. Analysis of the STEM-HAADF images shown in **Figure 2.7c** and **2.7g** and the elemental analysis in **Figure 2.7d, 2.7h** using EDX determined that there was coke residue with a measured carbon content around 3 wt% for LFNO(0.9:1) and 2.1 wt% for LFNO(1:0.9). The atomic analysis for the average catalyst nanoparticles for both systems also becomes Ni-rich Ni-Fe NPs after 24-hour aging where some of the FeO_x is re-introduced in the support. The formation of Ni-rich Ni-Fe NPs under DRM conditions is partially due to the presence of the Fe-FeO_x redox couple as corroborated by in-operando X-ray absorption studies[12]. The measured carbon content, however, was consistent across the catalyst and support material surface for all catalysts showing minimal coke formation. There was no evidence of filamentous forms of carbon for either of the catalysts. Despite the minimal coke residue, LFNO(1:0.9) was not significantly deactivated from coke formation in the form of relatively amorphous carbon on the catalyst surface. The inset in **Figure 2.7c** for LFNO(0.9:1) shows a mixture of amorphous and crystalline carbon on the surface of the Ni-Fe nanoparticles. The LFNO(0.9:1)

nanoparticles were completely deactivated after 24 hours, which is possibly due to the formation of graphitic coke. The LFNO(1:1) catalysts show a quick diminishment of activity initially but are stable at a lower conversion rate for both methane and carbon dioxide. The most stable catalyst was LFNO(1:0.9), where the smaller nanoparticles and larger surface area provided more stability. Primarily, the LFNO(1:0.9) catalyst performs the best in terms of activity, selectivity to $H_{2,}$ and overall stability.

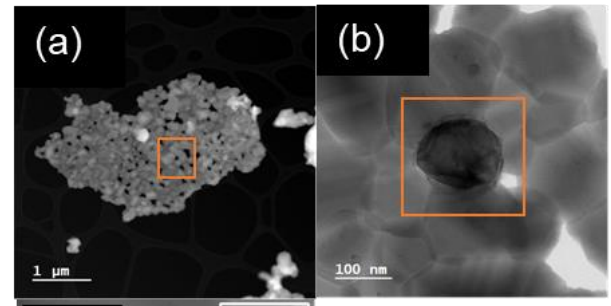

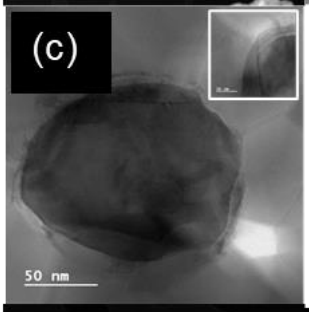

(d)

Element	Shell	Signal (counts)	Comp. (at.%)	Comp. (wt.%)	k-Factor	Det. Corr.
C	K	5127.5 ± 3.6	13.2	3.5	1.6	0.67
O	K	1.1e4 ± 3.6	16.7	5.9	1.3	0.79
La	L	3479.6 ± 7.5	0.86	2.6	1.7	0.98
Fe	K	4.2e4 ± 5.3	14.6	17.8	0.97	0.99
Ni	K	1.5e5 ± 5.5	54.6	70.2	1.0	1.0

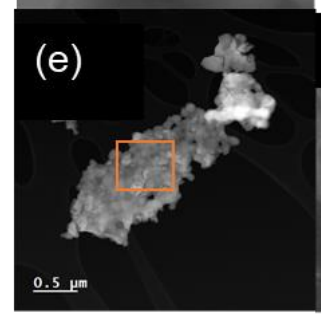

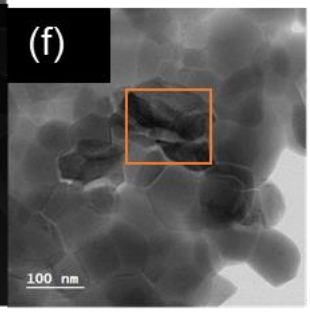

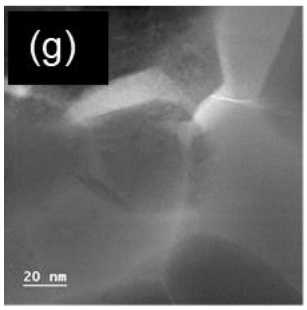

(h)

Element	Shell	Signal (counts)	Comp. (at.%)	Comp. (wt.%)	k-Factor	Det. Corr.
C	K	3720.3 ± 3.6	7.4	2.1	1.6	0.67
O	K	4.1e4 ± 3.6	49.7	19.0	1.3	0.79
La	L	5.3e4 ± 7.5	10.0	33.3	1.7	0.98
Fe	K	3.6e4 ± 5.3	9.6	12.8	0.97	0.99
Ni	K	8.6e4 ± 5.5	23.3	32.7	1.0	1.0

Figure 2.7: The STEM-BF HAADF images of 24 hour aged catalysts at different magnifications for (a)-(c) LFNO(0.9:1) with (d) elemental analysis within the measurement area of (b) and (e)-(g) LFNO(1:0.9) with (h) elemental analysis within the measurement area of (f). The inset of (c) shows the atomic resolution of the LFNO(0.9:1) nanoparticle.

2.4.4 DRM Temperature Programmed Surface Reaction

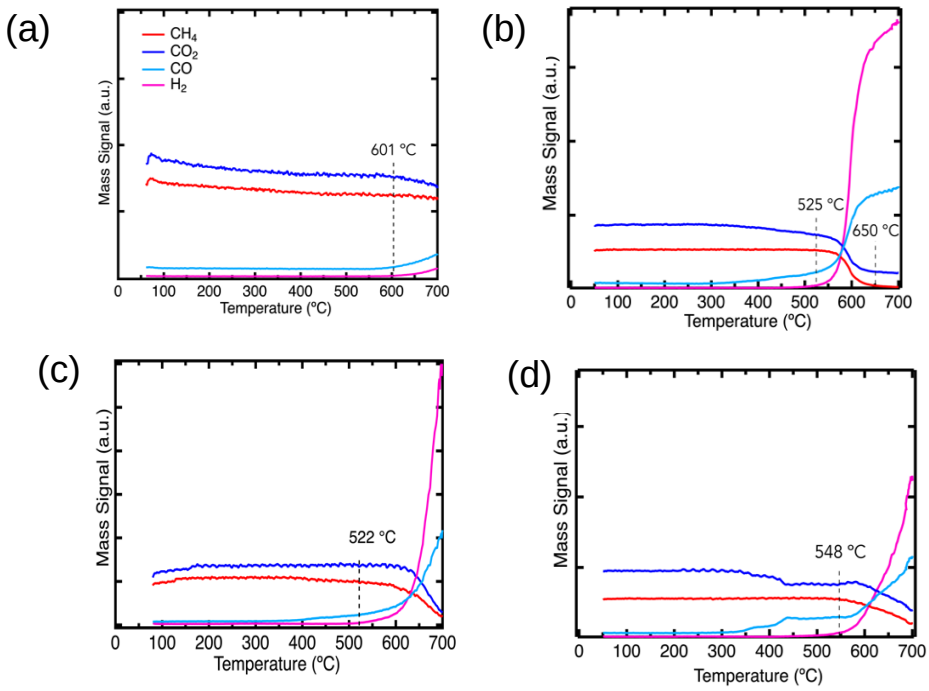

Figure 2.8: DRM TPSR mass response of (a) LFO, (b) LFNO(1:0.9), (c) LFNO(1:1) and (d) LFNO(0.9:1) after reduction at 700 °C.

DRM TPSR was employed to investigate the difference in the reactivity and CH_4 activation of the catalysts. **Figure 2.8** shows the DRM TPSR for LFO, LFNO(0.9:1), LFNO(1:1), and LFNO(1:0.9). The associated CH_4 activation temperature for LFO, LFNO(0.9:1), LFNO(1:1), and LFNO(1:0.9) occurs at 601°C, 548°C, 522°C and 525°C, respectively. TPSR for the support, LFO, shows minimal activation of the CO_2 and CH_4 starting at ~601°C producing CO-rich syngas. Presumably, the lattice Fe in pristine LFO promotes the RWGS reaction, while CH_4 is activated via the partial oxidation pathway with the lattice oxygen. For LFNO(0.9:1), there was a slight decrease of CO_2 starting at ~340°C that plateaued at ~440°C with a concomitant increase in CO. After CH_4

activation, the CO_2 and CH_4 concentrations decreased while the CO and H_2 increased. For LFNO(1:0.9), the CO_2 started to decline at ~340 °C with a continuous decrease in concentration until ~525°C when CH_4 was activated. Afterward, the CH_4 and CO_2 concentrations drastically decreased while the H_2 and CO concentrations rapidly increased, showing a much faster reforming reaction than LFNO(0.9:1). The activation of methane is complete at around 650°C showing effective activation of CH_4 and CO_2 within the temperature range studied. For LFNO(1:1), the CO_2 started to decline at ~350°C with a continuous decrease in concentration until ~522°C when CH_4 was activated. H_2 production for LFNO(1:0.9) and LFNO(1:1) exceeded that of LFNO(0.9:1) with an H_2/CO ratio of 0.88 and 0.8 versus 0.59. The maximum conversion for CH_4 for LFNO(1:0.9), LFNO(1:1) and LFNO(0.9:1)was 79%, 70% and 42%, respectively.

The TPSR results suggest that LFNO(1:0.9) and LFNO(1:1) is much more efficient in continuously producing syngas for industrial applications. Because the activation temperature is about the same, we presume that the active site is Ni; however, the marked performance difference is attributed to the increase in the number of active sites and larger surface area for the dehydrogenation of methane in LFNO(1:0.9) which is presumably more considerable than that of LFNO(1:1) and LFNO(0.9:1). The limiting factors for the performance of LFNO(0.9:1) is the lower number of Ni active sites on significantly larger nanoparticles resulting in lower CH_4 conversion rates and selectivity.

The LFNO catalysts were regenerated after 24-hour aging in 10%O_2/90%He for 2 hours, followed by a reduction in 5% H_2/He for 2 hours, both at 700°C. **Figure S2.7** shows the TPSR for the regenerated LFNO(1:0.9) and LFNO(0.9:1). The TPSR for

regenerated LFNO(1:0.9) indicates the activation temperature for CH_4 increases from 525°C to 580°C. The change in the CH_4 activation temperature is possibly contributed to a difference in the composition of the nanoparticle after regeneration. The conversion rates for the regenerated LFNO(1:0.9) is near the same values as that of the fresh catalyst, showing that the activity is reproducible. The TPSR for regenerated LFNO(0.9:1), however, shows a drastic decrease in the activity with a methane activation temperature increasing from ~548°C to ~615°C. A minimal amount of syngas was produced, and the CH_4 conversion rates decreased drastically from 2.6 μmoles/s.g to 0.55 μmoles/s.g. We surmise that the large Ni-Fe nanoparticles formed from LFNO(0.9:1) were not conducive to regeneration and re-introduction into the bulk of the perovskite matrix during the reoxidation cycle. The limited behavior displayed by LFNO(0.9:1) may indicate that the regenerability and sinter-resistance lauded for the use of exsolution or smart catalysts have limitations.

2.5. Conclusion

The catalytic activity of LFNO solid catalyst precursors was manipulated and tuned by a change in the La:Fe ratio, which ultimately influenced the exsolution behavior of the solid catalyst precursors. This study showed that a difference in the La:Fe ratio ultimately changed the composition, size, and dispersion of nanoparticles that influenced the overall activity, stability, and selectivity of the catalysts for DRM. The Physico-chemical characteristics, along with the catalytic performance of the materials, were studied using XRD, STEM-HAADF, SEM, BET, TPR, TPSR, and gas-phase reaction testing. The formed Ni-Fe alloy nanoparticles were active for the reforming reaction with

different activities and stabilities most likely connected to the composition and size of the exsolved nanoparticles. The best performer in terms of activity, selectivity, and stability was the LFNO(1:0.9) catalyst, where the larger surface area and basicity provided a separate active site for acidic CO_2 activation and the FeO_x of the alloyed nanoparticle gasified adsorbed carbon preventing blockage of Ni active sites. This study opens up avenues where stoichiometric manipulation of the catalyst precursor can potentially ensure that the formed catalysts are durable for prolonged performance in harsh conditions.

2.6. Supplementary Information

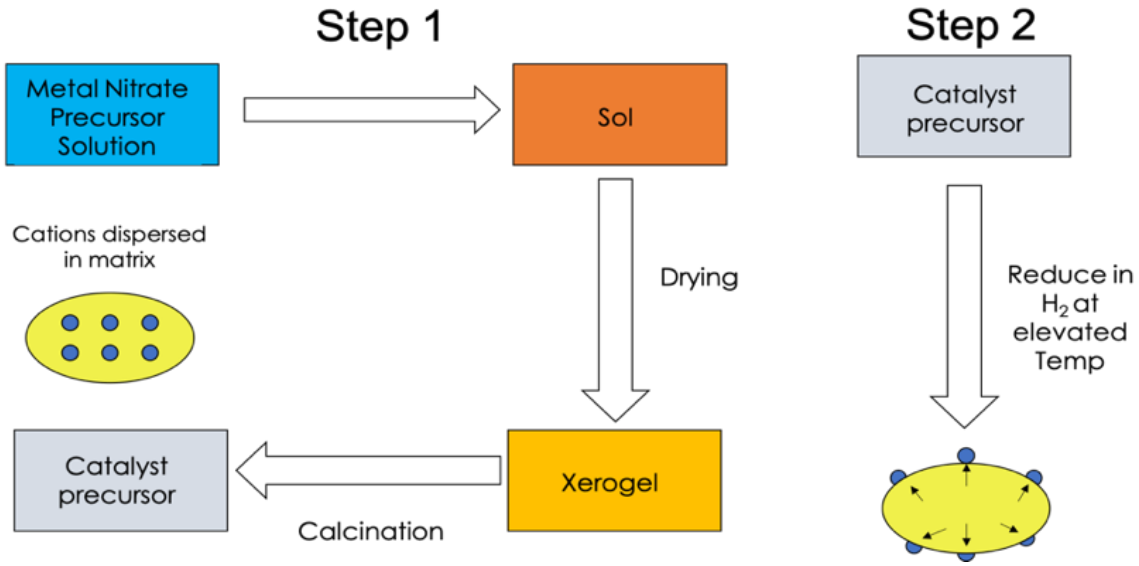

Figure S2.1 Schematic for the two-step process for the synthesis of the catalyst materials with step 1 as synthesis of the solid precursor using a modified sol-gel procedure and a subsequent reduction of the solid catalyst precursor at elevated temperatures in 5%H_2/He in step 2 to promote exsolution of the Ni-based metal catalyst.

2.6.1 X-ray diffraction and Rietveld Characterization Procedure

The measured XRD diffraction patterns were compared with the orthorhombic and cubic phase of $LaFeO_3$. The results obtained showed the best fit and agreement with the orthorhombic phase for all as-prepared and reduced materials. The results of the Rietveld refinement for the orthorhombic unit cell parameters is shown in Table S2.1.

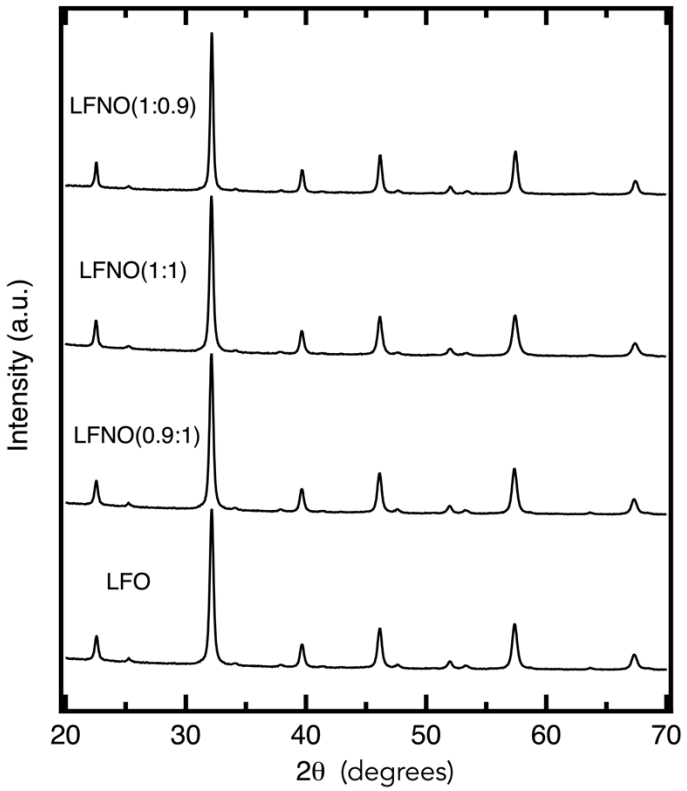

Figure S2.2: XRD of as-prepared LFO, LFNO(0.9:1), LFNO (1:1) and LFNO(1:0.9).

Table S2.1: Unit cell parameters and volume obtained by Rietveld refinement

Sample	Lattice Parameters			
	a (Å)	b (Å)	c (Å)	V ($Å^3$)
$LaFeO_3$ (as-prepared)	5.57	5.67	7.90	249.1
$LaFeO_3$ (reduced)	5.60	5.70	7.92	252.8
LFNO(0.9:1) (as-prepared)	5.57	5.66	7.90	248.8
LFNO(0.9:1) (reduced)	5.61	5.67	7.95	252.9
LFNO(1:0.9) (as-prepared)	5.56	5.67	7.87	248.0
LFNO(1:0.9) (reduced)	5.62	5.66	7.95	252.9
LFNO(1:1) (as-prepared)	5.57	5.66	7.94	250.2
LFNO(1:1) (reduced)	5.61	5.66	7.95	252.4

2.6.2 STEM – HAADF and Elemental Analysis

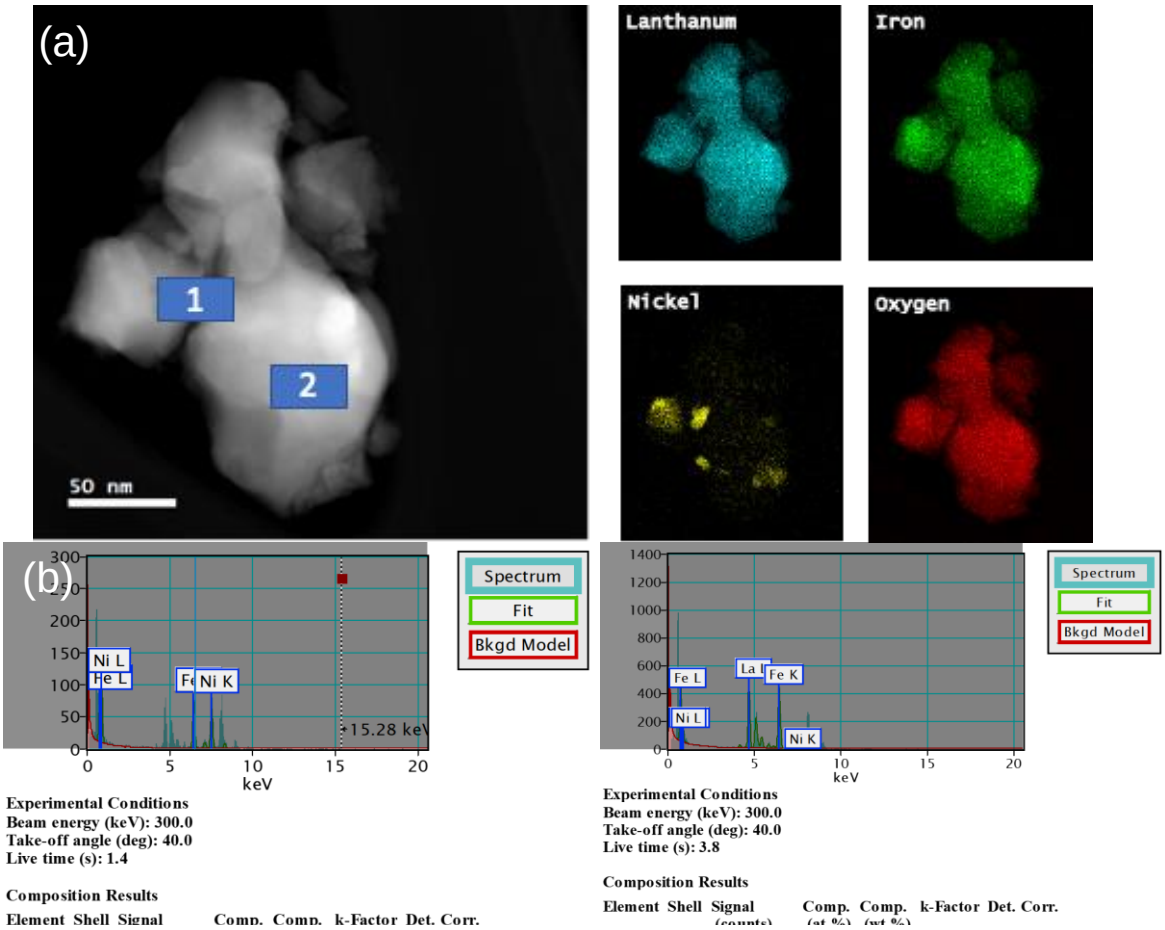

Figure S2.3: STEM – BF EDX images (a) with elemental analysis (b) of the cross-section of the exsolved nanoparticles of LFNO(0.9:1)

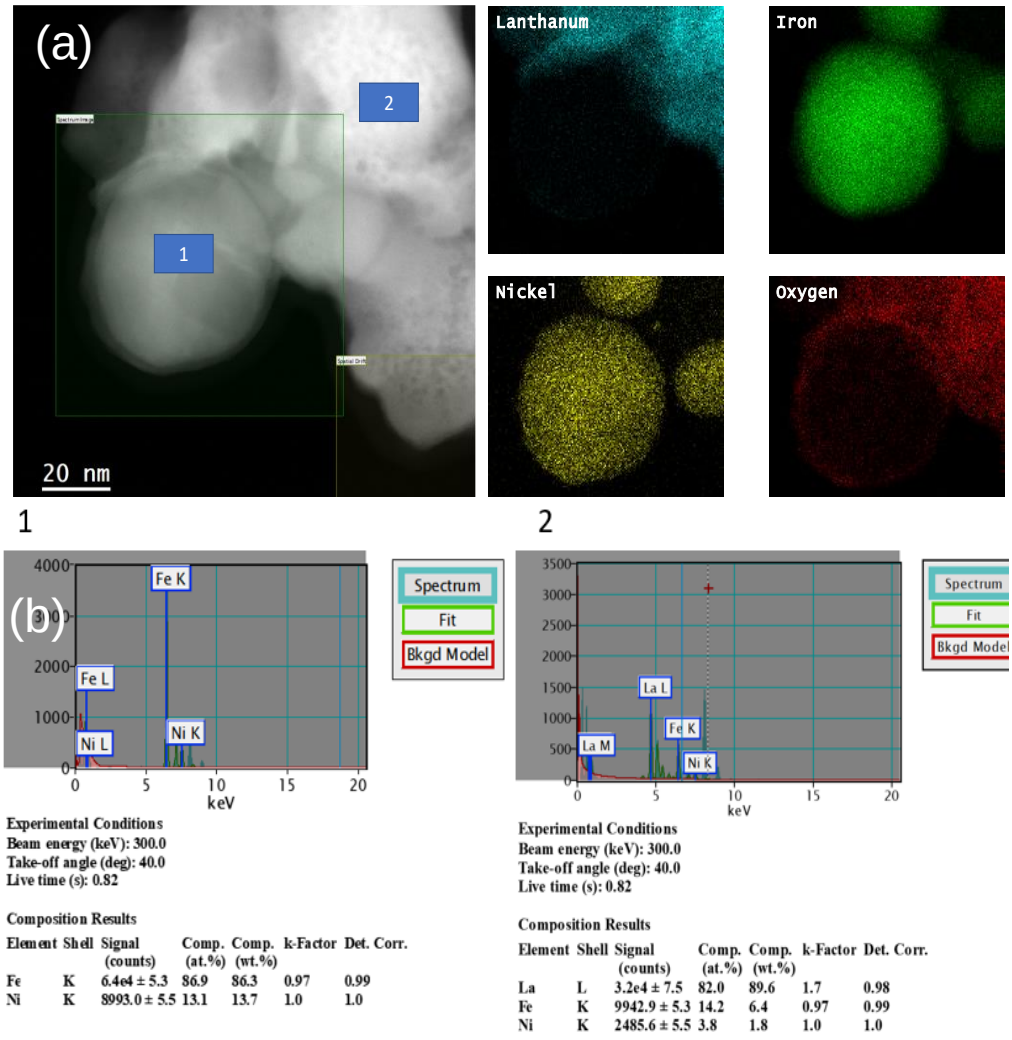

Experimental Conditions
Beam energy (keV): 300.0
Take-off angle (deg): 40.0
Live time (s): 0.82

Composition Results

Element	Shell	Signal (counts)	Comp. (at.%)	Comp. (wt.%)	k-Factor	Det. Corr.
Fe	K	6.4e4 ± 5.3	86.9	86.3	0.97	0.99
Ni	K	8993.0 ± 5.5	13.1	13.7	1.0	1.0

Experimental Conditions
Beam energy (keV): 300.0
Take-off angle (deg): 40.0
Live time (s): 0.82

Composition Results

Element	Shell	Signal (counts)	Comp. (at.%)	Comp. (wt.%)	k-Factor	Det. Corr.
La	L	3.2e4 ± 7.5	82.0	89.6	1.7	0.98
Fe	K	9942.9 ± 5.3	14.2	6.4	0.97	0.99
Ni	K	2485.6 ± 5.5	3.8	1.8	1.0	1.0

Figure S2.4: STEM – BF EDX images (a) with elemental analysis (b) of the cross-section of the exsolved nanoparticles of LFNO(1:1)

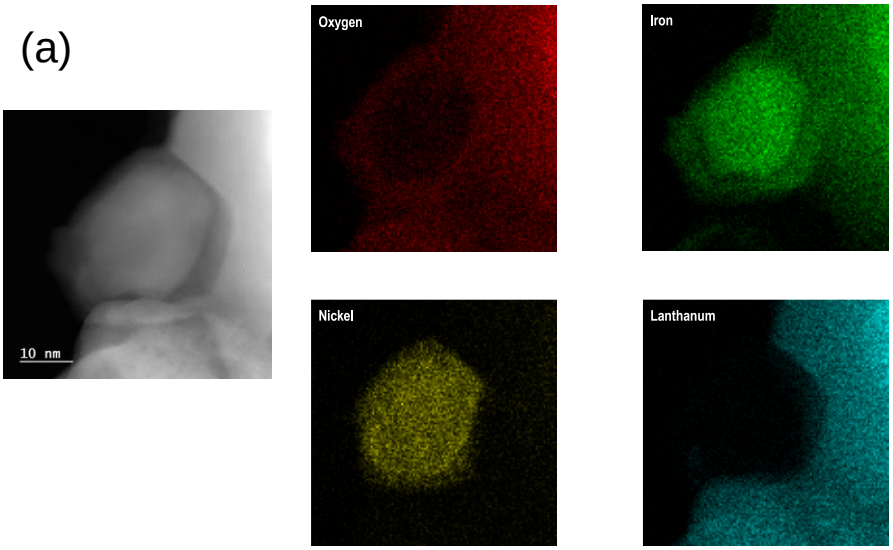

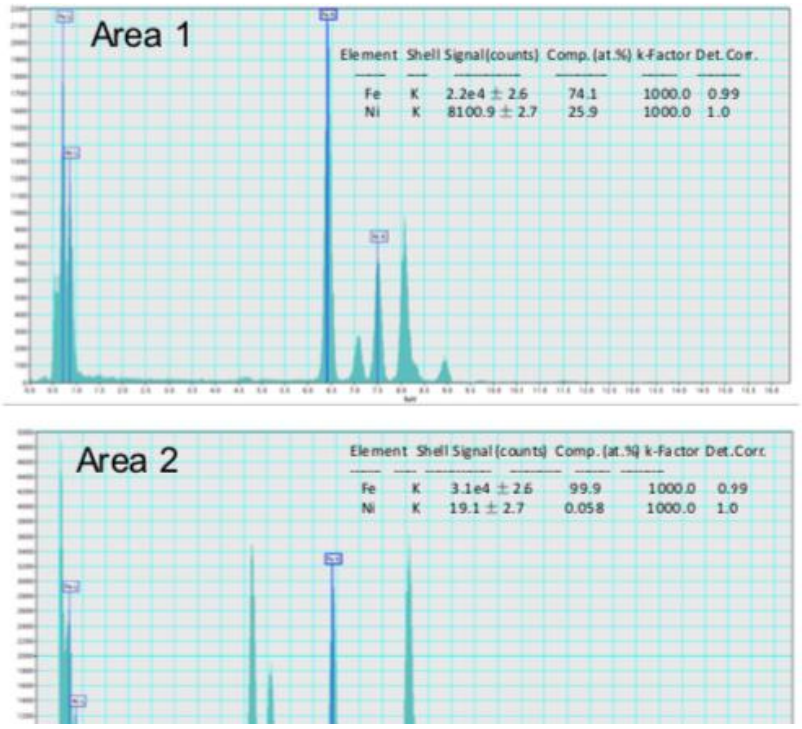

Figure S2.5: STEM – BF EDX images (a) with elemental analysis (b) of the cross-section of the exsolved nanoparticles of LFNO(1:0.9)

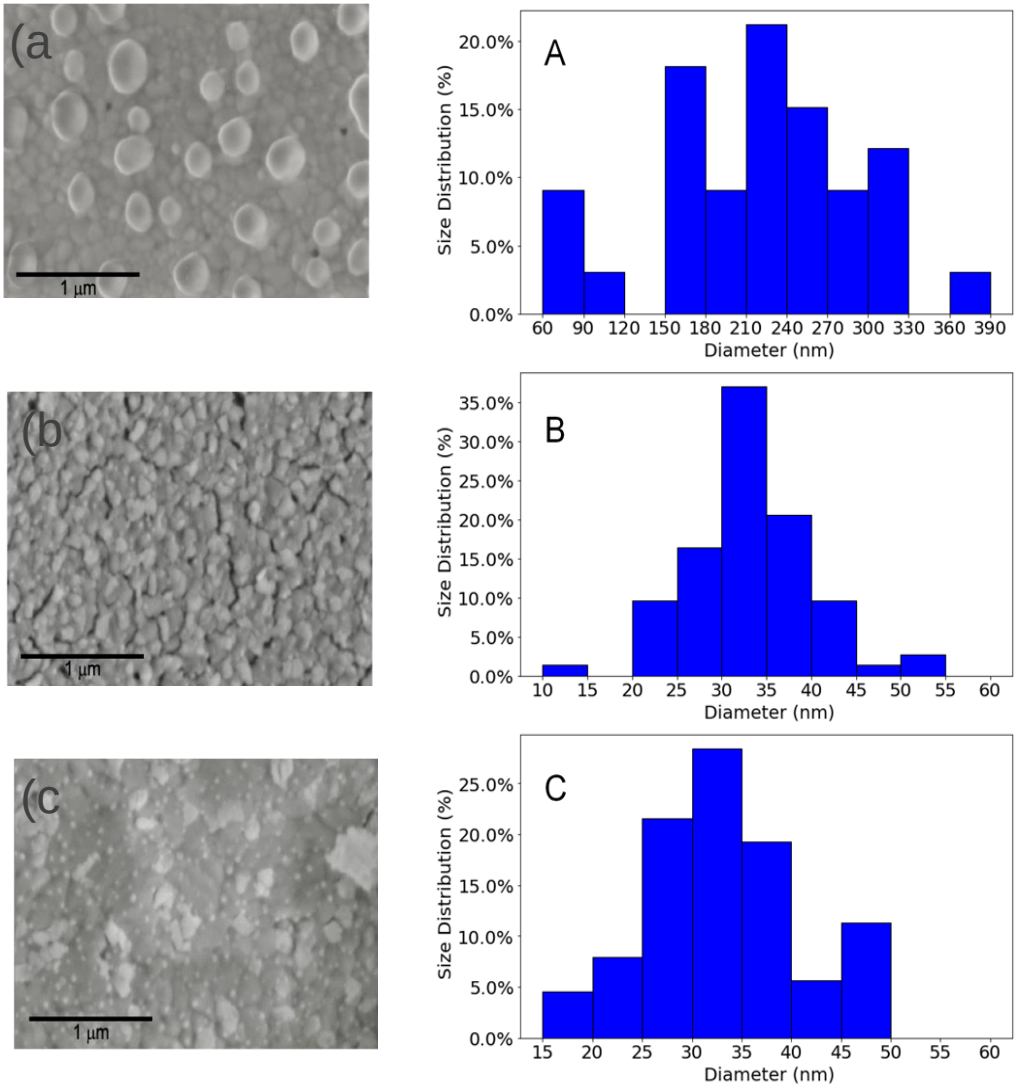

Figure S2.6: The SEM images and particle size distribution histograms of (a) LFNO (0.9:1), (b) LFNO(1:1) and (c) LFNO(1:0.9) after reduction at 700°C.

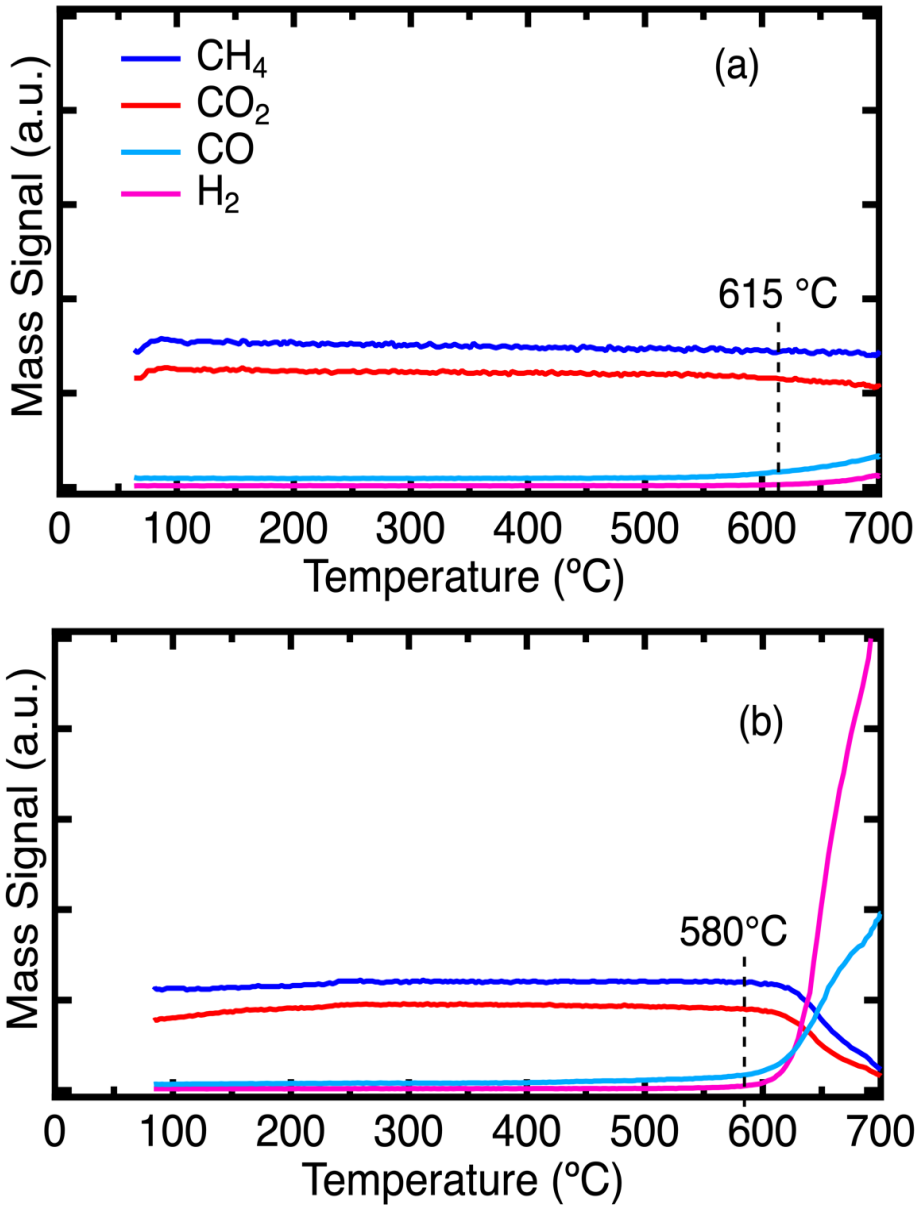

Figure S2.7: The TPSR of (a) LFNO(0.9:1) and (b) LFNO(1:0.9) after regeneration after 24-hour aging.

2.6.3 Catalyst Testing and Characterization

Table S2.2: Particle size distribution, dispersion and Ni:Fe composition as obtained from SEM and STEM-BF EDX measurements

Sample	Mean Diameter	D[a] (%)	Min.	Max.	SD	Ni:Fe
LFNO(0.9:1)	218	0.45	62.7	385	73.9	0.99
LFNO(1:0.9)	33.8	3.0	12.3	61.3	7.7	0.35
LFNO(1:1)	33.6	3.0	18.0	60.1	8.2	0.15

a Dispersion measurements were calculated from the mean diameter of NiFe nanoparticles using the STEM-BF mean diameter

Table S2.3: BET pore size and pore volume measurements for LFNO samples

Catalyst	BET surface area (m^2/g)	BJH Adsorption Pore volume (cm^3/g)	BJH Adsorption Pore size (nm)	BJH Desorption Pore size (nm)
LFNO(0.9:1)	6.27	0.059	13.1	14.1
LFNO(1:0.9)	13.96	0.185	52.5	33.0
LFNO(1:1)	10.80	0.062	24.2	23.8
Ni/α-Al_2O_3	16.97	0.063	16.5	14.6

Table S2.4: Quantities of gases desorbed during CO_2 Temperature Programmed Desorption of LFNO catalysts

Catalyst	CO_2 (mmoles/100mg)	CO (mmoles/100mg)	H_2O (mmoles/100mg)
LFNO(0.9:1)	0.0093	0.020	0.040
LFNO(1:0.9)	0.026	0.0013	0.044

Table S2.5: Rate of consumption of reactants for various catalysts. Regenerated rates are measured after 24-hour aging, regeneration and activity testing.

Catalyst	CH_4 rate (μmoles/s. g)	CO_2 rate (μmoles/s. g)
LFNO (0.9:1)	2.62	4.09
LFNO (0.9:1) regenerated	0.53	1.22
LFNO (1:0.9)	5.21	5.70
LFNO (1:0.9) regenerated	5.55	5.44
LFNO (1:1)	4.73	5.52
$Ni/\alpha\text{-}Al_2O_3$	6.65	6.19
$LaFeO_3$	0.55	1.21

2.7 References

(1) Pakhare, D.; Spivey, J. A Review of Dry (CO2) Reforming of Methane over Noble Metal Catalysts. *Chem. Soc. Rev.* **2014**, *43* (22), 7813–7837. https://doi.org/10.1039/c3cs60395d.

(2) Cañete, B.; Gigola, C. E.; Brignole, N. B. Synthesis Gas Processes for Methanol Production via CH4 Reforming with CO2, H2O, and O2. *Ind. Eng. Chem. Res.* **2014**, *53* (17), 7103–7112. https://doi.org/10.1021/ie404425e.

(3) Zhang, Q.; Kang, J.; Wang, Y. Development of Novel Catalysts for Fischer-Tropsch Synthesis: Tuning the Product Selectivity. *ChemCatChem* **2010**, *2* (9), 1030–1058. https://doi.org/10.1002/cctc.201000071.

(4) de Smit, E.; Weckhuysen, B. M. The Renaissance of Iron-Based Fischer–Tropsch Synthesis: On the Multifaceted Catalyst Deactivation Behaviour. *Chem. Soc. Rev.* **2008**, *37* (12), 2758. https://doi.org/10.1039/b805427d.

(5) Mota, N.; Alvarez-Galvan, C.; Navarro, R. M.; Fierro, J. L. G. Biogas as a Source of Renewable Syngas Production: Advances and Challenges. *Biofuels* **2011**, *2* (3), 325–343. https://doi.org/10.4155/bfs.11.15.

(6) Das, S.; Ashok, J.; Bian, Z.; Dewangan, N.; Wai, M. H.; Du, Y.; Borgna, A.; Hidajat, K.; Kawi, S. Silica–Ceria Sandwiched Ni Core–Shell Catalyst for Low Temperature Dry Reforming of Biogas: Coke Resistance and Mechanistic Insights. *Appl. Catal. B Environ.* **2018**, *230*, 220–236.

(7) Lavoie, J. M. Review on Dry Reforming of Methane, a Potentially More Environmentally-Friendly Approach to the Increasing Natural Gas Exploitation. *Front. Chem.* **2014**, *2*, 1–17. https://doi.org/10.3389/fchem.2014.00081.

(8) Arora, S.; Prasad, R. An Overview on Dry Reforming of Methane: Strategies to Reduce Carbonaceous Deactivation of Catalysts. *RSC Adv.* **2016**, *6*, 108668–108688. https://doi.org/10.1039/c6ra20450c.

(9) Wei, J.; Iglesia, E. Isotopic and Kinetic Assessment of the Mechanism of Reactions of CH 4 with CO2 or H2O to Form Synthesis Gas and Carbon on Nickel Catalysts. *J. Catal.* **2004**, *224* (2), 370–383.

(10) Wei, J.; Iglesia, E. Mechanism and Site Requirements for Activation and Chemical Conversion of Methane on Supported Pt Clusters and Turnover Rate Comparisons among Noble Metals. *J. Phys. Chem. B* **2004**, *108* (13), 4094–4103.

(11) Usman, M.; Wan Daud, W. M. A.; Abbas, H. F. Dry Reforming of Methane: Influence of Process Parameters—A Review. *Renew. Sustain. Energy Rev.* **2015**, *45*, 710–744. https://doi.org/10.1016/j.rser.2015.02.026.

(12) Kim, S. M.; Abdala, P. M.; Margossian, T.; Hosseini, D.; Foppa, L.; Armutlulu, A.; Van Beek, W.; Comas-Vives, A.; Copéret, C.; Müller, C. Cooperativity and Dynamics Increase the Performance of NiFe Dry Reforming Catalysts. *J. Am. Chem. Soc.* **2017**, *139* (5), 1937–1949. https://doi.org/10.1021/jacs.6b11487.

(13) Bian, Z.; Das, S.; Wai, M. H.; Hongmanorom, P.; Kawi, S. A Review on Bimetallic Ni-Based Catalysts for CO2 Reforming of Methane. *ChemPhysChem* **2017**, *18* (22), 3117–3134. https://doi.org/10.1002/cphc.201700529.

(14) Margossian, T.; Larmier, K.; Kim, S. M.; Krumeich, F.; Müller, C.; Copéret, C. Supported Bimetallic NiFe Nanoparticles through Colloid Synthesis for Improved Dry Reforming Performance. *ACS Catal.* **2017**, *7* (10), 6942–6948.

(15) Theofanidis, S. A.; Galvita, V. V.; Poelman, H.; Marin, G. B. Enhanced Carbon-Resistant Dry Reforming Fe-Ni Catalyst: Role of Fe. *ACS Catal.* **2015**, *5* (5), 3028–3039. https://doi.org/10.1021/acscatal.5b00357.

(16) San-José-Alonso, D.; Juan-Juan, J.; Illán-Gómez, M. J.; Román-Martínez, M. C. Ni, Co and Bimetallic Ni-Co Catalysts for the Dry Reforming of Methane. *Appl. Catal. A Gen.* **2009**, *371* (1), 54–59. https://doi.org/10.1016/j.apcata.2009.09.026.

(17) Crisafulli, C.; Scirè, S.; Maggiore, R.; Minicò, S.; Galvagno, S. Co2 Reforming of Methane over Ni-Ru and Ni-Pd Bimetallic Catalysts. *Catal. Letters* **1999**, *59* (1), 21–26. https://doi.org/10.1023/A:1019031412713.

(18) Seoka, S.-H.; Choia, S. H.; DuckPark, E.; Han, S. H.; Jae Sung Lee. Mn-Promoted Ni/Al2O3 Catalysts for Stable Carbon Dioxide Reforming of Methane. *J. Catal.* **2002**, *1* (1), 6–15.

(19) Rezaei, R.; Moradi, G.; Shahram, S. Dry Reforming of Methane over Ni-Cu/Al2O3 Catalyst Coatings in a Microchannel Reactor: Modeling and Optimization Using Design of Experiments. *Energy & Fuels* **2019**, *33* (7), 6689–6706.

(20) Horváth, A.; Guczi, L.; Kocsonya, A.; Sáfrán, G.; La Parola, V.; Liotta, L. F.; Pantaleo, G.; Venezia, A. M. Sol-Derived AuNi/MgAl2O4 Catalysts: Formation, Structure and Activity in Dry Reforming of Methane. *Appl. Catal. A Gen.* **2013**, *468* (5), 250–259. https://doi.org/10.1016/j.apcata.2013.08.053.

(21) Wu, H.; Pantaleo, G.; La Parola, V.; Venezia, A. M.; Collard, X.; Aprile, C.; Liotta, L. F. Bi- and Trimetallic Ni Catalysts over Al2O3 and Al2O3-MOx (M=Ce or Mg) Oxides for Methane Dry Reforming: Au and Pt Additive Effects. *Appl. Catal. B Environ.* **2014**, *156*, 350–361. https://doi.org/10.1016/j.apcatb.2014.03.018.

(22) Yu, M.; Zhu, Y. A.; Lu, Y.; Tong, G.; Zhu, K.; Zhou, X. The Promoting Role of Ag in Ni-CeO2 Catalyzed CH4-CO2 Dry Reforming Reaction. *Appl. Catal. B Environ.* **2015**, *165*, 43–56. https://doi.org/10.1016/j.apcatb.2014.09.066.

(23) Lim, Z. Y.; Wu, C.; Wang, W. G.; Choy, K. L.; Yin, H. Porosity Effect on ZrO2 Hollow Shells and Hydrothermal Stability for Catalytic Steam Reforming of Methane. *J. Mater. Chem. A* **2015**, *4*, 153–159. https://doi.org/10.1039/c5ta07015e.

(24) Wang, C.; Jie, X.; Qiu, Y.; Zhao, Y.; Al-Megren, H. A.; Alshihri, S.; Edwards, P. P.; Xiao, T. The Importance of Inner Cavity Space within Ni@SiO2 Nanocapsule Catalysts for Excellent Coking Resistance in the High-Space-Velocity Dry Reforming of Methane. *Appl. Catal. B Environ.* **2019**, *259*, 118019.

(25) Han, J. W.; Park, J. S.; Choi, M. S.; Lee, H. Uncoupling the Size and Support Effects of Ni Catalysts for Dry Reforming of Methane. *Appl. Catal. B Environ.* **2017**, *203*, 625–632. https://doi.org/10.1016/j.apcatb.2016.10.069.

(26) Tang, S.; Ji, L.; Lin, J.; Zeng, H. C.; Tan, K. L.; Li, K. CO2 Reforming of Methane to Synthesis Gas over Sol-Gel-Made Ni/γ-Al2O3 Catalysts from Organometallic Precursors. *J. Catal.* **2000**, *194* (2), 424–430. https://doi.org/10.1006/jcat.2000.2957.

(27) Li, X.; Li, D.; Tian, H.; Zeng, L.; Zhao, Z. J.; Gong, J. Dry Reforming of Methane over Ni/La2O3 Nanorod Catalysts with Stabilized Ni Nanoparticles. *Appl. Catal. B Environ.* **2017**, *202*, 683–694. https://doi.org/10.1016/j.apcatb.2016.09.071.

(28) Montero, C.; Ochoa, A.; Castaño, P.; Bilbao, J.; Gayubo, A. G. Monitoring Ni0 and Coke Evolution during the Deactivation of a Ni/La2O3-AAl2O3 Catalyst in Ethanol Steam Reforming in a Fluidized Bed. *J. Catal.* **2015**, *331*, 181–192.

(29) Valderrama, G.; Goldwasser, M. R.; Navarro, C. U. De; Tatibouët, J. M.; Barrault, J.; Batiot-Dupeyrat, C.; Martínez, F. Dry Reforming of Methane over Ni Perovskite Type Oxides. *Catal. Today* **2005**, *107*, 785–791.

(30) Gallego, G. S.; Batiot-Dupeyrat, C.; Barrault, J.; Mondragón, F. Dual Active-Site Mechanism for Dry Methane Reforming over Ni/La2O3 Produced from LaNiO3 Perovskite. *Ind. Eng. Chem. Res.* **2008**, *47* (23), 9272–9278. https://doi.org/10.1021/ie800281t.

(31) Song, Q.; Xiao, R.; Li, Y.; Shen, L. Catalytic Carbon Dioxide Reforming of Methane to Synthesis Gas over Activated Carbon Catalyst. *Ind. Eng. Chem. Res.* **2008**, *47* (13), 4349–4357.

(32) Mizuki, J.; Akao, T.; Tanaka, H.; Uenishi, M.; Kimura, M.; Okamoto, T.; Hamada, N. Self-Regeneration of a Pd-Perovskite Catalyst for Automotive Emissions Control. *Nature* **2002**, *418*, 164–167. https://doi.org/10.1038/nature00875.1.

(33) Neagu, D.; Oh, T. S.; Miller, D. N.; Ménard, H.; Bukhari, S. M.; Gamble, S. R.; Gorte, R. J.; Vohs, J. M.; Irvine, J. T. S. Nano-Socketed Nickel Particles with Enhanced Coking Resistance Grown in Situ by Redox Exsolution. *Nat. Commun.* **2015**, *6* (8120). https://doi.org/10.1038/ncomms9120.

(34) Zhao, B.; Yan, B.; Yao, S.; Xie, Z.; Wu, Q.; Ran, R.; Weng, D.; Zhang, C.; Chen, J. G. LaFe0.9Ni0.1O3perovskite Catalyst with Enhanced Activity and Coke-Resistance for Dry Reforming of Ethane. *J. Catal.* **2018**, *358*, 168–178. https://doi.org/10.1016/j.jcat.2017.12.012.

(35) Yang, Q.; Liu, G.; Liu, Y. Perovskite-Type Oxides as the Catalyst Precursors for Preparing Supported Metallic Nanocatalysts : A Review. *Ind. Eng. Chem. Res.* **2018**, *57* (1), 1–17. https://doi.org/10.1021/acs.iecr.7b03251.

(36) Oh, H. J.; Kang, J. G.; Heo, E.; Lee, S. H.; Choi, J. G. Kinetic Investigation of CO2-CH4 Reaction over Ni/La2O3 Catalyst Using Photoacoustic Spectroscopy. *Bull. Korean Chem. Soc.* **2014**, *35* (9), 2615–2620. https://doi.org/10.5012/bkcs.2014.35.9.2615.

(37) De Lima, S.; Assaf, M. Ni – Fe Catalysts Based on Perovskite-Type Oxides for Dry Reforming of Methane to Syngas. *Catal. Letters* **2006**, *108* (1), 63–70.

(38) Valderrama, G.; Kiennemann, A.; Goldwasser, M. R. La-Sr-Ni-Co-O Based Perovskite-Type Solid Solutions as Catalyst Precursors in the CO2 Reforming of Methane. *J. Power Sources* **2010**, *195*, 1765–1771. https://doi.org/10.1016/j.jpowsour.2009.10.004.

(39) Tsoukalou, A.; Imtiaz, Q.; Kim, S. M.; Abdala, P. M.; Yoon, S.; Müller, C. R. Dry-Reforming of Methane over Bimetallic Ni–M/La2O3 (M = Co, Fe): The Effect of the Rate of La2O2CO3 Formation and Phase Stability on the Catalytic Activity and Stability. *J. Catal.* **2016**, *343*, 208–214. https://doi.org/10.1016/j.jcat.2016.03.018.

(40) Oh, J. H.; Kwon, B. W.; Cho, J.; Lee, C. H.; Kim, M. K.; Choi, S. H.; Yoon, S. P.; Han, J.; Nam, S. W.; Kim, J. Y.; Jang, S. S.; Lee, K. B.; Ham, H. C. Importance of Exsolution in Transition-Metal (Co, Rh, and Ir)-Doped LaCrO3 Perovskite Catalysts for Boosting Dry Reforming of CH4 Using CO2 for Hydrogen Production. *Ind. Eng. Chem. Res.* **2019**, *58* (16), 6385–6393. https://doi.org/10.1021/acs.iecr.8b05337.

(41) Pakhare, D.; Schwartz, V.; Abdelsayed, V.; Haynes, D.; Shekhawat, D.; Poston, J.; Spivey, J. Kinetic and Mechanistic Study of Dry (CO2) Reforming of Methane over Rh-Substituted La2Zr2O7 Pyrochlores. *J. Catal.* **2014**, *316*, 78–92. https://doi.org/10.1016/j.jcat.2014.04.023.

(42) Katz, M. B.; Graham, G. W.; Duan, Y.; Liu, H.; Adamo, C.; Schlom, D. G.; Pan, X. Self-Regeneration of Pd-LaFeO 3 Catalysts: New Insight from Atomic-Resolution Electron Microscopy. *J. Am. Chem. Soc.* **2011**, *133* (45), 18090–18093. https://doi.org/10.1021/ja2082284.

(43) Zhang, S.; Katz, M. B.; Dai, S.; Zhang, K.; Du, X.; Graham, G. W.; Pan, X. New Atomic-Scale Insight into Self-Regeneration of Pt-CaTiO3 Catalysts: Incipient Redox-Induced Structures Revealed by a Small-Angle Tilting STEM Technique. *J. Phys. Chem. C* **2017**, *121* (32), 17348–17353.

(44) Oemar, U.; Ang, P. S.; Hidajat, K.; Kawi, S. Promotional Effect of Fe on Perovskite LaNixFe 1-XO3 Catalyst for Hydrogen Production via Steam Reforming of Toluene. *Int. J. Hydrogen Energy* **2013**, *38* (14), 5525–5534. https://doi.org/10.1016/j.ijhydene.2013.02.083.

(45) Onn, T. M.; Monai, M.; Dai, S.; Fonda, E.; Montini, T.; Pan, X.; Graham, G. W.; Fornasiero, P.; Gorte, R. J. Smart Pd Catalyst with Improved Thermal Stability Supported on High-Surface-Area LaFeO3Prepared by Atomic Layer Deposition. *J. Am. Chem. Soc.* **2018**, *140* (14), 4841–4848. https://doi.org/10.1021/jacs.7b12900.

(46) Neagu, D.; Tsekouras, G.; Miller, D. N.; Ménard, H.; Irvine, J. T. S. In Situ Growth of Nanoparticles through Control of Non-Stoichiometry. *Nat. Chem.* **2013**, *5* (11), 916–923. https://doi.org/10.1038/nchem.1773.

(47) Gao, Y.; Wang, J.; Lyu, Y.; Lam, K.; Ciucci, F. In Situ Growth of Pt3Ni Nanoparticles on an A-Site Deficient Perovskite with Enhanced Activity for the Oxygen Reduction Reaction. *J. Mater. Chem. A* **2017**, *5*, 6399–6404. https://doi.org/10.1039/c7ta00349h.

(48) Labhasetwar, N.; Saravanan, G.; Kumar Megarajan, S.; Manwar, N.; Khobragade, R.; Doggali, P.; Grasset, F. Perovskite-Type Catalytic Materials for Environmental Applications. *Sci. Technol. Adv. Mater.* **2015**, *16* (3), 1–13.

(49) Rodriguez-Carvajal, J. Recent advances in magnetic-structure determination by neutron powder diffraction. *Phys. B* **1993**, *192* (1–2), 55–69.

(50) Schneider, C. A.; Rasband, W. S.; Eliceiri, K. W. NIH Image to ImageJ: 25 Years of Image Analysis. *Nat. Methods* **2012**, *9* (7), 671–675.

(51) Rodrigues, L.; Silva, R.; Rocha, M.; Bargiela, P.; Brandao, S. Partial Oxidation of Methane on Ni and Pd Catalysts: Influence of Active Phase and CeO2 Modification. *Catal. Today* **2012**, *197* (1), 137–143.

(52) Chen, L.; Huang, Q.; Zhang, D.; Liu, W.; Yang, T. Temperature Programmed Surface Reaction Test of Co–Ni Bimetallic Aerogel Catalysts for Methane Reforming. *React. Kinet. Mech. Catal.* **2019**, *126*, 951–962.

(53) Uberuaga, B. P.; Vernon, L. J. Interstitial and Vacancy Mediated Transport Mechanisms in Perovskites: A Comparison of Chemistry and Potentials. *Solid State Ionics* **2013**, *253*, 18–26.

(54) Tomishige, K.; Li, D.; Tamura, M.; Nakagawa, Y. Nickel-Iron Alloy Catalysts for Reforming of Hydrocarbons: Preparation, Structure, and Catalytic Properties. *Catal. Sci. Technol.* **2017**, *7*, 3952–3979. https://doi.org/10.1039/c7cy01300k.

(55) Perry, N. H.; Bishop, S. R.; Tuller, H. L. Tailoring Chemical Expansion by Controlling Charge Localization: In Situ X-Ray Diffraction and Dilatometric Study of (La,Sr)(Ga,Ni)O3-δ Perovskite. *J. Mater. Chem. A* **2014**, *2* (44), 18906–18916. https://doi.org/10.1039/c4ta02972k.

(56) Zheng, Y.; Li, K.; Wang, H.; Tian, D.; Wang, Y.; Zhu, X.; Wei, Y.; Zheng, M.; Luo, Y. Designed Oxygen Carriers from Macroporous LaFeO3 Supported CeO2 for Chemical-Looping Reforming of Methane. *Appl. Catal. B Environ.* **2017**, *202*, 51–63. https://doi.org/10.1016/j.apcatb.2016.08.024.

(57) Zhu, X.; Li, K.; Neal, L.; Li, F. Perovskites as Geo-Inspired Oxygen Storage Materials for Chemical Looping and Three-Way Catalysis: A Perspective. *ACS Catal.* **2018**, *8* (9), 8213–8236. https://doi.org/10.1021/acscatal.8b01973.

(58) Wang, L.; Li, D.; Koike, M.; Koso, S.; Nakagawa, Y.; Xu, Y.; Tomishige, K. Catalytic Performance and Characterization of Ni-Fe Catalysts for the Steam Reforming of Tar from Biomass Pyrolysis to Synthesis Gas. *Appl. Catal. A Gen.* **2011**, *392* (1–2), 248–255. https://doi.org/10.1016/j.apcata.2010.11.013.

CHAPTER 3. EXSOLUTION OF EMBEDDED NI-FE-CO NANOPARTICLES: IMPLICATIONS FOR DRY REFORMING OF METHANE

The text of this dissertation chapter, in full, is a reprint of the material as it appears in "Exsolution of Embedded Ni-Fe-Co Nanoparticles: Implications for Dry Methane Reforming" published in ACS Applied Nano Materials, 2021. The text has been modified to fit the dissertation guidelines. The co-author Dr. Kandis Leslie Gilliard-Abdul-Aziz listed in that publication directed and supervised the research which forms the basis for this dissertation chapter.

3.1 Abstract

As a promising robust and thermally-stable dry methane reforming (DRM) catalyst, this work explores the use of perovskite precursors for the controlled nucleation and growth of NiFeCo nanoparticles from La(Fe,Ni,Co)O_3 precursor structures. We study the structure-reactivity relationship of the formed NiFeCo nanoparticles as a function of the reduction temperature, reaction environment, and bulk point defects. We closely examine different levers that can control the size, composition, and reactivity of NiFeCo nanoparticles. The material properties are investigated by a combination of characterization techniques such as X-ray diffraction (XRD), High-angle annular dark-field scanning transmission electron microscopy (HAADF-STEM), and Energy-dispersive X-ray spectroscopy (EDS). Dry reforming of methane (DRM) reaction testing and temperature-programmed surface reaction (TPSR) experiments are used to probe the catalyst performance and regenerability of the multi-metallic nanoparticles. NiFeCo nanoparticles formed from perovskite oxide precursors show a greater propensity to form alloys or aggregates than the conventional wet co-impregnation method. HAADF-STEM and TPSR experiments suggest that the NiFeCo nanoparticles formed are initially Fe-rich but become Ni and Co-rich in the reactive atmosphere after aging for 24 hours. This works provides insight into relevant factors that can control the properties of multi-metallic nanoparticles formed from perovskite oxide precursors.

3.2 Introduction

Dry reforming of methane (DRM) converts two major greenhouse gases, methane and carbon dioxide, to syngas. Syngas is a vital feedstock to produce chemical commodities

and fuels, including methanol and olefins[1]. Nickel (Ni) is a low-cost catalyst for DRM with the ability to activate both C-H and C-O bonds[2,3]. Ni is susceptible to the formation of coke, which limits its stability and potential commercialization for DRM. The side reactions responsible for coke formation are the Boudouard and methane cracking, where methane cracking is the main contributor of carbonaceous species[4,5]. Unfortunately, due to the endothermic nature of DRM, elevated temperatures (> 550 ºC) promote the thermodynamic driving force for carbon deposition.

One strategy to improve DRM catalyst stability has focused on alloying Ni using different promoters for prominent coke-resistance performance. This includes the combination of Ni with Fe[6–8], Co[9,10], Au[11], Ag[12], or Ru[13]. The combination of Ni and the promoter decreases coke deposition by gasifying the carbon or blocking the Ni undercoordinated sites responsible for coke deposition. The promotional effect of Ni and Fe is widely discussed for DRM. An in situ X-ray Diffraction (XRD) study by Theofanidis et.al[7] proposed that DRM over NiFe catalysts occurs through a Mars-van Krevelen type mechanism. The CH_4 is activated over Ni forming carbonaceous species, while CO_2 oxidizes Fe to FeO_x. The lattice oxygen from the FeO_x oxidizes the surface carbon to CO. Wang et al.[14] discussed a similar mechanism where FeO_x oxidizes carbonaceous species in steam tar reforming using NiFe bimetallic catalysts. However, when the surface concentration of Fe:Ni is high, there is a loss of C-H activation due to a decrease in the availability of surface Ni. Another promoter, Co, has a strong oxygen affinity that, when combined with Ni, can be correlated with oxidative gasification of the carbonaceous species[15]. A study by Zhang et al. on NiCo for DRM showed that the

bimetallic catalysts prohibit partial oxidation by CO_2 in DRM conditions due to electron transfer interactions between Ni and Co[16]. This was confirmed by monitoring the oxidation states of Ni and Co using in situ X-ray photoelectron spectroscopy (XPS). However, a higher concentration of Co substitution suppressed methane activation and diminished catalyst performance. Indeed, the use of promotors in Ni-based alloys must be done judiciously where an excess of Fe or Co can cause deactivation due to the oxidation of the alloy, resulting in dealloying and instability. Thus, Ni-based bimetallic catalysts are sensitive to dealloying during DRM, and usually, efforts to regenerate the performance are difficult.

To improve the stability of bimetallic alloys, there have been recent efforts to add a third metal to enhance performance. A study by Jin et al. added Cu to NiFe to form NiFeCu catalysts prepared using a hydrotalcite precursor on an Mg(Al)O matrix[17]. The doping of Cu inhibits the Fe segregation from the alloy. However, too high a concentration of Cu forms Ni-Cu alloys and deactivates due to the loss synergy between Ni and Fe. Theofandis et al. added Pd to NiFe catalysis using co-precipitation, which reduced the tendency of Fe to segregate from the alloy[18]. The addition of the Pd stabilizes the Fe-Ni by the formation of a core-shell thin layer of Fe-Ni-Pd. Joo et al. observed that the introduction of Fe to Ni-Co catalysts exsolved from $PrBaMn_{1.7}Co_{0.1}Ni_{0.2}O_{5+d}$ improved its stability for DRM[19]. The introduction of Co shifted the d-band center of the Co-Ni-Fe nanoparticles to enhance catalytic activity and stability. Therefore, Ni with two metal promotors is a useful strategy for improving the catalyst activity and stability for DRM.

This paper combines Ni, Fe, and Co, in which the Ni is active for methane activation. And the addition of Fe and Co decreases the occurrence of coke and improves DRM catalyst performance. Most multi-metallic catalysts are synthesized using co-precipitation, sol-gel, and impregnation[20]. However, the conventional synthesis strategies lack adequate controls for the catalyst size and composition of multimetallic nanoparticles, resulting in inhomogeneous catalyst properties that limit their reproducibility. To use suitable NiFeCo catalysts for DRM, several industrial criteria must be achieved where the composition and size of the Ni, Co, and Fe must be controllable. It is highly desirable to find a scalable synthesis strategy that can control the metal composition and size of the trimetallic Ni catalysts.

We use the inherent properties of perovskite precursors to form NiFeCo catalyst nanoparticles. When using perovskite precursors, the nanoparticles are formed on the perovskite oxide or oxide surface under reducing conditions[21–24]. The nanoparticles adhere firmly to the surface that lends, promoting marked stability against agglomeration and coking[25–29]. Prior studies have found that defects are crucial for controlling the diffusion and rate of exsolution of catalyst dopants in perovskite precursors[30]. For example, A-site cation vacancies increase the rate of B-site exsolution due to the formation of oxygen vacancies that accelerates the kinetics of metal exsolution and particle growth[30]. We examined the notion of bulk defect manipulation of perovskite oxide precursors to change the alloy composition, size, and shape of exsolved NiFe nanoparticles for DRM[31]. Our previous work tuned and regenerated the composition of NiFe bimetallic nanoparticles using in-situ exsolution from a perovskite precursor,

$La(Fe,Ni)O_3$. We found that the B-site metal redox properties can change nanoparticle formation and bulk crystal structure dynamics, influencing catalyst performance[32]. Additionally, we uncovered a limitation in the coke-resistance properties of the perovskite precursors where large NiFe nanoparticles formed considerable graphitic coke formation that limited the catalyst performance. Given the levers of control gleaned, perovskite precursors are an excellent platform material for tailored multimetallic catalysts for DRM, with improved thermal stability enhanced by a strong metal-support interaction.

This work aims to elucidate the structure-reactivity for trimetallic NiFeCo catalyst nanoparticles to improve their properties. We have prepared $La(Fe,Ni,Co)O_3$ perovskite precursors and compared their catalytic performance as a function of the catalyst metal composition and reduction temperature. We have systematically studied the systems and the influence of the partial substitution of Fe by Ni and Co, which alters the reducibility of the precursor, the kinetics of exsolution, and catalyst nanoparticle composition. The material properties and morphology of as-prepared and spent perovskite precursors were probed using X-ray diffraction (XRD), Scanning transmission electron microscopy (STEM) with energy dispersive spectroscopy (EDS), temperature-programmed reduction (TPR), and temperature-programmed surface reaction (TPSR). We optimize the catalyst performance and study the regenerability of the alloys and their composition. We show that despite the formation of smaller Fe-rich NiFeCo nanoparticles at lower temperatures, the nanoparticles become more enriched with Ni and Co as the DRM reaction progresses over 24 hours. The paper is structured to discuss the NiFeCo material properties and

morphology, the catalyst performance, and deactivation mechanisms. The last section of the article discusses the regeneration of the NiFeCo catalyst nanoparticles, rates of consumption, and apparent CH_4 activation energies.

3.3 Experimental Section

3.3.1 Perovskite Oxide Precursor Preparation

The perovskite oxide precursors were prepared by a citric acid sol-gel method similar to the Pechini method described elsewhere in literature[33]. Metal nitrate salts were used as precursors and mixed in stoichiometric quantities to form an aqueous solution. Citric acid (3 mols. /mol. perovskite) and ethylene glycol butyl ether (1 mol./ mol. perovskite) was added to the solution as it was stirred at 60 ºC on a hot plate magnetic stirrer. The solution was then placed in an oven at 110 ºC overnight. The resulting dried xerogel was ground with a mortar and pestle and calcined at, ramping up the temperature at 5 ºC/min to 700 ºC and dwelling for four hours in a muffle furnace. Exsolution of nanoparticles was carried out by reducing the as-prepared perovskite in a quartz tube microreactor (Hiden Analytical CATLAB). The catalysts were reduced in a 5% H_2/He stream, ramping the temperature up at 15 ºC/min and then holding at temperature (800 ºC or 950 ºC) for two hours. For simplification, the nomenclature of the materials synthesized has been designated as seen in **Table 3.1**. 5%Ni+5%Co/La_2O_3

Table 3.1. Nomenclature and stoichiometry of Ni-Co substituted $LaFeO_3$ perovskite samples synthesized for this study.

Sample	Stoichiometry
(A5)	$La_{0.9}FeNi_{0.05}Co_{0.05}O_3$
(B5)	$LaFe_{0.9}Ni_{0.05}Co_{0.05}O_3$
(B2)	$LaFe_{0.9}Ni_{0.02}Co_{0.08}O_3$
(B8)	$LaFe_{0.9}Ni_{0.08}Co_{0.02}O_3$

was prepared as a reference for comparison. La_2O_3 was prepared by a similar sol-gel method, and Ni and Co were deposited by wet impregnation using nitrate precursors.

3.3.2 Catalyst Characterization

Surface area and pore volume were calculated with N_2 adsorption isotherms and Brunauer-Emmett-Teller (BET) analysis with a Micromeritics ASAP 2020 instrument. Temperature Programmed Reduction (TPR) was conducted in our quartz tube microreactor during catalyst reduction, with the exit gases analyzed with a quadrupole mass spectrometer (Hiden Analytical QGA). X-ray Diffraction (XRD) spectra were collected on a PANalytical Empyrean Series 2 with a step-size of 0.026^o and dwell time of 30 seconds and were then analyzed with HighScore and FullProf[34] software. The atomic resolution images of the samples were acquired using Scanning Transmission Electron Microscopy (STEM) on a JEOL Grand ARM300CF TEM/STEM with double spherical aberration-correctors operated at 300kV STEM High-angle annular dark-field (HAADF) imaging mode. Simultaneously, the elemental mapping via energy-dispersive X-ray spectroscopy (EDS) was collected by the large angle dual dry solid-state 100 mm^2 detectors.

3.3.3 Catalyst Reaction Testing

DRM was conducted in the quartz tube microreactor (Hiden Analytical CATLAB), with the product stream analyzed with a Hiden quadrupole mass spectrometer. As-prepared catalysts were reduced in-situ in the quartz tube at either 800 ºC or 950 ºC before reaction testing. The reactant stream consisted of CH_4 (5%), CO_2

(5%), and He (90%, balance) for a total flow rate of 60 ml/min. Catalyst activity testing was done by measuring conversion at intervals of 50 ºC from 200 to 900 ºC, with a ramp rate of 10 ºC/min and dwelling over each temperature point of interest for 15 minutes. Catalyst aging tests were done by conducting the reaction at 900 ºC for 24 hours. The mass spectrometer was calibrated for relative sensitivity by measuring responses for a known concentration of individual gases diluted in helium. The pressure drop in the reactor was minimal, as determined by calibration tests with and without catalysts. Conversion of reactant gases was determined by calculating gas flow rates calculated from the MS response and the known relative sensitivities. The rates were calculated at conversions less than 15% to ensure differential reaction conditions. Temperature Programmed Surface Reactions (TPSR), a reactant gas stream with the same composition and flow rate mentioned earlier, was flown through the freshly reduced catalyst, with the temperature ramping up from room temperature 10 ºC/min. CO_2 Temperature Programmed Desorption (CO_2-TPD) was conducted by flowing 10% CO_2 (60 ml/min) at 50 ºC for 2 hours after, which temperature was ramped up at 10 ºC/min under He flow (40 ml/min).

3.4 Results and Discussion

3.4.1 X-ray Diffraction

The crystallinity of the as-prepared and reduced samples was determined using XRD. **Figure S3.1** shows the XRD spectra of the as-prepared $LaFeO_3$, A5, and B5 precursors. The as-prepared A5 and B5 spectra confirmed an orthorhombic (Pnma) perovskite structure that is almost identical to the $LaFeO_3$ sample. **Figure S3.1b** shows that the Ni and Co substituents were completely incorporated into the bulk of the $LaFeO_3$ host perovskite lattice, possibly residing in the B-site or as interstitials in the lattice or grain boundaries[35]. The ionic radii of Ni^{2+}(72 pm) and Co^{3+}(68 pm) are close in value to the ionic radii of the native Fe^{3+}(69 pm) in the lattice sites of the structure. The substituents were completely solubilized in the perovskite, and no impurity or segregated phases were detected within the limits of XRD. Rietveld refinement was used to quantitatively assess the minor differences in the crystallographic structure (**Table S3.1**). The sample with La

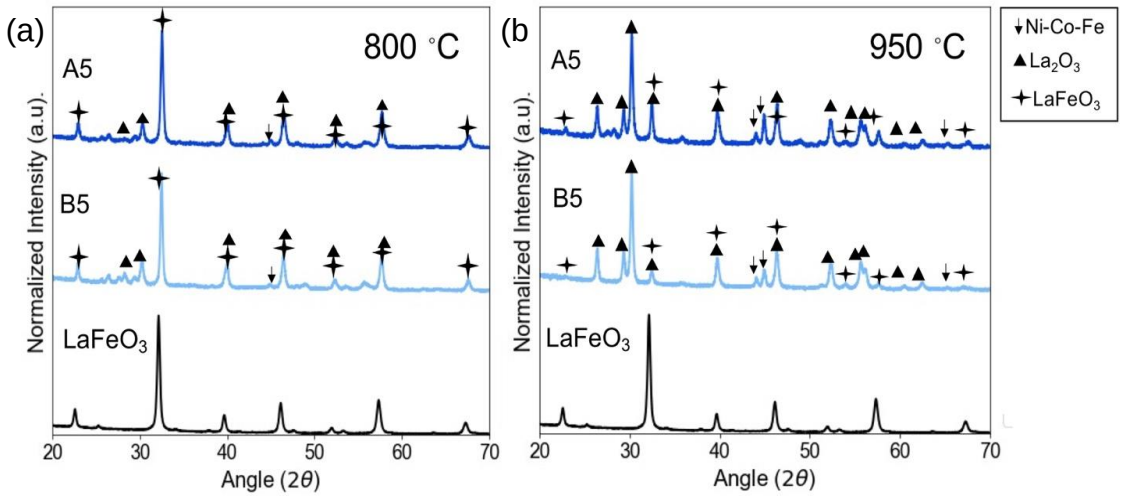

Figure 3.1. XRD of A5 and B5 catalysts after reduction at (a) 800 ºC and (b) 950 ºC for two hours.

sub-stoichiometry, A5, has a lattice volume reduction of 4.94% compared to that of the undoped $LaFeO_3$. In comparison, sample B5 had a volume reduction of 4.04%. The difference in the unit cell volumes between A5 and B5, though not very large, could be attributed to differences in the charge-balance compensation and minor perturbations of the unit cell through the formation of oxygen vacancies or valence compensation by the B-site metals[31].

The XRD spectra of the reduced samples at 800 ºC and 950 ºC, respectively, are shown in **Figure 3.1**. For the samples A5 and B5 reduced at 800 ºC, the spectra show that after reduction, the bulk is primarily $LaFeO_3$ with La_2O_3. The reflections at ~44 and ~45 2θ are attributed to the presence of NiFeCo[36] alloys, confirming the exsolution of multi-metallic nanoparticles. For the samples reduced at 950 ºC, the spectra show a dissolution of the perovskite oxide structure to form primarily La_2O_3 mixed with $LaFeO_3$ crystallites phase. The formation of La_2O_3 at elevated temperatures is due to the large proliferation of the solid-phase recrystallization to form larger NiFeCo catalyst nanoparticles with a simultaneous dissolution of the perovskite oxide lattice.

3.4.2 Nitrogen desorption and adsorption studies

The surface area measurements, pore volumes, and pore sizes obtained from BET nitrogen adsorption isotherms of the reduced catalysts are compared in **Table S3.2**. The sample A5 has a surface area of 3.5 m^2/g compared to a surface area of 3.2 m^2/g for the B5 sample. These are comparatively lower than the surface areas of 6.3-14 m^2/g observed for the $La(Fe/Ni)O_3$ perovskites we have discussed previously reduced at 700 ºC[31]. The

pore sizes calculated by the Barrett, Joyner and Halenda (BJH) method for adsorption isotherms is 10.95 nm for A5 and 16.92 nm for B5. The differences in the surface area could be attributed to the respective sizes of the NiFeCo catalyst nanoparticles and morphology. Perovskite oxide catalysts typically have lower surface areas due to the high temperatures required for their synthesis[37]. The high temperatures of reduction are also detrimental to these characteristics.

3.4.3 H_2 Adsorption-Desorption Analysis of the Perovskite Precursors

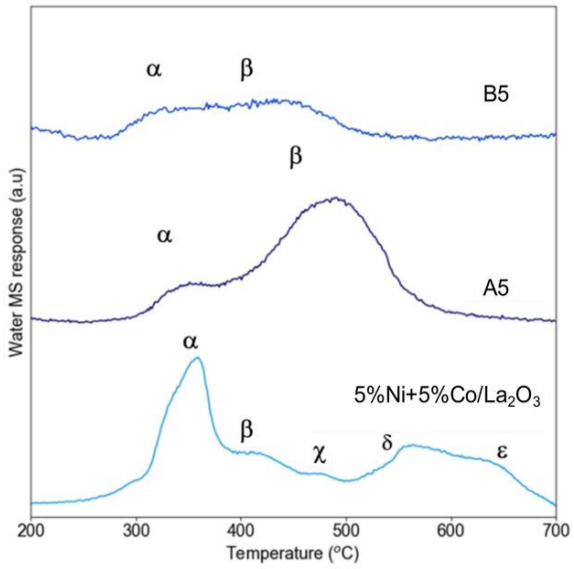

Figure 3.2. Temperature programmed reduction of the perovskite oxide precursors A5 and B5 compared to the reference catalyst made by co-impregnation.

H_2-TPR was used to study the precursors' reducibility and determine if there were any differences in the morphological properties of the catalysts compared to the 5%Ni+5%Co/La_2O_3 reference counterpart. The H_2-TPR of the catalyst precursors and reference catalyst is shown in **Figure 3.2**. **Figure 3.2** indicates that the TPR curve for A5 has two noticeable reduction peaks α at 330 ºC and 495 ºC, respectively. The peak at 330 ºC most likely contributes to the reduction of Ni^{3+} to Ni^{2+}, Ni^{2+} to $Ni^{0,}$ and the peak at 495 ºC is a convolution of the reduction of multiple metals, including, Co^{3+} to Co^{2+} and Fe^{3+} to Fe^{2+}. The TPR curve for B5 has two peaks that almost appear as one broad peak, α and β, at

~310 ºC and ~480 ºC. The peak at 310 ºC contributes to the reduction of Ni^{3+} to Ni^{2+}, Ni^{2+} to $Ni^{0,}$ and the peak at 480 ºC is a convolution of the reduction of multiple metals, including Co^{3+} to Co^{2+} and Fe^{3+} to Fe^{2+}. The coalescence of the B5 reduction peaks at lower temperatures may indicate that the Ni, Co, and Fe form an alloy and are strongly interacting. In contrast, the TPR for the reference catalyst, 5%Ni+5%Co/La_2O_3, has five peaks, α, β, χ, δ, ε at ~340 ºC, 420 ºC, 490 ºC, 580 ºC, and 640 ºC, respectively. The α peak at ~340 ºC is most likely the reduction of weakly interacting NiO[38]. The higher temperature peaks at 420 ºC and 490 ºC could be attributed to Ni^{2+} reduction closely interacting with Co_2O_3 or the support. The higher temperature peaks, δ and ε, correspond to the reduction of Co_2O_3.

As a comparison, we performed TPR and XRD measurements on reference perovskite precursors, $La_{0.9}FeCo_{0.1}O_3$ (A-LFCO) and $La_{0.9}FeNi_{0.1}O_3$(A-LFNO) shown in **Figure S3.2**. The XRD shows that after reduction at 700 ºC, the A-LFCO and A-LFNO form Co_2O_3 and $NiFe_2O_4$ nanoparticles, respectively. The TPR profiles for A-LFCO have reduction peaks at 450 ºC that corresponds to a reduction of Co^{+3} to $Co^{+2,}$ and the second peak at 520 ºC corresponds to Fe^{+3} to Fe^{+2} [39]. The peaks for A-LFNO are lower in temperature, which corresponds to the reduction of Ni^2 to Ni^0 and the reduction of Fe^{3+} to Fe^{2+}. Comparing the reference perovskite oxide TPRs with A5 and B5 shows that most catalyst nanoparticles formed are aggregates and closely interacting.

In comparison to the perovskite oxide peaks, the reference sample species synthesized through wet co-impregnation has multiple metallic species of Ni and Co, showing that the multi-metallic nanoparticles have a mixture of characteristics. The XRD

spectra of 5%Ni and 5% Co shown in **Figure S3.3** confirm the existence of mixed characteristics of the nanoparticles showing defined peaks for $NiCo_2O_4$, NiO, and Co_3O_4 (45 2θ). This demonstrates the inherent lack of control for the nucleation and growth of multimetallic nanoparticles using wet impregnation. In contrast, the perovskite precursor reduction peaks occur at lower temperatures and closer together, showing that most catalyst nanoparticles formed are aggregates and closely interacting.

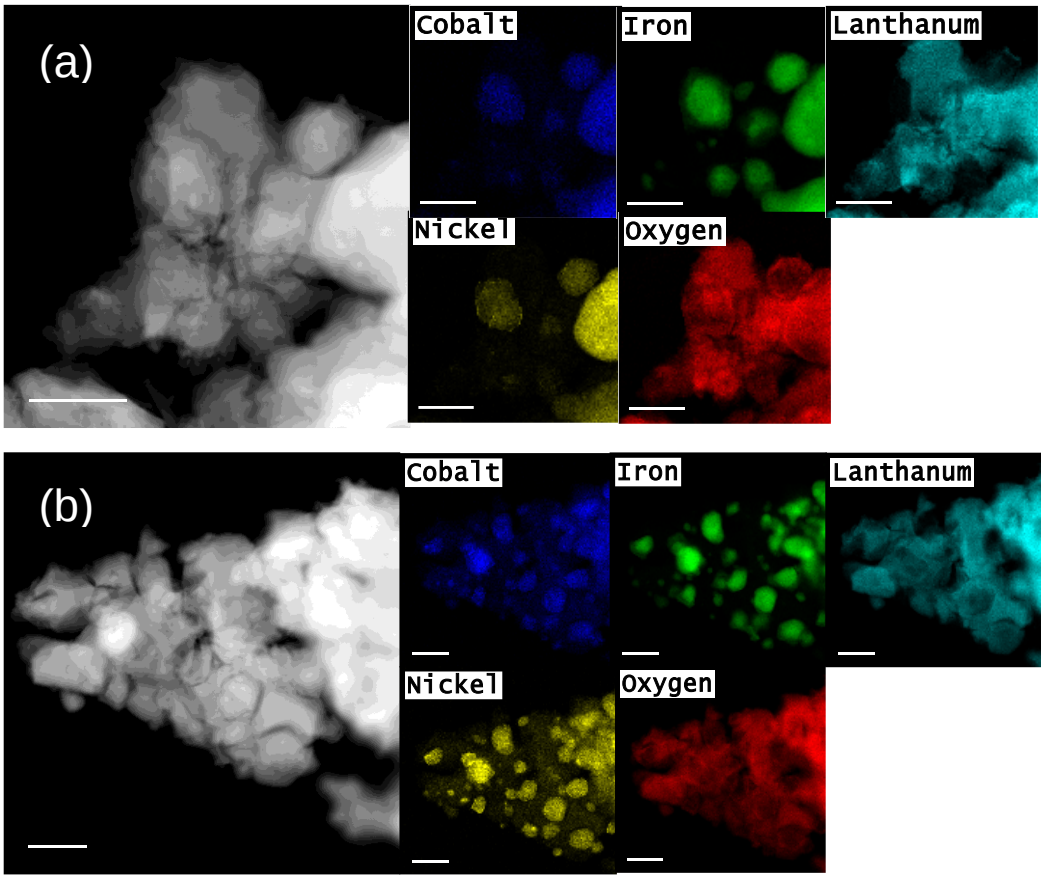

Figure 3.3. HAADF-STEM and EDS images of (a) A5 and (B5) catalysts after reduction at 950 ºC for two hours.

3.4.4. Scanning Transmission Electron Microscopy Imaging Analysis

HAADF-STEM imaging was used to study morphology, particle size, and dispersion of the catalyst nanoparticles reduced at 800 ºC and 950 ºC, respectively

(**Figure S3.4 and Figure 3.3**). The average particle size was calculated based on an average of 50 - 100 particles. The mean particle size for A5 and B5 reduced at 800 ºC was ~24 and 22 nm, respectively. In comparison, the mean particle size for 950 ºC was 97 nm for A5 and 66 nm for B5 catalysts. The nanoparticles formed are much larger than typical systems and are attributed to the extensive exsolution of the B-cations from the perovskite oxide lattice.

The composition of the particles and the support were analyzed with STEM-EDS. The segregation of Fe, Ni, and Co from the parent perovskite is apparent in the EDS maps (**Figure 3.3**). The images show that oxygen is mainly distributed over the support and the surface of the nanoparticles, which most likely have oxidized once removed ex situ. Elemental Fe desegregates from the multi-metallic alloy nanoparticles after exsolution to form an oxide shell over a core of metallic Ni-Co nanoparticles. A quantitative delineation of nanoparticle and support composition is shown in **Table 3.2**. The mean Ni composition, as the fraction of total metal content, in the nanoparticles formed by A5 reduced at 800 ºC is 7.3% and 6.6% for A5 reduced at 950 ºC. For the B5 catalyst, the Ni content in the nanoparticles is 10.1 % at 800 ºC and 5.7% for the sample reduced at 950 ºC. Analogously, the Co content of the catalyst nanoparticles is higher at the lower reduction temperature. The predominant theory in literature states that the exsolution of the metal dopants from perovskite precursors occurs as a function of their reducibility. Based on the TPRs and STEM-EDS images, we surmise that the NiFeCo nanoparticles formed are higher in Ni and Co at 800 ºC because of their lower reduction temperature to their metallic state in comparison to Fe. As

Table 3.2. Particle size, dispersion composition, and support composition of fresh (reduced at 800 ºC and 950 ºC for two hours) and aged (on reaction stream for 24 hours) catalysts as calculated from STEM-HAADF EDS.

Sample	**Size (nm)**	**Dispersion* (%)**	**Particle Composition (% of total metal content)**		**Support Composition (% of total metal content)**
			Ni%	**Co%**	**La %**
A5 800 ^{o}C reduced	24	4.2	7.3	7.3	88.8
A5 950 ^{o}C reduced	97	1.0	6.6	5.9	91.2
A5 aged	58	1.7	28	26.8	50
B5 800 ^{o}C reduced	23	4.4	19.4	15.2	60.5
B5 950 ^{o}C reduced	66	1.5	5.6	5.7	94.6
B5 aged	65	1.5	50.1	39.1	56

the temperature increases, more of the Fe in the lattice is reduced and exsolved in the formed nanoparticles. Therefore, the NiFeCo nanoparticles become more Fe-enriched as the reduction temperature increases. Thus, the temperature of reduction influences the composition and size of the formed nanoparticles.

3.4.5. Catalytic Activity and Stability

DRM was used to probe the catalyst performance of the NiFeCo catalyst nanoparticles (**Figure 3.4**). The Ni:Co ratio was changed to determine trends related to the structure-reactivity performance of the catalysts reduced at 950ºC (see **Table 3.1**). At high temperatures, the A5 sample had a higher conversion for methane and carbon dioxide conversion at ~90%, while B5, B8, and B2 had slightly lower conversions below ~80% for methane and ~90% for carbon dioxide. At lower temperatures below 800ºC, B8 and B2 perform about the same and have superior performance compared to B5 and A5. **Figure 3.4(b)** shows that after 24 hours on the reaction stream at 900ºC, A5 performed the best and remained stable in activity for up to 24 hours. In comparison, B8 and B5 had a slight increase over the initial 5 – 6 hours in activity and then plateaued. On the other hand, the Co-rich sample, B2, decreased activity throughout the 24-hour aging experiment. The overall catalyst that performed the best for the activity and stability was A5. The performance of A5 declined <10% over 24 hours, while B5 improved marginally during the first 4 hours and declined <5% after 24 hours.

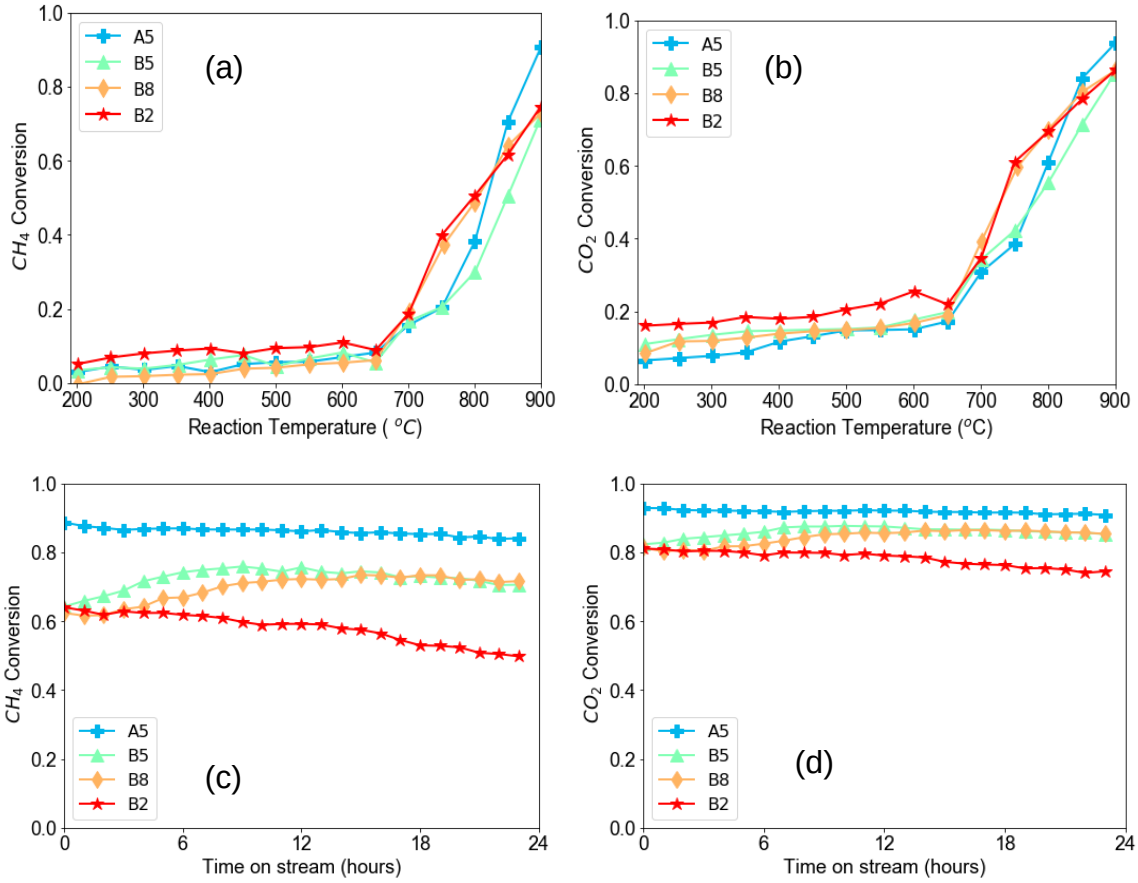

Figure 3.4. DRM conversion and stability data for A5, B5, B8 and B2 catalyst precursors after reduction at 950 ºC for two hours. (a) CH_4 DRM conversion data and (b) CO_2 DRM conversion data. (c) CH_4 DRM stability data and (d) CO_2 DRM stability data for up to 24 hours on stream at 900 ºC.

We surmise the A5 catalyst had the best performance due to the higher Ni content in the formed nanoparticles and inherent oxygen vacancies within the support that promote the activation of CH_4 and CO_2. For instance, A5 had the highest activity and stability attributed to the higher Nickel content of 6.6% versus that of the B5 of 5.6%. We surmise that the differences in the activity for the four catalysts are attributed to the composition of the exsolved nanoparticles and the defects inherent in the support. The inclusion of the A-site cation vacancies during the synthesis of the A5 perovskite oxide precursor promotes more of the Ni and Co component in the nanoparticle.

The samples A5 and B5 were examined under STEM in both bright field (BF) and HAADF modes along with EDS mapping to characterize the change in the nanoparticle's composition and size after 24-hour aging (**Figures S3.5**). The atomic analysis of the NiFeCo nanoparticles was measured and is shown in **Table 3.2**. The Ni and Co content for B5 increased significantly from less than 7% to 80% of the metal content in the nanoparticle while maintaining the same average nanoparticle size of 65 nm. The A5 nanoparticles after aging show that the concentration of the Ni and Co increased from ~12% to 50% of the nanoparticle composition. The average nanoparticle size for A5 was reduced from ~98 nm to ~58 nm. Interestingly, the change of the nanoparticle composition, size, and dispersion points to a mechanism where the alloy nanoparticles are not static but susceptible to the reaction environment. For DRM, multi-metallic nanoparticles are susceptible to the reaction environment, which manifests as desegregation during DRM. When Ni is alloyed with Fe, Fe is usually more predisposed to the CO_2 in the environment and forms a core shell. However, when using perovskite

precursor supports, the Fe in the adhered nanoparticle is oxidized and returns to the bulk of the support. The XRD spectra shown in **Figure S3.6** for A5 and B5 after 24-hour aging corroborates the finding where the material started with mostly NiFeCo supported on La_2O_3 and was converted to $LaFeO_3$ perovskite support. The redox nature of the DRM environment with H_2, CH_4, and CO being reductive and CO_2 being mildly oxidative changes the equilibrium state of exsolution. The nanoparticle size, dispersion, and composition of the NiFeCo catalyst nanoparticles respond to the environment, which manifests in changing the catalytic activity. This is, in part, why the B5 and B8 catalysts increase in activity as the reaction proceeds over 24 hours. Smaller and Ni-rich particles would also imply improved catalyst performance, as shown in the evolution of the activity for B5 and B8 in **Figures 3.4c** and **3.4d**.

3.4.6. Effect of reduction temperature to catalyst performance

It is imperative to reduce the perovskite precursor systems at temperatures higher than the expected reaction conditions. Otherwise, the nanoparticle will be pre-disposed to the environment and ripening effects. In this study, we reduced the perovskite precursors at 950 ºC since the DRM result in smaller nanoparticles. To test our hypothesis, we reduced the nanoparticles at 800 ºC to compare with the 950 ºC reduction system. As discussed earlier, the nanoparticles formed at 800 ºC for A5 and B5 are smaller and have more Ni and Co content than the 950 ºC reduced systems. We compared the activity and stability of the A5 and B5 catalysts reduced at 800 ºC to the catalysts reduced at 950 ºC (**Figure 3.5**). For the catalysts reduced at 800 ºC, the reaction activates much faster and earlier than the samples reduced at 950 ºC. At lower temperatures, the activity for A5 and B5 are

similar for methane and carbon dioxide conversions below 20%. At higher temperatures, the samples reduced at 800 ºC show, on average, an increase in activity towards methane activation at 900 ºC by 11% for A5 and 32% for B5. Quite interestingly, the H_2/CO ratio for the 800 ºC reduced catalysts are between 0.9 – 1, while the H_2/CO for the 950 ºC was between 1 – 1.1 (**Figure S3.7**). This possibly indicates that the 950 ºC reduced catalysts are more efficient in hydrogen production. This could potentially be attributed to the greater concentration of Fe in the NiFeCo nanoparticles that promote water gas shift. During 24-hour aging experiments, the 800 ºC reduced samples declined with additional time on stream. Interestingly, the 800 ºC declined to a similar activity as the 950 ºC reduced samples. Our hypothesis suggests that the perovskites, being dynamic materials, establish an equilibrium with the redox environments. Thus, the characteristics of the 800 ºC changed to a steady-state size and composition at 900 ºC. For both catalysts reduced at 950 ºC and 800 ºC, the A5 samples are superior in both activity and stability. We surmise that the greater concentration of the oxygen vacancies in A5 catalysts promotes the dry methane reforming reaction despite having a smaller Ni content when compared to B5.

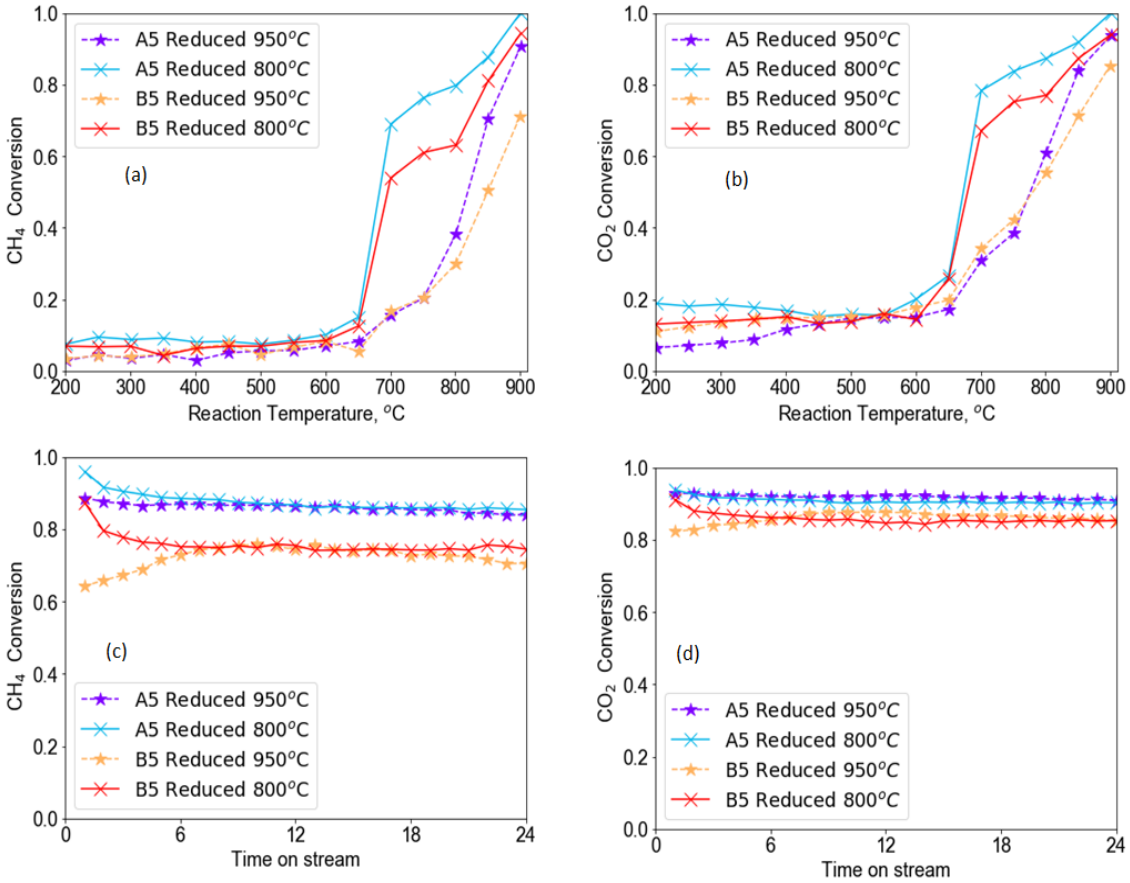

Figure 3.5. DRM conversions compared for samples reduced at 950 ˚C and 800 ºC. (a) Methane conversion for A5 and B5 and (b) Carbon Dioxide conversion for A5 and B5. (c) CH_4 DRM stability data and (d) CO_2 DRM stability data for up to 24 hours on stream at 900 ºC.

3.4.7 Elucidating Deactivation Mechanism

Further characterization of the catalyst systems was conducted to determine the stability of the catalysts and their pre-dominant deactivation mechanism over time. TPO in 20% O_2/He was subsequently measured after the aging experiments to compare the extent and qualitative nature of coking on the catalysts' surface (**Figure 3.6**). The NiFeCo nanoparticles from A5 showed significant evolution of CO, indicating the presence of carbonaceous species on the catalyst surface. The associated STEM-BF image shown in **Figure 3.6(b)** shows that there is a noticeable coat of carbon over the formed nanoparticles. Despite the appearance of coke, it is noteworthy that the A5 material remained the most stable catalyst overall, which we contribute to the Co addition. Our previous study implied a hypothesis where despite the basic characteristics of the support, the size of the nanoparticles in the perovskite precursor systems limits the coke-resistance behavior. As a result, the catalyst material deteriorated rapidly after 4 hours. However, the NiFeCo nanoparticles are more robust and stable over 24 hours. The B5 catalyst had minimal CO or CO_2 evolution showing little to no coke formation, as shown in **Figures 3.6(c)** and **3.6(d).** The coke deposition difference could be directly related to the notable size differences of the NiFeCo nanoparticles on A5 and B5 catalysts.

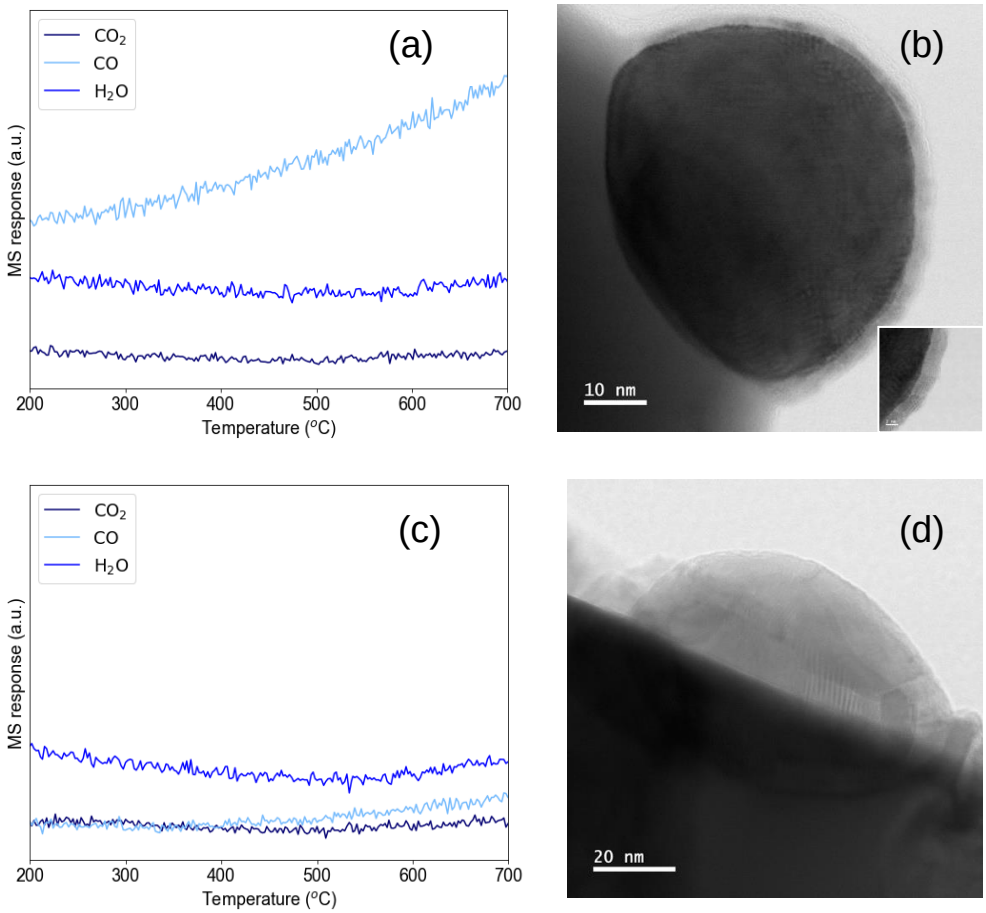

Figure 3.6. The TPO and STEM-BF analysis of A5 and B5 after 24-hour aging. MS profile TPO of (a) A5 and (c) B5. The STEM-BF images are shown in (c) A5 (The inset shows carbon formation on the surface) and (d) B5.

3.4.8. Probing Catalyst Regeneration using Temperature Programmed Surface Reactions

The key feature of using perovskite precursors to synthesize multi-metallic nanoparticles is the possibility of regenerating the catalyst nanoparticles. While regeneration has been studied extensively in monometallic systems, the implications for multi-metallic nanoparticles are relatively unknown. The catalysts' regenerability was compared by aging them in reaction conditions for 24 hours, followed by oxidizing in

20% O_2/He (60 mL/min) for two hours and re-reduction in identical conditions as described previously. The XRD profiles of the perovskite during the regeneration cycle are shown in **Figure S3.8**. The perovskite structure is regained upon reoxidation. The XRD spectra of the reduced and the re-reduced samples are similar. This is indicative of the cyclability of the catalyst material between the bulk perovskite and segregated states.

TPSR experiments were used to compare light-off and catalyst activity before and after regeneration. A comparison of the TPSRs can be seen in **Figures 3.7** and **3.8**. The as-prepared catalyst A5 activates CH_4 at ~705 ºC, but after regeneration, the light-off temperature increases to ~740 ºC. This possibly indicates nominal changes in the active sites for CH_4 activation. In comparison, the as-prepared B5 activates CH_4 at a slightly higher temperature of 730 ºC and increases to 740 ºC after regeneration. This shows that the B5 regeneration results in minimal changes to the catalyst properties.

TPSRs for both catalysts, A5 and B5, showed a slight increase in CO formation before methane activation occurred. To elucidate this mechanism, we conducted a TPSR on A-LFCO to study the effect of cobalt in DRM reaction conditions (**Figure S3.9**). The TPSR for DRM with the cobalt catalyst shows a shoulder beginning at 525 ºC and a prominent local maximum in CO formation at 710 ºC, coinciding with the onset of hydrogen formation. We surmise that CO_2 is consumed by metallic Co, which gets

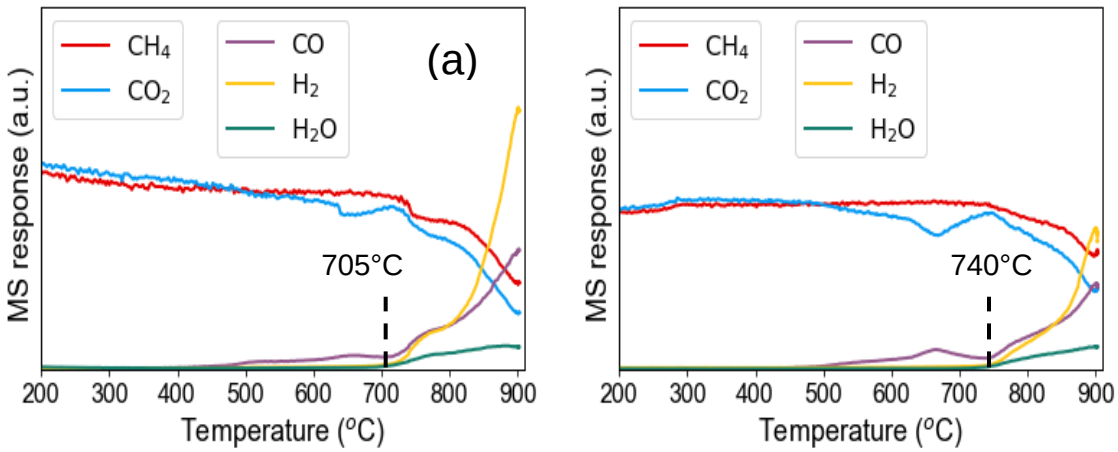

Figure 3.7. MS profiles of TPSR of DRM over (a) as-prepared A5 catalyst and (b) regenerated A5 catalyst after aging on DRM stream for 24 hours.

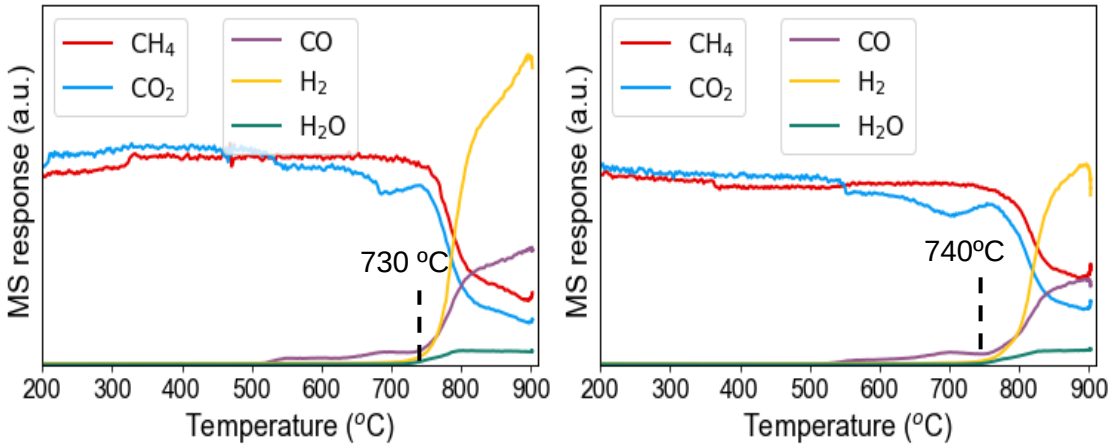

Figure 3.8. MS profiles of TPSR of DRM over (a) as-prepared B5 catalyst and (b) regenerated B5 catalyst after aging on DRM stream for 24 hours.

partially oxidized to Co^{2+}. Omata et al.[40] made similar observations while studying DRM over magnesia-supported Co catalysts. They concluded that CO_2 partially oxidizes metallic Co, which passivates its catalytic function. A-LFCO is active for methane consumption, albeit much less than samples with nickel, and has a methane consumption of 1.02 μmol/s.g. catalyst. It also is more selective for RWGS and had an H_2/CO ratio of only 0.25. Presumably, the lower activity and selectivity to RWGS is due to the partial

oxidation of Co by CO_2. The low selectivity of Co towards DRM also explains the difference in the performance of B2 relative to B5 and B8. As cobalt is unable to suppress RWGS, a higher Co content decreases the H_2/CO ratio due to the formation of water or gasification of coke.

3.4.9. Apparent Activation Energies and Consumption Rates for As-Prepared and Regenerated Catalysts

The CH_4 apparent activation energies for the as-prepared and regenerated catalysts are shown in **Table 3.3**. The reaction rate for methane consumption was 5.04 μmol/s.g. the catalyst for as-prepared A5 compared to 2.07 μmol/s. g. for regenerated A5 at 950 ºC. The H_2/CO ratio for A5 decreased from 1.2 to 0.47 due to increased hydrogen consumption in the reverse water gas shift reaction or coke gasification. For B5, the decline in activity after regeneration was much smaller, with methane consumption rates falling from 3.91 μmol/s.g. catalyst to 2.96 μmol/s.g. catalyst. The H_2/CO ratio decreased from 0.96 to 0.66. Both catalysts were active for syngas formation after regeneration, indicating that synergistic interactions between multi-metallic catalysts and strong support interactions in the nanoparticles afford resistance to sintering and coking. However, regenerated catalysts were less selective for syngas formation, with a marked increase in RWGS reaction. The changes in the activity and selectivity after the regeneration cycle may point to a mechanism where the systems were not completely regenerated, but the properties of the catalysts changed. We surmise that the re-oxidation process changed the properties of the perovskite precursors influencing the rate of exsolution, leading to a decline in activity and selectivity towards RWGS over DRM.

Table 3.3. A comparison of the consumption rates and apparent activation energy for the perovskite oxide catalyst precursors measured @900 ºC

Catalyst	CH_4 rate (μmol/s. g. cat.)	CO_2 rate (μmol/s. g. cat.)	H_2/CO @ 900 ºC	CH_4 Activation Energy (kJ/mol. K)
A5 (950 ºC reduced)	5.04	5.02	1.19	47.7
A5 (800 ºC reduced)	5.61	5.40	1.45	48.8
A5 regenerated	2.07	3.38	0.47	55.7
B5 (950 ºC reduced)	3.91	4.57	0.96	41.3
B5 (800 ºC reduced)	5.15	4.94	0.96	47.1
B5 regenerated	2.96	3.96	0.66	63.8
B2 As-prepared	4.18	4.66	0.54	58.4
B8 As-prepared	3.98	4.66	1.00	45.4
A-LFCO	1.02	2.21	0.25	58.1
$Ni+Co/La_2O_3$ As-prepared	4.96	4.95	0.95	48.5
$Ni+Co/La_2O_3$ regenerated	5.51	5.16	1.04	44.4
Ni/La_2O_3 from $LaNiO_3$	------	------	------	68 [42]
$La_{0.9}FeNi_{0.1}O_3$	2.62	4.09	------	142.5 [32]
$LaFe_{0.9}Ni_{0.1}O_3$	5.21	5.70	------	135.5 [32]

The activation energies of the as-prepared catalysts are similar (48, 41, and 45 kJ/mol for A5, B5, and B8) to the reference 5%Ni+5%Co/La_2O_3 sample of 44.4 kJ/mol. These activation energies are lower than the reported 68 kJ/mol for Ni/La_2O_3 derived from $LaNiO_3$[41]. Despite our systems, A5 and B5, having larger nanoparticles greater than 20 nm, the catalysts were more active. We believe the improved activity is due to the multi-metallic synergy of Ni, Fe, and Co that allows for effective methane activation on the catalyst surface. We also compared with similar perovskite precursors that have only Ni and Fe, $La_{0.9}FeNi_{0.1}O_3$, and $LaFe_{0.9}Ni_{0.1}O_3$. The activation energies in this study with the inclusion of Co drastically improved the CH_4 activation energy dramatically. By substituting Co in the perovskite precursor, the nanoparticles formed were smaller. The activation energies confirm the synergistic relationship between Ni, Fe, and Co for DRM and their enhanced performance.

3.5. Conclusions

This study has examined the structure-reactivity relationship of NiFeCo catalyst nanoparticles derived from perovskite oxide precursors. The implications of the study serve to not only look to perovskite precursors as a method for the synthesis of multi-metallic nanoparticles but to understand how these properties change as a function of reaction conditions. The conclusions of this study are multi-faceted and show the utility of NiFeCo nanoparticles for DRM.

- The NiFeCo formed using La(Fe,Ni,Co)O_3 perovskite precursors are more likely to form homogeneous pseudo-alloy nanoparticles when compared to the conventional wet impregnation method. This was corroborated by the TPR and

STEM-BF imaging which confirmed the formation of aggregates of Ni, Fe, and Co.

- We have shown the effects of A-site cation deficiency, B-site cation composition, and reduction temperature as levers to control the composition of the form NiFeCo nanoparticles. The perovskite precursor with inherent A-site cation deficiencies, A5, was the best catalyst overall. We suggest that the improved performance compared to the other catalysts studied is due to the higher Ni content and greater concentration of oxygen vacancies that promote CO_2 and CH_4 activation.
- Our studies indicated the role of the reduction temperature to control the nanoparticle properties. The NiFeCo nanoparticles formed at 800 ºC were smaller than the nanoparticles formed at 950 ºC. Still, when the 800 ºC systems were exposed to the DRM reaction environment over time, the activity declined to a similar activity profile of the 950 ºC reduced materials. Thus, our study suggests that multi-metallic perovskite precursor systems are dynamical and predisposed to the reaction environment. This must be considered for using perovskite precursors in other thermochemical reactions at elevated temperatures.
- Based on the TPO, the A5 nanoparticles had some coke on the surface despite showing the best performance overall. The inclusion of Co in the NiFeCo nanoparticle ensured adequate activation of CH_4 despite coke development. We surmise that the coke formation is from the initial large size of the nanoparticles.

B5 did not show evidence of coking, which we suggest is due to the smaller nanoparticles.

- Finally, we probed the regeneration of the NiFeCo nanoparticles and determined that the catalysts are regenerable, as corroborated by XRD, HAADF-STEM analysis and TPSR. However, changes to the perovskite precursor during the redox cycle will influence the exsolution of the metal constituents affecting the catalyst performance.
- A comparison of the rates of consumption and activation energies shows that the NiFeCo were synergistic in improving the activation of CH_4, especially when compared to other perovskite precursor systems. An introduction of Co improved long-term performance compared to perovskite precursor catalysts with only Ni and Fe. However, as seen by the performance of the B2 catalyst, there exists an optimal amount of Co beyond which it is detrimental for DRM activity.

Based on this work, we determined some relevant factors that control and influence performance characteristics for multi-metallic catalysts derived from perovskite precursors. This knowledge can be used to design multi-metallic catalysts tailored for DRM with prolonged activity and stability despite coke-formation.

3.6. Supplementary data

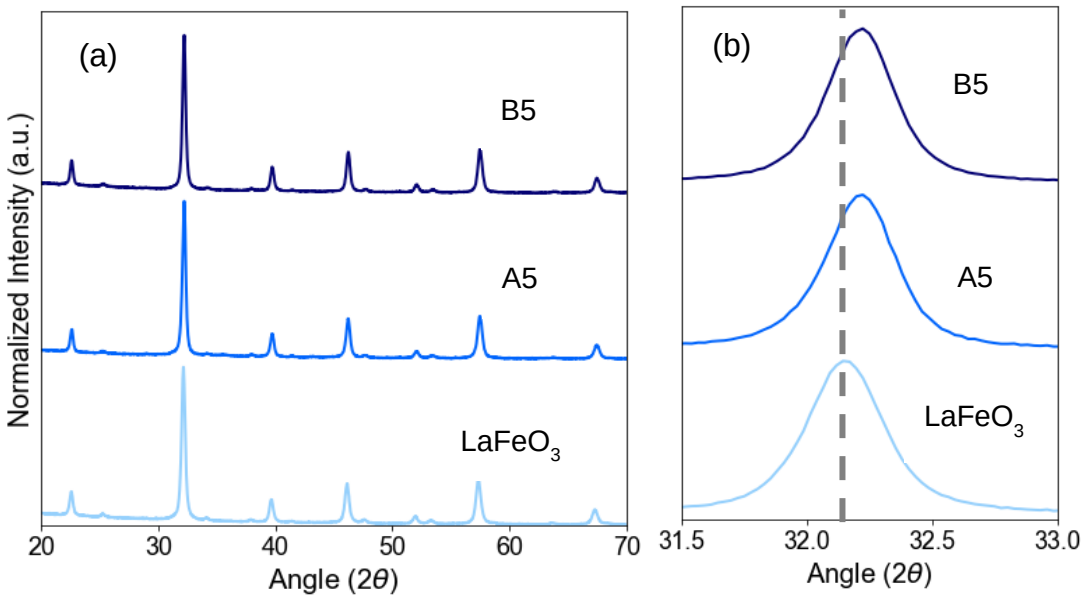

Figure S3.1. X-Ray Diffractograms of as-prepared perovskite precursors of (a) A5, B5 and pristine $LaFeO_3$. (b) The (121) primary $LaFeO_3$ peak at 32.1 2θ red shift due to the volume change for the incorporation of Ni and Co in the lattice.

Sample	a(Å)	b(Å)	c(Å)	V(Å^3)
$LaFeO_3$	5.6	5.66	7.94	252
A5	5.52	5.55	7.81	240
B5	5.53	5.57	7.85	242

Table S3.1. Lattice parameters and unit cell volume of as-prepared catalyst precursors, $LaFeO_3$, A5 and B5, as calculated by Rietveld refinement of the associated XRD patterns.

Table S3.2. Surface area and porosity of reduced catalyst samples as measured by N_2 adsorption isotherm at 77K.

Sample	BET surface area (m^2/g)	BJH Adsorption Pore Volume (cm^3/g)	BJH Adsorption Pore diameter (nm)	BJH Desorption Pore diameter (nm)
(A5)	3.535	0.0074	10.95	6.82
(B5)	3.172	0.0094	16.92	10.1

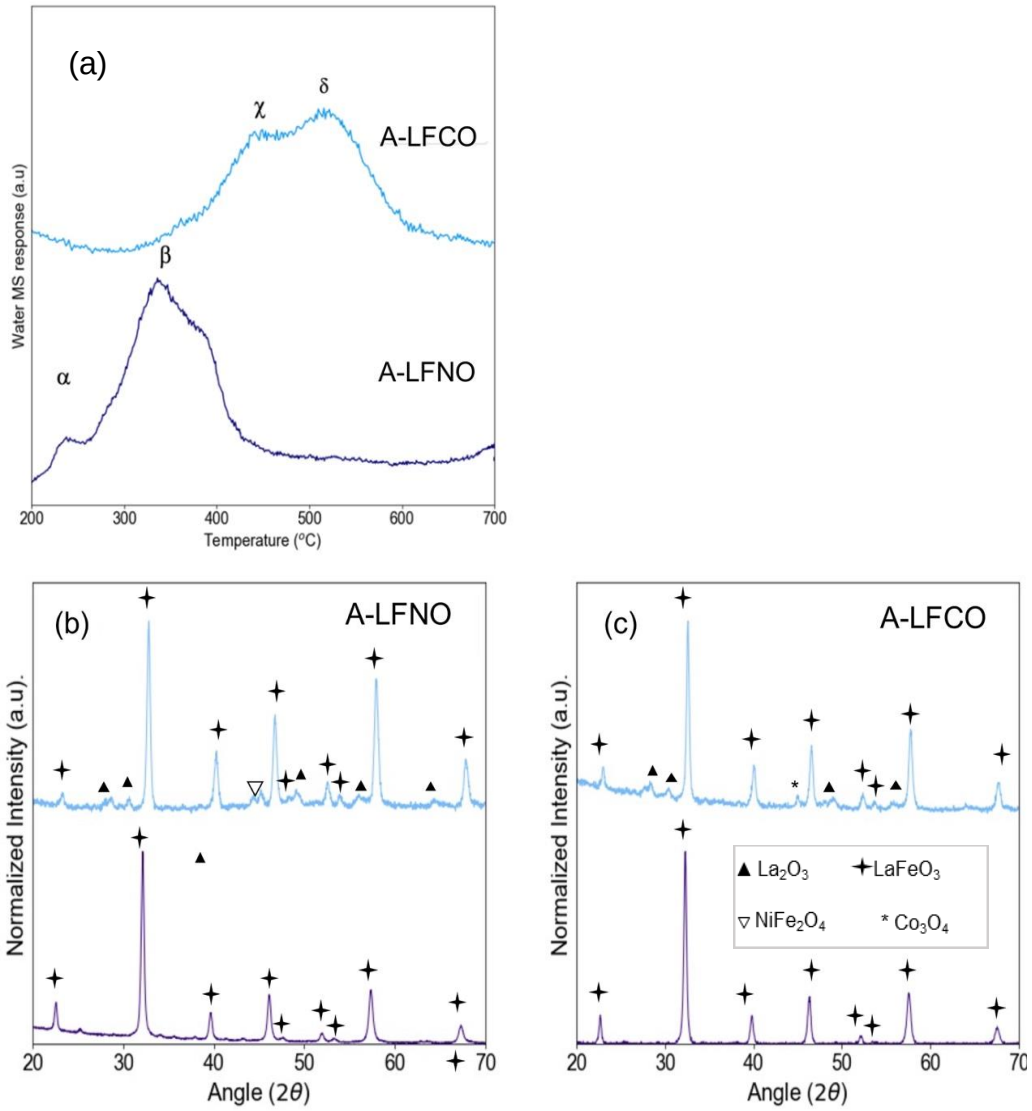

Figure S3.2. TPR of $La_{0.9}FeCo_{0.1}O_3$ and $La_{0.9}FeNi_{0.1}O_3$, (b) X-ray diffraction spectra of $La_{0.9}FeNi_{0.1}O_3$ and (c) $La_{0.9}FeCo_{0.1}O_3$.

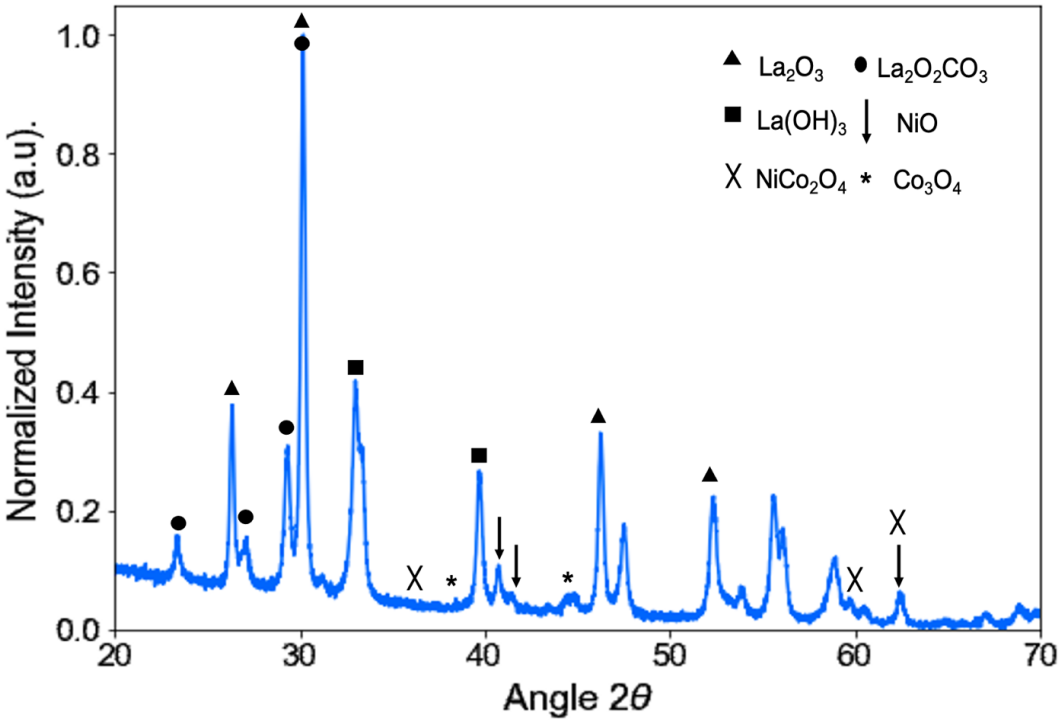

Figure S3.3. XRD spectra of 5%Ni+5%Co supported on La_2O_3.

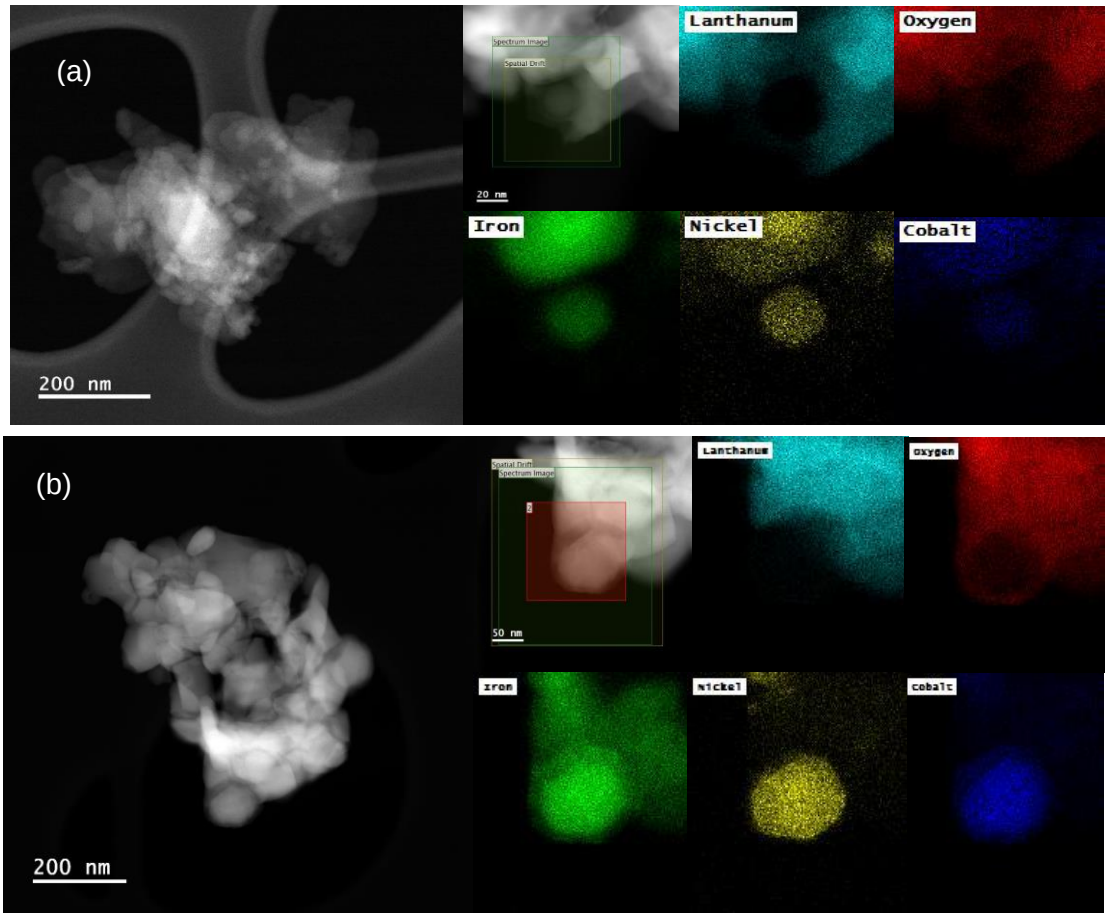

Figure S3.4. STEM-HAADF and EDS images of (a) A5 and (b) B5 catalyst samples after reduction at 800°C.

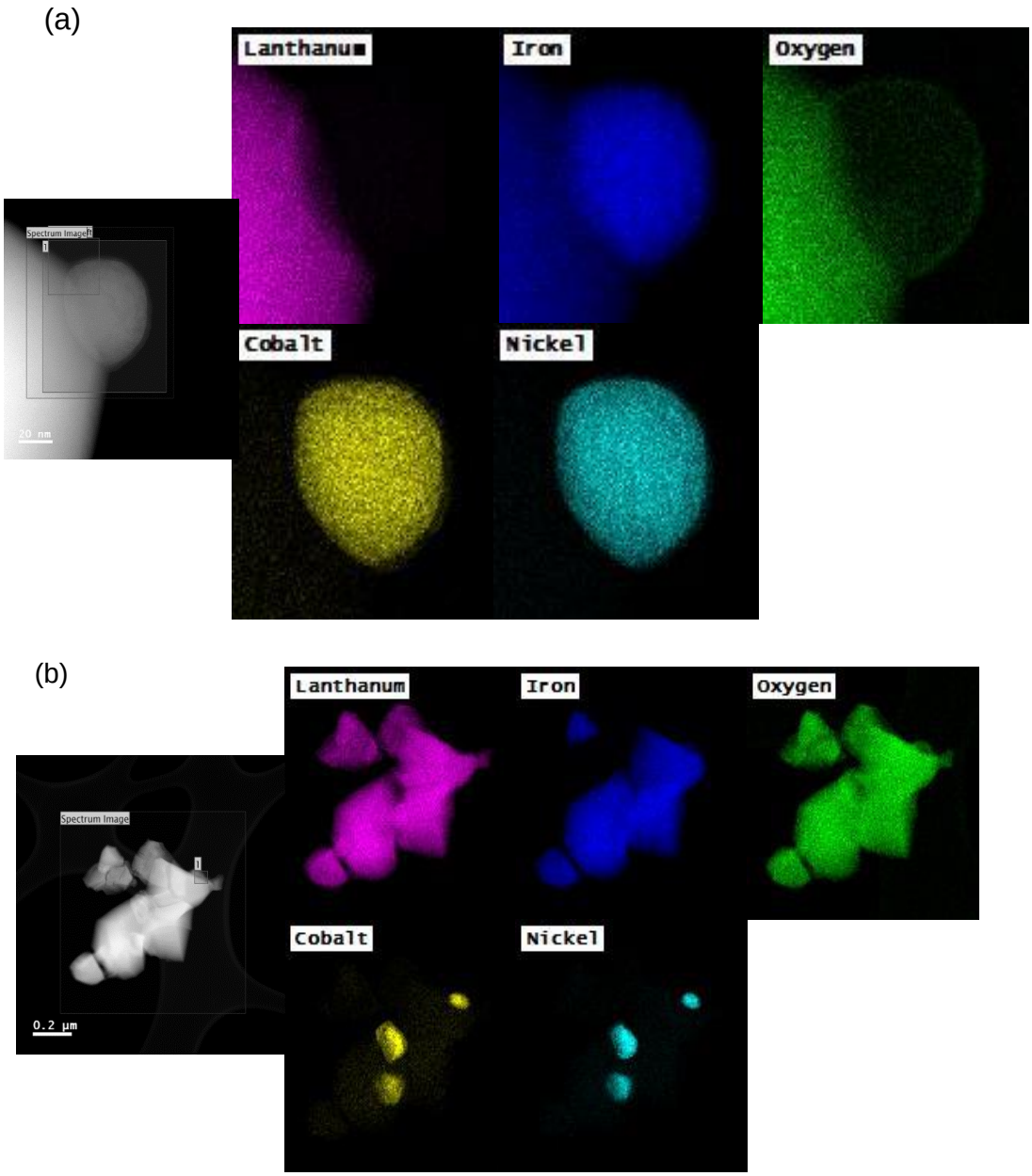

Figure S3.5. STEM-HAADF images of the NiFeCo nanoparticles on the (a) A5 perovskite precursors aged after 24 hours on stream and (b) B5 catalyst aged after 24 hours on stream.

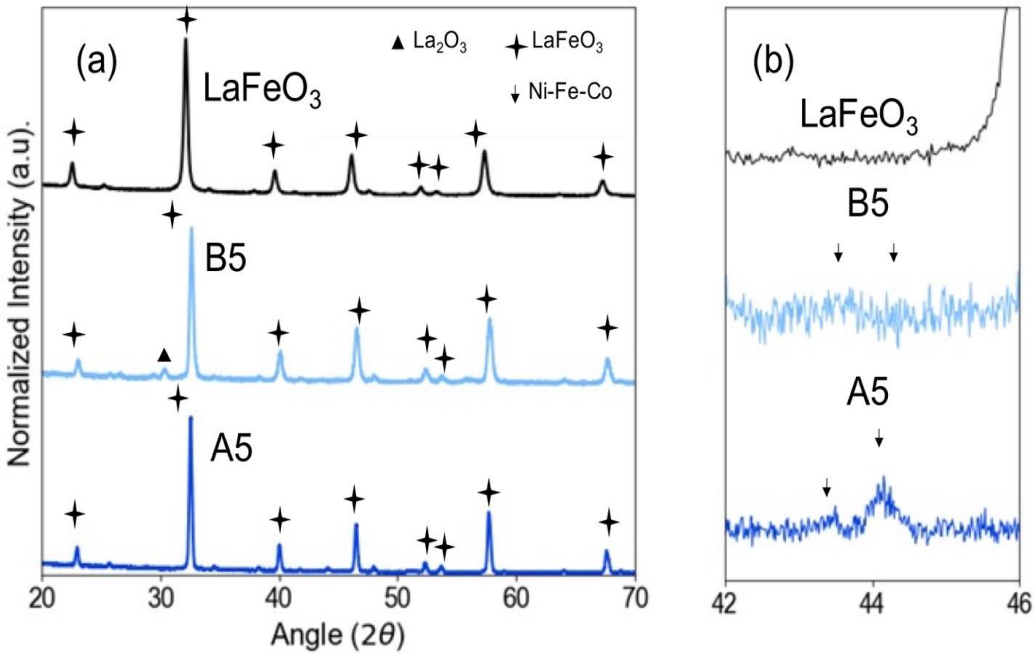

Figure S3.6. XRD of perovskite precursors of (a) A5, B5 after 24 hour aging. (b) Zoomed inset around primary $LaFeO_3$ peak at 32.1° (c) Zoomed inset around the Ni-Co-Fe alloy peaks around 41°-46°.

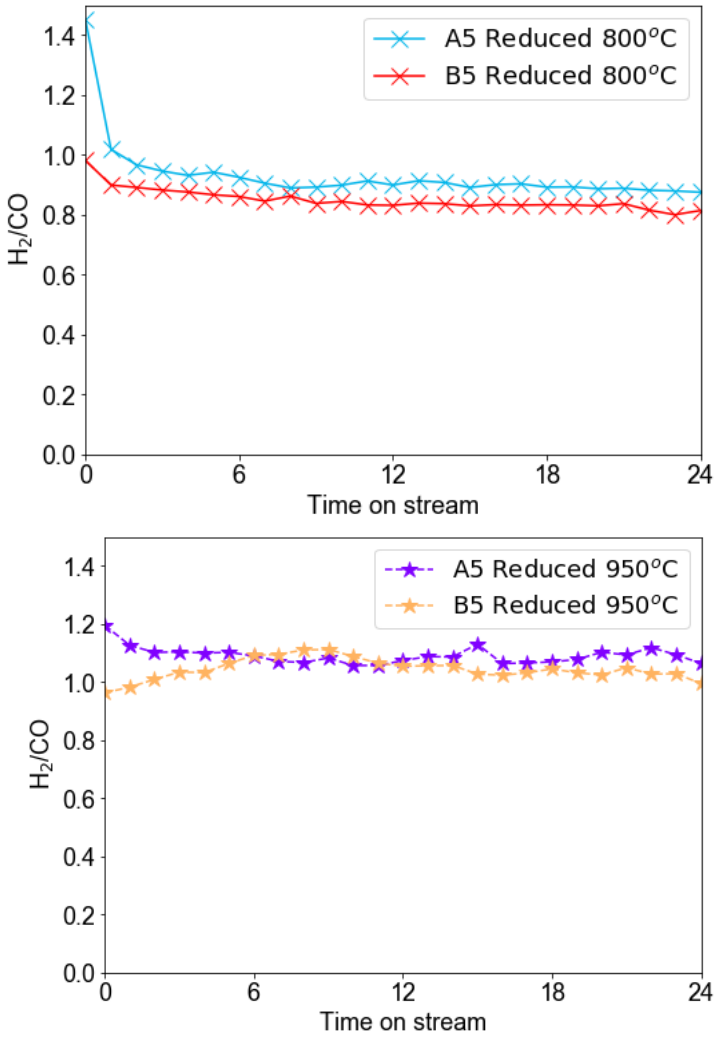

Figure S3.7. H_2/CO for A5 and B5 reduced at (a) 800°C and (b) 950°C for 2 hours.

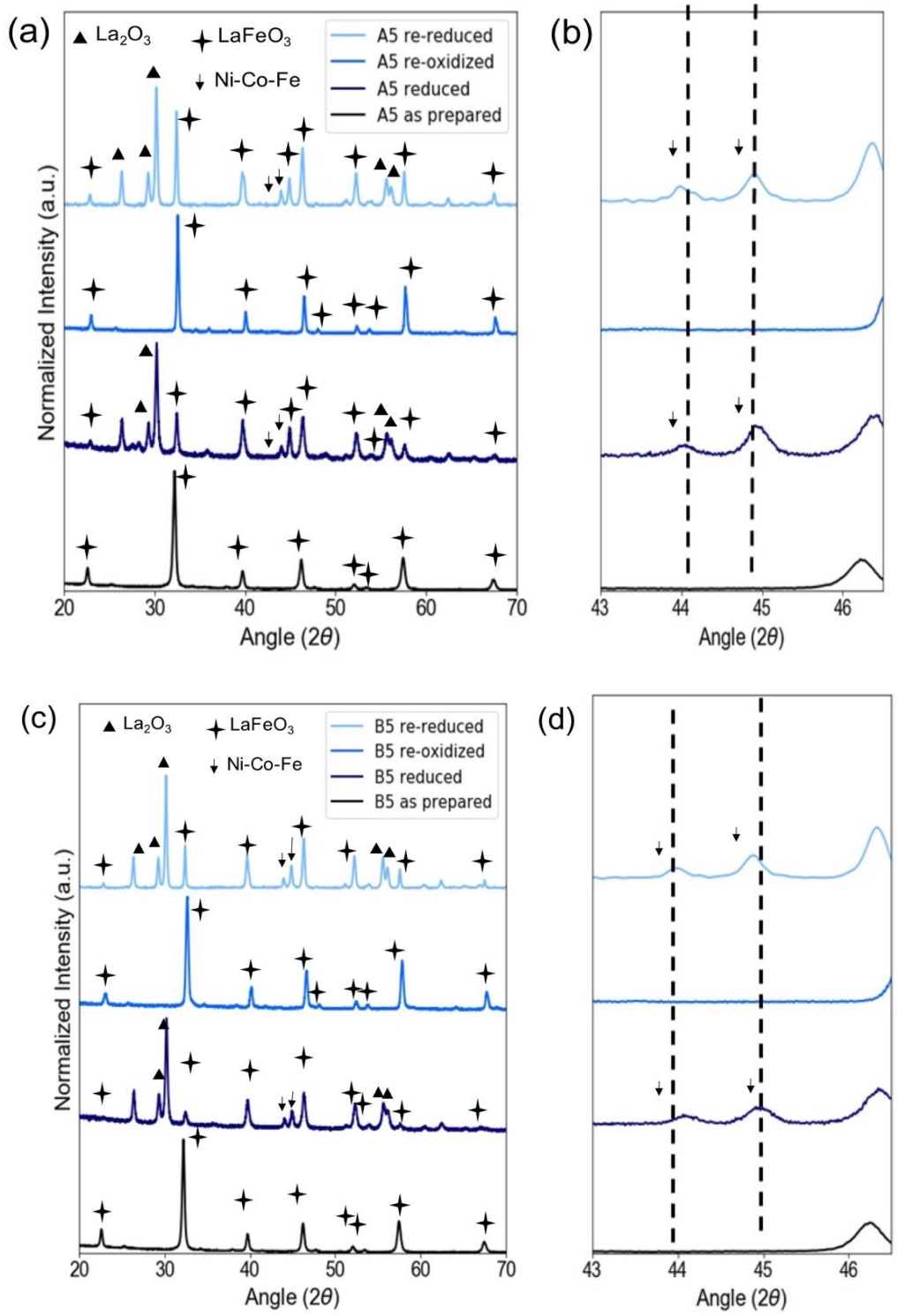

Figure S3.8. XRD spectra for A5 and B5 during 1 regeneration cycle, the XRD for (a,b) A5 and (c,d) B5 shows as-prepared, reduced, re-oxidized and re-reduced materials at 950ºC. The insets around the NiFeCo alloy peaks (b,d) around 41°-46º shows the formation of the perovskite oxide to the nanoparticles.

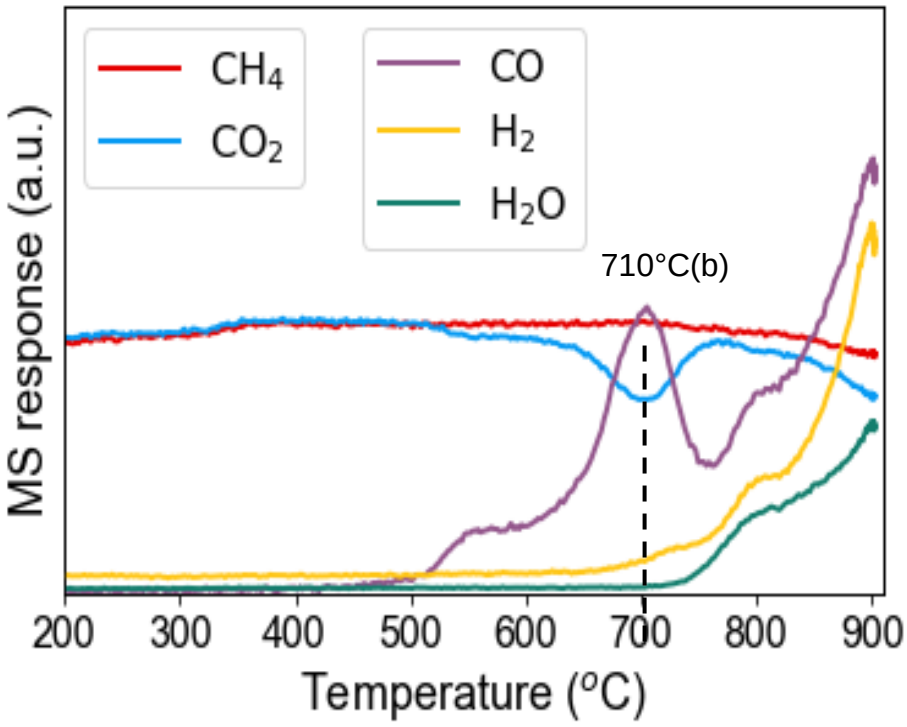

Figure S3.9. MS profiles of Temperature Programmed Surface Reaction (TPSR) of DRM over $La_{0.9}FeCo_{0.1}O_3$ reduced at 950°C.

3.7 References Cited

(1) Lavoie, J.-M. Review on Dry Reforming of Methane, a Potentially More Environmentally-Friendly Approach to the Increasing Natural Gas Exploitation. *Front. Chem.* **2014**, *2* (November), 1–17. https://doi.org/10.3389/fchem.2014.00081.

(2) Wei, J.; Iglesia, E. Mechanism and Site Requirements for Activation and Chemical Conversion of Methane on Supported Pt Clusters and Turnover Rate Comparisons among Noble Metals. *J. Phys. Chem. B* **2004**, *108* (13), 4094–4103. https://doi.org/10.1021/jp036985z.

(3) Wei, J.; Iglesia, E. Isotopic and Kinetic Assessment of the Mechanism of Reactions of CH 4 with CO2 or H2O to Form Synthesis Gas and Carbon on Nickel Catalysts. *J. Catal.* **2004**, *224* (2), 370–383. https://doi.org/10.1016/j.jcat.2004.02.032.

(4) Arora, S.; Prasad, R. An Overview on Dry Reforming of Methane: Strategies to Reduce Carbonaceous Deactivation of Catalysts. *RSC Adv.* **2016**, *6*, 108668–108688. https://doi.org/10.1039/c6ra20450c.

(5) Pakhare, D.; Spivey, J. A Review of Dry (CO2) Reforming of Methane over Noble Metal Catalysts. *Chem. Soc. Rev.* **2014**, *43* (22), 7813–7837. https://doi.org/10.1039/c3cs60395d.

(6) Kim, S. M.; Abdala, P. M.; Margossian, T.; Hosseini, D.; Foppa, L.; Armutlulu, A.; Van Beek, W.; Comas-Vives, A.; Copéret, C.; Müller, C. Cooperativity and Dynamics Increase the Performance of NiFe Dry Reforming Catalysts. *J. Am. Chem. Soc.* **2017**, *139* (5), 1937–1949. https://doi.org/10.1021/jacs.6b11487.

(7) Theofanidis, S. A.; Galvita, V. V.; Poelman, H.; Marin, G. B. Enhanced Carbon-Resistant Dry Reforming Fe-Ni Catalyst: Role of Fe. *ACS Catal.* **2015**, *5* (5), 3028–3039. https://doi.org/10.1021/acscatal.5b00357.

(8) Margossian, T.; Larmier, K.; Kim, S. M.; Krumeich, F.; Müller, C.; Copéret, C. Supported Bimetallic NiFe Nanoparticles through Colloid Synthesis for Improved Dry Reforming Performance. *ACS Catal.* **2017**, *7* (10), 6942–6948.

(9) Bian, Z.; Das, S.; Wai, M. H.; Hongmanorom, P.; Kawi, S. A Review on Bimetallic Nickel-Based Catalysts for CO 2 Reforming of Methane. *ChemPhysChem* **2017**, *18* (22), 3117–3134.

(10) San-José-Alonso, D.; Juan-Juan, J.; Illán-Gómez, M. J.; Román-Martínez, M. C. Ni, Co and Bimetallic Ni-Co Catalysts for the Dry Reforming of Methane. *Appl. Catal. A Gen.* **2009**, *371* (1), 54–59. https://doi.org/10.1016/j.apcata.2009.09.026.

(11) Horváth, A.; Guczi, L.; Kocsonya, A.; Sáfrán, G.; La Parola, V.; Liotta, L. F.; Pantaleo, G.; Venezia, A. M. Sol-Derived AuNi/MgAl2O4 Catalysts: Formation, Structure and Activity in Dry Reforming of Methane. *Appl. Catal. A Gen.* **2013**, *468* (5), 250–259. https://doi.org/10.1016/j.apcata.2013.08.053.

(12) Yu, M.; Zhu, Y. A.; Lu, Y.; Tong, G.; Zhu, K.; Zhou, X. The Promoting Role of Ag in Ni-CeO2 Catalyzed CH4-CO2 Dry Reforming Reaction. *Appl. Catal. B Environ.* **2015**, *165*, 43–56. https://doi.org/10.1016/j.apcatb.2014.09.066.

(13) Crisafulli, C.; Scirè, S.; Maggiore, R.; Minicò, S.; Galvagno, S. Co2 Reforming of Methane over Ni-Ru and Ni-Pd Bimetallic Catalysts. *Catal. Letters* **1999**, *59* (1), 21–26. https://doi.org/10.1023/A:1019031412713.

(14) Wang, L.; Li, D.; Koike, M.; Koso, S.; Nakagawa, Y.; Xu, Y.; Tomishige, K. Catalytic Performance and Characterization of Ni-Fe Catalysts for the Steam Reforming of Tar from Biomass Pyrolysis to Synthesis Gas. *Appl. Catal. A Gen.* **2011**, *392* (1–2), 248–255. https://doi.org/10.1016/j.apcata.2010.11.013.

(15) Wang, H.; Dong, X.; Zhao, T.; Yu, H.; Li, M. Dry Reforming of Methane over Bimetallic Ni-Co Catalyst Prepared from La(Co x Ni 1-x) 0.5 Fe 0.5 O 3 Perovskite Precursor: Catalytic Activity and Coking Resistance. *Appl. Catal. B Environ.* **2019**, *245* (December 2018), 302–313. https://doi.org/10.1016/j.apcatb.2018.12.072.

(16) Zhang, J.; Wang, H.; Dalai, A. K. Development of Stable Bimetallic Catalysts for Carbon Dioxide Reforming of Methane. *J. Catal.* **2007**, *249* (2), 300–310. https://doi.org/10.1016/j.jcat.2007.05.004.

(17) Jin, F.; Fu, Y.; Kong, W.; Wang, J.; Cai, F.; Yuan, C.; Pan, B.; Zhang, J.; Sun, Y. Stable Trimetallic NiFeCu Catalysts with High Carbon Resistance for Dry Reforming of Methane. *Chempluschem* **2020**, *85* (6), 1120–1128.

(18) Theofanidis, S. A.; Galvita, V. V.; Sabbe, M.; Poelman, H.; Detavernier, C.; Marin, G. B. Controlling the Stability of a Fe–Ni Reforming Catalyst: Structural Organization of the Active Components. *Appl. Catal. B Environ.* **2017**, *209*, 405–416. https://doi.org/10.1016/j.apcatb.2017.03.025.

(19) Joo, S.; Kim, K.; Kwon, O.; Oh, J.; Kim, H. J.; Zhang, L.; Zhou, J.; Wang, J.; Jeong, H. Y.; Han, J. W.; Kim, G. Enhancing Thermocatalytic Activities by Upshifting the D-Band Center of Exsolved Co-Ni-Fe Ternary Alloy Nanoparticles for the Dry Reforming of Methane. *Angew. Chemie Int. Ed.* **2021**, *60* (29), 15912–15919. https://doi.org/10.1002/anie.202101335.

(20) Loza, K.; Heggen, M.; Epple, M. Synthesis, Structure, Properties, and Applications of Bimetallic Nanoparticles of Noble Metals. *Adv. Funct. Mater.* **2020**, *30* (21), 1909260. https://doi.org/10.1002/adfm.201909260.

(21) Lin, C.; Jang, J. B.; Zhang, L.; Stach, E. A.; Gorte, R. J. Improved Coking Resistance of "Intelligent" Ni Catalysts Prepared by Atomic Layer Deposition. *ACS Catal.* **2018**, *8* (8), 7679–7687. https://doi.org/10.1021/acscatal.8b01598.

(22) Tanaka, H.; Tan, I.; Uenishi, M.; Taniguchi, M.; Kimura, M.; Nishihata, Y. LaFePdO 3 Perovskite Automotive Catalyst Having a Self-Regenerative Function. *J. Alloys Compd.* **2006**, *412*, 1071–1077. https://doi.org/10.1016/j.jallcom.2004.12.138.

(23) Tanaka, H.; Uenishi, M.; Taniguchi, M.; Tan, I.; Narita, K.; Kimura, M.; Kaneko, K.; Nishihata, Y.; Mizuki, J. The Intelligent Catalyst Having the Self-Regenerative Function of Pd, Rh and Pt for Automotive Emissions Control. *Catal. Today* **2006**, *117* (1–3), 321–328. https://doi.org/10.1016/j.cattod.2006.05.029.

(24) Bekheet, M. F.; Delir Kheyrollahi Nezhad, P.; Bonmassar, N.; Schlicker, L.; Gili, A.; Praetz, S.; Gurlo, A.; Doran, A.; Gao, Y.; Heggen, M.; Niaei, A.; Farzi, A.; Schwarz, S.; Bernardi, J.; Klötzer, B.; Penner, S. Steering the Methane Dry Reforming Reactivity of Ni/La2O3 Catalysts by Controlled In Situ Decomposition of Doped La2NiO4 Precursor Structures. *ACS Catal.* **2021**, *11* (1), 43–59.

(25) Neagu, D.; Oh, T. S.; Miller, D. N.; Ménard, H.; Bukhari, S. M.; Gamble, S. R.; Gorte, R. J.; Vohs, J. M.; Irvine, J. T. S. Nano-Socketed Nickel Particles with Enhanced Coking Resistance Grown in Situ by Redox Exsolution. *Nat. Commun.* **2015**, *6* (8120). https://doi.org/10.1038/ncomms9120.

(26) Katz, M. B.; Graham, G. W.; Duan, Y.; Liu, H.; Adamo, C.; Schlom, D. G.; Pan, X. Self-Regeneration of Pd-LaFeO 3 Catalysts: New Insight from Atomic-Resolution Electron Microscopy. *J. Am. Chem. Soc.* **2011**, *133* (45), 18090–18093. https://doi.org/10.1021/ja2082284.

(27) Oemar, U.; Ang, P. S.; Hidajat, K.; Kawi, S. Promotional Effect of Fe on Perovskite LaNixFe 1-XO3 Catalyst for Hydrogen Production via Steam Reforming of Toluene. *Int. J. Hydrogen Energy* **2013**, *38* (14), 5525–5534. https://doi.org/10.1016/j.ijhydene.2013.02.083.

(28) Zhang, S.; Katz, M. B.; Dai, S.; Zhang, K.; Du, X.; Graham, G. W.; Pan, X. New Atomic-Scale Insight into Self-Regeneration of Pt-CaTiO3 Catalysts: Incipient Redox-Induced Structures Revealed by a Small-Angle Tilting STEM Technique. *J. Phys. Chem. C* **2017**, *121* (32), 17348–17353.

(29) Neagu, D.; Kyriakou, V.; Roiban, I. L.; Aouine, M.; Tang, C.; Caravaca, A.; Kousi, K.; Schreur-Piet, I.; Metcalfe, I. S.; Vernoux, P.; Van De Sanden, M. C. M.; Tsampas, M. N. In Situ Observation of Nanoparticle Exsolution from Perovskite Oxides: From Atomic Scale Mechanistic Insight to Nanostructure Tailoring. *ACS Nano* **2019**, *13* (11), 12996–13005. https://doi.org/10.1021/acsnano.9b05652.

(30) Neagu, D.; Tsekouras, G.; Miller, D. N.; Ménard, H.; Irvine, J. T. S. In Situ Growth of Nanoparticles through Control of Non-Stoichiometry. *Nat. Chem.* **2013**, *5* (11), 916–923. https://doi.org/10.1038/nchem.1773.

(31) Shah, S.; Sayono, S.; Ynzunza, J.; Pan, R.; Xu, M.; Pan, X.; Gilliard-Abdulaziz, K. L. The Effects of Stoichiometry on the Properties of Exsolved Ni-Fe Alloy Nanoparticles for Dry Methane Reforming. *AIChE J.* **2020**, *66* (12), e17078. https://doi.org/https://doi.org/10.1002/aic.17078.

(32) Ciambelli, P.; Cimino, S.; De Rossi, S.; Lisi, L.; Minelli, G.; Porta, P.; Russo, G. AFeO3 (A = La, Nd, Sm) and LaFe1-XMgxO3 Perovskites as Methane Combustion and CO Oxidation Catalysts: Structural, Redox and Catalytic Properties. *Appl. Catal. B Environ.* **2001**, *29* (4), 239–250. https://doi.org/10.1016/S0926-3373(00)00215-0.

(33) Labhasetwar, N.; Saravanan, G.; Kumar Megarajan, S.; Manwar, N.; Khobragade, R.; Doggali, P.; Grasset, F. Perovskite-Type Catalytic Materials for Environmental Applications. *Sci. Technol. Adv. Mater.* **2015**, *16* (3), 1–13.

(34) Rodriguez-Carvajal, J. Recent Advances in Magnetic Structure Determination by Neutron Powder Diffraction. *Phys. B* **1993**, *192* (1–2), 55–69.

(35) Uberuaga, B. P.; Vernon, L. J. Interstitial and Vacancy Mediated Transport Mechanisms in Perovskites: A Comparison of Chemistry and Potentials. *Solid State Ionics* **2013**, *253*, 18–26.

(36) Santaya, M.; Trolani, H.; Caneiro, A.; Mogni, L. Ternary Ni–Co–Fe Exsolved Nanoparticles/Perovskite System for Energy Applications: Nanostructure Characterization and Electrochemical Activity. *ACS Appl. Energy Mater.* **2020**, *3* (10), 9228–9233. https://doi.org/10.1021/acsaem.0c01997.

(37) Yang, Q.; Liu, G.; Liu, Y. Perovskite-Type Oxides as the Catalyst Precursors for Preparing Supported Metallic Nanocatalysts : A Review. *Ind. Eng. Chem. Res.* **2018**, *57* (1), 1–17. https://doi.org/10.1021/acs.iecr.7b03251.

(38) Montero, C.; Ochoa, A.; Castaño, P.; Bilbao, J.; Gayubo, A. G. Monitoring Ni^0 and Coke Evolution during the Deactivation of a Ni/La2O3-AAl2O3 Catalyst in Ethanol Steam Reforming in a Fluidized Bed. *J. Catal.* **2015**, *331*, 181–192. https://doi.org/10.1016/j.jcat.2015.08.005.

(39) Zhao, K.; He, F.; Huang, Z.; Wei, G.; Zheng, A.; Li, H.; Zhao, Z. Perovskite-Type Oxides LaFe1-XCoxO3 for Chemical Looping Steam Methane Reforming to Syngas and Hydrogen Co-Production. *Appl. Energy* **2016**, *168*, 193–203. https://doi.org/10.1016/j.apenergy.2016.01.052.

(40) Omata, K.; Nukui, N.; Hottai, T.; Yamada, M. Cobalt-Magnesia Catalyst by Oxalate Co-Precipitation Method for Dry Reforming of Methane under Pressure. *Catal. Commun.* **2004**, *5* (12), 771–775. https://doi.org/10.1016/j.catcom.2004.09.014.

(41) Sierra Gallego, G.; Batiot-Dupeyrat, C.; Barrault, J.; Mondragón, F. Dual Active-Site Mechanism for Dry Methane Reforming over Ni/La 2 O 3 Produced from LaNiO3 Perovskite. *Ind. Eng. Chem. Res.* **2008**, *47* (23), 9272–9278.

CHAPTER 4. DYNAMIC TRACKING OF NIFE SMART CATALYSTS USING IN SITU X-RAY ABSORPTION SPECTROSCOPY FOR THE DRY METHANE REFORMING REACTION

4.1 Abstract

The exsolution of nanoparticles from perovskite precursors has been explored as a route to synthesize catalysts with sinter- or coke-resistance. The characteristics of these exsolved nanoparticles are highly dynamic depending on the redox nature of the environment to which they are subjected. To develop their properties for thermo- and electrocatalytic applications, it is necessary to track the states and behavior of exsolved catalysts with in-situ and ex-situ characterization. In this study, we conduct in-situ X-ray Absorption Spectroscopy (XAS) along with ex-situ Scanning Transmission electron microscopy High-angle annular dark-field (STEM-HAADF), and Energy-Dispersive X-ray spectroscopy analysis of the parent perovskite oxide precursor, $LaFe_{0.8}Ni_{0.2}O_3$, as its structure forms bimetallic NiFe nanoparticles and evolves in oxidative, reductive and dry methane reforming environments. We develop a theory that NiFe exsolution is a function of the reduction potential where $LaFe_{0.8}Ni_{0.2}O_3$ transforms to Ni-Fe alloy supported on LaO_x-$LaFeO_x$. The Ni starts to exsolve at 350 ºC while most Fe exsolves at 700 ºC. During dry methane reforming conditions, the Fe is oxidized by CO_2 during the reaction and re-enters the perovskite as $LaFeO_3$, while Ni remains on the surface as nanoparticles in the metallic state. During the oxidative regeneration phase, most of the Fe re-enters the bulk perovskite phase while Ni is partially regenerated with a small percentage oxidized to large NiO nanoparticles. This study sheds light on the exsolution and regeneration of

bimetallic alloy nanoparticles and the influence of the reaction conditions on their catalyst performance.

4.2 Introduction

The phenomenon of exsolution in so-called “smart” or “intelligent” catalysts has been studied extensively in the catalysis and solid-oxide fuel cell community as a means for developing sinter- or coke- resistant catalysts. Typically, exsolution occurs under a reducing environment where the reducible catalyst metals that constitute the A or B site of the ABO_3-type structure emerge from the perovskite matrix and form nanoparticles on the surface of the parent oxide[1–3] Additionally, these materials have the possibility for regeneration where exposure to an oxidative environment re-introduces the cations back into the bulk of the perovskite structure. The strong-support interaction and regenerability have been especially advantageous for Ni and Ni-alloy catalysts used for the Dry methane reforming (DMR). Thus, perovskite precursors provide a promising avenue for regenerable robust catalysts for thermocatalytic reactions.

$LaFeO_3$ was one of the first perovskite oxide materials to exhibit exsolution behavior for intelligent catalysts and had a high thermal stability above 800 °C[4]. The strong-support interaction between the exsolved catalyst nanoparticles and the parent oxide is useful in maintaining high metal dispersion during thermal cycling[5]. The reversibility of exsolution in an oxidizing environment also allows for the regeneration of catalysts through simple redox cycling. The influence of factors that control the properties of the exsolved nanoparticles have been explored using bulk defect chemistry[6–

[8], compositional changes of the perovskite support[4,9–11] and reduction temperature[9], which allow for the rational design of catalysts.

In our prior studies, we have explored exsolution as a facile pathway for synthesizing bimetallic or multi-metallic catalysts to enhance catalyst activity and stability for dry methane reforming[12–14]. The combination of Ni with Fe as catalysts has been studied for their stability towards coking and sintering[15–20]. In reaction conditions of dry reforming, steam reforming, or partial oxidation of methane, Fe^0/FeO_x activates CO_2 and oxidizes surface carbon species, and this prevents or minimizes deactivation due to coking[21,22]. Yet, there are few studies that explore the dynamicity of the NiFe alloy systems as the nanoparticles are formed, used in the reaction and possibly re-emerged back in the support under oxidative environment. In our prior studies, we have explored exsolution as a facile pathway for synthesizing bimetallic or multi-metallic catalysts to enhance catalyst activity and stability for dry methane reforming[12–14]. The combination of Ni with Fe as catalysts has been studied for their stability towards coking and sintering[15–20]. In reaction conditions of dry reforming, steam reforming, or partial oxidation of methane, Fe^0/FeO_x activates CO_2 and oxidizes surface carbon species, and this prevents or minimizes deactivation due to coking[21,22]. Yet, there are few studies that explores the dynamicity of the NiFe alloy systems as the nanoparticles are formed, used in the reaction and possibly re-emerged back in the support under oxidative environment.

In this article, we capture the transition of Ni and Fe as they diffuse, nucleate and form nanoparticles from the $La_{0.8}Fe_{0.8}Ni_{0.2}O_3$ perovskite precursors in reductive, oxidative, and reaction environments. In-situ X-ray Absorption Spectroscopy (XAS)

captures the changing electronic and coordination environments surrounding Ni and Fe as exsolution gradually occurs during reduction and reverses during oxidation. Similarly, we also use in situ XAS as a tool to observe the interaction between metallic Ni, Fe, and the parent perovskite during the dry methane reforming (DMR) reaction. This is supported by catalytic reaction studies, temperature-programmed adsorption studies, ex-situ Scanning Transmission Electron Microscopy - High-Angle Annular Dark Field (STEM-HAADF) with Energy Dispersive X-ray Spectroscopy (EDS) for samples subjected to reduction, re-oxidation or during reaction as a function of time. Our observations from XAS and STEM-HAADF indicate that the catalyst nanoparticles initially lead to the formation of Ni-rich NiFe nanoparticles with an fcc structure possibly forming a sequential alloying process. Extensive exposure in the reductive environment changes the size and composition of the NiFe catalysts which inherently changes the selectivity for DRM. During the DRM reaction, most of the Fe returns to the perovskite support and Ni remains in the metallic state in the form of the nanoparticles. XAS and STEM-HAADF results shows that the NiFe catalysts are partially regenerated with most of the Fe and Ni returning back to the support.

4.3 Experimental Section

4.3.1 Catalyst Preparation

All chemicals and reagents were used as received. The perovskite oxide precursor, nominally $LaFe_{0.8}Ni_{0.2}O_{3-x}$, was prepared using the sol-gel Pechini method as described in literature[23]. $La(NO_3)_3.6H_2O$ (Alfa Aesar), $Fe(NO_3)_3.9H_2O$ (Acros Organics), and $Ni(NO_3)_2$ (Alfa Aesar) were mixed in stoichiometric quantities and dissolved in 10

mL of DI water. The beaker was placed on a hot plate at 60 °C and stirred until fully dissolved. The anhydrous citric acid (Alfa Aesar) in a 3 mols./mol ratio perovskite and 1.08 mL of ethylene glycol butyl ether (Sigma Aldrich) in a 1 mol./mol ratio perovskite was mixed with 30 mL of DI water in a separate beaker. The citric acid/ ethylene glycol solution was subsequently added dropwise to the precursor solution and stirred. The mixture was evaporated in a drying oven at 110 °C overnight. The resulting xerogel was finely ground using a mortar and pestle and calcined at 800 °C for 2 h with a heating rate of 5 °C/min. The samples were then reduced in a quartz tube microreactor, plugged by silica wool (Hiden Analytical CATLAB, Warrington, United Kingdom) in 5%H_2/He ramping up to 700 °C at 10 °C/min for varied dwelling periods (0 min,10 min, 30 min, 60 min, 90 min, and 120 min) to observe the exsolution of the metals from the perovskite oxide precursor before performing steady-state catalyst testing. Reoxidation or regeneration of the perovskite oxide precursor was carried out in the same quartz tube microreactor by heating 100 mg of material to 700 °C at 10 °C/min for 2 hours in a 20% O_2/He gas mixture.

4.4 Catalyst Characterization

4.4.1 Temperature Programmed Reduction

Temperature Programmed Reduction (TPR) was performed in a quartz tube microreactor (Hiden Analytical CATLAB, Warrington, United Kingdom) at 700 ºC with a 10 ºC/min ramp rate, in 5% H_2/He (60 ml/min) and held at varying times (10 min, 30 min, 60 minutes, 90 minutes, and 120 minutes). The samples were reduced to induce exsolution of NiFe nanoparticles from the perovskite oxide precursor. The Mass spectral

responses for water (m/z =18) and hydrogen (m/z =2) were recorded to determine peaks in hydrogen consumption during the reduction of the material.

4.4.2 Dry methane reforming catalyst testing

DRM was performed in a fixed-bed reactor at atmospheric pressure. 100 mg of catalyst was loaded in the same quartz tube microreactor (Hiden Analytical CATLAB, Warrington, United Kingdom). The quartz tube was plugged with silica wool. Before catalytic testing, the material was reduced at 700ºC in 5%H_2/95%He, with a 60 ml/min flow rate at varying times (for 0, 10, 30, 60, and 120 minutes) to promote exsolution of the Ni and Fe. After reduction, the material was kept at 700 ºC for catalytic testing and was performed under steady-state conditions. The catalytic feed mixture consisted of 5% CH_4, 5% CO_2, and balance He and a total flow rate of 60 mL/min. The concentrations of CO and H_2 were analyzed by a Hiden Quantitative Gas Analyzer (QGA) mass spectrometer. The mass spectrometer was calibrated using sensitivity analysis of the QGA-MS towards specific gases relative to the He carrier gas. The conversion values were quantified using the mass spectral response and measured gas flow rates. The mass spectrometer was calibrated for relative sensitivity by measuring responses for a known concentration of individual gases diluted in helium. The pressure drop in the reactor was minimal, as determined by calibration tests with and without catalysts. Conversion of reactant gases was determined by calculating gas flow rates calculated from the MS response and the known relative sensitivities.

$$X_{CH_4} = 1 - \frac{Volume\ of\ CH_4\ out}{Volume\ of\ CH_4\ in}$$

$$X_{CO_2} = 1 - \frac{Volume\ of\ CO_2\ out}{Volume\ of\ CO_2\ in}$$

4.4.3 Transmission electron microscopy and Scanning Transmission electron microscopy

Elemental analysis and morphological features were observed using TEM (Titan Thermi-300kC, FEI) EDS, and STEM imaging. TEM samples were prepared by dispersing samples in DI water, sonicating for 10 min, and depositing them onto ultrathin carbon films on holy carbon supports with a 400-mesh copper grid (Ted Pella, Redding CA) using a 1 mL pipette.

4.4.4 X-ray Diffraction

X-ray Diffraction (XRD) patterns for the as prepared and reduced samples were collected on a PANalytical Empyrean Series 2 with a step-size of 0.026º and a dwell time of 30 seconds. The spectra were collected in a range of 2θ from 5° to 90° with a Cu K-α radiation source.

4.5 X-ray Absorption Spectroscopy (XAS)

In-situ XAS characterization experiments were conducted at beamline 9-3 at the Stanford Synchrotron Radiation Lightsource (SSRL). Samples were loaded in a quartz tube (OD=1.0 mm, ID=0.96 mm) mounted on a tube reactor[24]. The catalyst sample was scanned in fluorescence mode with a passivated implanted planar silicon (PIPS) detector and a Soller slit. A liquid nitrogen cooled Si(220), ϕ=(0) monochromator was used to select photon energy. For calibration, Fe foil was measured simultaneously for every scan. Scans were collected using continuous scanning mode, with each full Extended X-ray Absorption Fine Structure (EXAFS) scan taking 92 seconds. The scans were

collected by alternating between Fe K-edge (E_0 = 7112 eV) and Ni K-edge (E_0 = 8333 eV). To capture the spectral evolution during changes in redox conditions, the 92s-EXAFS scans were continuously collected. The following are the redox conditions that were performed on the sample during the in-situ XAS measurement:

(1) A Temperature-Programmed Reduction with temperature ramp of 10°C/min and dwell at 700ºC in 5%H_2/He for 30 minutes.

(2) DMR mixture of 5% CH_4 + 5% CO_2 balanced by nitrogen was introduced at 700°C using the reduced sample from (1), the following reduction and then a purge in He.

(3) A Temperature-Programmed Oxidation in 20% O_2/He of the post-reduced sample from (1) with a ramp of 10°C/min from room temperature to 700°C and a dwell time of 30 minutes.

Each scan represented a temperature difference of ~15°C. EXAFS measurements were conducted at the end of each stage (1, 2 and 3), as mentioned above, after cooling down to room temperature in He flow (20 sccm) to minimize thermal disorder effect that dampens the EXAFS. Four to nine successive scans were measured for signal averaging to improve signal-to-noise ratio. The data collected were calibrated, merged, and normalized with the Athena interface of the Demeter package[25].

Linear combination fitting (LCF) tool in Athena was performed on the X-ray absorption near-edge structure (XANES) spectra using appropriate basis spectra. Each fit was constrained to fractions between 0 and 1, and the total sum of the fractions was not constrained to 1.

For multivariate curve resolution-alternating least squares (MCR-ALS) analysis, the whole energy range (8140 – 9130 eV) of the spectra were fitted in MATLAB based code[26,27].

For EXAFS modelling, Artemis interface of the Demeter package was used. The EXAFS models were optimized in R-space using using k^1, k^2, and k^3 weightings, obeying the Nyquist criterion. Amplitude reduction factor, S_0^2, was determined to be 0.64 for Fe K-edge and 0.92 for Ni K-edge by fitting EXAFS data collected for Fe foil and Ni foil. The EXAFS data was fitted to scattering paths generated from crystal structures of metallic Ni (Materials Project, mp-23), NiO (Materials Project, mp-19009), and $LaFeO_3$ (Materials Project, mp-22590) using the FEFF6 code provided by Artemis.

4.6 Results and Discussion

4.6.1 As prepared $LaFe_{0.8}Ni_{0.2}O_3$ Perovskite Precursor

The Fe and Ni K-edge XANES spectra of the steady states are shown in **Figure 4.1**, and the EXAFS spectra are shown in **Figure S4.1**. For Fe K-edge, the as-prepared state of $LaFe_{0.8}Ni_{0.2}O_3$ perovskite looks identical to $LaFeO_3$ in both XANES and EXAFS (as shown in **Figure S4.2** and **Figure S4.3(a, c))**, suggesting that the Fe atoms in the $LaFe_{0.8}Ni_{0.2}O_3$ perovskite adopt $LaFeO_3$-like structure, despite the presence of Ni atoms. On the other hand, the Ni K-edge XANES of the as-prepared state resembles $LaNiO_3$ (**Figure S4.2**). However, the Ni K-edge EXAFS of the as-prepared state (shown in **Figure S4.3(b, d)**) looks closer to $LaFeO_3$, which has the orthorhombic crystal structure rather than rhombohedral structure of $LaNiO_3$. $LaFeO_3$ and $LaNiO_3$ have distinct EXAFS features as demonstrated by their spectra, and our XAS data indicates that the Ni atoms of

the $LaFe_{0.8}Ni_{0.2}O_3$ perovskite are clearly incorporated into the orthorhombic structure of $LaFeO_3$. This can additionally be confirmed by direct overlap between the Fe and Ni K-edge EXAFS spectra of as-prepared state (shown in **Figure S4.4**). The observation of orthorhombic crystal structure for $LaFe_{0.8}Ni_{0.2}O_3$ perovskite is also consistent with the XRD data (shown in **Figure 4.1(c)**). The XRD spectra show that the Ni atoms are fully soluble in the $LaFeO_3$ lattice, and there are no visible peaks of NiO or Ni phases present. The slight discrepancy in the XANES spectral shape, where the Ni K-edge as-prepared state XANES looks more like $LaNiO_3$ than $LaFeO_3$, may have to do with different electronic structure effect induced by Ni versus Fe. Steiger et al. also reports the Ni K-edge XAS spectrum of $LaFe_{0.8}Ni_{0.2}O_{3-\delta}$ perovskite, orthorhombic as confirmed by XRD, to have the identical XANES shape as our data[28]. In agreement with the discussion above, the EXAFS modelling (as shown in **Figure S4.5(a)** and **Table S4.1**) shows that the as-prepared state at Fe K-edge is identical to the bulk $LaFeO_3$, while the as-prepared state at Ni K-edge is adequately modelled with the $LaFeO_3$ crystal structure that has Fe core atom swapped out with Ni (as shown in **Figure S4.6(a)** and **Table S4.2**).

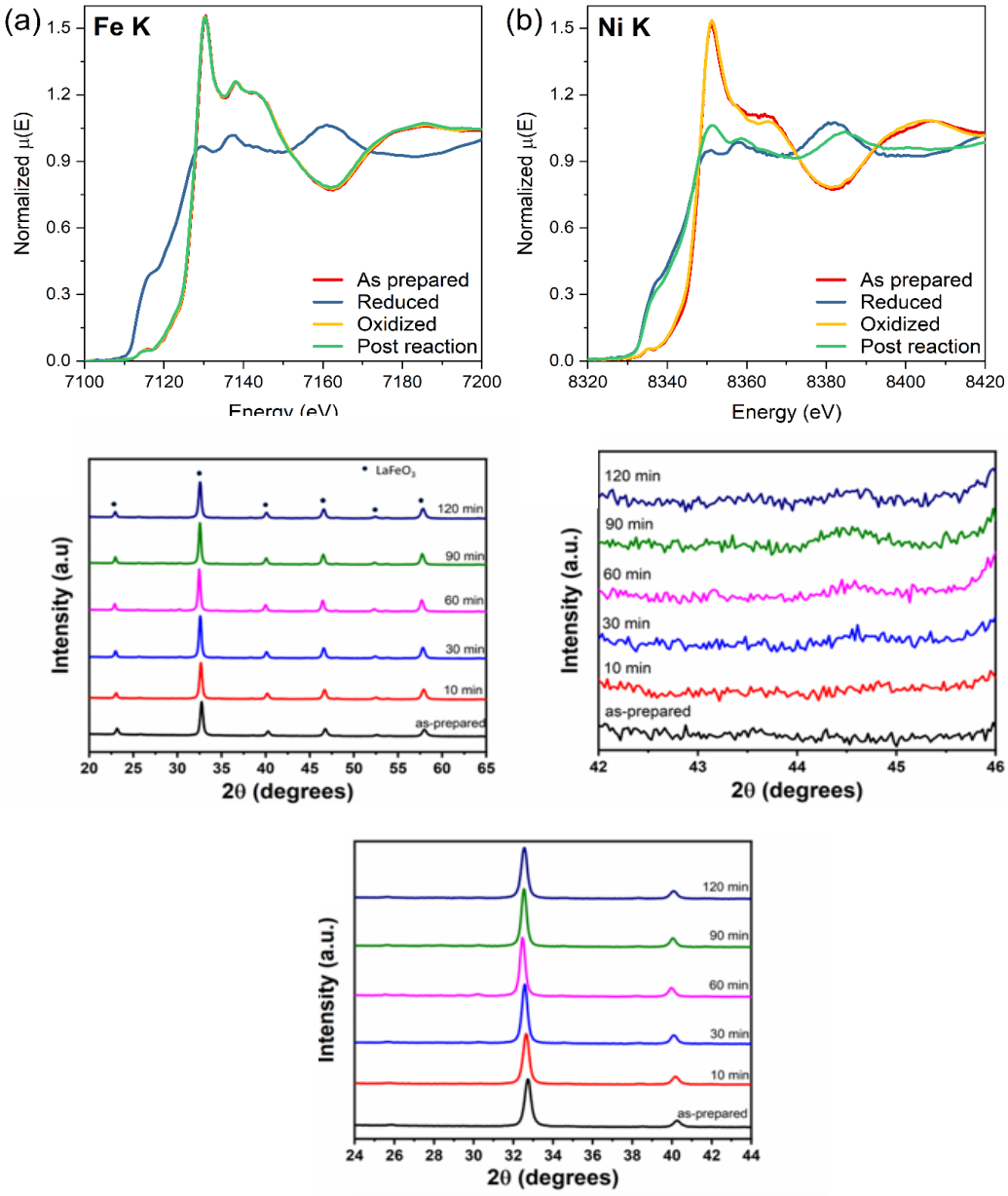

Figure 4.1. (a) Fe K-edge and (b) Ni K-edge XANES spectra of $LaFe_{0.8}Ni_{0.2}O_3$ collected at room temperature for as prepared sample, after reduction in 5% H_2, oxidation in 20% O_2 and reaction in DRM conditions. (c) XRD of $LaFe_{0.8}Ni_{0.2}O_3$ as-prepared and reduced (10 min, 30min, 60min, 90 min, 120 min) in 5%H_2/He at 700°C (d) XRD of $LaFe_{0.8}Ni_{0.2}O_3$ from 42-46° 2θ and (e) 24-43° 2θ.

4.6.2 Reduction of $LaFe_{0.8}Ni_{0.2}O_3$ – Formation of NiFe catalyst nanoparticles

The as-prepared $LaFe_{0.8}Ni_{0.2}O_3$ was reduced at 700°C at time intervals of 10 min, 30 min, 60 min, 90 min and 120 min. **Figure 4.1(d)** shows the growth of a new reflection at ~44.5° 2θ as the reduction time increases which confirms the formation of predominantly Ni-Fe alloy nanoparticles. **Figure 4.1(e)** shows that after reduction the main diffraction peaks for $LaFeO_3$ are red-shifted, showing that a greater degree of reduction reduces the unit cell. A closer inspection of the 32.4° 2θ peak (111) shows a shift to a lower 2θ when reduced between 10 min to 1 h due to reduction of Ni and Fe in the lattice to form ions with larger radii[29]. The shift to a higher 2θ may be due to by the Ni and Fe diffusing out of the lattice to form nanoparticles and causing shrinkage in the unit cell lattice. The perovskite oxide precursor lattice expands at earlier reduction times up to 60 minutes and contracts at longer reduction durations longer than 1 hour to take into account the greater extent of exsolution and catalyst nanoparticle formation. Metallic Ni has a larger radius than ionic Ni^{+2} and $Ni^{+3,}$ and its presence in the lattice of the perovskite also leads to lattice expansion[30]. Gradually, exsolution drives the metallic nickel outward, and the lattice contracts. STEM-HAADF and EDS measurements were used for the elemental and structural morphology of the catalyst nanoparticles and the perovskite precursors after each reduction step (as-prepared, 10 min, 30 min, 60 min, 90 min, and 120 min) at 700ºC in a reducing environment of 5%H_2/He. The STEM-HAADF image of the as-prepared sample shown in **Figure 4.2(a)** shows no visible nickel or iron nanoparticles, which corroborates the XRD spectra that the Ni is fully soluble in the perovskite oxide lattice. After 10 minutes of reduction, small nickel nanoparticles emerge

from the perovskite precursor onto the surface with an average size of 12 nm ± 5 nm. After 30 minutes of reduction, the nanoparticle density significantly increases with little change to the average particle size of 11 nm ± 5 nm. After 60 min of reduction, an increase in particle size is observed (20 nm ± 6 nm), and the average number of nanoparticles decreases. At 90 min, the nanoparticle size increases, and larger particles are seen along with small nanoparticles making the average particle size 16 nm ± 8. At 2 hours, the nickel nanoparticles have formed larger particles, and the smaller particles have reduced in quantity.

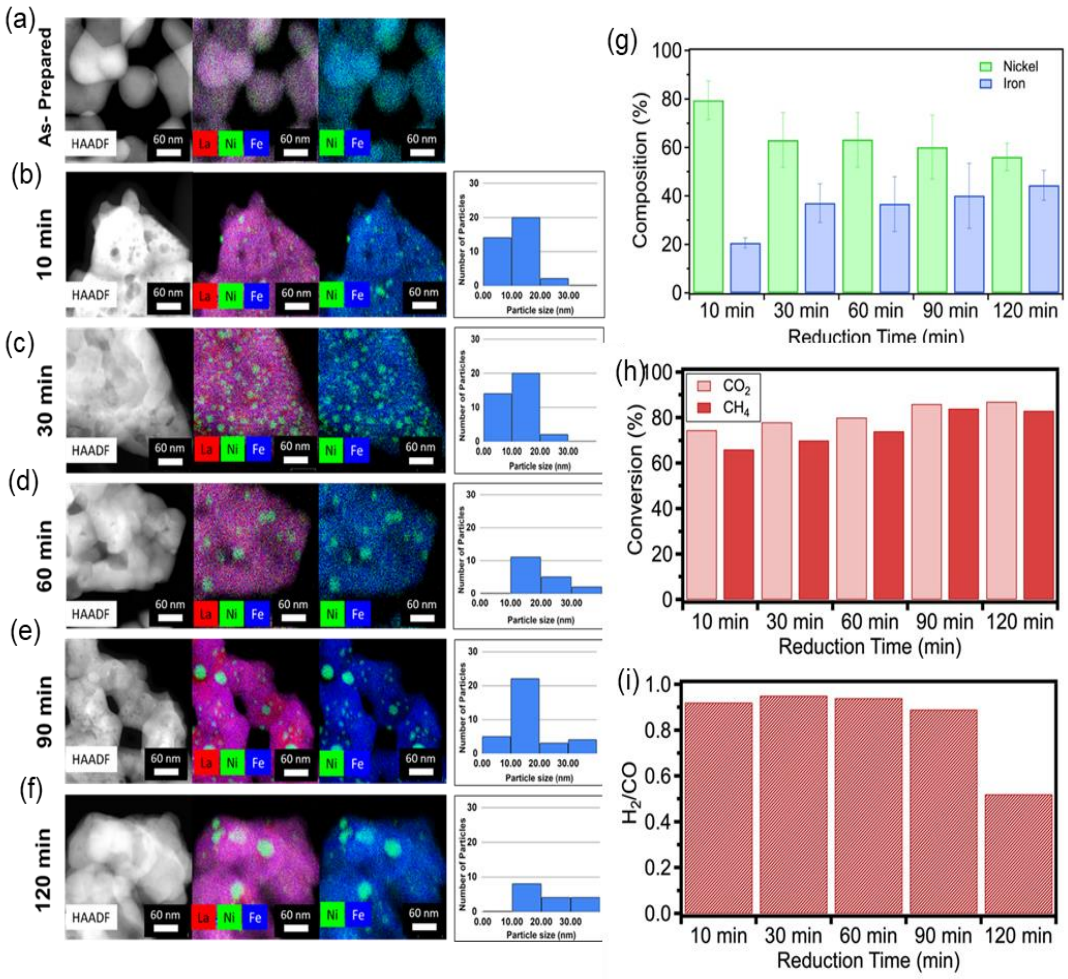

Figure 4.2. STEM- HAADF images of $LaFe_{0.8}Ni_{0.2}O_{3-x}$ perovskite precursors (a) as-prepared and after reduction in 5%H_2/He for a reduction time of (b) 10 minutes, (c) 30 minutes, (d) 60 minutes, (e) 90 minutes and (f) 120 minutes. The adjacent histograms show the size distribution of the exsolved nanoparticles. (g) Shows an evolution of particle composition over increasing reduction time. (h) DRM CO_2 and CH_4 conversion and (i) H_2/CO as a function of the reduction time.

Figure 4.2(b) shows the concentration of Fe and Ni in the catalyst nanoparticle supported on parent perovskite, as determined by EDS. The EDS composition is an average of the nanoparticle compositions for at least 4 - 8 nanoparticles in an image. The EDS compositional measurements are shown in **Figures S4.7-4.10**. The as-prepared perovskite precursor has more iron than nickel in the bulk, corresponding to 75% ± 3 % Fe and 25% ± 3% Ni at time zero. After 10 min reduction at 700ºC, nucleation occurs, and nickel nanoparticles begin to emerge with an average size of 11 nm ± 5 nm. The elemental particle composition is 80% ± 8 % Ni and 20% ± 3% Fe. At 30 min, the concentration is 63% ± 11% Ni and 37% ± 8% Fe. At 60 min, the concentration is similar

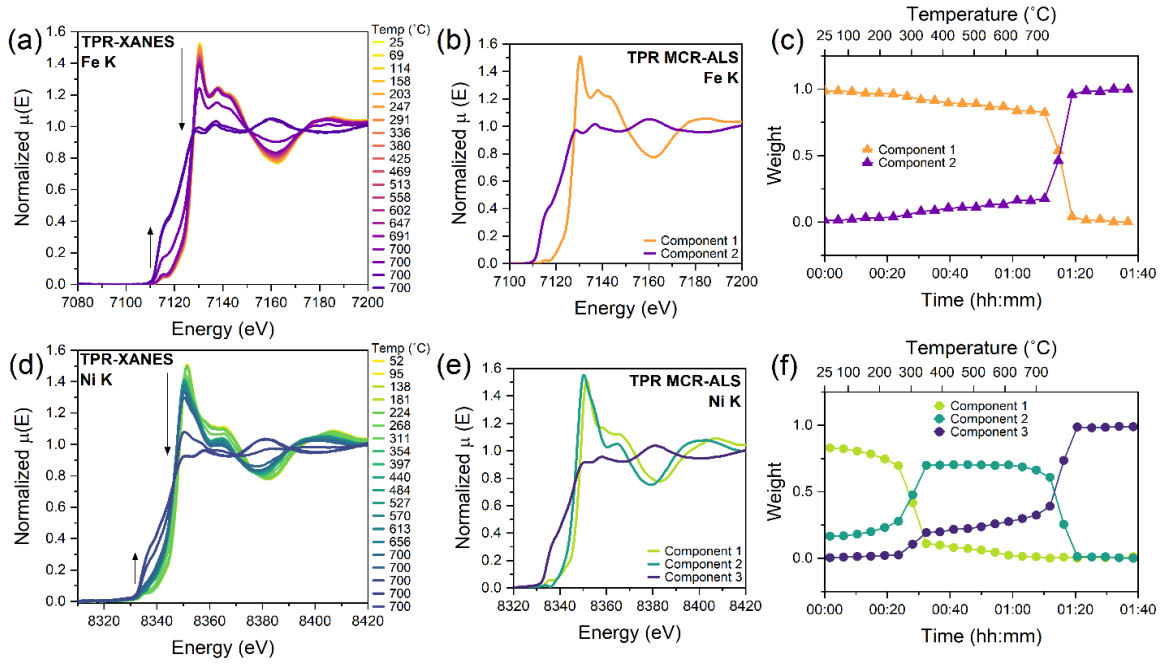

Figure 4.3. (a, d) Evolution of XANES spectra collected during TPR of $LaFe_{O.8}Ni_{0.2}O_3$ at Fe K-edge and Ni K-edge respectively. (b) and (e) show component spectra obtained by MCR-ALS. Concentration profiles of the components are shown in (c) and (f).

to the 30-minute reduced samples with 63% ± 11% Ni and 37% ± 11% Fe. The 90-min reduced compositional concentration is 60 % ± 13% Ni and 40% ± 13% Fe. After 2 hours of reduction, the nanoparticle concentration gradually increases in Fe content with a concentration of 56 % ± 6% Ni and 44% ± 6% Fe. The wide standard deviation in the concentration of the nanoparticles varies due to the differences in elemental composition of nanoparticles at the edge of the samples versus those on the terrace or bulk of the materials. The higher concentration of Ni compared to Fe in the initial reduction time indicates that the rate of exsolution is higher in nickel than iron. As expected, the exsolution of the cations is a function of their reduction potential or reducibility. Ni has a

higher reducibility and exsolves out of the LFNO bulk material before Fe. The Fe increases in concentration as reduction time increases and plateaus at ~44%, reaching a steady-state maximum concentration inside the nanoparticle after 90 minutes of reduction.

The mechanism for NiFe catalyst nanoparticle formation includes the initial nucleation and growth of Ni nanoparticles that, over time, grow with a predominant Ostwald ripening mechanism. This is validated by a similar study by Lai and Manthiram that suggested that particle growth during exsolution occurs through mechanisms involving coalescence or Ostwald ripening[9]. The authors describe that both mechanisms can occur and how the strong metal-support interaction (SMSI) promotes one growth mechanism over the other. With SMSI, the nanoparticles become less mobile and decrease the rate of coalescence. In Ostwald ripening, smaller particles can migrate on the surface of the support and merge into a larger particle like a dissolution-condensation mechanism[31]. They claim that Ostwald ripening is usually the dominant mechanism at elevated temperatures, but both mechanisms may be present. Despite these systems being denoted as sinter-resistance, we also hypothesize that that a longer reduction duration at elevated temperatures promotes nanoparticle nucleation and particle growth. This likely causes a decrease in the areal density of nanoparticles as the reduction time is increased.

The Fe and Ni K-edge *in situ* XAS measurements were performed to understand the exsolution dynamics of the perovskite. The XANES spectral evolutions of the $LaFe_{0.8}Ni_{0.2}O_3$ perovskite during temperature programmed reduction (exsolution) are shown in **Figure 4.3(a)** and **4.3(d)**. At both edges, the reduction of the perovskite over

the temperature ramp from ambient to 700°C is observed, as indicated by the decrease in the whiteline intensity and the growth of the pre-edge peaks (7112 eV for Fe and 8333 eV for Ni) that correspond to metallic states. According to the MCR-ALS analysis, shown in **Figure 4.3(b)** and **4.3(e)**, $LaFe_{0.8}Ni_{0.2}O_3$ shows distinct reduction dynamics at the two edges, involving different number of components. At Fe K-edge, MCR-ALS determines that two components can fully describe the exsolution process with minimum residuals (shown in **Figure S4.11a**). The XANES spectra of the two MCR-ALS components for Fe K-edge, shown in **Figure 4.3(b)**, indicates that the component 1 represents the starting state that is $LaFeO_3$-like, while the component 2 resembles the metallic state with face-centered cubic (fcc) structure. The identity of the reduced state of Fe K-edge is discussed in more detail in the following steady state discussion. The concentration profile, shown in **Figure 4.3(c)**, reveals that full reduction to the metallic state occurs shortly after reaching 700°C at Fe K-edge. While the Fe edge involves direct conversion between two states, the exsolution process at Ni K-edge comprises of three unique components according to the MCR-ALS, shown in **Figure 4.3(e)** and **4.3(f)** (residuals shown in **Figure S4.11(b)**). The isosbestic points are not observed in the XANES spectra (**Figure 4.3(d)**), which is an additional implication that the reduction process at Ni K-edge is not a one-step transformation. The first transition takes place at around 270°C, while the second transition occurs after reaching 700°C, about the same time as the Fe converts into the reduced state. The component 1 is the as-prepared state that is $LaFeO_3$-like phase, while the component 3 is identical to metallic Ni. The component 2 resembles $La_2Ni_2O_5$ as shown in **Figure S4.12**. In literature, the reduction of $LaNiO_3$ has been

reported to involve intermediate phase of $La_2Ni_2O_5$, with reduction temperature at around 275-7°C under reducing environment[32,33]. As the temperature increases, it is reported that metallic Ni, in the form of amorphous phase or very small crystallites, starts to develop around ~400°C for the reduction of $LaNiO_3$. The same behavior is observed in Ni K-edge XAS data during reduction (**Figure 4.3(f)**) in which gradual growth of metallic Ni is detected during the temperature ramp between 350°C and 700°C under 5%H_2/He, before making the big-step transformation into bulk metallic structure at 10 minutes into reaching 700°C. The *in situ* XAS data during reduction corroborates TPR data obtained in the laboratory (**Figure S4.13**), which shows two reduction events at 290°C and 760°C. The low temperature peak agrees with the first transition observed in Ni K-edge at 270°C, while the high temperature peak can be correlated to the second transition in both Fe and Ni K-edges during the dwelling period at 700°C. These reduction temperatures are in good agreement with literature on the temperature programmed reduction of $LaFe_{0.8}Ni_{0.2}O_3$[34–36].

The Fe and Ni K-edge XANES spectra of reduced state, collected at room temperature, are shown in **Figure 4.1** (EXAFS in **Figure S4.1**). As briefly mentioned above, both the Fe K-edge and Ni K-edge spectra after reduction represent the metallic state specifically in fcc structure. In XANES, the metallic fcc structure is characterized by the double humps in the whiteline region, and this is observed in first-row transition metals that adopt fcc structure, such as metallic Ni and Cu. The resemblance becomes clear when both Fe and Ni K-edge XANES spectra of the reduced state are compared to the metallic Ni spectrum (shown in **Figure S4.2(b)**). While the metallic Fe at ambient

environment forms body-centered cubic (bcc) structure, it is reported to adopt fcc structure at elevated temperature and pressure, and the XANES shape of the Fe transforms into the characteristic fcc spectrum[37]. The Fe K-edge XANES collected for the reduced perovskite indicates that Fe exists in the fcc structure, which is strong evidence that Fe is forming an alloy with Ni. The EXAFS comparison shows good overlap between the Fe and Ni K-edge data (**Figure S4.14**), demonstrating that they share the identical structure. Compared to pure Ni metal, the reduced state of the perovskite shows expanded crystal lattice structure, as indicated by the higher frequency k-space oscillations and the R-space peaks slightly shifted to longer distances. The EXAFS modelling (shown in **Figure S4.5b** and **S4.6b** and **Table S4.1** and **S4.2**) also results in about 1% lattice expansion for the reduced state perovskite, at both Fe and Ni K-edges, compared to the pure Ni metal. The overall expansion of the crystal lattice observed for the reduced state is in good agreement with the literature that reports larger lattice constant (3.57-3.59 Å) for FeNi alloy than that of pure Ni metal (3.52Å)[38–40]. Another significant observation from the reduced state XAS data is that neither the Ni or Fe K-edge data shows the remnants of perovskite phase, indicating that majority of the Fe and Ni exsolve out of the parent perovskite structure to form FeNi alloy. This differs from the XRD (**Figure 4.1**) and STEM-HAADF images (**Figure 4.2(b,f)**) where some residual Fe is still in the lattice in the form of $LaFeO_3$. We suspect that the differences in the potential outcomes are attributed to the different heat transport profiles of the reactors in the laboratory and at the synchrotron. Note that quartz tubes used for ex-situ studies in the lab facility (OD: 6mm) and for in-situ studies at the synchrotron facility (OD: 1mm) are

different. The quantity of sample (100mg v/s 4 mg) introduced and the gas flow rates (60 ml/min v/s 20 ml/min) also differ, thus the outcomes of post-reduction, oxidation and reaction are not identical. Comparing the two packed bed reactors the ratio of perovskite weight to hydrogen flow rate is 2 g.s in the lab where ex-situ experiments were conducted and 0.24 g.s at the beamline where in-situ experiments were conducted. Assuming identical rate of exsolution, the rate of "consumption" of the perovskite should be 8 times greater in the in-situ studies.

4.6.3 Dry Methane Reforming

The DMR catalytic activity was performed at 700^{o}C to investigate the catalytic performance of the emerged catalyst nanoparticles after varying the reduction times at 10 min, 30 min, 60 min, 90 min, and 120 min. The catalytic performance is shown in **Figure 4.2**. For the system reduced at 10 minutes, the catalytic conversion starts at 66% for CH_4 and 75% for CO_2. The CH_4 and CO_2 conversion increases until 90 minutes, where the conversion for CH_4 and CO_2 is 82% and 84%, respectively. At 120 min, CO_2 conversion increases to 87%, and CH_4 conversion decreases slightly to 83%. The H_2/CO ratio starts at 0.9 for the 10 minutes reduced samples and increases to 0.95 for the 30 minutes reduced samples. At 60 min and 90 min, the H_2/CO decreases slightly to 0.94 and 0.89, respectively. At 120 min, the H_2/CO falls significantly to 0.52, indicating an increase in the production of CO and an increase in the RWGS reaction.

The H_2/CO ratio is highest after 30 minutes of reduction with a Ni concentration of 65 at.% and Fe concentration of 35 at.%. At higher concentrations of Fe, the relative activity of the catalyst to activate CH_4 decreases with a concomitant increase in CO_2

consumption[41]. Moreover, CO_2 can itself oxidize the perovskite. A more reduced perovskite-based catalyst has a greater propensity to consume CO_2 to oxidize constituent metals, particularly Fe, and fill the vacant O sites of the support. This suggests that the composition of the exsolved nanoparticles and Ni to Fe ratio composition plays an important role in the H_2/CO conversion efficiency. It is difficult to independently assess contribution of either factor individually, as both particle size and Ni:Fe ratio vary as exsolution progresses. We did not observe a large increase in water formation in the product stream, ruling out a significant increase in reverse water gas shift reaction. Thus, the lower H_2/CO ratio is due to an increased CO_2 consumption in part from the partial

oxidation of the perovskite and Fe/FeO_x. The increase of the Fe concentration above a certain threshold in the NiFe nanoparticles decreases the catalytic activity towards

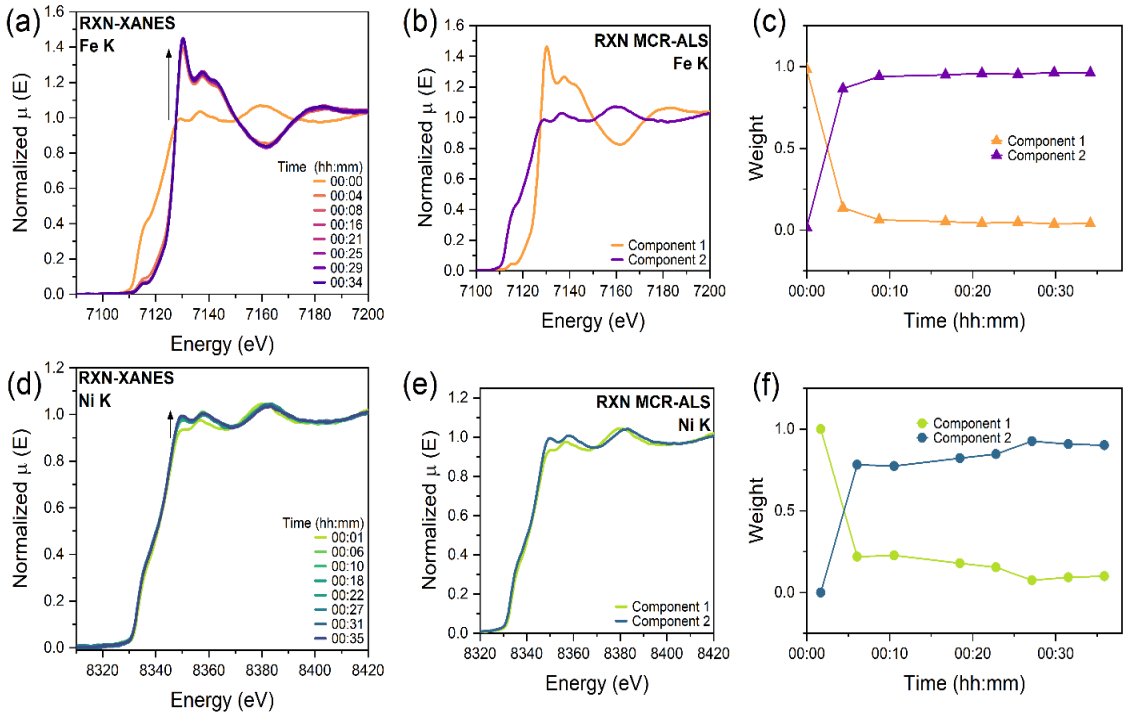

Figure 4.4 (a, d) Evolution of XANES spectra collected during DRM reaction at 700°C of LaFeO.8Ni0.2O3 at Fe K-edge and Ni K-edge respectively. (b) and (e) show component spectra obtained by MCR-ALS. Concentration profiles of the components are shown in (c) and (f).

methane activation.

4.6.4 Dry Methane Reforming – Implications for NiFe Catalyst Dynamics

The Fe and Ni K-edge spectra were collected while the reaction gas mixture was introduced to the reduced perovskite at 700°C. As shown in the XANES evolution in **Figure 4.4(a)** and **4.4(d)**, the instantaneous change is observed with the introduction of reaction gas during the first scan. The Fe K-edge XANES shows almost complete transformation into $LaFeO_3$-like spectrum within a scan (4 minutes). The Ni K-edge

XANES also completes the changeover within a scan, maintaining the overall metallic spectral shape except a slight increase in the whiteline intensity, suggesting slight oxidation. Once at steady state, the perovskite was cooled down to collect room temperature XAS spectra at Fe and Ni K-edges, which are shown in **Figure 4.1** and **Figure S4.1**. The Fe K-edge post reaction XAS spectrum looks identical to the as-prepared state, indicating that the Fe in the alloy returns to the perovskite structure when exposed to the reaction gas mixture. On the other hand, the Ni K-edge post reaction spectrum looks like a mixture of metallic and oxidic Ni phases, as indicated by the whiteline intensity. The EXAFS suggests the small degree of Ni-O scattering contribution, in agreement with XANES interpretation. Other than the presence of Ni-O scattering in the low k region, the overall EXAFS spectrum retains the fcc structure after reaction. When compared to the reduced state EXAFS, however, the post reaction data shows slightly contracted bond distances. In fact, the post reaction EXAFS overlaps with that of pure Ni metal (shown in **Figure S4.16**), suggesting that the Ni in the post reaction state exists as pure Ni metallic rather than as FeNi alloy, with small fraction of oxidic Ni. The observation of pure metallic Ni-like structure at Ni K-edge agrees with the behavior of Fe K-edge, in which all Fe atoms seem to have returned into the perovskite phase. The LCF analysis on the post-reaction Ni K-edge XANES indicates about 13% oxidic Ni presence (shown in **Figure S4.17**). The EXAFS modeling results can be found in **Figure S4.5d** and **S4.6d** and **Table S4.1** and **S4.2**.

EXAFS findings suggest that the majority of Fe in the perovskite-based catalyst is oxidized upon being introduced to the DRM environment. This is similar to

Theofanidis et al.[21] who suggested that in the redox environment of dry methane reforming for NiFe supported on $MgAl_2O_4$, Fe is oxidized to FeO_x while Ni retains its metallic state. In the case of dynamic supports such as perovskites, our observations with XAS, suggest that the complete oxidation of Fe during DRM is simultaneous with its reentry in the parent perovskite. Ni-rich nanoparticles activate CH_4 for the DRM reaction while Fe-FeOx redox couple prevent deactivation by preventing oxidation of the metallic Ni and also oxidizing any carbon products. This has a stabilizing effect on the perovskite-based catalyst in the DRM environment.

4.6.5 Oxidative Regeneration of $LaFe_{0.8}Ni_{0.2}O_3$ Perovskite Precursors

Figure S4.18 shows STEM/EDS of LFNO sample reduced for 30 min and after oxidation at 700ºC for 120 min. After a reduction in a 5%H_2/95%He environment for 30 min the average NiFe particle size is 12 nm ± 5 nm, with a Ni concentration of 67.1%, and Fe is 32.9%. We oxidized the material in air at 700ºC for 120 min. An increase in nanoparticle particle size is seen with less particle population. The average particle size after oxidation is 37 ± 16 nm. After oxidation, the catalyst particle concentration is 98.3 at.% Ni and 1.7 at.% Fe, suggesting that a majority of the Fe metal in the NiFe catalyst nanoparticles returns back to the support. It also indicates that nickel has a lower propensity for oxidation than iron and the Ni reincorporation into the parent perovskite is relatively sluggish compared to Fe.

The Fe and Ni K-edge *in situ* XAS measurements were performed to study the regeneration process of the perovskite after the exsolution of nanoparticles. The XANES spectral evolutions of the $LaFe_{0.8}Ni_{0.2}O_3$ perovskite during temperature programmed

oxidation (TPO), or the regeneration step, and the respective MCR-ALS analysis results are shown in **Figure 4.5**. Both edges show gradual oxidation as indicated by the increase in whiteline intensity. The MCR-ALS indicates that the TPO at both Fe and Ni K-edges involve three components with minimal residuals (shown in **Figure S4.19**). Analysis of the three component spectra for Fe K-edge TPO, as shown in **Figure 4.5(b)**, suggests that the oxidation of fcc metallic Fe involves the intermediate state of γ-Fe_2O_3 phase before reaching the final state of $LaFeO_3$. The XANES comparison of the component 2, the intermediate state, to the γ-Fe_2O_3 spectrum is shown in **Figure S4.20**. The appearance of γ-Fe_2O_3 phase is not surprising since one known solid-state synthesis method for $LaFeO_3$ is mixing La_2O_3 and Fe_2O_3 together[42,43]. For the case of Ni K-edge, the MCR-ALS indicates that the TPO involves the intermediate state of NiO before reaching the final state. The final state mostly resembles the as-prepared state, which has $LaFeO_3$-like structure. The exact composition of the final state at Ni K-edge after oxidation will be reviewed in more detail during the steady state discussion.

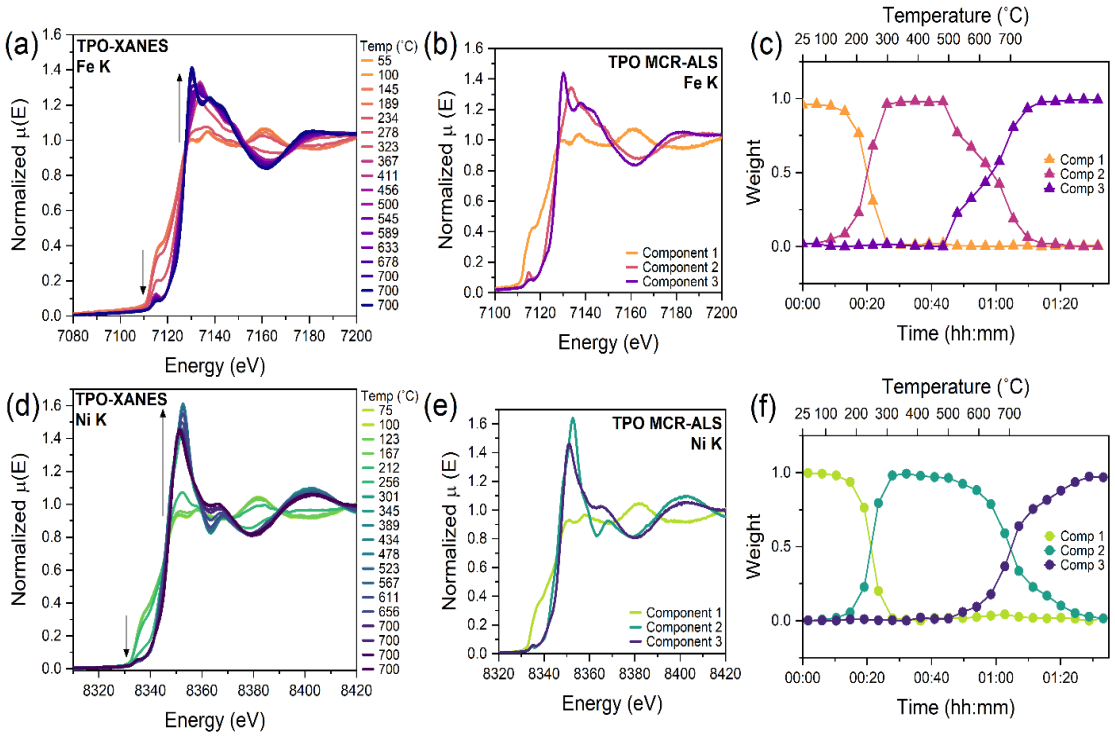

Figure 4.5. (a, d) Evolution of XANES spectra collected during TPO of $LaFeO_{0.8}Ni_{0.2}O_3$ at Fe K-edge and Ni K-edge respectively. (b) and (e) show component spectra obtained by MCR-ALS. Concentration profiles of the components are shown in (c) and (f).

As shown in the concentration profile plot in **Figure 4.5(c)**, the first transition from the starting metallic state to the intermediate state occurs at around 270˚C for both Fe and Ni K-edge during TPO. The second transition from the intermediate state to the final state for the Fe K-edge happens over the 500–700 ˚C, with 50% conversion at 660˚C and complete transformation within 5 minutes of reaching 700˚C. In contrast, the second transition for the Ni K-edge spans a longer period, where the conversion starts to happen slowly at around 500˚C and completes after 30 minutes into achieving 700˚C. The concentration profiles give insight into the kinetics of regeneration process of exsolved nanoparticles. While the first transformation of metallic FeNi nanoparticles into the γ-Fe_2O_3 and NiO phases happens at similar rate, the second transformation into the final states occurs in different fashion for Fe and Ni K-edges. Generally, the underlying factors

that determine the regenerability of exsolved nanoparticles are complex and include size effects of the nanoparticles[44], surface and bulk defects such as oxygen vacancies (and grain boundaries[45,46]) and the metal-oxygen bond strength[47]. The STEM-HAADF EDS images and XAS data suggest that the regeneration of Ni and Fe are different and could be attributed to the relative size effects of the nanoparticles. STEM-HAADF images shows that after oxidation some Ni is re-introduced in the lattice, however, the remaining Ni is oxidized and forms large nanoparticles (> 35 nm). We propose that the pre-dominant factor that limit some of the Ni re-entry back into the perovskite lattice is due to the sintering of the Ni nanoparticles during the oxidation phase into a critical size that prohibits dissolution. A similar phenomenon was studied by Katz et al. where small nanoparticles of Pt were re-dispersed back into the $CaTiO_3$ lattice, however, larger nanoparticles had a stronger propensity to coarsen and remained on the surface[44].

The Fe and Ni K-edge XANES spectrum of the oxidized state, collected at room temperature, are shown in **Figure 4.1**, and the EXAFS spectra are shown in **Figure S4.1**. The Fe K-edge XANES and EXAFS of the oxidized state look identical to the as-prepared state, or $LaFeO_3$, indicating that all the Fe has returned to the perovskite. On the other hand, the Ni K-edge shows mixture of NiO and as-prepared state. The LCF on the Ni K-edge XANES shows that the oxidized state consists of 87% as-prepared and 13% NiO phases (shown in **Figure S4.21**), suggesting that 13% of Ni from the nanoparticle does not return to the perovskite. The contribution from NiO in the oxidized state is also visible in the R-space of EXAFS spectrum (shown in **Figure S4.22**) where the peak at 2.6Å (phase uncorrected) is positioned at the same distance as the Ni-Ni scattering peak

from NiO. The EXAFS modeling gives adequate fit with the bulk $LaFeO_3$-like structure (Fe swapped with Ni) and the Ni-Ni scattering path taken from NiO. This corroborates STEM-EDS HAADF findings that show some Ni reincorporated in the perovskite lattice but mostly remain on the surface as predominantly NiO nanoparticles. The EXAFS

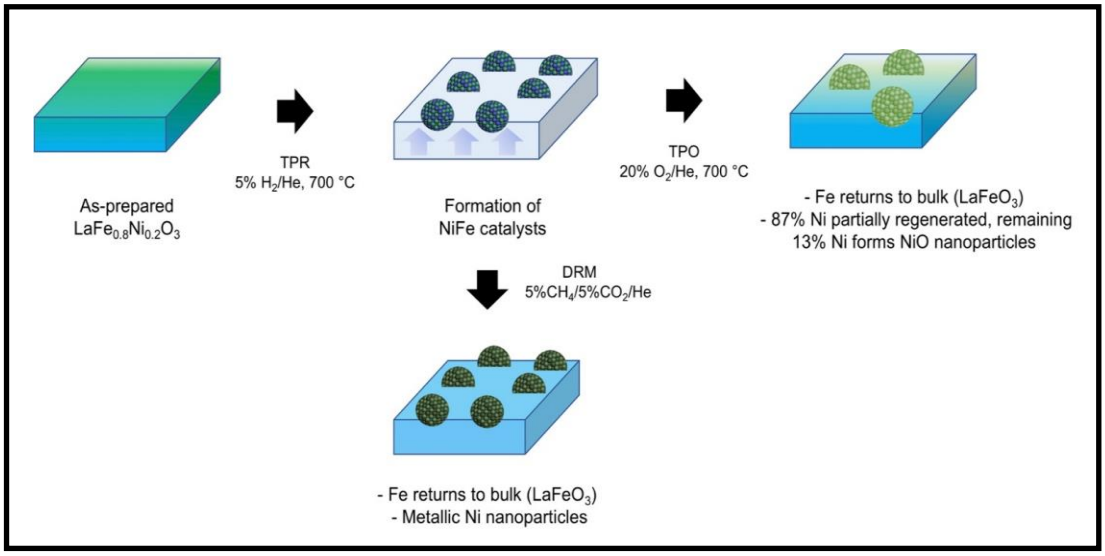

Figure 4.6. Pictorial scheme of the dynamic interplay of NiFe formation from exsolution and changes due to exposure to oxidative and reactive environments.

modeling results can be found in **Figure S4.5c** and **S6c** and **Table S1** and **S2**.

4.7 Proposed Mechanism of Ni-Fe dynamics from perovskite precursors

Figure 4.6 summarizes the formation, regeneration, and dynamical behavior of NiFe catalysts. It follows from the results that the exsolution of Fe is reversible while Ni is partially reversible or regenerated. Moreover, given the predisposition of Ni to be reduced, Ni exsolves earlier than Fe during the reduction. As the perovskite-based sample is further subjected to reducing conditions at elevated temperatures, the exsolution of Fe

follows and the metallic phase changes the composition and is gradually enriched from Ni to NiFe nanoparticles. During regeneration in an oxidative environment, Fe is preferentially oxidized before Ni and almost immediately re-enters the perovskite phase. The oxidation and re-entry of Ni is more gradual, and a significant portion of Ni goes through an intermediate NiO state. The implication of this for catalysis is that in DRM environments, the redox cycling of Fe stabilizes the catalyst by keeping Ni in its metallic state, which is key for activating C-H bonds. The presence of Fe also suppresses the complete decomposition of the perovskite seen in $LaNiO_3$ perovskites[28,48]. The presence of Fe allows for the regeneration of the catalysts to happen at a relatively lower temperatures than what is required for $LaNiO_3$.

4.8 Conclusion

The dynamics of Fe and Ni in $LaFe_{0.8}Ni_{0.2}O_3$ perovskite were studied using a combination of in-situ X-ray absorption spectroscopy, STEM-HAADF EDS imaging, XRD and catalytic studies. The progression of the exsolution of Ni and Fe in redox conditions were tracked. Analysis of the XANES spectra confirms that Ni exsolves earlier and faster than Fe during reduction, while the trend is reversed during oxidation. The progress lends itself to a surface alloying mechanism as a function of the reducibility of the B-cations. During the dry methane reforming reaction, Iron from the NiFe alloy nanoparticle re-enters the bulk of the support within minutes of initiating the reaction. We propose that dry methane reforming over exsolved Ni-Fe nanoparticles supported over parent perovskite occurs with methane activated by Ni-rich nanoparticles. During the oxidative regenerative cycle, the intermediate states of NiO and γ-Fe_2O_3 were identified

with EXAFS as states prior to re-entry in the bulk perovskite. Approximately ~13% of Ni remains on the surface as large oxidic Ni nanoparticle catalysts. Understanding the dynamics of the exsolution process from perovskite precursors in different redox environments is incumbent to achieve the goal of developing tunable alloy catalysts. This study serves as a guide to rationally design alloy catalysts through carefully controlling the kinetics of exsolution and further implications for regenerable alloy catalysts.

4.9 Acknowledgments

Use of the Stanford Synchrotron Radiation Lightsource, SLAC National Accelerator Laboratory is supported by the U.S. Department of Energy, Office of Basic Energy Sciences under Contract No. DE-AC02-76SF00515. The Co-ACCESS center at SLAC is supported by the U.S. Department of Energy, Office of Science, Office of Basic Energy Sciences, Chemical Sciences, Geosciences, and Biosciences. I would also like to acknowledge the support from Dr. Adam Hoffman and Dr. Griffin Canning for XAS measurements and training for data analysis. Dr. Luz Cruz conducted microscopy imaging for the study. Dr. Jiyun Hong is a co-author of the study and contributed equally to XAS analysis. Dr. Simon Bare and Dr. Kandis Leslie Abdul-Aziz were co-advisors for the study.

4.10 Supporting Information

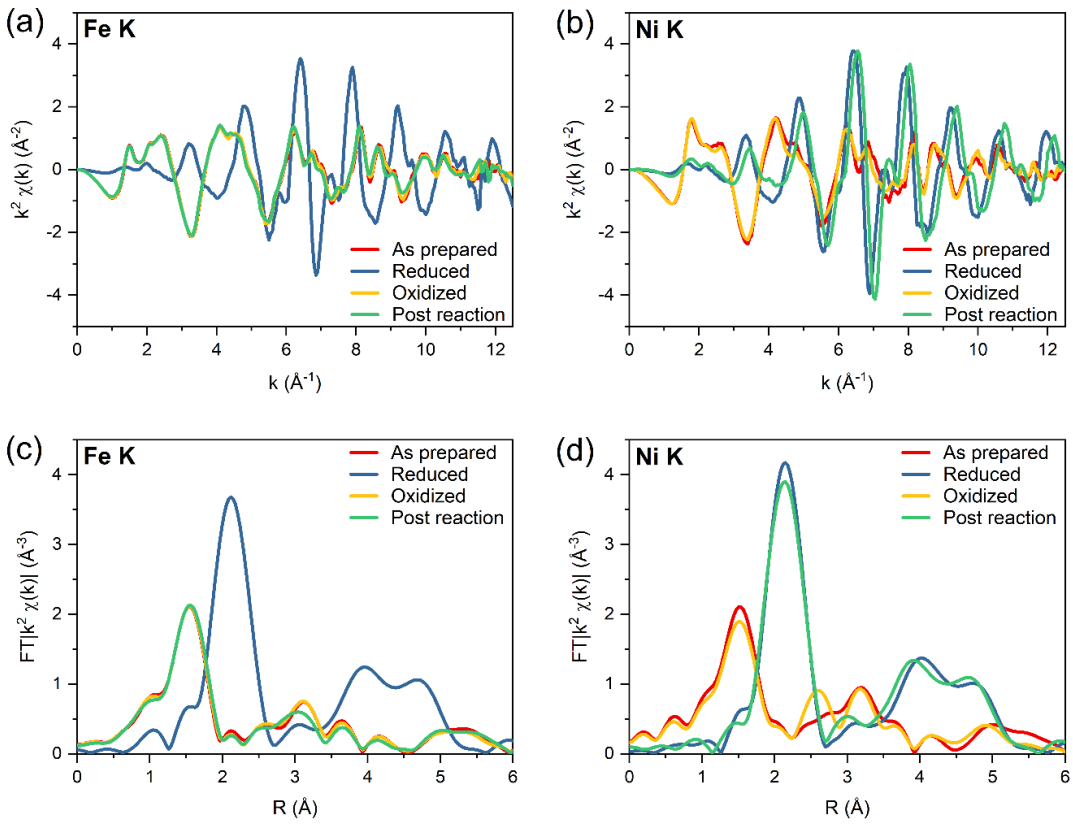

Figure S4.1. The k^2-weighted EXAFS spectra of as prepared, reduced, oxidized and post-reaction $LaFe_{0.8}Ni_{0.2}O_3$. The k-space and magnitude R-space EXAFS are shown in (a) and (c) for Fe K-edge, and in (b) and (d) for Ni K-edge.

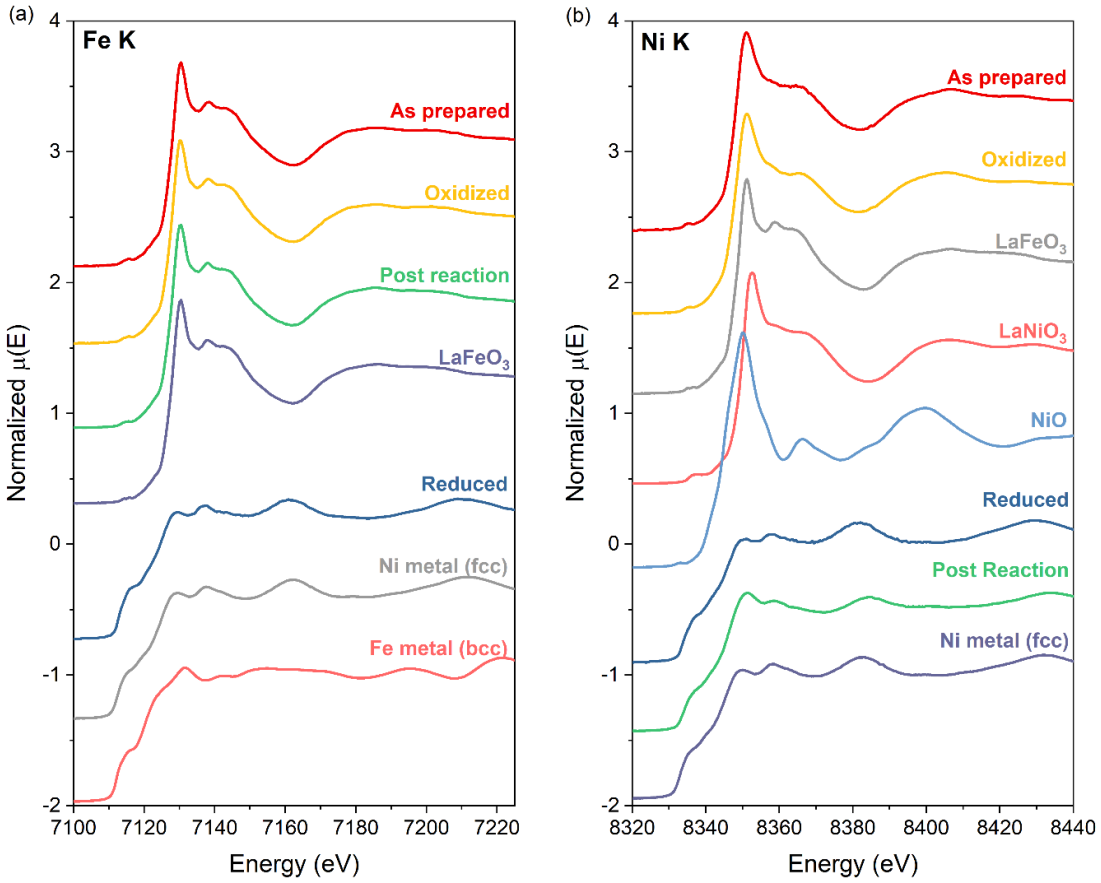

Figure S4.2. (a) Fe K-edge and (b) Ni K-edge XANES spectra of as prepared, reduced, oxidized and post-reaction $LaFe_{0.8}Ni_{0.2}O_3$ compared to different reference materials.

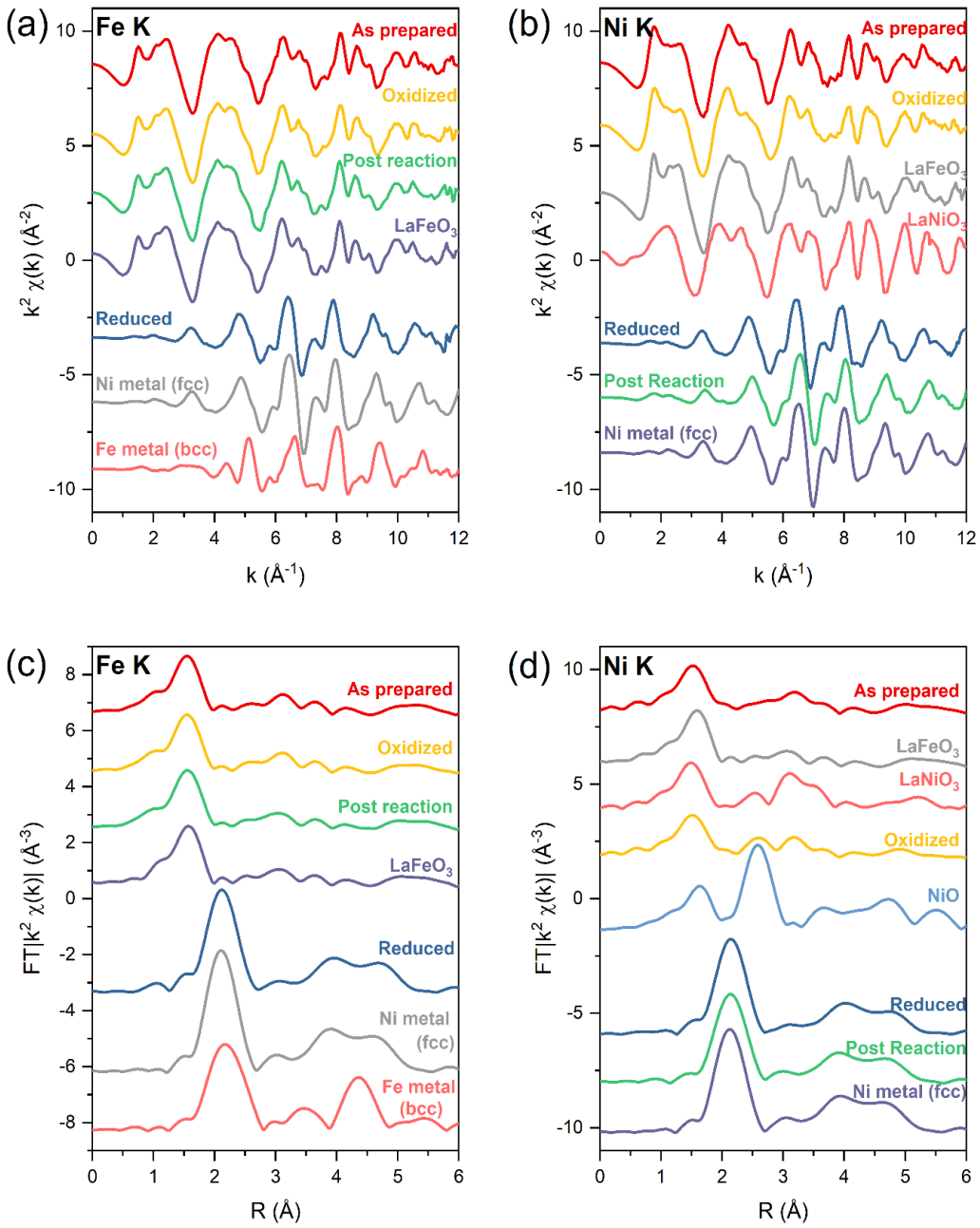

Figure S4.3. The k^2-weighted EXAFS spectra of as prepared, reduced, oxidized and post-reaction $LaFe_{0.8}Ni_{0.2}O_3$, along with reference materials for comparison. The k-space and magnitude R-space EXAFS are shown in (a) and (c) for Fe K-edge, and in (b) and (d) for Ni K-edge.

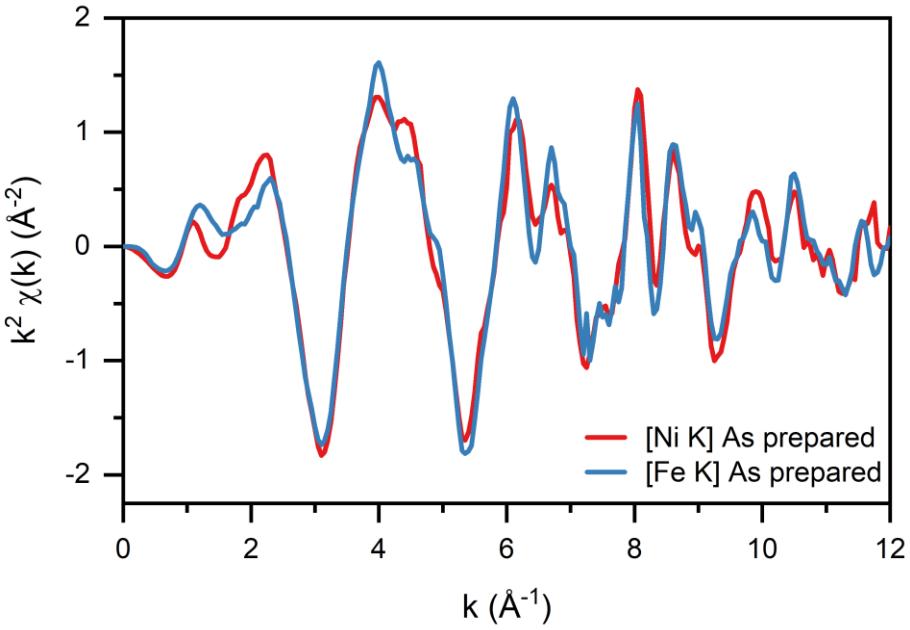

Figure S4.4. The k^2-weighted k-space EXAFS, at Ni K-edge (red) and Fe K-edge (blue), of as-prepared $LaFe_{0.8}Ni_{0.2}O_3$ overlayed for comparison.

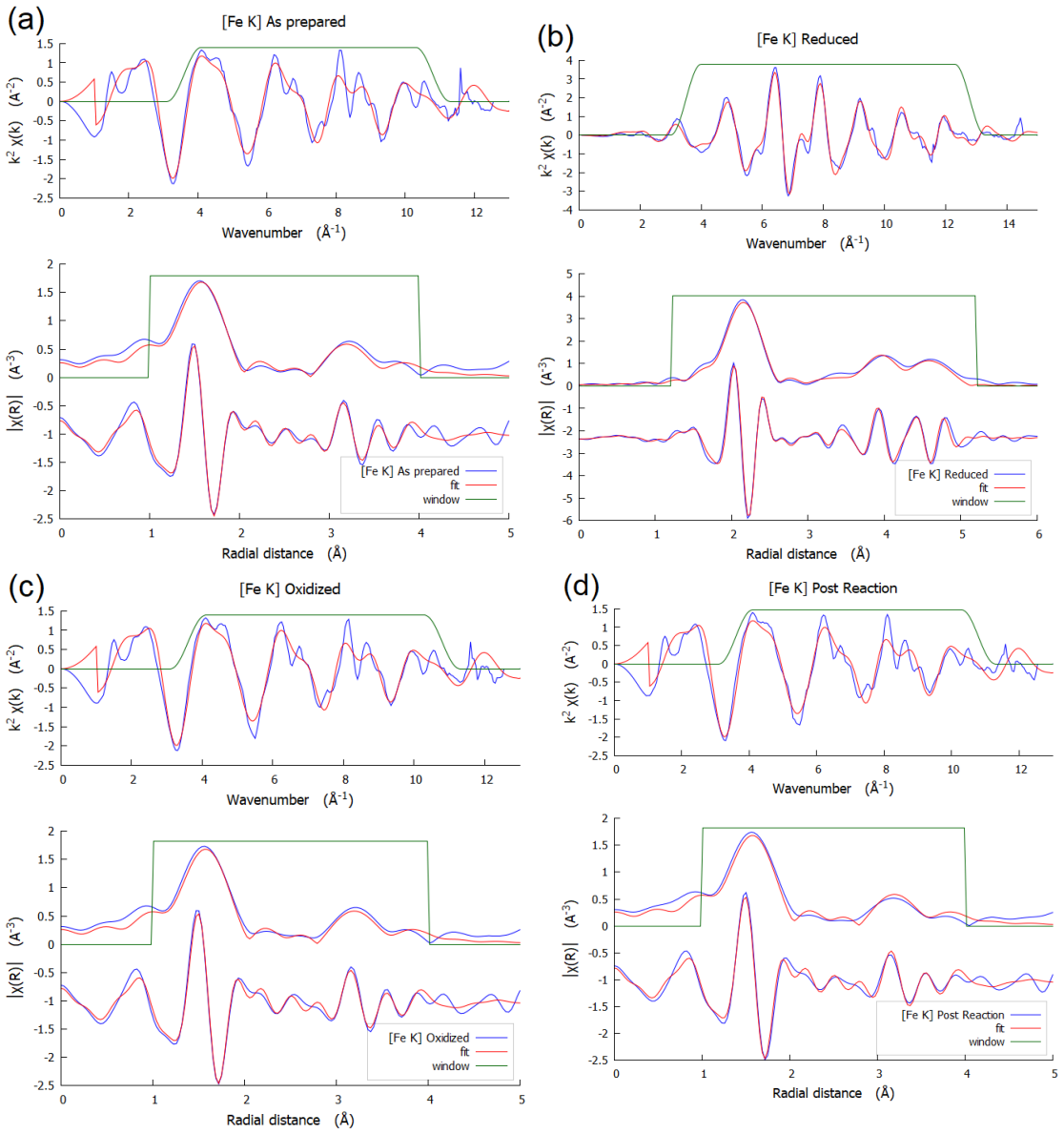

Figure S4.5. Fe K-edge EXAFS fits of (a) as prepared, (b) reduced, (c) oxidized, and (d) post reaction states of $LaFe_{0.8}Ni_{0.2}O_3$ perovskite. In each plot, top panel shows the k^2-weighted k-space EXAFS, while the bottom panel shows k^2-wieghted magnitude and imaginary R-space. For (a) as prepared, (c) oxidized, and (d) post reaction spectra, the k-window of 3.6 – 10.8 $Å^{-1}$ was used for Fourier transform, and the R-space of 1 – 4.0 Å was used. For (b) reduced spectrum, the k-window of 3.5 – 12.8 $Å^{-1}$ was used for Fourier transform, and the R-space of 1.2 – 5.2 Å was used.

Table S4.1. Fitting parameters from Fe K-edge EXAFS modelling.

Sample	Path[a]	CN [b]	R (Å) [c]	10^{-3} σ^2 (Å^2) [d]	ΔE_0 (eV) [e]	R-factor (%)
As prepared [f]	• Fe-O	6	1.99 ± 0.00	1.4 ± 0.3	4.1 ± 0.6	2.0
	• Fe-La	8	3.38 ± 0.01	11 ± 0.7		
	• Fe-M*	6	4.05 ± 0.01	12 ± 1.8		
Reduced [g]	□ Fe-M_1	12	2.51 ± 0.01	5.8 ± 0.4	-2.7 ± 1.1	3.2
	□ Fe-M_2	6	3.55 ± 0.01	13 ± 4		
	□ Fe-M_3	24	4.35 ± 0.01	8.3 ± 1.3		
	□ Fe-M_4	12	5.02 ± 0.01	8.0 ± 1.1		
Oxidized [f]	• Fe-O	6	1.99 ± 0.00	1.4 ± 0.3	4.1 ± 0.6	2.0
	• Fe-La	8	3.38 ± 0.01	11 ± 0.7		
	• Fe-M	6	4.05 ± 0.01	12 ± 1.8		
Post Reaction [f]	• Fe-O	6	1.99 ± 0.00	1.4 ± 0.3	4.1 ± 0.6	2.0
	• Fe-La	8	3.38 ± 0.01	11 ± 0.7		
	• Fe-M	6	4.05 ± 0.01	12 ± 1.8		

Value of S_0^2= 0.64, obtained from Fe foil fit, was used. The fit of Fe foil is shown in Figure S# and Table S#.

[a] Scattering paths were generated using crystallographic data of $LaFeO_3$(•) and fcc metallic Ni that has the core atom substituted with Fe (□).

[b] Coordination number.

[c] Bond distance.

[d] Mean-square deviation in bond distance.

[e] Inner potential correction.

[f] As prepared, oxidized and post reaction fits were done simultaneously by sharing all parameters.

[g] Reduced state was modelled using isotropic lattice expansion model. The resulting expansion parameter, α, is 0.8 ± 0.3%, which indicates 0.8% expansion with respect to the bulk Ni metal (α = 0.0 ± 0.2 %)

* M represents neighboring atom that is either Ni or Fe, which are indistinguishable in XAS.

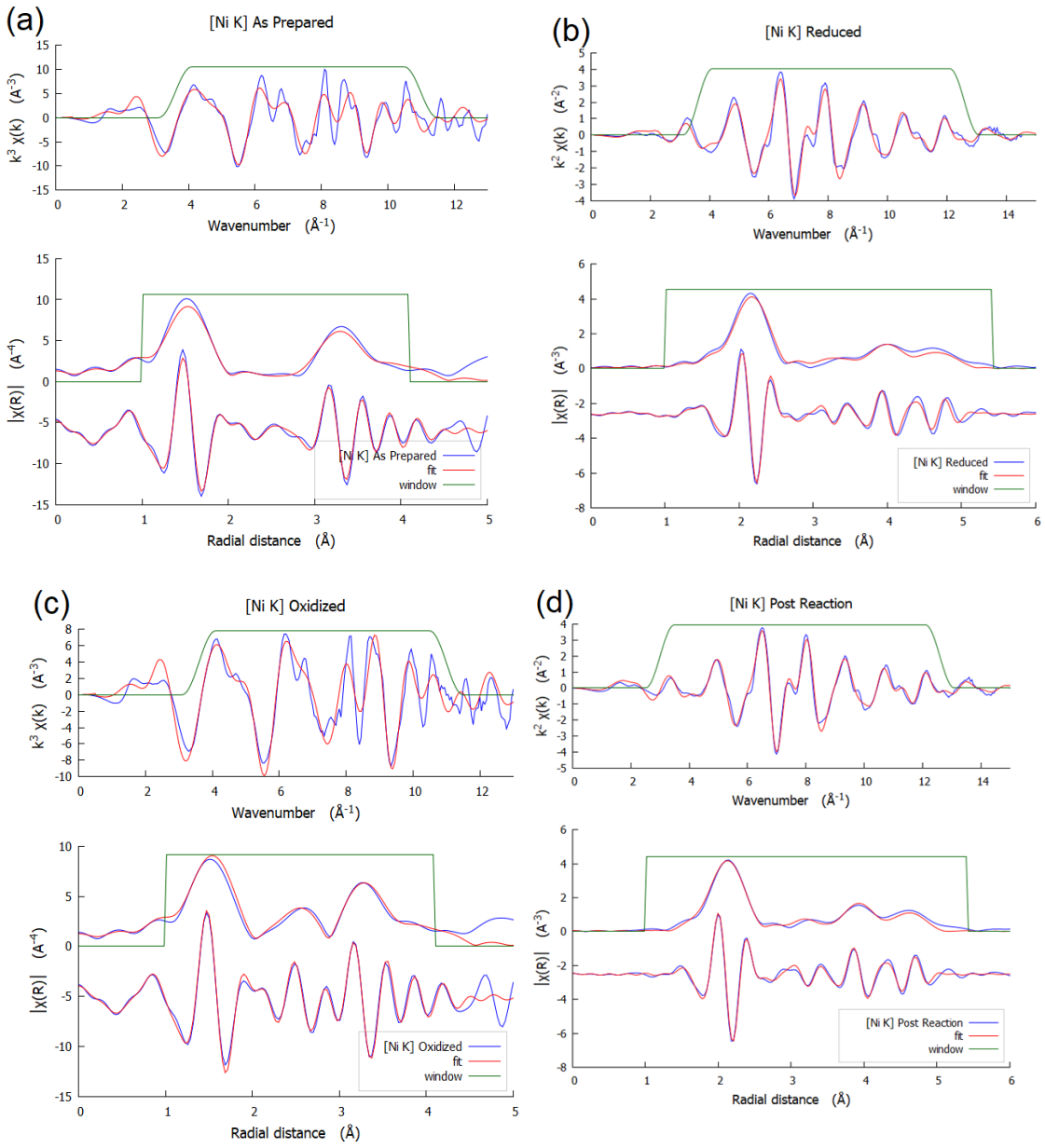

Figure S4.6. Ni K-edge EXAFS fits of (a) as prepared, (b) reduced, (c) oxidized, and (d) post reaction states of $LaFe_{0.8}Ni_{0.2}O_3$ perovskite. In each plot, top panel shows the k^2-weighted k-space EXAFS, while the bottom panel shows k^2-wieghted magnitude and imaginary R-space. For (a) as prepared and (c) oxidized spectra, the k-window of 3.6 – 11 $Å^{-1}$ was used for Fourier transform, and the R-space of 1 – 4.1 Å was used. For (b) reduced and (d) post reaction spectra, the k-window of 3.3 – 12.6 $Å^{-1}$ was used for Fourier transform, and the R-space of 1 – 5.4 Å was used.

Table S4.2. Fitting parameters from Ni K-edge EXAFS modelling.

Sample	Path[a]	CN [b]	R (Å) [c]	σ^2 (Å^2) [d]	ΔE_0 (eV) [e]	R-factor (%)
As prepared[f]	• Ni-O	6	1.96 ± 0.01	5.5 ± 0.4	1.0 ± 0.9	1.2
	• Ni-La	8	3.35 ± 0.01	17 ± 1		
	• Ni-M*	6	4.27 ± 0.01	9.5 ± 1.5		
Reduced[g]	□ Ni-M_1	12	2.52 ± 0.00	6.8 ± 0.4	-7.1 ± 0.7	3.4
	□ Ni-M_2	6	3.56 ± 0.00	9.4 ± 0.9		
	□ Ni-M_3	24	4.36 ± 0.01	9.4 ± 0.9		
	□ Ni-M_4	12	5.03 ± 0.01	9.4 ± 0.9		
Oxidized[f]	• Ni-O	6	1.96 ± 0.01	5.5 ± 0.4	1.0 ± 0.9	1.2
	• Ni-La	8	3.35 ± 0.01	17 ± 1		
	• Ni-M	6	4.27 ± 0.01	9.5 ± 1.5		
	♠ Ni-Ni	2.4 ± 1.0	2.95	8.8 ± 0.9	1.7 ± 1.3	
Post Reaction[h]	□ Ni-M_1	12	2.48 ± 0.00	7.1 ± 0.5	-7.1 ± 0.7	3.2
	□ Ni-M_2	6	3.51 ± 0.00	8.9 ± 0.9		
	□ Ni-M_3	24	4.30 ± 0.01	8.9 ± 0.9		
	□ Ni-M_4	12	4.97 ± 0.01	8.9 ± 0.9		

Value of S_0^2= 0.92, obtained from Ni foil fit, was used. The fit of Ni foil is shown in Figure S# and Table S#.

[a] Scattering paths were generated using crystallographic data of $LaFeO_3$ that has the core atom substituted with Fe (•), fcc metallic Ni (□), and NiO (♠).

[b] Coordination number.

[c] Bond distance.

[d] Mean-square deviation in bond distance.

[e] Inner potential correction.

[f] As prepared and oxidized fits were done simultaneously by sharing all parameters, except the additional Ni-Ni scattering path for the oxidized fit.

[g] Reduced fit was modelled using isotropic lattice expansion model. The resulting expansion parameter, α, is 1.1 ± 0.2%, which indicates slight expansion with respect to the Ni metal (α = 0.0 ± 0.2 %)

[h] Post reaction fit was modelled using isotropic lattice expansion model, and the additional Ni-O scattering path. The resulting expansion parameter, α, is -0.2 ± 0.2%, which indicates negligible change with respect to the bulk Ni metal (α = 0.0 ± 0.2 %)

* M represents neighboring atom that is either Ni or Fe, which are indistinguishable in XAS.

(a)

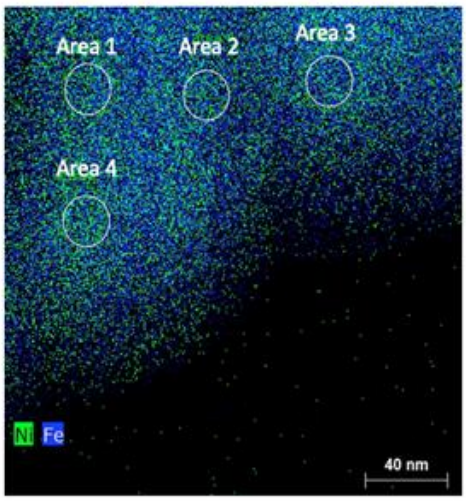

Area 1

Element	series	Net	[wt.%]	[norm. wt.%]	[norm. at.%]	Error in wt.% (3 Sigma)
Nickel	K-series	619	25.13579	25.13579	24.21195	4.030721
Iron	K-series	2028	74.86421	74.86421	75.78805	8.668407
		Sum:	100	100	100	

Area 2

Element	series	Net	[wt.%]	[norm. wt.%]	[norm. at.%]	Error in wt.% (3 Sigma)
Nickel	K-series	605	27.72953	27.72953	26.74441	4.472153
Iron	K-series	1735	72.27047	72.27047	73.25559	8.636102
		Sum:	100	100	100	

Area 3

Element	series	Net	[wt.%]	[norm. wt.%]	[norm. at.%]	Error in wt.% (3 Sigma)
Nickel	K-series	660	22.04025	22.04025	21.19796	3.469836
Iron	K-series	2569	77.95975	77.95975	78.80204	8.653033
		Sum:	100	100	100	

Area 4

Element	series	Net	[wt.%]	[norm. wt.%]	[norm. at.%]	Error in wt.% (3 Sigma)
Nickel	K-series	344	21.83351	21.83351	20.99699	4.336726
Iron	K-series	1354	78.16649	78.16649	79.00301	9.869599
		Sum:	100	100	100	

(b)

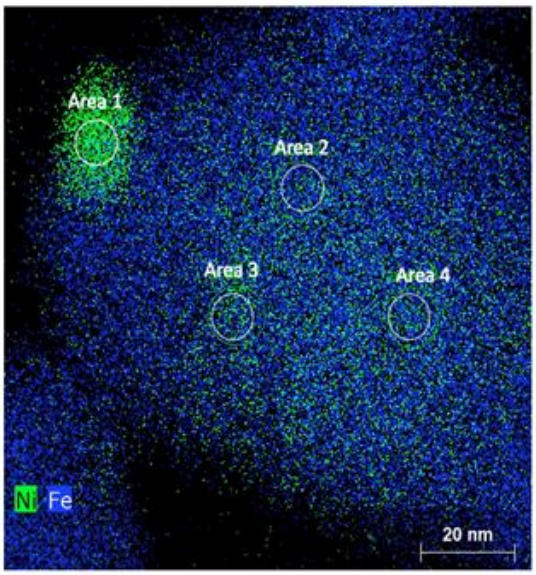

Spectrum: area 1

Element	Series	Net	unn. C [wt.%]	norm. C [wt.%]	Atom. C [at.%]	Error (3 Sigma) [wt.%]
Nickel	K-series	446	79.44	79.44	78.61	14.11
Iron	K-series	127	20.56	20.56	21.39	6.22
		Total:	100.00	100.00	100.00	

Spectrum: area 2

Element	Series	Net	unn. C [wt.%]	norm. C [wt.%]	Atom. C [at.%]	Error (3 Sigma) [wt.%]
Nickel	K-series	332	24.41	24.41	23.50	4.90
Iron	K-series	1132	75.59	75.59	76.50	9.99
		Total:	100.00	100.00	100.00	

Spectrum: area 3

Element	Series	Net	unn. C [wt.%]	norm. C [wt.%]	Atom. C [at.%]	Error (3 Sigma) [wt.%]
Nickel	K-series	353	25.89	25.89	24.95	5.08
Iron	K-series	1112	74.11	74.11	75.05	9.84
		Total:	100.00	100.00	100.00	

Spectrum: area 4

Element	Series	Net	unn. C [wt.%]	norm. C [wt.%]	Atom. C [at.%]	Error (3 Sigma) [wt.%]
Nickel	K-series	371	29.97	29.97	28.94	5.76
Iron	K-series	951	70.03	70.03	71.06	9.71
		Total:	100.00	100.00	100.00	

Figure S4.7. STEM-HAADF EDS images with associated areas for compositional analysis of $LaFe_{0.8}Ni_{0.2}O_3$ (a) as-prepared and (b) after 10-minute reduction.

(a)

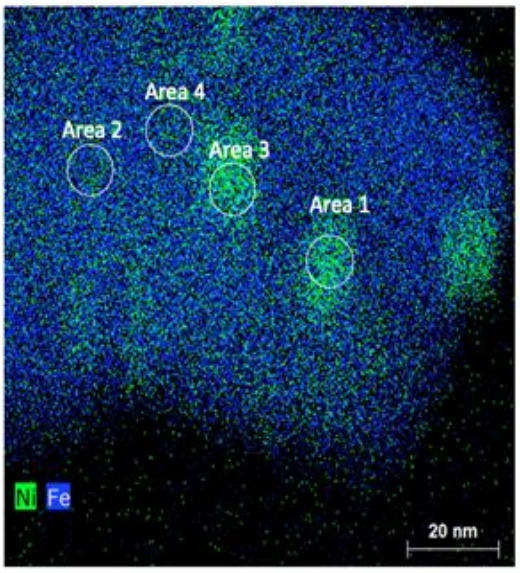

Spectrum: 001

Element	Series	Net unn. C [wt.%]	norm. C [wt.%]	Atom. C [at.%]	Error (3 Sigma) [wt.%]
Nickel	K-series	20011	71.34	71.34	70.31	6.70
Iron	K-series	8843	28.66	28.66	29.69	2.83
Total:			100.00	100.00	100.00	

Spectrum: 002

Element	Series	Net unn. C [wt.%]	norm. C [wt.%]	Atom. C [at.%]	Error (3 Sigma) [wt.%]
Nickel	K-series	2613	45.18	45.18	43.95	5.03
Iron	K-series	3488	54.82	54.82	56.05	5.84
Total:			100.00	100.00	100.00	

Spectrum: 003

Element	Series	Net unn. C [wt.%]	norm. C [wt.%]	Atom. C [at.%]	Error (3 Sigma) [wt.%]
Nickel	K-series	915	54.92	54.92	53.69	7.72
Iron	K-series	825	45.08	45.08	46.31	6.54
Total:			100.00	100.00	100.00	

Spectrum: 004

Element	Series	Net unn. C [wt.%]	norm. C [wt.%]	Atom. C [at.%]	Error (3 Sigma) [wt.%]
Nickel	K-series	1962	44.37	44.37	43.15	5.20
Iron	K-series	2705	55.63	55.63	56.85	6.14
Total:			100.00	100.00	100.00	

(b)

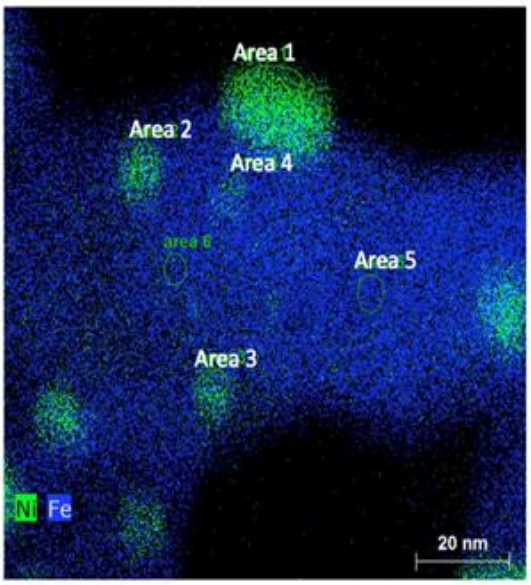

Spectrum: area 1

Element	Series	Net unn. C [wt.%]	norm. C [wt.%]	Atom. C [at.%]	Error (3 Sigma) [wt.%]
Nickel	K-series	997	75.69	75.69	74.77	10.35
Iron	K-series	352	24.31	24.31	25.23	4.77
Total:			100.00	100.00	100.00	

Spectrum: area 2

Element	Series	Net unn. C [wt.%]	norm. C [wt.%]	Atom. C [at.%]	Error (3 Sigma) [wt.%]
Nickel	K-series	507	59.91	59.91	58.71	10.18
Iron	K-series	373	40.09	40.09	41.29	7.65
Total:			100.00	100.00	100.00	

Spectrum: area 3

Element	Series	Net unn. C [wt.%]	norm. C [wt.%]	Atom. C [at.%]	Error (3 Sigma) [wt.%]
Nickel	K-series	807	53.89	53.89	52.65	7.86
Iron	K-series	760	46.11	46.11	47.35	6.86
Total:			100.00	100.00	100.00	

Spectrum area 4

Element	series	Net	[wt.%]	[norm. wt.%]	[norm. at.%]	Error in wt.% (3 Sigma)
Nickel	K-series	47	14.95636	14.95636	14.33501	7.210487
Iron	K-series	294	85.04364	85.04364	85.66499	17.73447
		Sum:	100	100	100	

Spectrum: area 5

Element	Series	Net unn. C [wt.%]	norm. C [wt.%]	Atom. C [at.%]	Error (3 Sigma) [wt.%]
Nickel	K-series	25	3.81	3.81	3.63	2.53
Iron	K-series	701	96.19	96.19	96.37	14.59
Total:			100.00	100.00	100.00	

Figure S4.8. STEM-HAADF EDS images with associated areas for compositional analysis of $LaFe_{0.8}Ni_{0.2}O_3$ (a) after 30-minute reduction and (b) after 60-minute reduction.

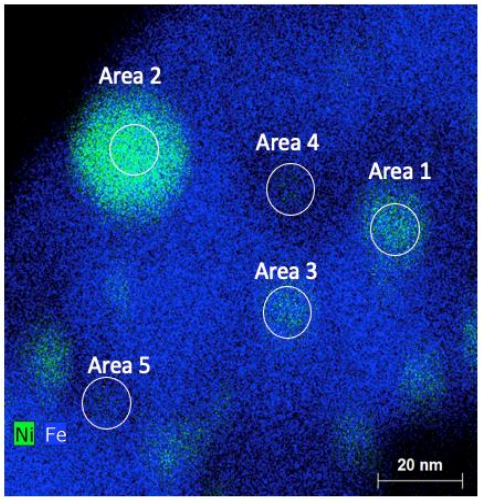

Spectrum: 001

Element	Series	Net unn. C [wt.%]	norm. C [wt.%]	Atom. C [at.%]	Error (3 Sigma) [wt.%]
Nickel	K-series	2835	58.52	58.52	57.31	6.42
Iron	K-series	2211	41.48	41.48	42.69	4.76
		Total:	100.00	100.00	100.00	

Spectrum: 002

Element	Series	Net unn. C [wt.%]	norm. C [wt.%]	Atom. C [at.%]	Error (3 Sigma) [wt.%]
Nickel	K-series	13932	74.04	74.04	73.07	7.04
Iron	K-series	5374	25.96	25.96	26.93	2.67
		Total:	100.00	100.00	100.00	

Spectrum: 003

Element	Series	Net unn. C [wt.%]	norm. C [wt.%]	Atom. C [at.%]	Error (3 Sigma) [wt.%]
Nickel	K-series	1836	47.22	47.22	45.98	5.61
Iron	K-series	2256	52.78	52.78	54.02	6.01
		Total:	100.00	100.00	100.00	

Spectrum: 004

Element	Series	Net unn. C [wt.%]	norm. C [wt.%]	Atom. C [at.%]	Error (3 Sigma) [wt.%]
Nickel	K-series	47	5.13	5.13	4.90	2.52
Iron	K-series	954	94.87	94.87	95.10	13.11
		Total:	100.00	100.00	100.00	

Spectrum: 005

Element	Series	Net unn. C [wt.%]	norm. C [wt.%]	Atom. C [at.%]	Error (3 Sigma) [wt.%]
Nickel	K-series	20	5.60	5.60	5.34	3.86
Iron	K-series	426	94.40	94.40	94.66	17.04
		Total:	100.00	100.00	100.00	

Figure S4.9. STEM-HAADF EDS images with associated areas for compositional analysis for $LaFe_{0.8}Ni_{0.2}O_3$ after 90-minute reduction.

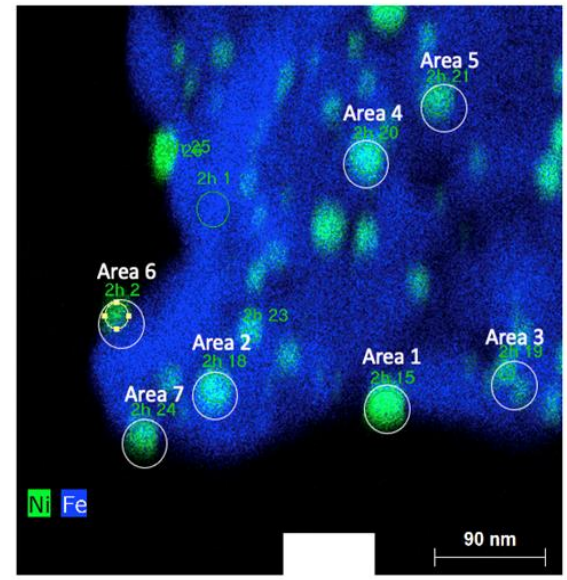

Area 1

Element	series	Net	[wt.%]	[norm. wt.%]	[norm. at.%]	Error in wt.% (1 Sigma)
Nickel	K-series	9837	67.90835	67.90835	70.43822	3.163153
Iron	K-series	3692	32.09165	32.09165	29.56178	2.074996
		Sum:	100	100	100	

Area 2

Element	series	Net	[wt.%]	[norm. wt.%]	[norm. at.%]	Error in wt.% (1 Sigma)
Iron	K-series	6117	48.03717	48.03717	48.47539	3.594882
Nickel	K-series	6307	51.96283	51.96283	51.52461	3.721673
		Sum:	100	100	100	

Area 3

Element	series	Net	[wt.%]	[norm. wt.%]	[norm. at.%]	Error in wt.% (1 Sigma)
Nickel	K-series	1326	52.23471	52.23471	52.86232	4.188116
Iron	K-series	1138	47.76529	47.76529	47.13768	4.026435
		Sum:	100	100	100	

Area 4

Element	series	Net	[wt.%]	[norm. wt.%]	[norm. at.%]	Error in wt.% (1 Sigma)
Nickel	K-series	6041	53.41976	53.41976	54.02873	3.544065
Iron	K-series	5016	46.58024	46.58024	45.97127	3.330394
		Sum:	100	100	100	

Area 5

Element	series	Net	[wt.%]	[norm. wt.%]	[norm. at.%]	Error in wt.% (1 Sigma)
Nickel	K-series	3281	53.66928	53.66928	54.31851	3.605818
Iron	K-series	2687	46.33072	46.33072	45.68149	3.369148
		Sum:	100	100	100	

Area 6

Element	series	Net	[wt.%]	[norm. wt.%]	[norm. at.%]	Error in wt.% (1 Sigma)
Nickel	K-series	4393	57.58554	57.58554	60.64635	3.919067
Iron	K-series	2320	42.41446	42.41446	39.35365	3.447697
		Sum:	100	100	100	

Area 7

Element	series	Net	[wt.%]	[norm. wt.%]	[norm. at.%]	Error in wt.% (1 Sigma)
Nickel	K-series	3510	56.59606	56.59606	58.32758	3.643504
Iron	K-series	2299	43.40394	43.40394	41.67242	3.227334
		Sum:	100	100	100	

Figure S4.10. STEM-HAADF EDS images with associated areas for compositional analysis of $LaFe_{0.8}Ni_{0.2}O_3$ after 120-minute reduction.

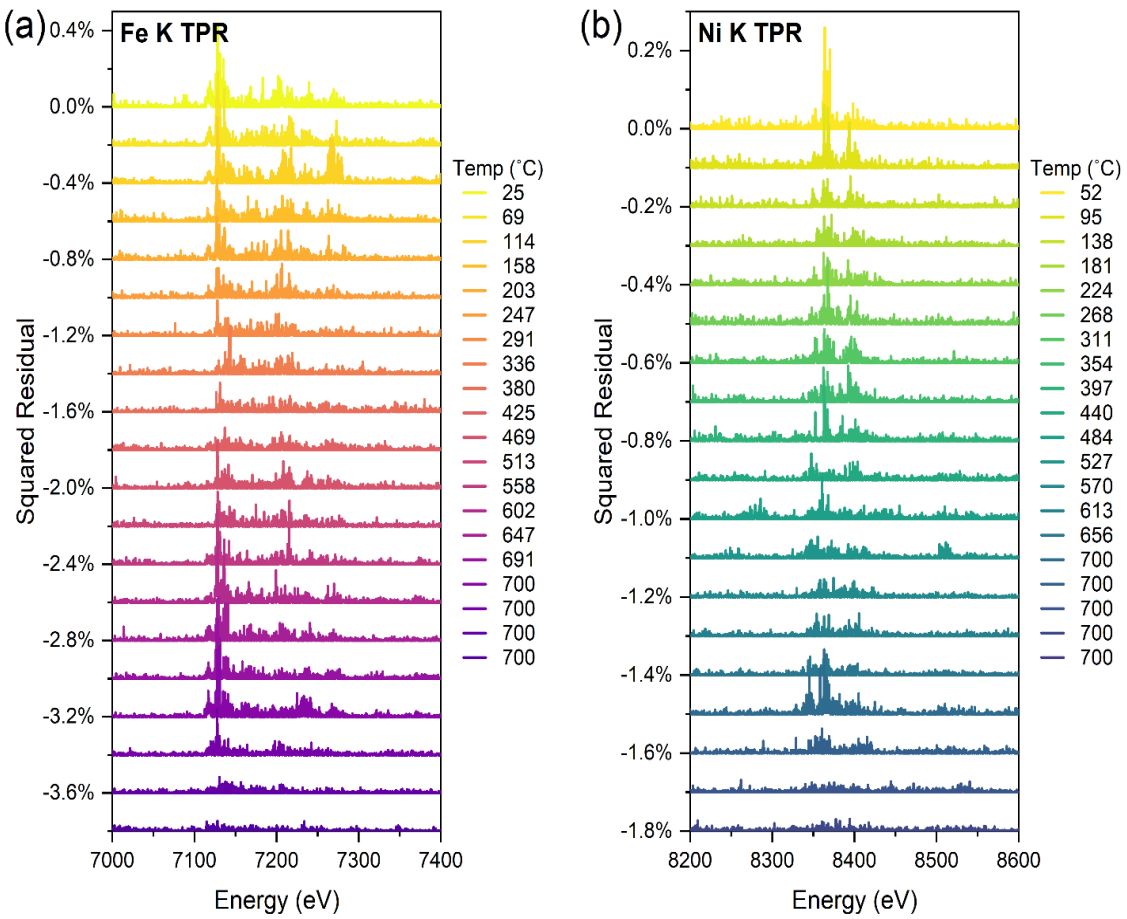

Figure S4.11. Residuals from the MCR-ALS analysis of XAS spectra at (a) Fe K-edge and (b) Ni K-edge of LaFe0.8Ni0.2O3 during TPR, showing the XANES region.

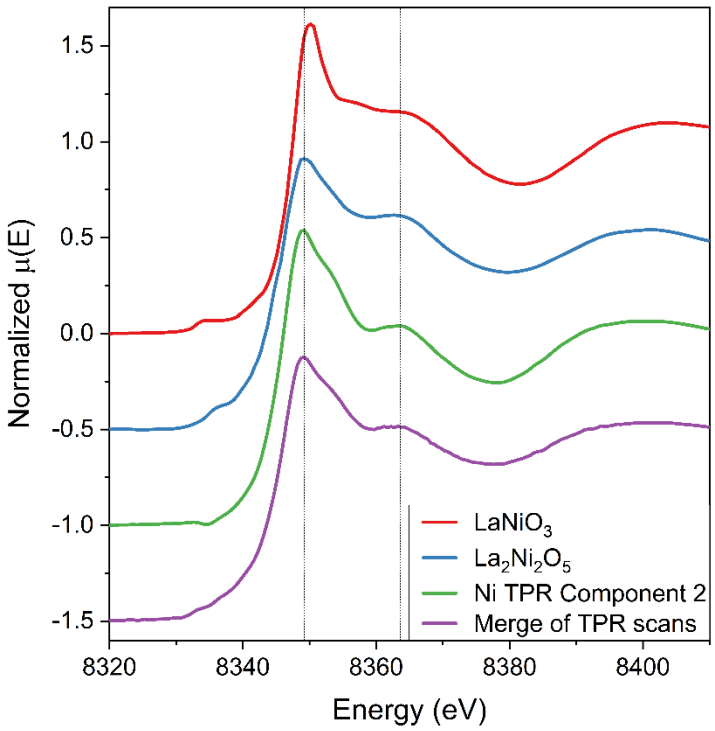

Figure S4.12. XANES spectrum of the Component 2 (green) from MCR-ALS analysis of Ni K-edge XAS during TPR, compared to the XANES spectra of $LaNiO_3$ (red) and $La_2Ni_2O_5$ (blue). The XANES spectrum of merged scans at 700˚C during TPR is also shown in purple.

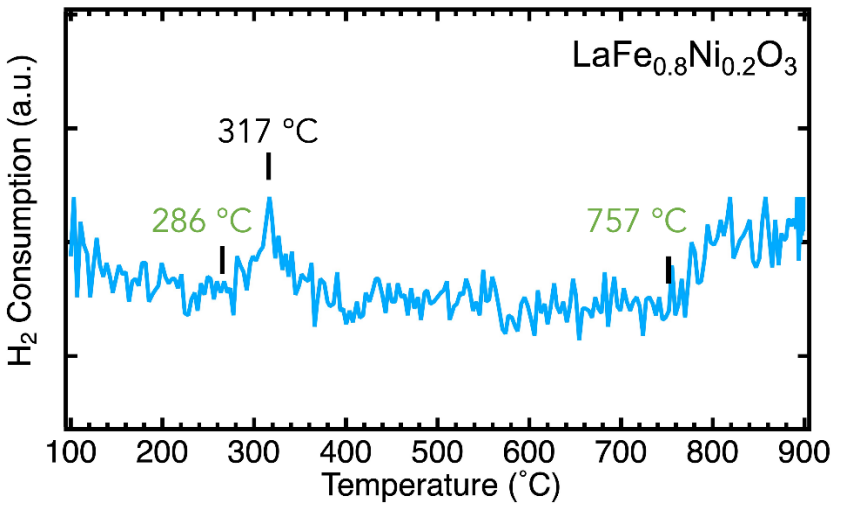

Figure S4.13. In-lab temperature-programmed reduction of $LaFe_{0.8}Ni_{0.2}O_3$.

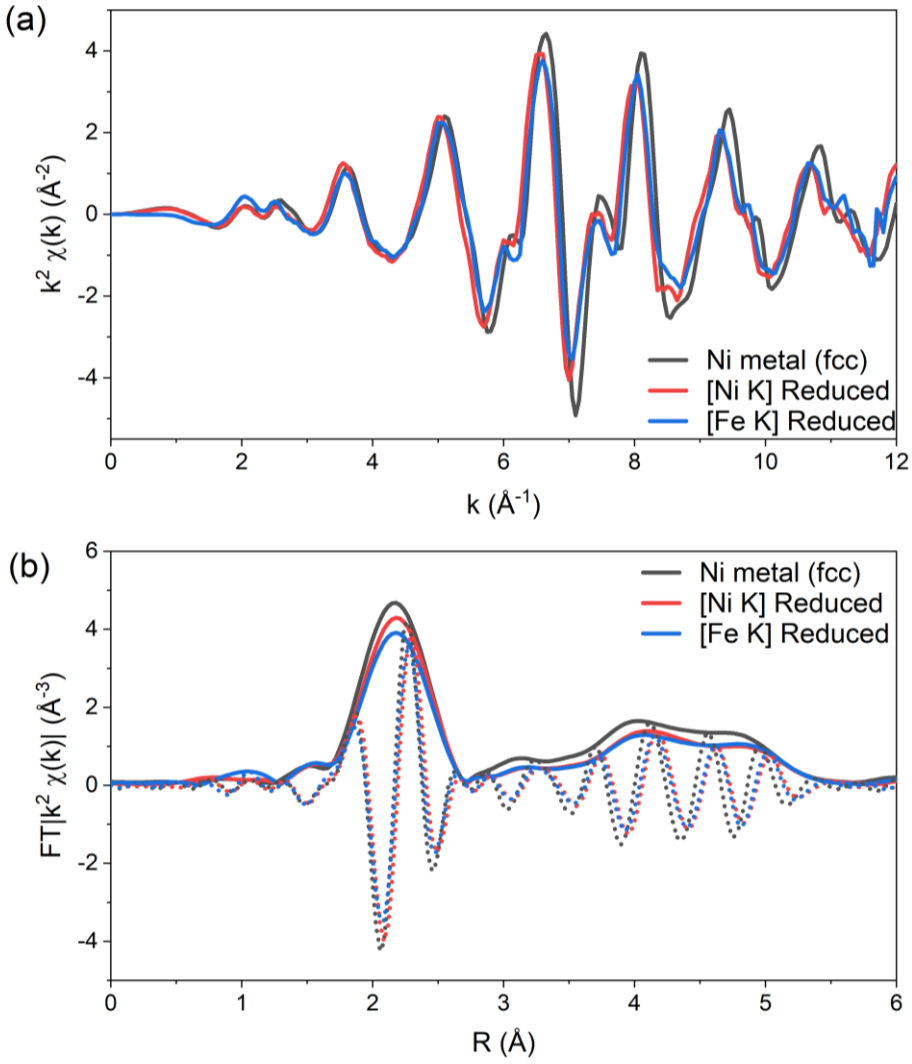

Figure S4.14. The k^2-weighted EXAFS of the reduced $LaFe_{0.8}Ni_{0.2}O_3$ at Ni K-edge and Fe K-edge compared to the and fcc Ni metal, shown in (a) k-space and (b) magnitude R-space.

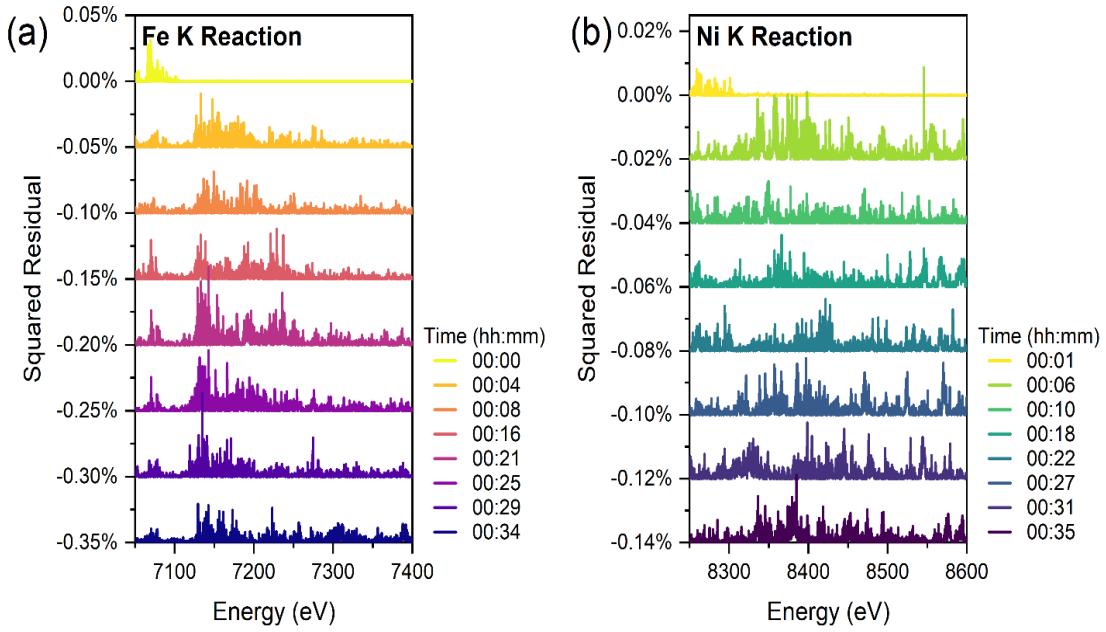

Figure S4.15. Residuals from the MCR-ALS analysis of XAS spectra at (a) Fe K-edge and (b) Ni K-edge of $LaFe_{0.8}Ni_{0.2}O_3$ during DRM reaction, showing the XANES region.

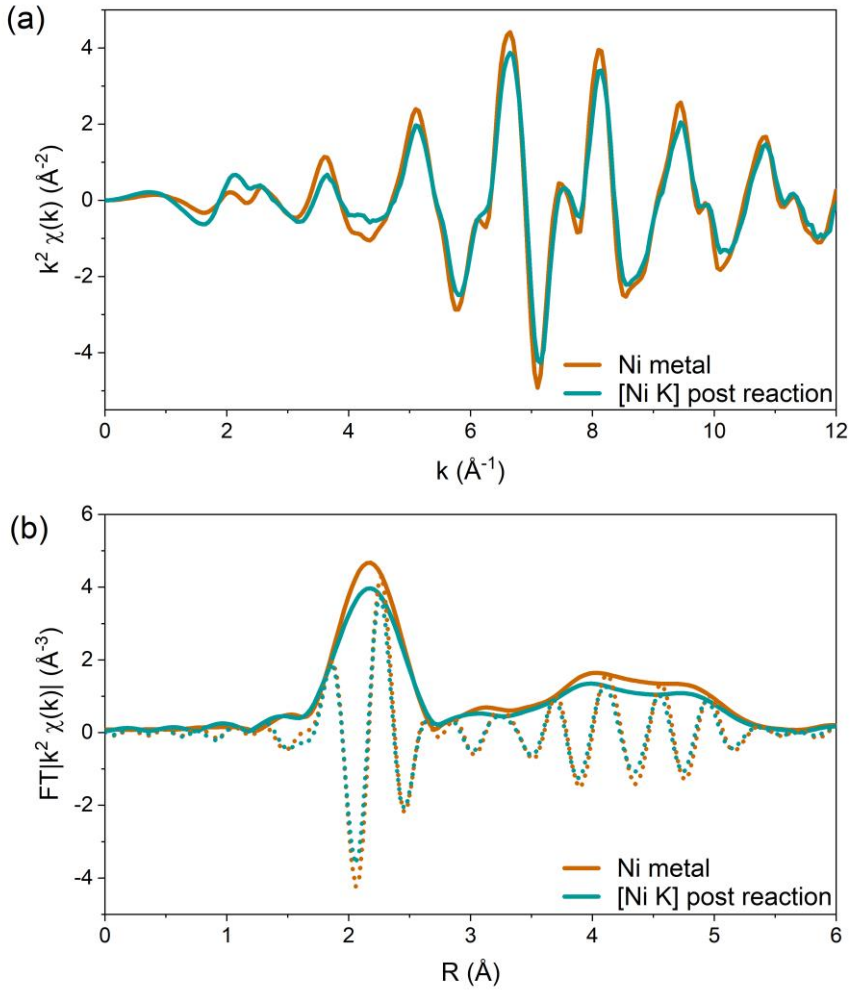

Figure S4.16. The k^2-weighted EXAFS of the post-reaction $LaFe_{0.8}Ni_{0.2}O_3$ at Ni K-edge compared to fcc Ni metal, shown in (a) k-space and (b) magnitude R-space.

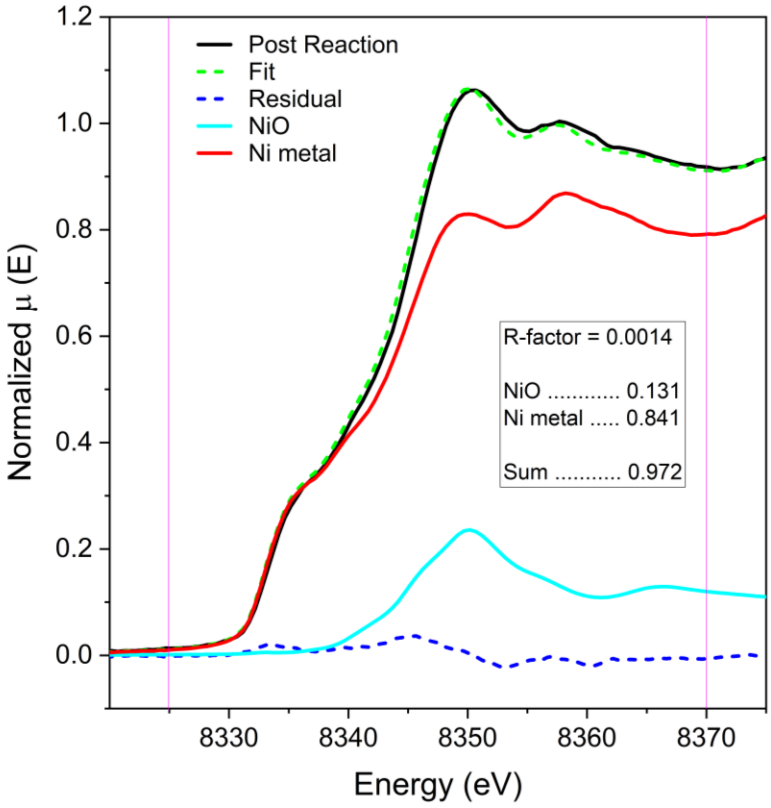

Figure S4.17. Linear combination fitting of Ni K-edge XANES of the post-reaction $LaFe_{0.8}Ni_{0.2}O_3$ using NiO and Ni metal as basis spectra. The fit result is shown inside the inset.

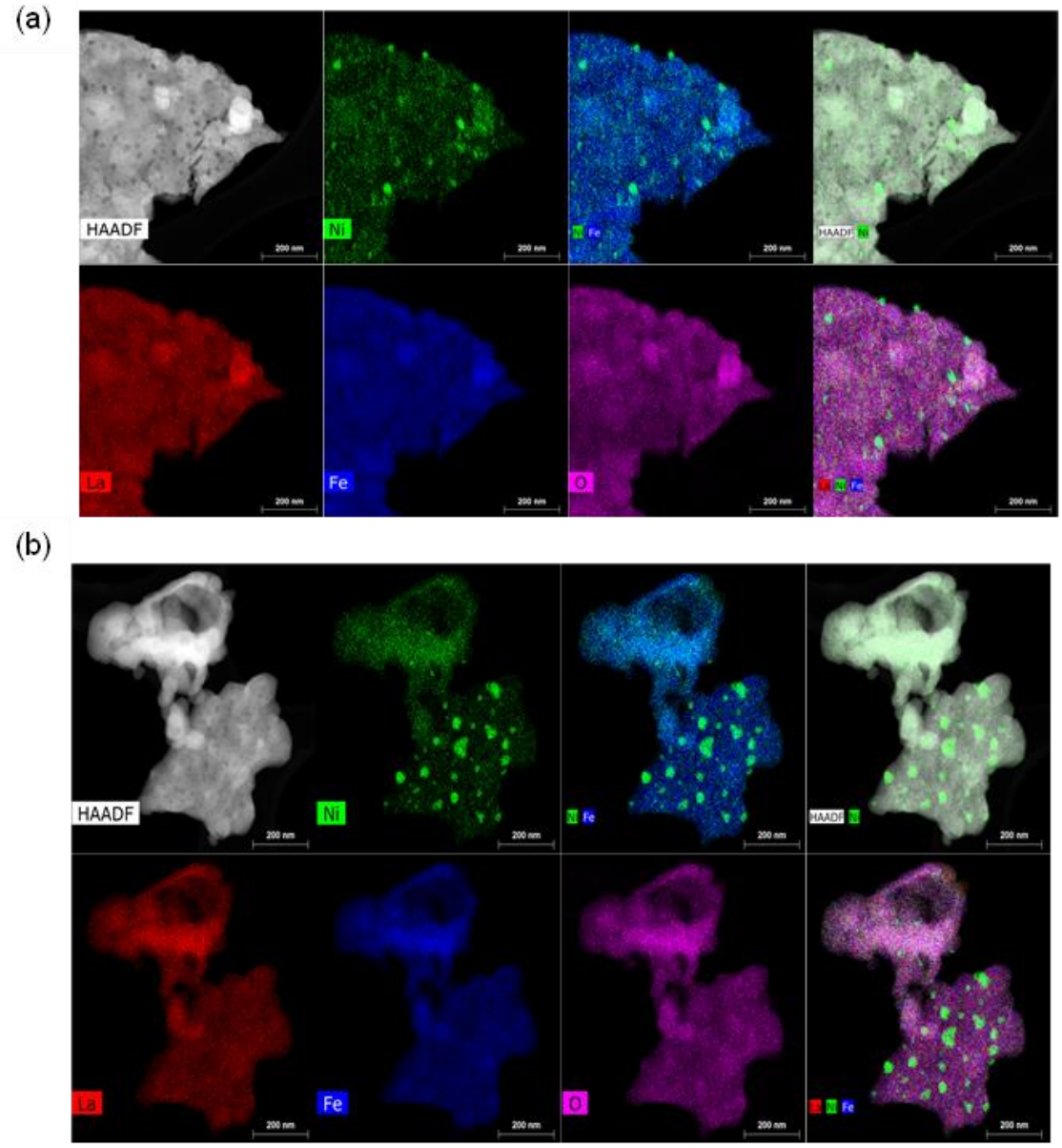

Figure S4.18. STEM-HAADF EDS images of 30-minute reduced $LaFe_{0.8}Ni_{0.2}O_3$ (a) prior to reaction and (b) after 2-hour oxidation in 20% O_2/He.

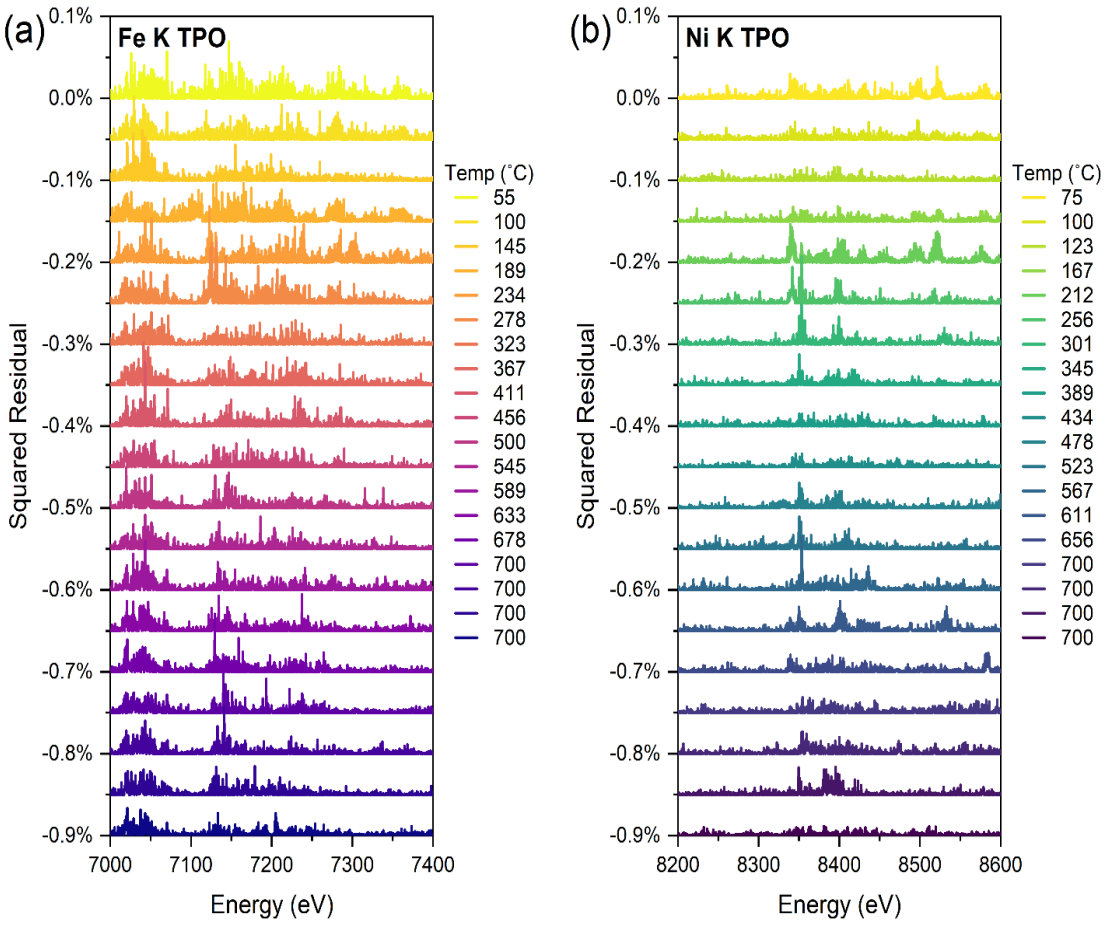

Figure S4.19. Residuals from the MCR-ALS analysis of XAS spectra at (a) Fe K-edge and (b) Ni K-edge of $LaFe_{0.8}Ni_{0.2}O_3$ during TPO, showing the XANES region.

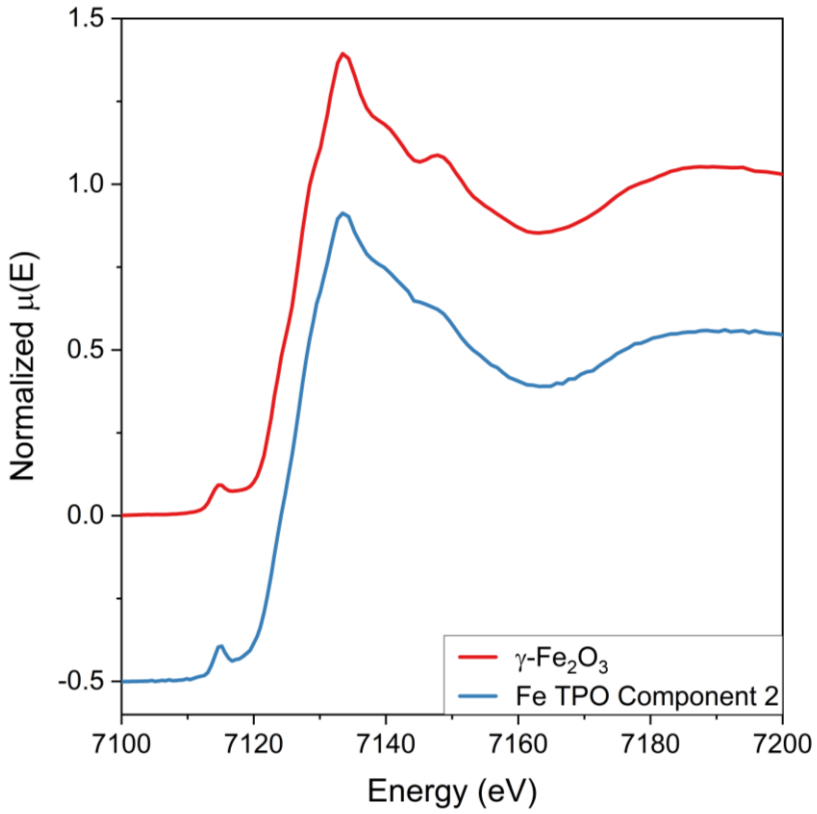

Figure S4.20. XANES spectrum of the Component 2 from MCR-ALS analysis of Fe K-edge XAS during TPO, compared to the XANES spectrum of γ-Fe_2O_3.

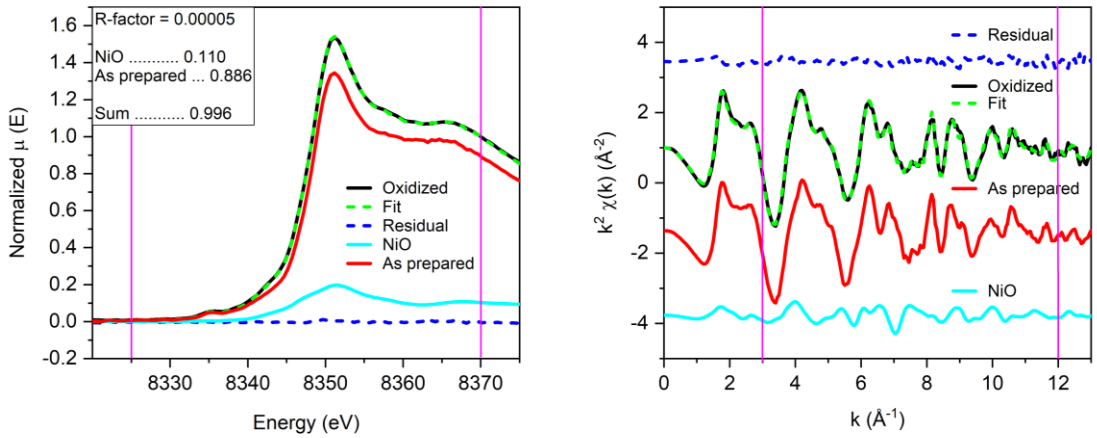

Figure S4.21. Linear combination fitting of Ni K-edge XANES (left) and EXAFS (right) of the oxidized $LaFe_{0.8}Ni_{0.2}O_3$ using as-prepared spectrum and NiO as basis spectra.

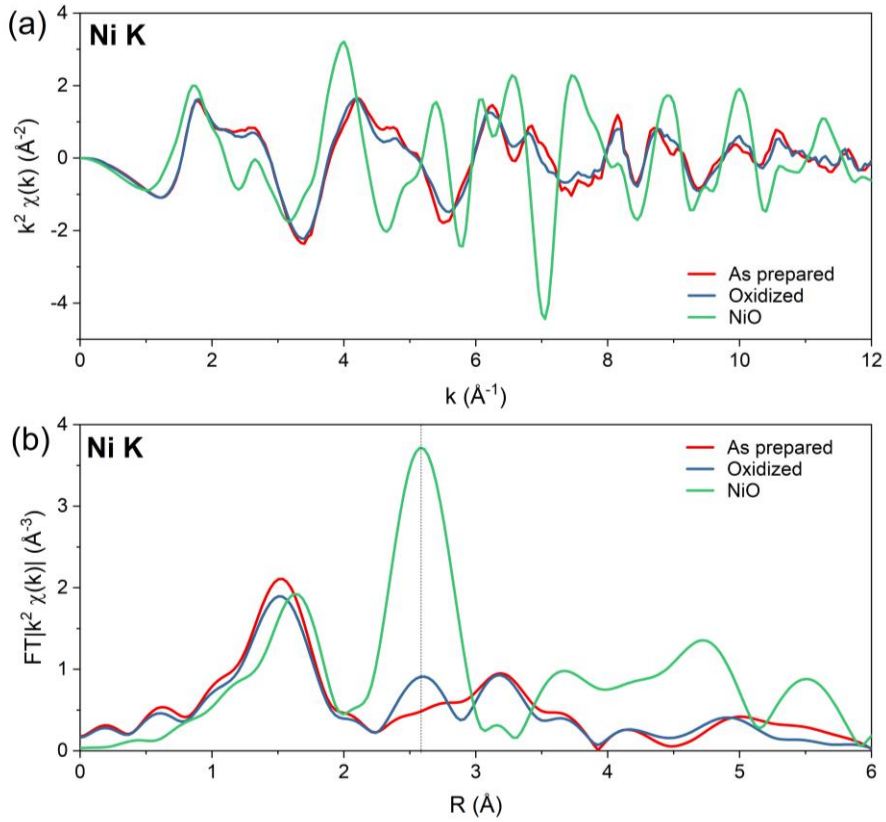

Figure S4.22. The k^2-weighted EXAFS of the oxidized $LaFe_{0.8}Ni_{0.2}O_3$ at Ni K-edge shown in (a) k-space and (b) magnitude R-space, in comparison to the as-prepared $LaFe_{0.8}Ni_{0.2}O_3$ and NiO.

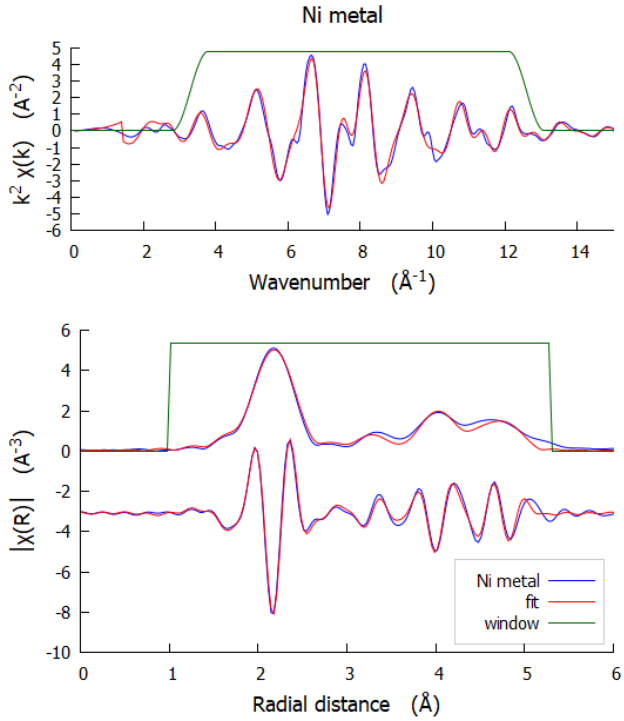

Figure S4.23. EXAFS fit of Ni metal, collected to determine the S_0^2, is shown in k^2-weighted k-space (top) and in magnitude and imaginary R-space (bottom). The k-window of 3.3 – 12.6Å^{-1} was used for Fourier transform, and the R-space of 1 – 5.3Å was modelled.

Table S4.3. Fitting parameters from Ni K-edge EXAFS modelling of Ni metal.

Sample	Path[a]	CN[b]	R (Å)[c]	10^{-3} σ^2 (Å^2)[d]	ΔE_0 (eV)[e]	S_0^2[f]	R-factor (%)
Ni metal*	Ni-Ni_1	12	2.51 ± 0.01	6.9 ± 0.7	7.6 ± 0.8	0.92 ± 0.08	2.5
	Ni-Ni_2	6	3.55 ± 0.01	10.4 ± 0.1			
	Ni-Ni_3	24	4.35 ± 0.01	8.7 ± 1.1			
	Ni-N_4	12	5.02 ± 0.01	7.5 ± 1.0			

[a] Scattering paths were generated using crystallographic data of fcc metallic Ni.

[b] Coordination number.

[c] Bond distance.

[d] Mean-square deviation in bond distance.

[e] Inner potential correction.

[f] Amplitude reduction factor

* Ni metal was modelled using isotropic lattice expansion model. The resulting expansion parameter, α, is 0.0 ± 0.2% with the cif file used.

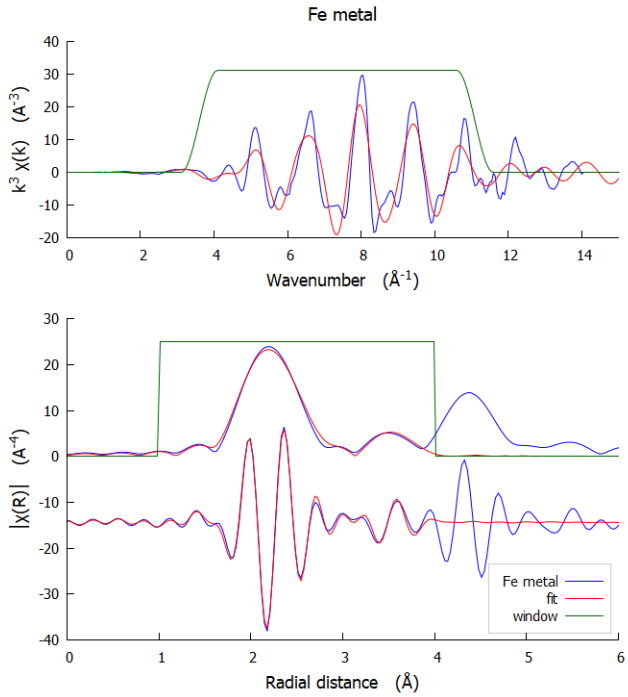

Figure S4.24. EXAFS fit of Fe metal, collected to determine the S02, is shown in k2-weighted k-space (top) and in magnitude and imaginary R-space (bottom). The k-window of 3.6 – 11.1Å^{-1} was used for Fourier transform, and the R-space of 1.0 – 4.0 Å was modelled.

Table S4.4 Fitting parameters from Fe K-edge EXAFS modelling of Fe metal

Sample	Path[a]	CN[b]	R (Å) [c]	10^{-3} σ^2 ($Å^2$) [d]	ΔE_0 (eV) [e]	S_0^2 [f]	R-factor (%)
Fe metal	Fe-Fe_1	8	2.45 ± 0.02	5.7 ± 3.3	-8.4 ± 3.7	0.64± 0.3	2.0
	Fe-Fe_2	6	2.82 ± 0.02	3.5 ± 3.3			
	Fe-Fe_3	12	4.03 ± 0.04	9.4 ± 4.5			

[a] Scattering paths were generated using crystallographic data of bcc metallic Fe.

[b] Coordination number.

[c] Bond distance.

[d] Mean-square deviation in bond distance.

[e] Inner potential correction.

[f] Amplitude reduction factor

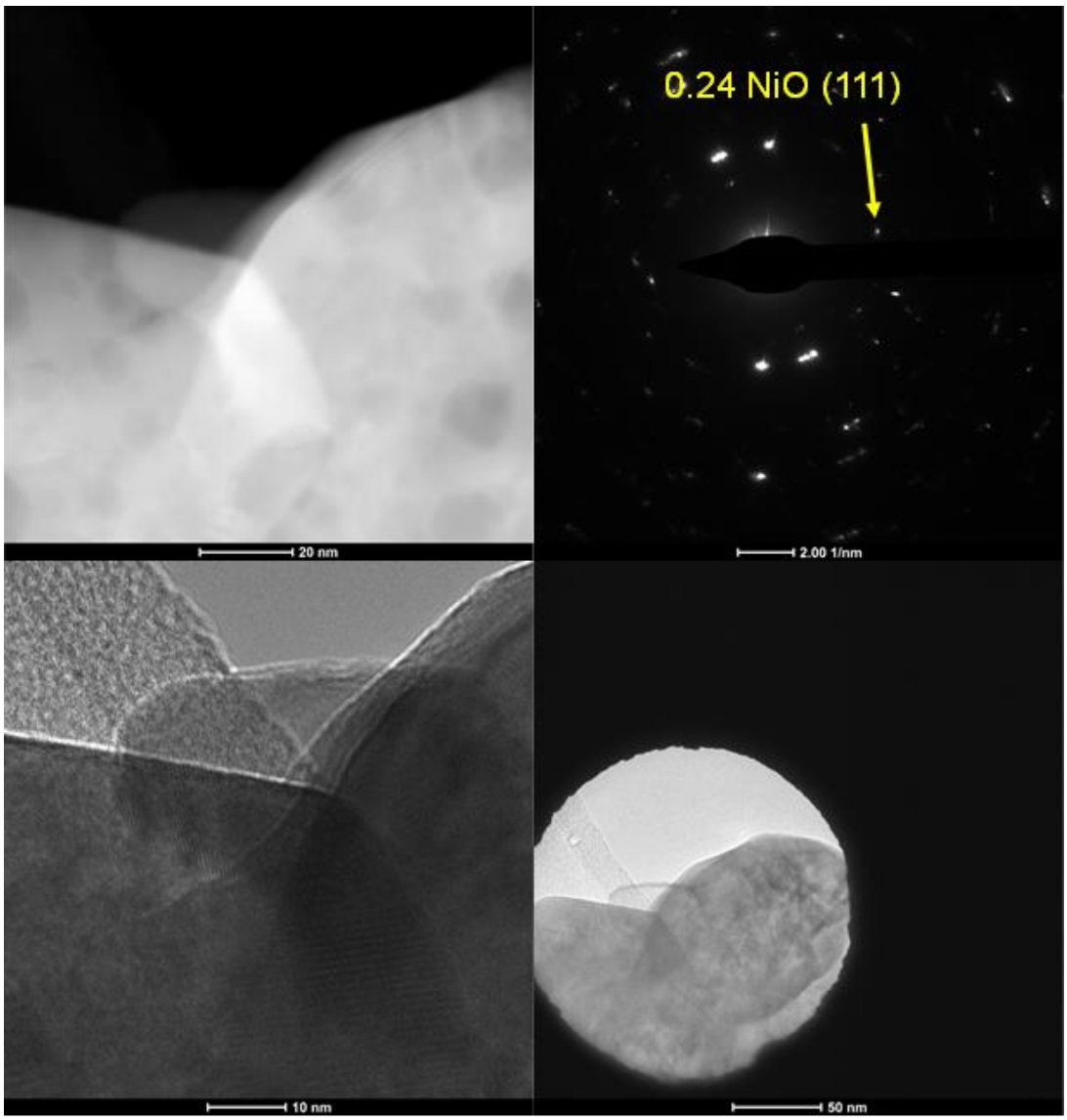

Figure S4.25. Selected area electron diffraction of select nanoparticles confirms the formation of NiO after the oxidation regenerative step on 30-minute reduced $LaFe_{0.8}Ni_{0.2}O_3$.

Table S4.5. Surface area of $LaFe_{0.8}Ni_{0.2}O_3$ as a function of the reduction time.

Reduction time	BET surface Area
10 min	4.3 m^2/g
30 min	6.5 m^2/g
60 min	7.8 m^2/g
90 min	6.2 m^2/g

4.11 References

(1) Nishihata, Y.; Mizuki, J. Self-Regeneration of a Pd-Perovskite Catalyst for Automotive Emissions Control. *Nature* **2002**, *418* (x), 164–167. https://doi.org/10.1038/nature00875.1.

(2) Tanaka, H.; Tan, I.; Uenishi, M.; Taniguchi, M.; Kimura, M.; Nishihata, Y. LaFePdO 3 Perovskite Automotive Catalyst Having a Self-Regenerative Function. *J. Alloys Compd.* **2006**, *412*, 1071–1077.

(3) Mizuki, J.; Akao, T.; Tanaka, H.; Uenishi, M.; Kimura, M.; Okamoto, T.; Hamada, N. Self-Regeneration of a Pd-Perovskite Catalyst for Automotive Emissions Control. *Nature* **2002**, *418*, 164–167. https://doi.org/10.1038/nature00875.1.

(4) Deng, J.; Cai, M.; Sun, W.; Liao, X.; Chu, W.; Zhao, X. S. Oxidative Methane Reforming with an Intelligent Catalyst: Sintering-Tolerant Supported Nickel Nanoparticles. *ChemSusChem* **2013**, *6* (11), 2061–2065.

(5) Cao, A.; Lu, R.; Veser, G. Stabilizing Metal Nanoparticles for Heterogeneous Catalysis. *Phys. Chem. Chem. Phys.* **2010**, *12* (41), 13499–13510. https://doi.org/10.1039/c0cp00729c.

(6) Neagu, D.; Tsekouras, G.; Miller, D. N.; Ménard, H.; Irvine, J. T. S. In Situ Growth of Nanoparticles through Control of Non-Stoichiometry. *Nat. Chem.* **2013**, *5* (11), 916–923. https://doi.org/10.1038/nchem.1773.

(7) Oh, T.; Rahani, E. K.; Neagu, D.; Irvine, J. T. S.; Shenoy, V. B.; Gorte, R. J.; Vohs, J. M. Evidence and Model for Strain-Driven Release of Metal Nanocatalysts from Perovskites during Exsolution. **2015**, 5106–5110. https://doi.org/10.1021/acs.jpclett.5b02292.

(8) Shah, S.; Sayono, S.; Ynzunza, J.; Pan, R.; Xu, M.; Pan, X.; Gilliard-Abdulaziz, K. L. The Effects of Stoichiometry on the Properties of Exsolved Ni-Fe Alloy Nanoparticles for Dry Methane Reforming. *AIChE J.* **2020**, *66* (12), e17078. https://doi.org/https://doi.org/10.1002/aic.17078.

(9) Lai, K. Y.; Manthiram, A. Evolution of Exsolved Nanoparticles on a Perovskite Oxide Surface during a Redox Process. *Chem. Mater.* **2018**, *30* (8), 2838–2847. https://doi.org/10.1021/acs.chemmater.8b01029.

(10) Lai, K.; Manthiram, A. Self-Regenerating Co − Fe Nanoparticles on Perovskite Oxides as a Hydrocarbon Fuel Oxidation Catalyst in Solid Oxide Fuel Cells. *Chem. Mater.* **2018**, *30* (8), 2515–2525.

(11) Shah, S.; Xu, M.; Pan, X.; Gilliard-Abdulaziz, K. L. Exsolution of Embedded Ni–Fe–Co Nanoparticles: Implications for Dry Reforming of Methane. *ACS Appl. Nano Mater.* **2021**, *4* (8), 8626–8636. https://doi.org/10.1021/acsanm.1c02268.

(12) Arora, S.; Prasad, R. An Overview on Dry Reforming of Methane: Strategies to Reduce Carbonaceous Deactivation of Catalysts. *RSC Adv.* **2016**, *6*, 108668–108688. https://doi.org/10.1039/c6ra20450c.

(13) Wei, Z.; Sun, J.; Li, Y.; Datye, A. K.; Wang, Y. Bimetallic Catalysts for Hydrogen Generation. *Chem. Soc. Rev.* **2012**, *41* (24), 7994–8008. https://doi.org/10.1039/c2cs35201j.

(14) Bian, Z.; Das, S.; Wai, M. H.; Hongmanorom, P.; Kawi, S. A Review on Bimetallic Ni-Based Catalysts for CO2 Reforming of Methane. *ChemPhysChem* **2017**, *18* (22), 3117–3134. https://doi.org/10.1002/cphc.201700529.

(15) Kim, S. M.; Abdala, P. M.; Margossian, T.; Hosseini, D.; Foppa, L.; Armutlulu, A.; Van Beek, W.; Comas-Vives, A.; Copéret, C.; Müller, C. Cooperativity and Dynamics Increase the Performance of NiFe Dry Reforming Catalysts. *J. Am. Chem. Soc.* **2017**, *139* (5), 1937–1949. https://doi.org/10.1021/jacs.6b11487.

(16) Margossian, T.; Larmier, K.; Kim, S. M.; Krumeich, F.; Müller, C.; Copéret, C. Supported Bimetallic NiFe Nanoparticles through Colloid Synthesis for Improved Dry Reforming Performance. *ACS Catal.* **2017**, *7* (10), 6942–6948. https://doi.org/10.1021/acscatal.7b02091.

(17) Zhang, J.; Wang, H.; Dalai, A. K. Development of Stable Bimetallic Catalysts for Carbon Dioxide Reforming of Methane. *J. Catal.* **2007**, *249* (2), 300–310. https://doi.org/10.1016/j.jcat.2007.05.004.

(18) Tsoukalou, A.; Imtiaz, Q.; Kim, S. M.; Abdala, P. M.; Yoon, S.; Müller, C. R. Dry-Reforming of Methane over Bimetallic Ni–M/La2O3 (M = Co, Fe): The Effect of the Rate of La2O2CO3 Formation and Phase Stability on the Catalytic Activity and Stability. *J. Catal.* **2016**, *343*, 208–214. https://doi.org/10.1016/j.jcat.2016.03.018.

(19) Zhao, B.; Yan, B.; Yao, S.; Xie, Z.; Wu, Q.; Ran, R.; Weng, D.; Zhang, C.; Chen, J. G. LaFe0.9Ni0.1O3perovskite Catalyst with Enhanced Activity and Coke-Resistance for Dry Reforming of Ethane. *J. Catal.* **2018**, *358*, 168–178. https://doi.org/10.1016/j.jcat.2017.12.012.

(20) Wang, L.; Li, D.; Koike, M.; Koso, S.; Nakagawa, Y.; Xu, Y.; Tomishige, K. Catalytic Performance and Characterization of Ni-Fe Catalysts for the Steam Reforming of Tar from Biomass Pyrolysis to Synthesis Gas. *Appl. Catal. A Gen.* **2011**, *392* (1–2), 248–255. https://doi.org/10.1016/j.apcata.2010.11.013.

(21) Theofanidis, S. A.; Galvita, V. V.; Poelman, H.; Marin, G. B. Enhanced Carbon-Resistant Dry Reforming Fe-Ni Catalyst: Role of Fe. *ACS Catal.* **2015**, *5* (5), 3028–3039. https://doi.org/10.1021/acscatal.5b00357.

(22) Theofanidis, S. A.; Galvita, V. V.; Sabbe, M.; Poelman, H.; Detavernier, C.; Marin, G. B. Controlling the Stability of a Fe–Ni Reforming Catalyst: Structural Organization of the Active Components. *Appl. Catal. B Environ.* **2017**, *209*, 405–416. https://doi.org/10.1016/j.apcatb.2017.03.025.

(23) Labhasetwar, N.; Saravanan, G.; Kumar Megarajan, S.; Manwar, N.; Khobragade, R.; Doggali, P.; Grasset, F. Perovskite-Type Catalytic Materials for Environmental Applications. *Sci. Technol. Adv. Mater.* **2015**, *16* (3), 1–13. https://doi.org/10.1088/1468-6996/16/3/036002.

(24) Bare, S. R.; Yang, N.; Kelly, S. D.; Mickelson, G. E.; Modica, F. S. Design and Operation of a High Pressure Reaction Cell for in Situ X-Ray Absorption Spectroscopy. *Catal. Today* **2007**, *126* (1–2), 18–26.

(25) Ravel, B.; Newville, M. ATHENA, ARTEMIS, HEPHAESTUS: Data Analysis for X-Ray Absorption Spectroscopy Using IFEFFIT. *J. Synchrotron Radiat.* **2005**, *12* (4), 537–541. https://doi.org/10.1107/S0909049505012719.

(26) Van Ravenhorst, I. K.; Hoffman, A. S.; Vogt, C.; Boubnov, A.; Patra, N.; Oord, R.; Akatay, C.; Meirer, F.; Bare, S. R.; Weckhuysen, B. M. On the Cobalt Carbide Formation in a Co/TiO2Fischer-Tropsch Synthesis Catalyst as Studied by High-Pressure, Long-Term Operando X-Ray Absorption and Diffraction. *ACS Catal.* **2021**, *11* (5), 2956–2967. https://doi.org/10.1021/acscatal.0c04695.

(27) Vogt, C.; Meirer, F.; Monai, M.; Groeneveld, E.; Ferri, D.; van Santen, R. A.; Nachtegaal, M.; Unocic, R. R.; Frenkel, A. I.; Weckhuysen, B. M. Dynamic Restructuring of Supported Metal Nanoparticles and Its Implications for Structure Insensitive Catalysis. *Nat. Commun.* **2021**, *12* (1), 1–10. https://doi.org/10.1038/s41467-021-27474-3.

(28) Steiger, P.; Delmelle, R.; Foppiano, D.; Holzer, L.; Heel, A. Structural Reversibility and Nickel Particle Stability in Lanthanum Iron Nickel Perovskite-Type Catalysts. **2017**, 2505–2517. https://doi.org/10.1002/cssc.201700358.

(29) Tsekouras, G.; Neagu, D.; Irvine, J. T. S. Step-Change in High Temperature Steam Electrolysis Performance of Perovskite Oxide Cathodes with Exsolution of B-Site Dopants. *Energy Environ. Sci.* **2013**, *6* (1), 256–266.

(30) Marrocchelli, D.; Perry, N. H.; Bishop, S. R. Understanding Chemical Expansion in Perovskite-Structured Oxides. *Phys. Chem. Chem. Phys.* **2015**, *17* (15), 10028–10039. https://doi.org/10.1039/c4cp05885b.

(31) Asoro, M. A.; Ferreira, P. J.; Kovar, D. In Situ Transmission Electron Microscopy and Scanning Transmission Electron Microscopy Studies of Sintering of Ag and Pt Nanoparticles. *Acta Mater.* **2014**, *81*, 173–183.

(32) Levitz, P.; Crespin, M.; Gatineau, L. Reduced Forms of LaNiO$_3$ Perovskite. *J. Chem. SOC., Faraday Trans. 2* **1983**, *79*, 1195–1203.

(33) Moriga, T.; Kikkawa, S.; Takahashi, M.; Kana-Maru, F.; Nakabayashi, I. Xafs Study on Reduction Process of Pauli-Paramagnetic Lanio3 to Antiferromagnetic Lajnio3. *Jpn. J. Appl. Phys.* **1993**, *32*, 764–766. https://doi.org/10.7567/JJAPS.32S2.764.

(34) Oemar, U.; Ang, P. S.; Hidajat, K.; Kawi, S. Promotional Effect of Fe on Perovskite LaNixFe 1-XO3 Catalyst for Hydrogen Production via Steam Reforming of Toluene. *Int. J. Hydrogen Energy* **2013**, *38* (14), 5525–5534. https://doi.org/10.1016/j.ijhydene.2013.02.083.

(35) Provendier, H.; Petit, C.; Estournès, C.; Libs, S.; Kiennemann, A. Stabilisation of Active Nickel Catalysts in Partial Oxidation of Methane to Synthesis Gas by Iron Addition. *Appl. Catal. A Gen.* **1999**, *180* (1–2), 163–173. https://doi.org/10.1016/S0926-860X(98)00343-3.

(36) Steiger, P.; Delmelle, R.; Foppiano, D.; Holzer, L.; Heel, A.; Nachtegaal, M.; Kröcher, O.; Ferri, D. Structural Reversibility and Nickel Particle Stability in Lanthanum Iron Nickel Perovskite-Type Catalysts. *ChemSusChem* **2017**, *10* (11), 2505–2517. https://doi.org/10.1002/cssc.201700358.

(37) Torchio, R.; Boccato, S.; Miozzi, F.; Rosa, A. D.; Ishimatsu, N.; Kantor, I.; Sévelin-Radiguet, N.; Briggs, R.; Meneghini, C.; Irifune, T.; Morard, G. Melting Curve and Phase Relations of Fe-Ni Alloys: Implications for the Earth's Core Composition. *Geophys. Res. Lett.* **2020**, *47* (14), 1–7. https://doi.org/10.1029/2020GL088169.

(38) Bi, Q.; Wang, X.; Gu, F.; Du, X.; Bao, H.; Yin, G.; Liu, J.; Huang, F. Prominent Electron Penetration through Ultrathin Graphene Layer from FeNi Alloy for Efficient Reduction of CO2 to CO. *ChemSusChem* **2017**, *10* (15), 3044–3048.

(39) Nady, N.; Salem, N.; Mohamed, M. A. A.; Kandil, S. H. Iron-Nickel Alloy with Starfish-like Shape and Its Unique Magnetic Properties: Effect of Reaction Volume and Metal Concentration on the Synthesized Alloy. *Nanomaterials* **2021**, *11* (11). https://doi.org/10.3390/nano11113034.

(40) Kadziołka-Gaweł, M.; Zarek, W.; Popiel, E.; Chrobak, A. The Crystal Structure and Magnetic Properties of Selected Fcc FeNi and Fe40Ni40B20 Alloys. *Acta Phys. Pol. A* **2010**, *117* (2), 412–414.

(41) Ko, J.; Kim, B. K.; Han, J. W. Density Functional Theory Study for Catalytic Activation and Dissociation of CO2 on Bimetallic Alloy Surfaces. *J. Phys. Chem. C* **2016**, *120* (6), 3438–3447. https://doi.org/10.1021/acs.jpcc.6b00221.

(42) Sorescu, M.; Xu, T.; Burnett, J. D.; Aitken, J. A. Investigation of LaFeO3 Perovskite Growth Mechanism through Mechanical Ball Milling of Lanthanum and Iron Oxides. *J. Mater. Sci.* **2011**, *46* (20), 6709–6717.

(43) Mutter, D.; Schierholz, R.; Urban, D. F.; Heuer, S. A.; Ohlerth, T.; Kungl, H.; Elsässer, C.; Eichel, R. A. Defects and Phase Formation in Non-Stoichiometric LaFeO3: A Combined Theoretical and Experimental Study. *Chem. Mater.* **2021**, *33* (24), 9473–9485. https://doi.org/10.1021/acs.chemmater.1c02106.

(44) Katz, M. B.; Zhang, S.; Duan, Y.; Wang, H.; Fang, M.; Zhang, K.; Li, B.; Graham, G. W.; Pan, X. Reversible Precipitation/Dissolution of Precious-Metal Clusters in Perovskite-Based Catalyst Materials: Bulk versus Surface Re-Dispersion. *J. Catal.* **2012**, *293*, 145–148. https://doi.org/10.1016/j.jcat.2012.06.017.

(45) Kousi, K.; Tang, C.; Metcalfe, I. S.; Neagu, D. Emergence and Future of Exsolved Materials. *Small* **2021**, *17* (21). https://doi.org/10.1002/smll.202006479.

(46) Katz, M. B.; Graham, G. W.; Duan, Y.; Liu, H.; Adamo, C.; Schlom, D. G.; Pan, X. Self-Regeneration of Pd-LaFeO 3 Catalysts: New Insight from Atomic-Resolution Electron Microscopy. *J. Am. Chem. Soc.* **2011**, *133* (45), 18090–18093.

(47) Liu, T.; Zhao, Y.; Zhang, X.; Zhang, H.; Jiang, G.; Zhao, W.; Guo, J.; Chen, F.; Yan, M.; Zhang, Y.; Wang, Y. Robust Redox-Reversible Perovskite Type Steam Electrolyser Electrode Decorated with: In Situ Exsolved Metallic Nanoparticles. *J. Mater. Chem. A* **2020**, *8* (2), 582–591. https://doi.org/10.1039/c9ta06309a.

(48) Bekheet, M. F.; Delir, P.; Nezhad, K.; Bonmassar, N.; Gili, A.; Praetz, S.; Gurlo, A.; Doran, A.; Gao, Y.; Heggen, M.; Niaei, A.; Farzi, A.; Schwarz, S.; Bernardi, J. Steering the Methane Dry Reforming Reactivity of Ni / La 2 O 3 Catalysts by Controlled In Situ Decomposition of Doped La 2 NiO 4 Precursor Structures. *ACS Catal.* **2021**, *11*, 43–59.

CHAPTER 5. COMPLEX ALLOY AND HETEROSTRUCTURE NANOPARTICLES DERIVED FROM PEROVSKITE OXIDE PRECURSORS FOR CATALYTIC DRY METHANE REFORMING

The text of this dissertation chapter, in full, is a reprint of the material as it appears in "Complex Alloy and Heterostructure Nanoparticles Derived from Perovskite Oxide for Catalytic Dry Methane Reforming" published in ACS Applied Nano Materials, 2022. The text has been modified to fit the dissertation guidelines. The co-author Dr. Kandis Leslie Gilliard-Abdul-Aziz listed in that publication directed and supervised the research which forms the basis for this dissertation chapter.

5.1. Abstract

The controllable synthesis of complex concentrated alloy nanoparticles with five elements remains challenging using conventional synthesis strategies. This article presents a general route for combining the five elements, Ni, Fe, Co, Cu, and Pd, in a nanoparticle using the exsolution mechanism from $LaFe_{0.7}Ni_{0.1}Co_{0.1}Cu_{0.05}Pd_{0.05}O_3$ perovskite oxide precursors. The perovskite precursors were reduced at 700 ºC and 900 ºC and were compared for their difference in nanoparticle size, shape, and composition. The reduction of the precursors at elevated temperatures yielded NiFeCoCuPd nanoparticles with a size-dependent phase transition from complex concentrated alloy to phase-separated heterostructures decorating the surface of the parent perovskite support. The evolution of the nanoparticle properties, including size and composition, were studied to determine the growth behavior of the multi-metallic nanoparticles. The materials were characterized with X-ray diffraction, Scanning Transmission Electron Microscopy, and Energy Dispersive X-ray Spectroscopy to elucidate the structure-function relationship between material properties and performance for the dry methane reforming reaction. The NiFeCoCuPd catalyst nanoparticles had significant conversion and selectivity to syngas formation with excellent stability, and no decline in activity was observed. Our findings indicate that smaller concentrated alloy nanoparticles (~10 nm) are more effective for methane activation than larger (> 20 nm) phase-separated nanoparticles.

5.2 Introduction

Complex concentrated alloy[1] (CCA) with multiple metals has unique physical and chemical properties for many applications, including catalysis[2–5], sensing[6,7], and energy-related applications. In catalysis, the synergy between the electronic interactions of the metals is advantageous for various electrocatalytic reactions where the CCA NPs display superior stability, selectivity, and activity compared to conventional alloys[2,8–11]. However, the intrinsic stability of CCA NPs is also beneficial for thermocatalytic applications as the alloy concentration and structure can tune the adsorption of molecules and intermediate species on the surface[4]. Nevertheless, few studies have probed the catalytic activity of CCA nanoparticles for thermocatalytic reactions[12]. The most notable studies investigated CCA NPs for ammonia oxidation[13], ammonia decomposition[14], and, most recently, CO_2 hydrogenation. We surmise that using CCAs with Ni, Fe, Pd, Cu, and Co will benefit reactions where the deactivation mechanism includes coking, sintering, or oxidation of the active component(s). Rapid deactivation due to coking and sintering is a common issue for Ni-based catalysts for the dry methane reforming (DMR) reaction, where the Ni catalyst deactivates due to a build-up of carbon deposition on the nanoparticle surface.

The combination of two or three elements has been advantageous for Ni-based catalysts for DMR, where the alloys work synergistically to activate the reactant molecules, CH_4 and CO_2, and have improved stability[15,16]. Despite the improvements, the catalysts can still deactivate due to oxidation and desegregation of the alloy metals. The interactions between elements of four or five metals afford a unique formation and

architecture that result in advanced properties, including improved selectivity. To improve catalyst resilience for DMR, we explore using CCAs consisting of Ni and Pd. This article discusses a facile synthesis strategy for the exsolution or formation of NiFeCoCuPd CCA NPs derived from $LaFe_{0.7}Ni_{0.1}Co_{0.1}Cu_{0.05}Pd_{0.05}O_3$ perovskite oxide precursors and examines their inherent performance for the DMR reaction.

The primary strategies to synthesize CCA nanoparticles involve using bulk solution synthesis[17,18], aerosol[19], microemulsion[20], and carbothermal shock[1,2]. For the carbothermal shock process, the metal precursors are heated rapidly to induce alloying of multiple elements into a solid-state solution phase and then quenched. The non-equilibrium conditions promote the formation of complex concentrated alloy nanomaterials[1]. However, controlling nucleation and growth rate for multiple elements on the supported substrate is challenging. Alternative strategies are needed to effectively control the CCA catalyst nanoparticle properties for use in thermo- and electro- catalytic applications.

Our group has developed a synthesis strategy that takes advantage of the exsolution of nanoparticles from perovskite precursors to form bi- and tri-metallic alloys[15,16]. We have used the knowledge gleaned to establish a synthesis strategy that uses the process of exsolution or nanoparticle formation from perovskite oxide precursors to form CCA NPs exsolved on the surface consisting of NiFeCoCuPd (**Figure 5.1**). Select families of perovskite oxides can serve as a platform to synthesize nanoparticles that are stabilized due to the strong adherence of exsolved nanoparticles to the parent perovskite support.

Thus, synthesizing CCA NPs through exsolution provides the beneficial property of inherently stable nanoparticles at elevated temperatures.

This article discusses a facile synthesis strategy for the synthesis of CCA nanoparticles. We chose Ni, Co, Cu, Fe, and Pd as their combination is applicable for

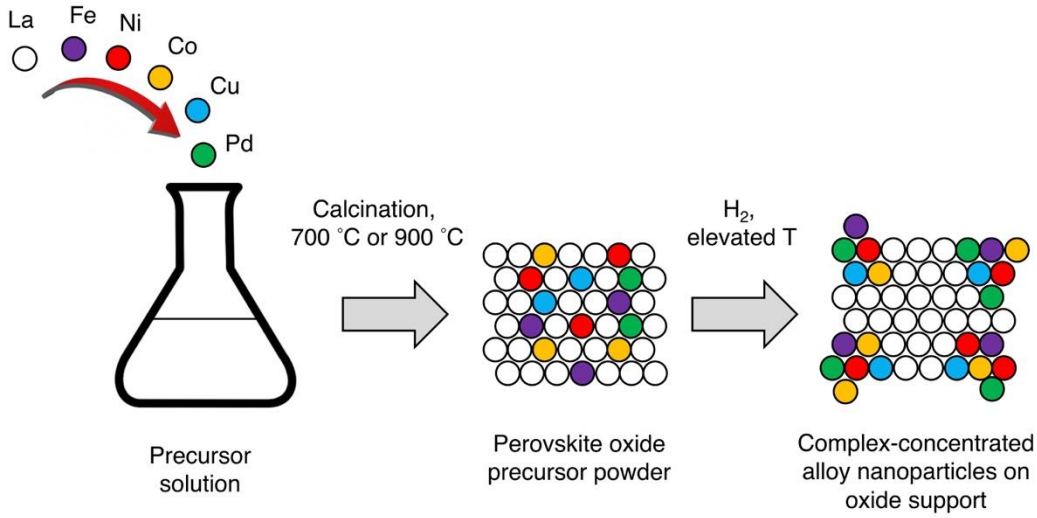

Figure 5.1. Synthesis of the CCA or multi-elemental nanoparticles using the exsolution mechanism of perovskite precursors.

DMR. The materials were analyzed using X-ray diffraction (XRD) and atomic level resolution scanning transmission electron microscopy with energy-dispersive X-ray spectroscopy (STEM-EDS). We then probed the catalytic activity, stability, and selectivity of the exposed nanoparticles for DMR using reaction studies and temperature-programmed surface reaction (TPSR).

5.3 Materials Preparation

The perovskite oxide precursors were prepared with a method similar to the citric acid sol-gel type pechini method. Nitrate salts of the constituent metals were mixed in stoichiometric ratios and dissolved in water. Citric acid (3 mol. /mol. perovskite) and

ethylene glycol butyl ether (1 mol./ mol. perovskite) were subsequently added while the solution was being stirred and heated at 60°C. The solution was dried overnight at 110 °C which resulted in the formation of a xerogel. The xerogel was ground finely in a mortar-pestle and the calcined in a muffle furnace at 800 °C for 4 hours.

The oxides were reduced in a quartz tube microreactor (HIDEN Analytical CATLAB) in 5% H_2/He, ramping up to the eventual reduction temperature (700 °C or 900 °C) and held for the desired dwell time.

5.4 Materials Characterization

Powder X-ray Diffractograms (XRD) were collected on a PANalytical Empyrean Series 2 with a step-size of 0.013° and time per step of 30 seconds and were then analyzed with HighScore software. The atomic resolution images of the samples were acquired using Scanning Transmission Electron Microscopy (STEM) on a JEOL Grand ARM300CF TEM/STEM with double spherical aberration-correctors operated at 300kV STEM High-angle annular dark-field (HAADF) imaging mode. Simultaneously, the elemental mapping via energy-dispersive X-ray spectroscopy (EDS) was collected by the large angle dual dry solid-state 100 mm^2 detectors. Gold supported holey carbon membrane grids were used as sample holder for STEM imaging to prevent any metallic signals from the support to appear in the EDS analysis. Analysis of the SEM images for particle size distribution was done using the ImageJ software[21]. Over 25 particles were analyzed for each of the samples for calculating size distribution of the nanoparticles.

5.5 Catalytic Testing

Catalytic testing for Dry Reforming of Methane over the complex concentrated alloys was conducted in the quartz tube microreactor (Hiden Analytical CATLAB), plugged by quartz wool, with the product stream analyzed with a Hiden quadrupole mass spectrometer. Prior to reaction, fresh samples of the perovskite oxide precursors were reduced in the quartz tube as described above and then cooled to room temperature. Catalytic activity was tested by ramping the temperature at 10 °C/min and then dwelling at intervals of 50 °C in an environment of 5% CH_4/ 5% CO_2/He. Stability tests were conducted after activity tests, by dwelling in the reaction mixture at 700 °C for 24 hours. Temperature Programmed Surface Reaction (TPSR) tests were carried out by subjecting fresh reduced samples to a ramp from room temperature to 700 °C at 10 °C/min in the reaction mixture. Temperature programmed oxidation (TPO) experiments were conducted after aging tests with a gas mixture of 20%O_2/He to a ramp from room temperature to 800 °C at 10 °C/min. The evolution of CO_2 and CO was used to determine the quantity and qualitative nature of carbon species formed on the catalyst surface during aging.

The mass spectrometer was calibrated by measuring relative sensitivities of each gas relative to the carrier helium gas. Composition of the product stream was determined by normalizing MS responses with known relative sensitivities. Pressure drop was determined to be minimal by comparing experiments with gas flow with and without catalysts. Conversion of methane and carbon dioxide were calculated as:

$$x_{CH_4} = \left(1 - \frac{volume\ of\ CH_4\ in\ product\ stream}{volume\ of\ CH_4\ in\ inlet\ stream}\right) \times 100\%$$

$$x_{CO_2} = \left(1 - \frac{volume\ of\ CO_2\ in\ product\ stream}{volume\ of\ CO_2\ in\ inlet\ stream}\right) \times 100\%$$

5.6 Results and Discussion

Figure 5.1 shows the schematic for the formation of the NiFeCoCuPd nanoparticles using exsolution from the doped $LaFeO_3$-based precursors. The process first involves

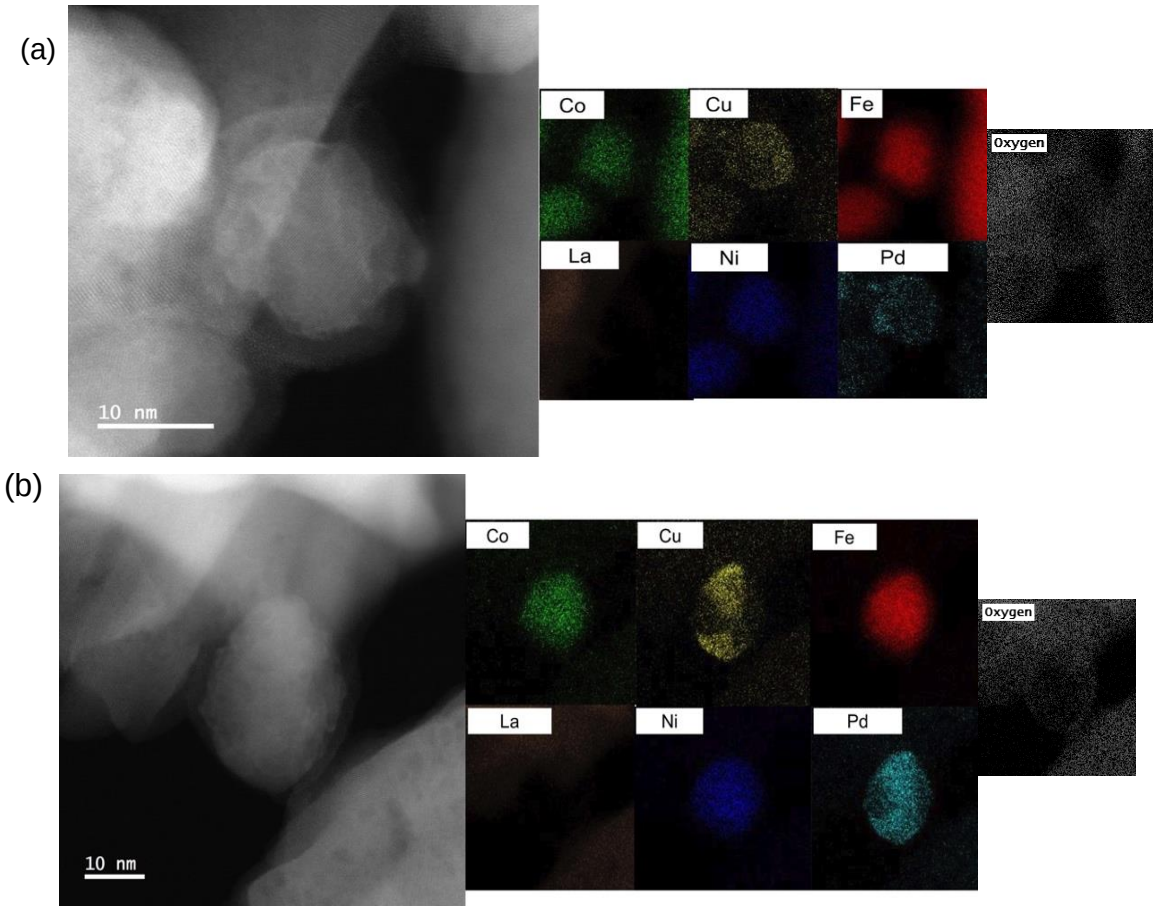

Figure 5.2. STEM-HAADF and EDS maps of the LaFeNiCoCuPd perovskite precursor after reduction at (a) 700°C for 2 hours and (b) reduction at 900°C for 2 hours.

synthesizing bulk $LaFe_{0.7}Ni_{0.1}Co_{0.1}Cu_{0.05}Pd_{0.05}O_3$ material where the Ni, Co, Cu, Fe, and Pd are incorporated in the perovskite oxide lattice. The solution is dried to form a xerogel and calcined at elevated temperatures to form a mixed-oxide powder. Following the powder synthesis using the sol-gel method, the exsolution of the nanoparticles occurs under a reduction environment where it is assumed the nanoparticles are formed as a function of the reduction potential. We reduced the samples to 5%H_2/He at 700 ºC (NiFeCoCuPd-700) and 900 ºC (NiFeCoCuPd-900) to change the composition, size, and dispersion of the nanoparticles. The reduction temperature influences the extent to which constituent metals in the perovskite reduce and their relative rates of diffusion, thus altering their composition. As observed in our previous study, reduction at a higher temperature led to the enrichment of Fe in Ni-Co-Fe nanoparticles and the formation of larger nanoparticles[16].

Figure S5.1 shows the XRD diffraction spectra of the as-prepared materials, showing the primary diffraction peak of the parent perovskite oxide, $LaFeO_3$. The XRD pattern for the as-prepared materials confirms that the dopant metals are most likely substituted in the lattice or exist as interstitials. Additionally, there are no impurity oxides prevalent in the materials before reduction. The XRD spectra after reduction indicate partial dissolution of $LaFeO_3$ to La_2O_3. **Figure 5.2** shows the STEM-HAADF EDS images of the multi-element nanoparticles at 700ºC and 900ºC. It can be observed from the images that the formed nanoparticles are spherical and supported on a La_2O_3-$LaFeO_3$ substrate, as corroborated by XRD.

The reduction temperature controls the size and composition of the exsolved complex concentrated alloy nanoparticles. The STEM-HAADF EDS images suggest that the nanoparticles formed at 700 ºC consist of multiple elements of Ni, Cu, Pd, Co, and Fe and that the main phase of the particle is metallic, containing all five metals. Interestingly, a closer inspection of the nanoparticles after reduction at 900 ºC shows that the nanoparticles are inhomogeneous, where Cu and Pd prefer to overlap and Ni, Fe, and Co prefer to form a solid solution within the nanoparticle (**Figure S5.2**). The NiFeCuCoPd-900 structure adopts a phase-separated heterostructure which could be attributed to the larger average size of the nanoparticles formed compared to NiFeCuCoPd-700. The average nanoparticle size for 900 ºC was 29 ± 9 nm. The size distribution of the nanoparticles is shown in **Figure S5.3**. The composition measured by EDS at 700 ºC is Ni 12.7 at.%, Fe 56.8 at.%, Co 9.4 at%, Cu at.4.2%,%, and Pd 5.2 at%. The average size calculated from the average of the nanoparticle sizes was 12 ± 5 nm. The composition for the 900 ºC nanoparticles is Ni 10.1.%, Fe 69.8 at.%, Co 11.9 at.%, Cu 3.1 at.%,.%, and Pd 3.1 at%. (**Figures S5.4-S5.6**). The composition of the nanoparticles becomes more Fe-rich as the reduction temperature increases. This corroborates prior findings in which the Fe exsolution is pre-dominant at elevated temperatures. The bulk exsolution also indicates a trend where nanoparticles can transition from CCA single-phase to a phase-separated heterostructure at higher reduction temperatures.

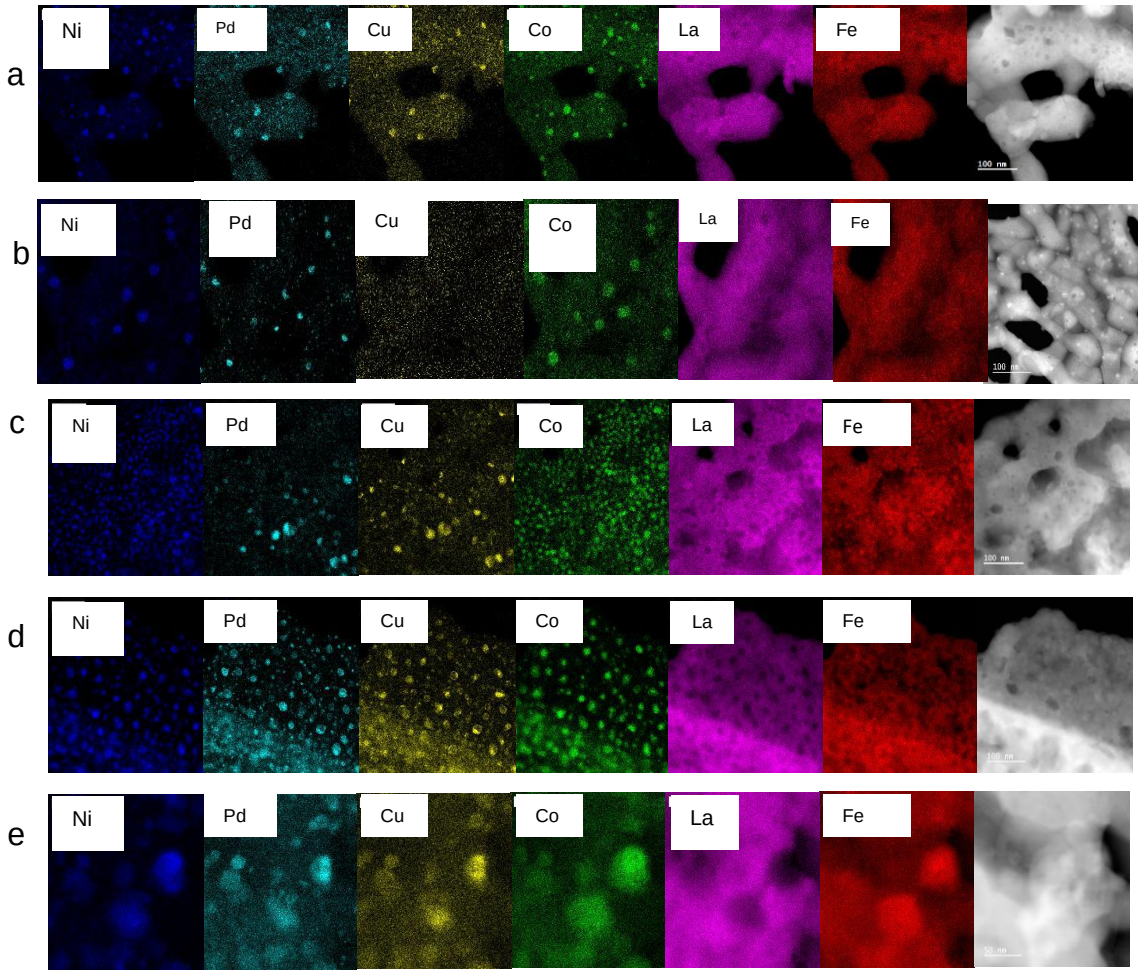

Figure 5.3. STEM-EDS mapping of LaFeCoCuPdO3 after reduction at 700°C for (a) 0 min (b) 10 min (c) 30 min (d) 60 min and (e) 120 min. Scale bars are 100 nm.

We evaluated the exsolution mechanism as a function of the reduction dwell time to determine the alloying behavior and nanoparticle growth mechanism from the $LaFe_{0.7}Ni_{0.1}Co_{0.1}Cu_{0.05}Pd_{0.05}O_3$ precursor. We first carried out reductive heating in 5%H_2/He from room temperature to 700 °C and set the dwell time to 0 minutes, 10 minutes, 30 minutes, 60 minutes, and 120 minutes (**Figure 5.3, Figures S5.5, S5.8-5.12**). The samples were subsequently imaged using STEM- HAADF and EDS. As shown in **Figure 5.3**, at 0 minutes of dwell time, the nanoparticle system has dispersed nanoparticles of NiPdCoCu with an average nanoparticle size of 18 ± 5 nm. After 30

minutes of dwell, more NiPdCoCu nanoparticles are formed with an average size of 17 ± 12 nm. After 60 minutes, the size distribution of the NiPdCuCo nanoparticles becomes noticeably larger, indicating a possible sintering mechanism. **Figure S5.13** shows a comparative view of the nanoparticles as a function of the reduction time at 30 minutes, 60 minutes, and 120 minutes. Analysis of the EDS indicates that after a reduction of 60 minutes, the nanoparticles show a transition into a phase-separated heterostructure, suggesting that the transformation from single-phase CCA to a phase-separated heterostructure is related to the size of the nanoparticles. The elements segregate into a distinct heterostructure where the Ni, Co, and Fe form a single phase separate from Pd and Cu. We surmise that the phase of the exsolved NiFeCoCuPd catalysts is size-dependent and is correlated with the reduction temperature and dwell time. After 120 minutes dwell, we start to see noticeable Fe exsolution within the nanoparticles of NiFeCuCoPd with a nanoparticle size of 21 ± 9 nm. Localized clusters of B-site metals are visible alongside dispersed metals in the EDS images. These represent the nanoparticles formed upon exsolution from the perovskite. As the perovskite-based sample is reduced for a longer duration, more B-site metals are reduced, leading to nanoparticle growth.

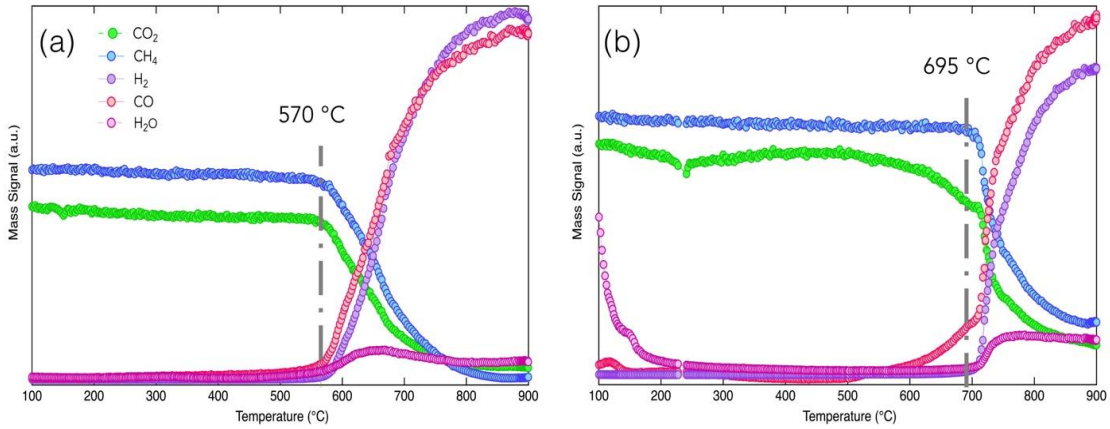

Figure 5.4. Temperature programmed surface reaction of (a) NiFeCoCuPd-700 reduced for 2 hours and (b) NiFeCoCuPd-900 reduced for 2 hours.

The unique segregation of multi-constituent elements from solid-phase alloy to multimetallic heterostructure nanoparticles has been documented elsewhere. Cui et al. prepared multi-principal elemental intermetallic nanoparticles containing Pt, Pd, Au, Fe, Co, Ni, Cu, and Sn. The STEM-HAADF images confirmed that the nanoparticles formed are initially disordered solid-solution alloys that transition to multi-principal elemental intermetallic nanoparticles after Joule heating. The study also indicated a size dependence on the phase of the nanoparticles where smaller nanoparticles (~5 nm) exhibited either partial or full ordered alloy nanoparticles. Nanoparticles larger than ~60 nm formed phase-separated heterostructures. The study theorized that the phase transition was attributed to the differences in the surface energy and surface area. We surmise that a higher reduction temperature or longer reduction time increases the size of the exsolved nanoparticles and increases the surface energy (decreases the surface area), driving the phase transition from single-phase CCA to phase-separated heterostructures.

We probed the catalyst performance of NiFeCoCuPd-700 and NiFeCoCuPd-900 for DMR and their ability to activate CH_4. A mixture of CH_4 and CO_2 was passed through the fixed bed of the NiFeCoCuPd-700 and NiFeCoCuPd-900 catalysts, respectively. The TPSR analysis was helpful because it could probe the activation of CO_2 and CH_4 and track the syngas formed. Our initial assessment of the efficiency of methane activation was conducted using the temperature-programmed surface reaction measurement, as shown in **Figure 5.4**. The NiFeCoCuPd-700 reaction had a superior performance for activating methane at ~570ºC versus 695ºC for NiFeCoCuPd- 900. The

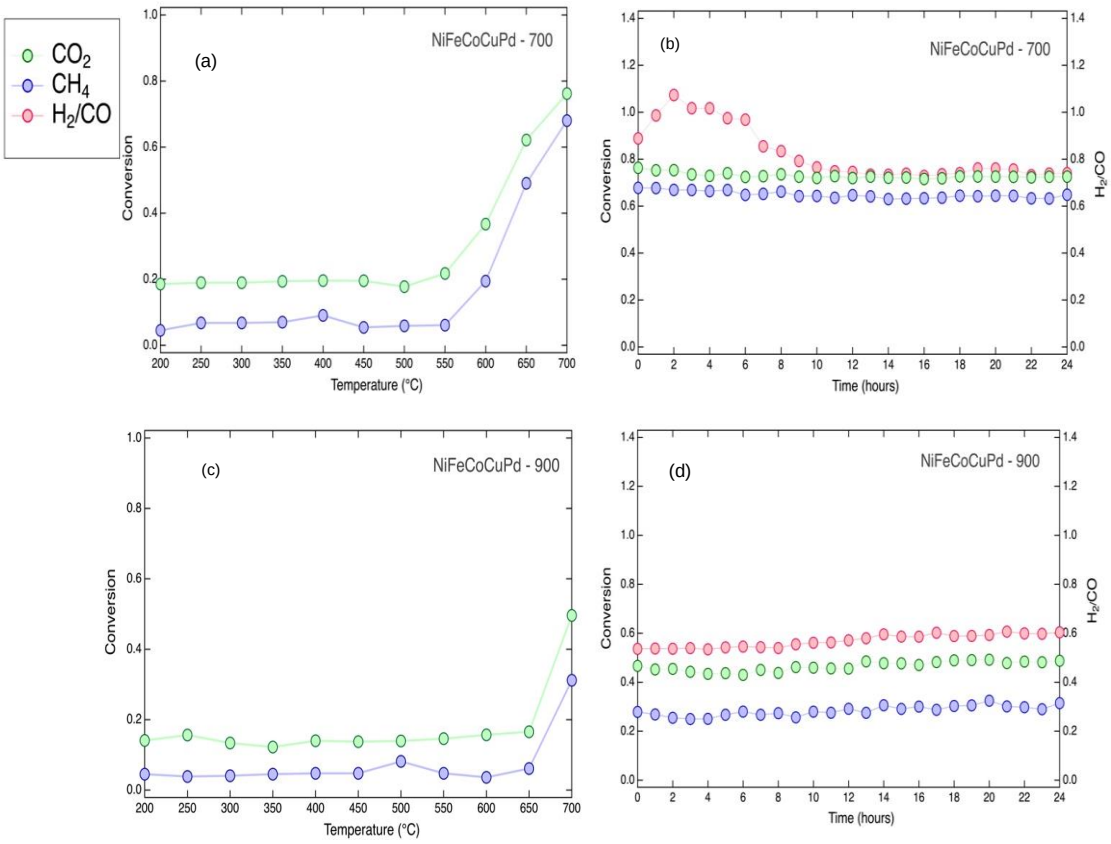

Figure 5.5. The catalytic stability and activity of NiFeCoCuPd-700 reduced for 2 hours (a) and (b) and NiFeCoCuPd-900 reduced for 2 hours (c) and (d).

methane activation energy for NiFeCoCuPd-700 was 128.1 kJ/mol K and for NiFeCoCuPd-900 was 243 kJ/mol K. The corresponding activation energies for CO_2 activation energies are 58.3 kJ/mol. K and 158.6 kJ/mol. K, respectively. The improved activation performance of NiFeCoCuPd-700 activation efficiency for both methane and carbon dioxide could be attributed to the relative size differences in the nanoparticles (i.e., smaller surface area) and the higher concentration of the active components for C-H activation (Ni, Pd) compared to NiFeCoCuPd-900. The activation energies for CH_4 and CO_2 activation over various Ni and Pd catalysts have been reported to be ~70-100

kJ/mol[21,22]. The as-prepared NiFeCoCuPd-700 has a considerably lower barrier for CO_2 and CH_4 activation compared to reported values. In contrast, NiFeCoCuPd-900 has a noticeably higher barrier than NiFeCoCuPd-700 and catalysts in literature. Both catalysts show remarkably low activation energies after aging for 24 hours (discussed further in this article). For NiFeCoCuPd-700, syngas production is initially CO-rich at low temperatures and then becomes hydrogen-rich at elevated temperatures. **Figure 5.4b** shows that NiFeCoCuPd-900 forms CO-rich syngas at all reaction temperatures. They show that the composition differences due to the reduction temperature can control the activity and selectivity of the reaction.

We also probed the catalytic activity, stability, and selectivity of these nanoparticles for the DRM (**Figure 5.5**). For instance, the NiFeCoCuPd-700 had superior performance than NiFeCoCuPd-900, where the CO_2 and CH_4 conversion was (~68%, 64%) compared to (42%, 38%). We then probed for catalytic stability as the nanoparticle deactivation can occur due to coking, partial oxidation, or dealloying. We investigated the catalytic stability for the exsolved nanoparticles to maintain activity and selectivity on the stream of the nanoparticles and observed that the CH_4 and CO_2 conversions maintained steady catalytic activity for 24 hours. Initially, the H_2/CO ratio for NiFeCoCuPd-700 had some variability during the initial 8-hour period until reaching a steady state of ~0.8 for the remaining 16 hours. This variability could have been attributed to the composition of the nanoparticles reaching a steady state in the reaction environment. For NiFeCoCuPd-900, the H_2/CO ratio reaches a steady state of ~0.6 after the first couple of hours.

The synergy of the metals for both catalysts improved the resilience to coking and sintering of the nanoparticles for DMR. Temperature programmed oxidation (TPO) was performed on the spent catalysts to measure the evolution of CO_2 and CO from the combustion of coke (**Figure S5.14**). The amount of coke formed on the catalyst after aging was 0.06 mg/100 mg of catalyst for the NiFeCoCuPd-700 and 1.45 mg for NiFeCoCuPd-900. Where NiFeCoCuPd-900 had a noticeably sizeable CO_2 peak observed around ~550°C. We surmise that the greater amount of coke deposition is attributed to the larger size of nanoparticles exhibited by NiFeCoCuPd-900 compared to the NiFeCoCuPd-700 samples. The NiFeCoCuPd-700 sample shows better activity towards DRM despite the aging process, with 75% conversion of CH_4 seen at 700 °C compared to 68% seen in the sample before aging. The aged sample showed activation energies of 45.8 kJ/mol and 34.7 kJ/mol for CH_4 and CO_2, respectively.

The structure-function of the exsolved nanoparticles as a function of dwell time was analyzed using temperature-programmed surface reactions to ascertain reactivity to the composition and size of the nanoparticles (**S5.15,** and **Table S5.1**). Comparing samples with different reduction dwell times, the 10-minute reduced sample had the highest activity with a CH_4 rate of 5.96 μmol/s.g. cat. As the dwell time reduction increases, the nanoparticle's activity declines. Probing the nanoparticles with EDS shows that the composition of Fe increases with dwell time, which we surmise causes a decline in methane activation. It has been observed in Ni-Fe catalyst systems that beyond an optimal point, a higher composition of Fe in the catalysts can cause a decline in catalytic activity while improving coke-resistance[23,24]. The light-off temperatures for the samples

in increasing order of reduction dwell time are 477 ºC, 481ºC, 509 ºC, 543 ºC, and 583 ºC. The results indicate that larger nanoparticles with phase separation are less efficient in activating methane than smaller single-phase CCA nanoparticles. XRD of NiFeCoCuPd-700 after aging in DRM conditions for 24 hours (**Figure S5.16**) shows a structure similar to $LaFeO_3$. This is similar to our observations with Ni-Co doped LaFeO3 where the XRD after aging also resembled the perovskite structure[16]. The peak corresponding to the Ni-Fe alloy at 44.5° was also suppressed. This is because exsolution can proceed in forward and backward directions in the redox environment of the DRM reaction and the nanoparticle size and composition then reflect a different equilibrium.

In our previous work using perovskite precursors to synthesize alloy nanoparticle catalysts, we observed that Ni-Fe nanoparticles showed a considerable decline in activity over long times on stream of DRM. In comparison, the NiFeCoCuPd nanoparticles in this study show no decrease in activity due to stabilization provided by the interaction of the various metals, whether in a single-phase or heterostructure configuration. Furthermore, the NiFeCoCuPd NPs have a lower light-off temperature for both CO_2 and CH_4 when compared to the trimetallic Ni-Co-Fe catalysts discussed in prior work. The introduction of Pd enhances the reducibility of Ni and its activity towards methane activation[25]. The introduction of Cu improves oxygen mobility and plays a crucial role in activating C-H bonds[26]. For example, Han et al. showed that up to an optimal level, the presence of Cu in Ni nanoparticles could improve CO_2 activation during dry methane reforming[26]. We presume that the smaller single-phase CCA has improved performance due to the synergistic interaction of Ni with Pd and Cu and to the larger surface area. In contrast, the

larger NiFeCoCuPd have minimal interaction of Cu and Pd with Ni limiting the synergistic interaction.

In this study, we have demonstrated the exsolution mediated synthesis of NiFeCoCuPd nanoparticles using perovskite oxide precursors. The exsolution process exhibits a size dependence for the pre-dominant phase, where a shorter reduction time or lower reduction temperature promotes a single-phase CCA configuration. In contrast, higher reduction temperatures and longer reduction times promote a phase-separated heterostructure with two distinct domains. The reduction temperature also acts as a control for imparting nanoparticles with different properties to activate CH_4. The positive effects of highly dispersed active nanoparticles on the oxide matrix during the reaction had superior catalytic stability where DRM activity was steady for up to 24 hours. We believe that the exsolution of perovskites is a facile and flexible method for synthesizing CCA or multi-elemental nanoparticles with a possible control on the pre-dominant phase for the exsolved nanoparticles.

5.7 Acknowledgments

This research was partially supported by the National Science Foundation Materials Research Science and Engineering Center program through the UC Irvine Center for Complex and Active Materials (DMR-2011967). The authors also acknowledge the use of facilities and instrumentation at the UC Irvine Materials Research Institute (IMRI) supported in part by the National Science Foundation Materials Research Science and Engineering Center program through the UC Irvine Center for Complex and Active

Materials (DMR-2011967). I would also like to acknowledge the contribution of Jacob Graves who assisted with catalyst synthesis as part of the project.

5.8. Supplementary Information

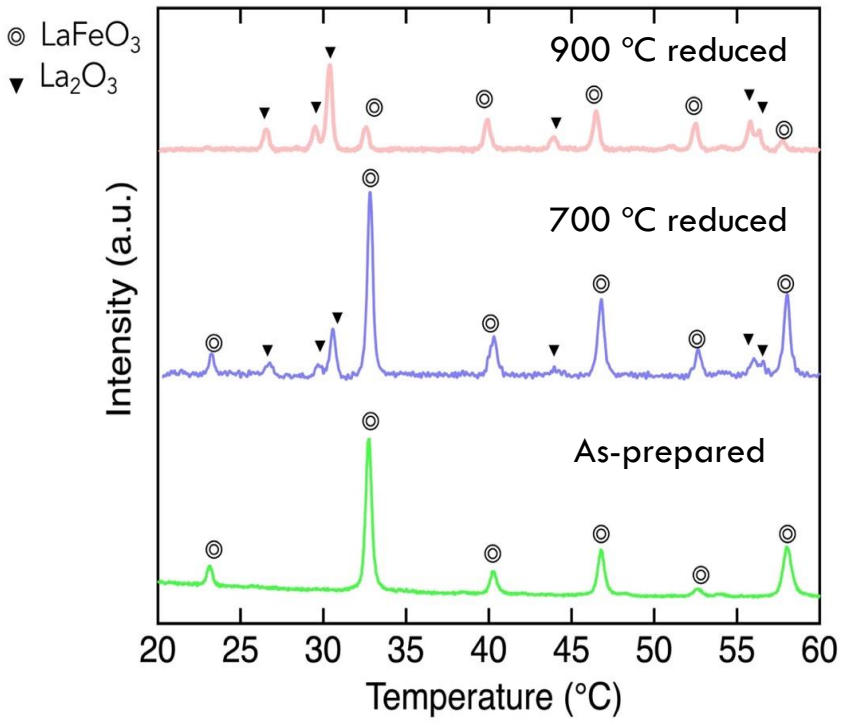

Figure S5.3. The XRD diffraction pattern of the 900 ºC reduced (top), 700 ºC reduced (middle) and as-prepared (bottom).

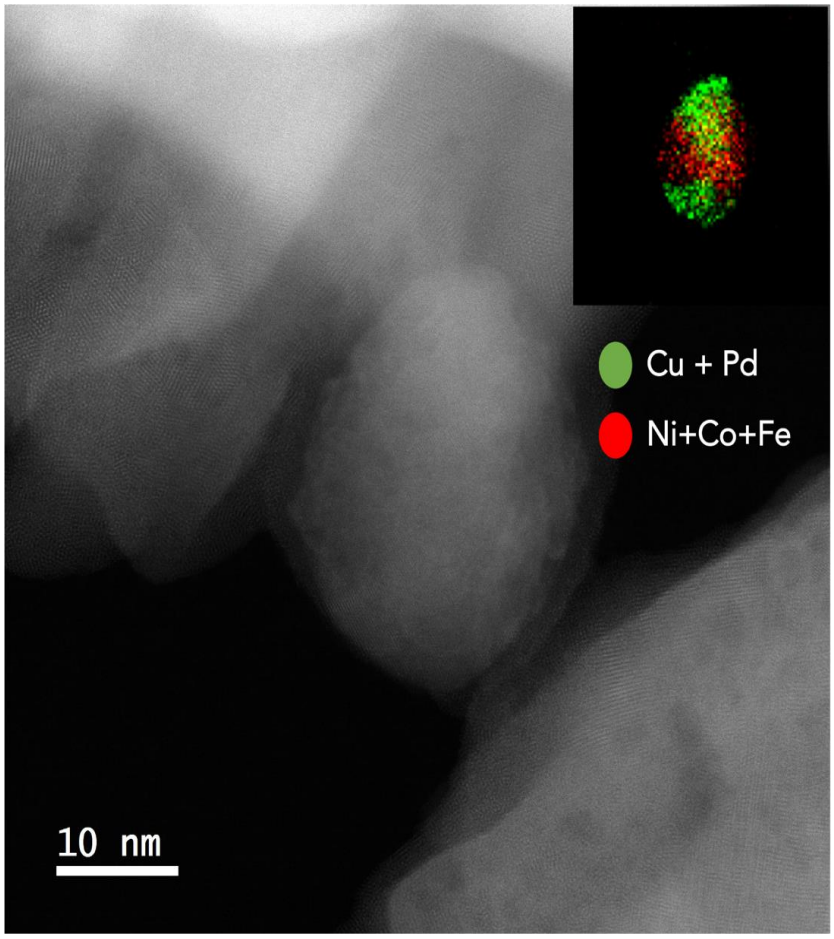

Figure S5.4. Composition of the NiFeCoCuPd-900 with EDS mapping shows that the overlap of the elements have preferable orientation with the nanoparticle. Cu and Pd prefer to overlap as Ni, Co and Fe prefer to form a solid solution.

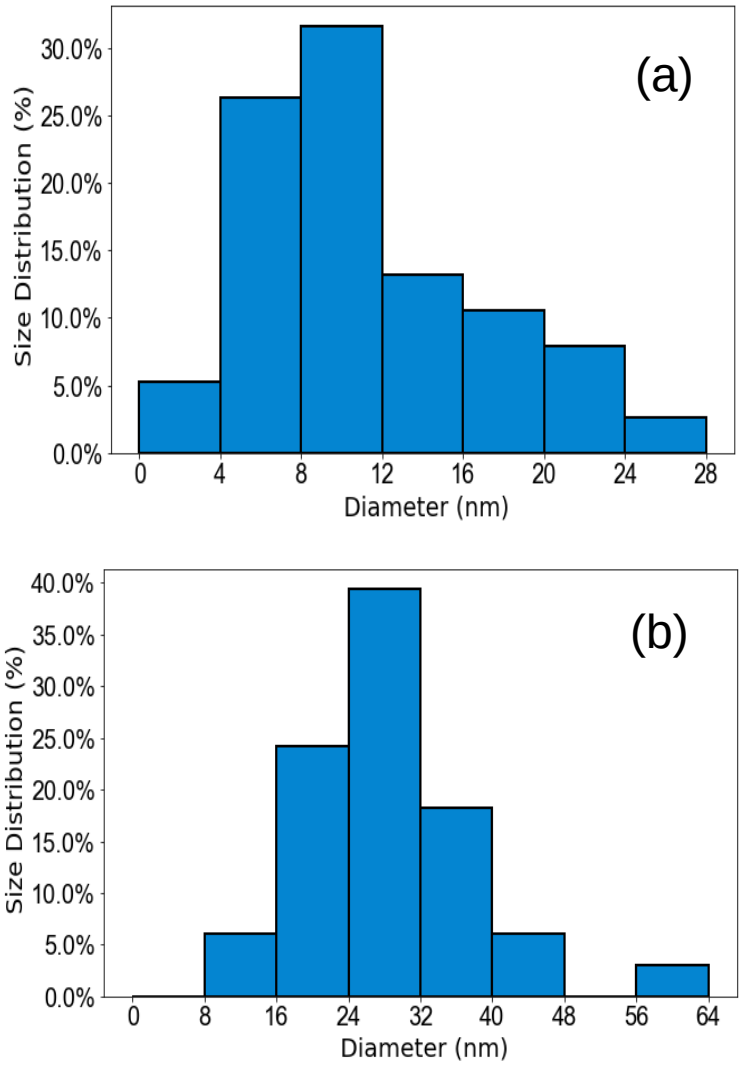

Figure S5.3. Histogram of size distribution of nanoparticles exsolved from (a) NiFeCoCuPd-700 and (b) NiFeCoCuPd-900.

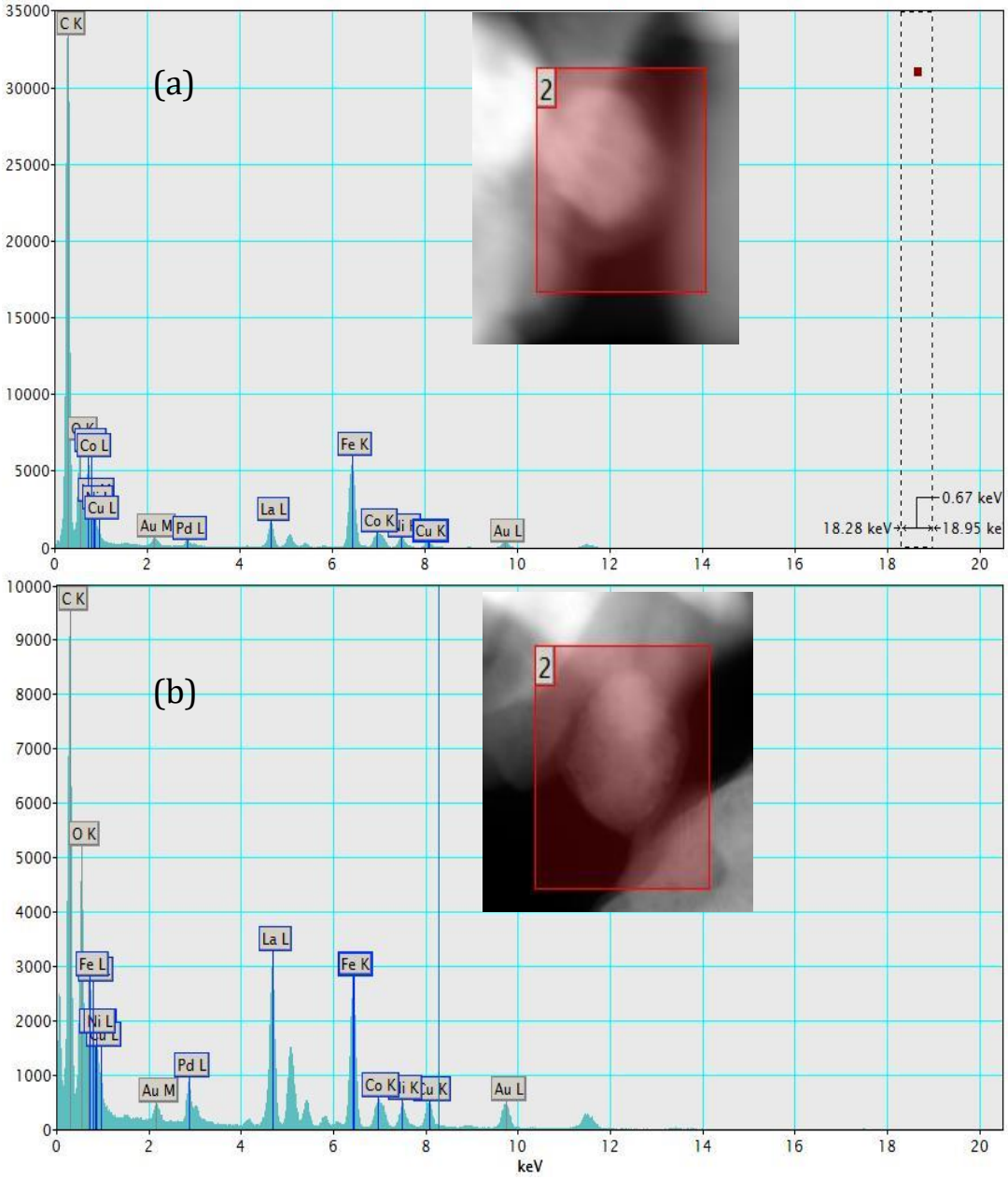

Figure S5.4. EDS spectra of exsolved particles on (a) NiFeCoCuPd-700 and (b) NiFeCoCuPd-900.

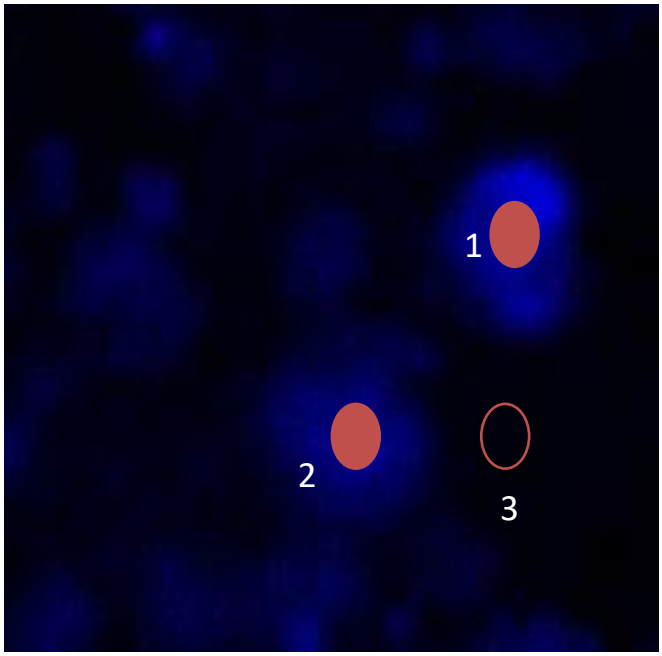

Composition Results 1

Element	Shell	Signal (cts.)	Comp. (at.%)	Comp. (wt.%)
O	K	7.5e4 ± 3.6	58.9	22.1
Pd	L	1.4e4 ± 6.0	2.4	6.0
La	L	8.6e4 ± 7.5	10.5	34.1
Fe	K	1.1e5 ± 5.3	19.1	25.0
Co	K	2.1e4 ± 5.4	3.6	5.0
Ni	K	1.9e4 ± 5.5	3.3	4.6
Cu	K	1.2e4 ± 5.5	2.2	3.3

Composition Results 2

Element	Shell	Signal (cts.)	Comp.(at.%)	Comp. (wt.%)
O	K	8.8e4 ± 3.6	60.1	21.5
Pd	L	1.2e4 ± 6.0	1.8	4.2
La	L	1.3e5 ± 7.5	14.1	43.7
Fe	K	1.2e5 ± 5.3	17.5	21.9
Co	K	1.7e4 ± 5.4	2.6	3.4
Ni	K	1.5e4 ± 5.5	2.2	2.9
Cu	K	1.1e4 ± 5.5	1.6	2.3

Composition Results 3

Element	Shell	Signal (cts.)	Comp.(at.%)	Comp.(wt.%)
O	K	7.5e4 ± 3.6	63.4	20.8
Pd	L	5138.0 ± 6.0	0.92	2.0
La	L	1.6e5 ± 7.5	21.2	60.4
Fe	K	6.8e4 ± 5.3	12.6	14.4
Co	K	4307.0 ± 5.4	0.8	0.97
Ni	K	1544.5 ± 5.5	0.29	0.35
Cu	K	4001.1 ± 5.5	0.78	1.0

Figure S5.5. Compositional analysis of selected areas of STEM-HAADF micrograph of NiFeCoCuPd reduced at 700°C for 120 min.

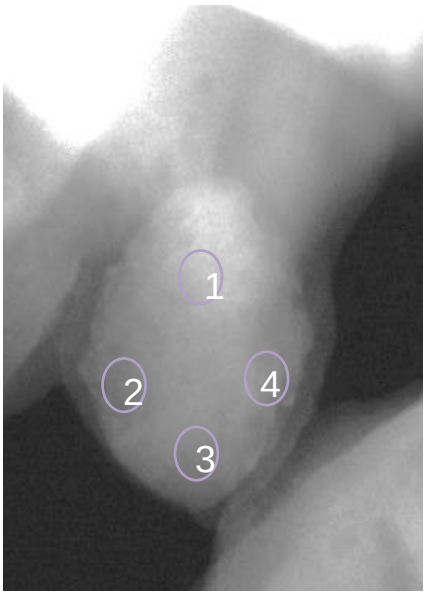

Composition Results 1

Element	Shell	Signal (cts.)	Comp.(at.%)	Comp.(wt.%)
O	K	1456.8 ± 3.6	34.2	9.6
Pd	L	2040.2 ± 6.0	10.1	18.8
La	L	3011.6 ± 7.5	11.1	26.8
Fe	K	5392.1 ± 5.3	27.6	26.9
Co	K	975.5 ± 5.4	5.1	5.2
Ni	K	937.5 ± 5.5	4.9	5.1
Cu	K	1293.3 ± 5.5	7.0	7.7

Composition Results 2

Element	Shell	Signal (cts.)	Comp.(at.%)	Comp.(wt.%)
O	K	969.3 ± 3.6	42.0	15.2
Pd	L	709.6 ± 6.0	6.5	15.7
La	L	219.8 ± 7.5	1.5	4.7
Fe	K	3789.5 ± 5.3	35.8	45.2
Co	K	603.5 ± 5.4	5.8	7.7
Ni	K	623.9 ± 5.5	6.1	8.1
Cu	K	242.8 ± 5.5	2.4	3.5

Composition Results 3

Element	Shell	Signal (cts.)	Comp.(at.%)	Comp.(wt.%)
O	K	643.0 ± 3.6	27.3	8.0
Pd	L	1666.8 ± 6.0	14.9	29.3
La	L	125.0 ± 7.5	0.83	2.1
Fe	K	3907.5 ± 5.3	36.1	37.1
Co	K	554.0 ± 5.4	5.2	5.6
Ni	K	687.6 ± 5.5	6.5	7.1
Cu	K	946.5 ± 5.5	9.2	10.8

Composition Results 4

Element	Shell	Signal (cts.)	Comp.(at.%)	Comp.(wt.%)
O	K	1202.3 ± 3.6	42.1	14.8
Pd	L	889.4 ± 6.0	6.6	15.4
La	L	559.5 ± 7.5	3.1	9.4
Fe	K	4444.2 ± 5.3	33.9	41.7
Co	K	758.0 ± 5.4	5.9	7.6
Ni	K	784.7 ± 5.5	6.2	8.0
Cu	K	281.3 ± 5.5	2.3	3.2

Figure S5.6. Compositional analysis of selected areas of STEM-HAADF micrograph of NiFeCoCuPd reduced at 900°C for 120 min.

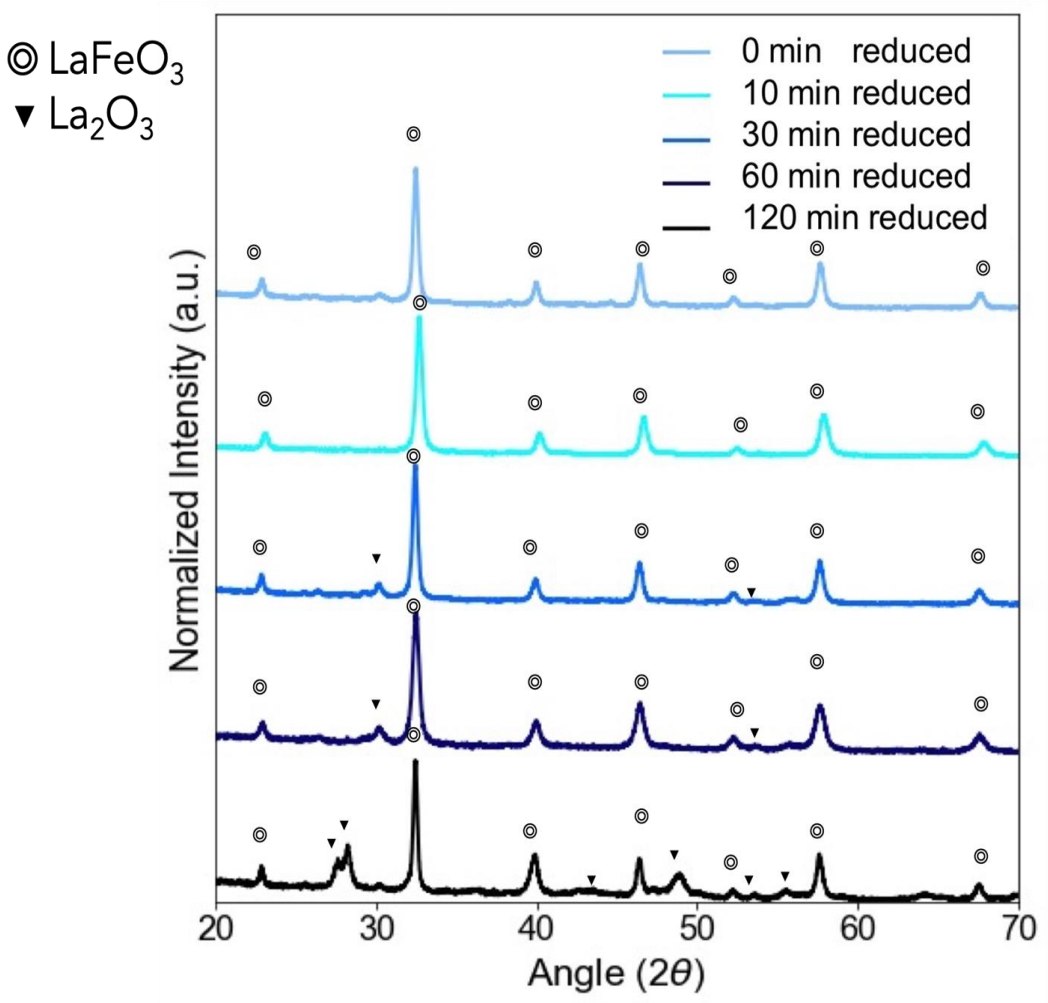

Figure S5.7. X-ray diffractograms of samples reduced for different reduction times at 700 °C

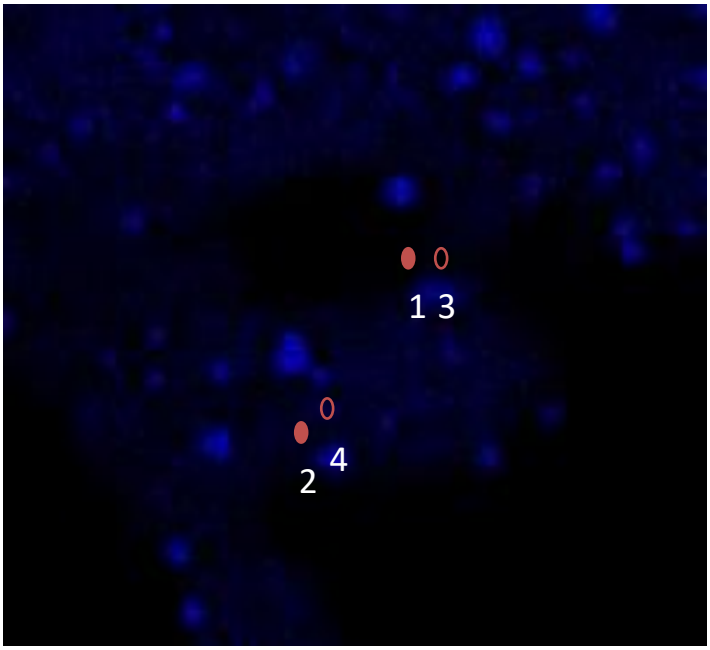

Composition Results 1

Element	Shell	Signal(cts.)	Comp.(at.%)	Comp.(wt.%)
O	K	276.3 ± 3.6	39.1	11.8
Pd	L	301.2 ± 6.0	9.0	18.1
La	L	369.8 ± 7.5	8.2	21.4
Fe	K	239.4 ± 5.3	7.4	7.8
Co	K	413.7 ± 5.4	12.9	14.3
Ni	K	503.3 ± 5.5	16.0	17.6
Cu	K	232.7 ± 5.5	7.5	9.0

Composition Results 2

Element	Shell	Signal (counts)	Comp. (at.%)	Comp. (wt.%)
O	K	1441.7 ± 3.6	58.7	20.3
Pd	L	464.5 ± 6.0	4.0	9.2
La	L	2101.1 ± 7.5	13.4	40.2
Fe	K	988.1 ± 5.3	8.8	10.6
Co	K	618.9 ± 5.4	5.5	7.1
Ni	K	650.8 ± 5.5	5.9	7.5
Cu	K	398.8 ± 5.5	3.7	5.1

Composition Results 3

Element	Shell	Signal(cts.)	Comp(at.%)	Comp.(wt.%)
O	K	1107.1 ± 3.6	65.5	22.7
Pd	L	52.9 ± 6.0	0.66	1.5
La	L	2055.3 ± 7.5	19.0	57.3
Fe	K	856.8 ± 5.3	11.0	13.4
Co	K	111.6 ± 5.4	1.5	1.9
Ni	K	76.0 ± 5.5	1.0	1.3
Cu	K	101.1 ± 5.5	1.4	1.9

Composition Results 4

Element	Shell	Signal(cts.)	Comp.(at.%)	Comp. (wt.%)
O	K	1495.8 ± 3.6	71.3	27.2
Pd	L	68.3 ± 6.0	0.69	1.7
La	L	2268.5 ± 7.5	16.9	55.9
Fe	K	749.5 ± 5.3	7.8	10.3
Co	K	98.7 ± 5.4	1.0	1.5
Ni	K	109.7 ± 5.5	1.2	1.6
Cu	K	105.1 ± 5.5	1.1	1.7

Figure S5.8. Compositional analysis of selected areas of STEM-HAADF micrograph of NiFeCoCuPd reduced at 700°C for 0 min.

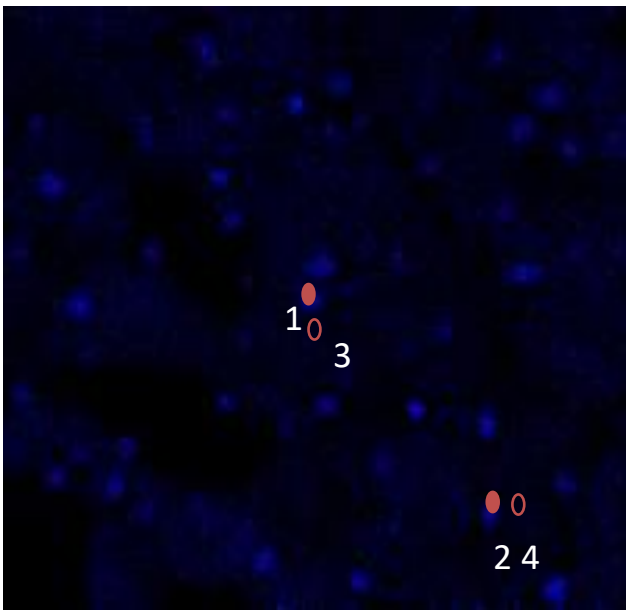

Composition Results 1

Element	Shell	Signal (cts.)	Comp. (at.%)	Comp(wt.%)
O	K	1109.9 ± 3.6	64.9	23.7
Pd	L	287.7 ± 6.0	3.6	8.6
La	L	1564.5 ± 7.5	14.3	45.3
Fe	K	697.3 ± 5.3	8.9	11.3
Co	K	323.9 ± 5.4	4.2	5.6
Ni	K	294.9 ± 5.5	3.9	5.2
Cu	K	20.1 ± 5.5	0.27	0.39

Composition Results 2

Element	Shell	Signal (cts.)	Comp. (at.%)	Comp. (wt.%)
O	K	928.9 ± 3.6	66.5	24.7
Pd	L	167.0 ± 6.0	2.5	6.2
La	L	1329.7 ± 7.5	14.9	47.9
Fe	K	581.6 ± 5.3	9.1	11.7
Co	K	203.9 ± 5.4	3.2	4.4
Ni	K	232.2 ± 5.5	3.7	5.1
Cu	K	1.3 ± 5.5	0.021	0.031

Composition Results 3

Element	Shell	Signal (cts.)	Comp.(at.%)	Comp(wt.%)
O	K	1037.8 ± 3.6	64.9	21.9
Pd	L	64.7 ± 6.0	0.85	1.9
La	L	2074.1 ± 7.5	20.3	59.5
Fe	K	799.8 ± 5.3	10.9	12.8
Co	K	106.6 ± 5.4	1.5	1.8
Ni	K	99.3 ± 5.5	1.4	1.7
Cu	K	16.6 ± 5.5	0.24	0.32

Composition Results 4

Element	Shell	Signal (cts)	Comp. (at.%)	Comp.(wt.%)
O	K	950.3 ± 3.6	67.4	23.8
Pd	L	81.1 ± 6.0	1.2	2.9
La	L	1703.1 ± 7.5	18.9	57.8
Fe	K	633.6 ± 5.3	9.8	12.0
Co	K	77.7 ± 5.4	1.2	1.6
Ni	K	84.4 ± 5.5	1.3	1.7
Cu	K	10.9 ± 5.5	0.18	0.25

Figure S5.9. Compositional analysis of selected areas of STEM-HAADF micrograph of NiFeCoCuPd reduced at 700°C for 10 min.

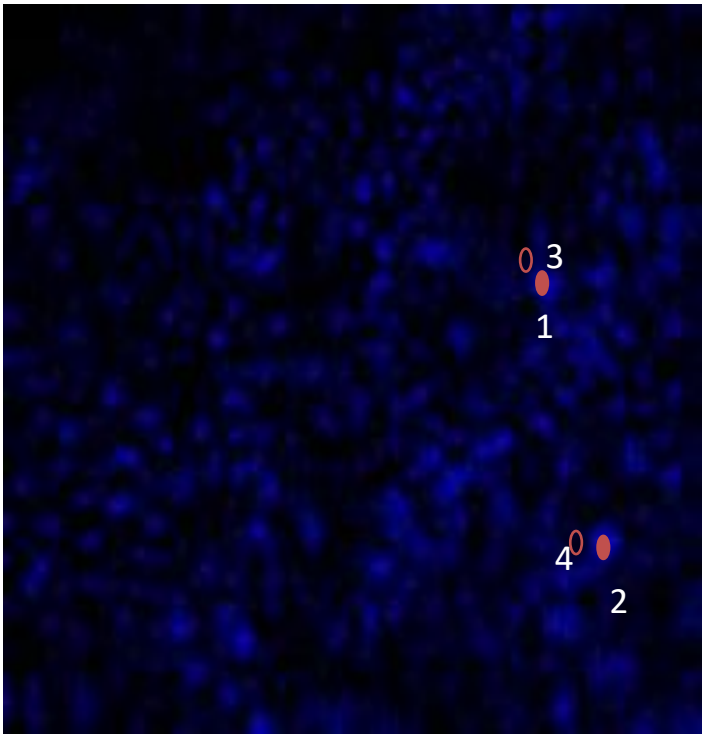

Composition Results 1

Element	Shell	Signal (cts.)	Comp.(at.%)	Comp.(wt.%)
O	K	1960.7 ± 3.6	59.0	19.7
Pd	L	194.2 ± 6.0	1.2	2.7
La	L	3741.7 ± 7.5	17.6	51.0
Fe	K	1857.1 ± 5.3	12.2	14.2
Co	K	654.3 ± 5.4	4.3	5.3
Ni	K	592.9 ± 5.5	4.0	4.9
Cu	K	248.1 ± 5.5	1.7	2.3

Composition Results 3

Element	Shell	Signal(cts.)	Comp(at.%)	Comp.(wt.%)
O	K	1503.3 ± 3.6	69.4	25.6
Pd	L	42.0 ± 6.0	0.41	1.0
La	L	2487.8 ± 7.5	17.9	57.5
Fe	K	1086.3 ± 5.3	10.9	14.1
Co	K	56.8 ± 5.4	0.58	0.79
Ni	K	38.1 ± 5.5	0.39	0.53
Cu	K	36.1 ± 5.5	0.38	0.56

Composition Results 2

Element	Shell	Signal (cts.)	Comp.(at.%)	Comp.(wt.%)
O	K	1821.7 ± 3.6	55.7	18.3
Pd	L	252.9 ± 6.0	1.6	3.6
La	L	3474.4 ± 7.5	16.6	47.4
Fe	K	2323.7 ± 5.3	15.5	17.7
Co	K	662.5 ± 5.4	4.5	5.4
Ni	K	667.8 ± 5.5	4.6	5.5
Cu	K	232.4 ± 5.5	1.6	2.1

Composition Results 4

Element	Shell	Signal (cts.)	Comp.(at.%)	Comp.(wt.%)
O	K	2681.1 ± 3.6	65.5	21.8
Pd	L	77.0 ± 6.0	0.4	0.88
La	L	5679.1 ± 7.5	21.7	62.7
Fe	K	1852.3 ± 5.3	9.9	11.4
Co	K	199.9 ± 5.4	1.1	1.3
Ni	K	127.7 ± 5.5	0.7	0.85
Cu	K	142.4 ± 5.5	0.8	1.1

Figure S5.10. Compositional analysis of selected areas of STEM-HAADF micrograph of NiFeCoCuPd reduced at 700°C for 30 min.

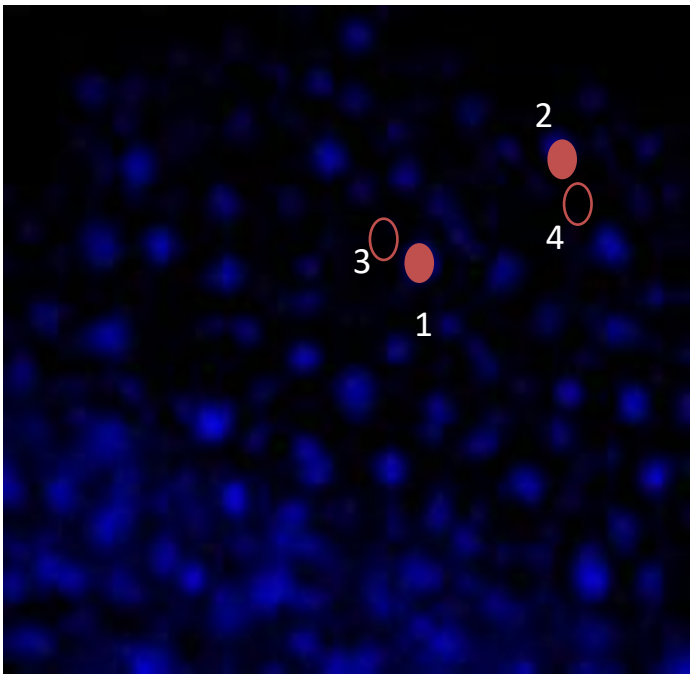

Composition Results 1

Element	Shell	Signal (cts.)	Comp.(at.%)	Comp (wt.%)
O	K	3261.5 ± 3.6	60.4	21.8
Pd	L	667.0 ± 6.0	2.6	6.3
La	L	4425.2 ± 7.5	12.8	40.1
Fe	K	1942.7 ± 5.3	7.8	9.9
Co	K	1624.2 ± 5.4	6.6	8.8
Ni	K	1687.7 ± 5.5	7.0	9.3
Cu	K	632.6 ± 5.5	2.7	3.8

Composition Results 2

Element	Shell	Signal (cts.)	Comp. (at.%)	Comp.(wt.%).
O	K	3114.3 ± 3.6	61.6	23.1
Pd	L	684.1 ± 6.0	2.9	7.1
La	L	3630.0 ± 7.5	11.2	36.5
Fe	K	1983.3 ± 5.3	8.5	11.2
Co	K	1565.7 ± 5.4	6.8	9.4
Ni	K	1261.9 ± 5.5	5.6	7.7
Cu	K	750.2 ± 5.5	3.4	5.1

Composition Results 3

Element	Shell	Signal (cts.)	Comp.(at.%)	Comp.(wt.%)
O	K	3767.1 ± 3.6	71.1	27.3
Pd	L	52.6 ± 6.0	0.21	0.54
La	L	5746.6 ± 7.5	17.0	56.5
Fe	K	2647.5 ± 5.3	10.9	14.6
Co	K	59.4 ± 5.4	0.25	0.35
Ni	K	11.5 ± 5.5	0.048	0.068
Cu	K	113.7 ± 5.5	0.49	0.75

Composition Results 4

Element	Shell	Signal (cts.)	Comp.(at.%)	Comp.(wt.%)
O	K	2842.8 ± 3.6	73.1	28.7
Pd	L	0.0 ± 0.0	0.0	0.0
La	L	4160.0 ± 7.5	16.7	57.1
Fe	K	1696.7 ± 5.3	9.5	13.0
Co	K	38.0 ± 5.4	0.22	0.31
Ni	K	6.4 ± 5.5	0.037	0.053
Cu	K	82.5 ± 5.5	0.49	0.76

Figure S5.11. Compositional analysis of selected areas of STEM-HAADF micrograph of NiFeCoCuPd reduced at 700°C for 60 min.

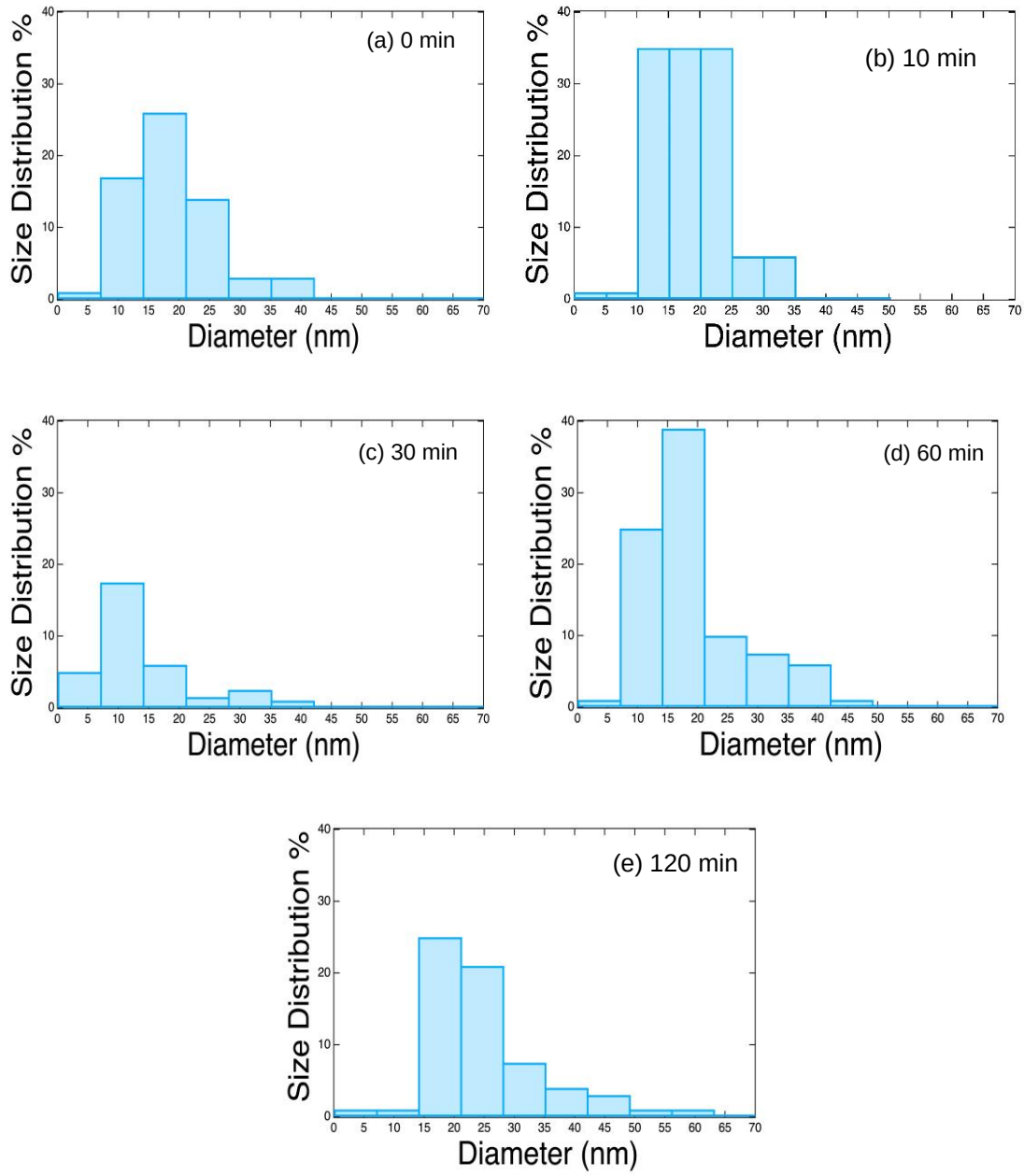

Figure S5.12. Histogram of size distribution of nanoparticles exsolved from NiFeCoCuPd reduced at 700°C for (a)0 minutes (b) 10 minutes (c) 30 minutes (d) 60 minutes and (e) 120 minutes.

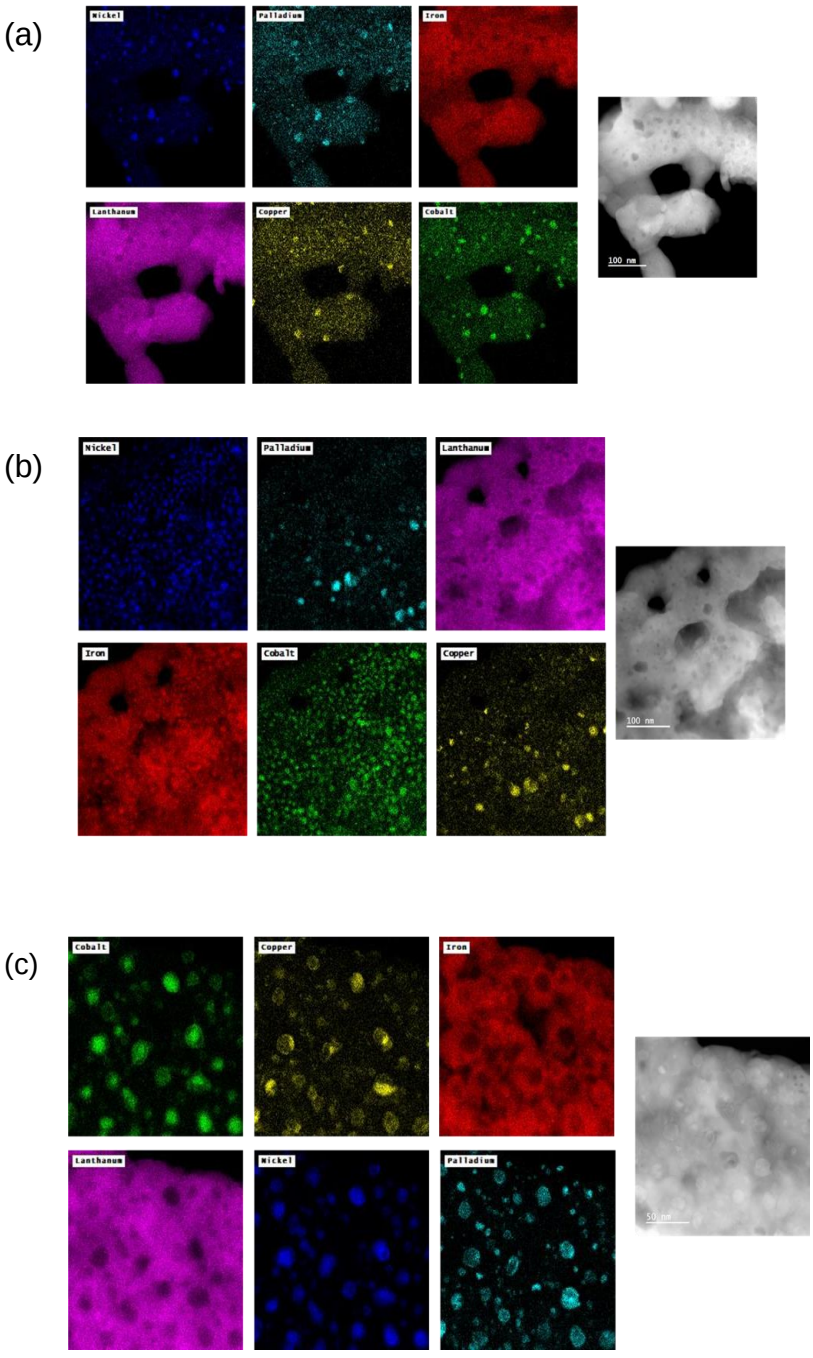

Figure S5.13. Composition of select samples of NiFeCoCuPd-700, (a) after 30-minute reduction, (b) after 60-minute reduction and (c) after 120-minute reduction. The images show that the atomic arrangement of the elements change as the reduction time increases and the nanoparticles become larger.

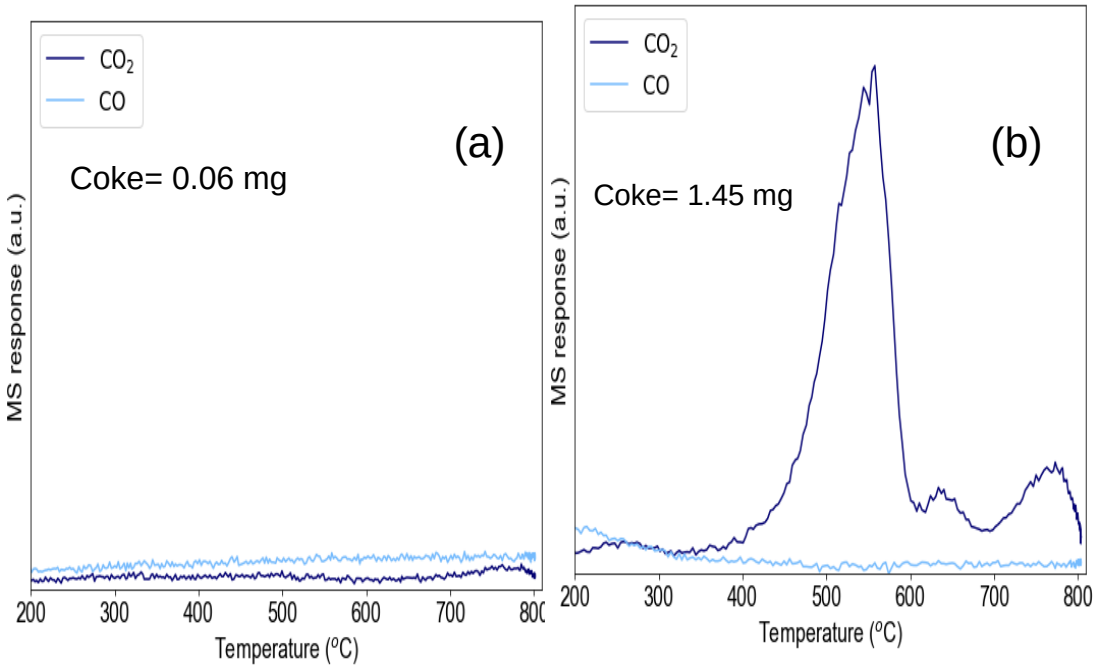

Figure S5.14. Temperature Programmed Oxidation of CCA catalysts after aging in DRM reaction conditions for 24 hours shows evolution of CO_2 and CO (a) NiFeCoCuPd-700 and (b) NiFeCoCuPd-900.

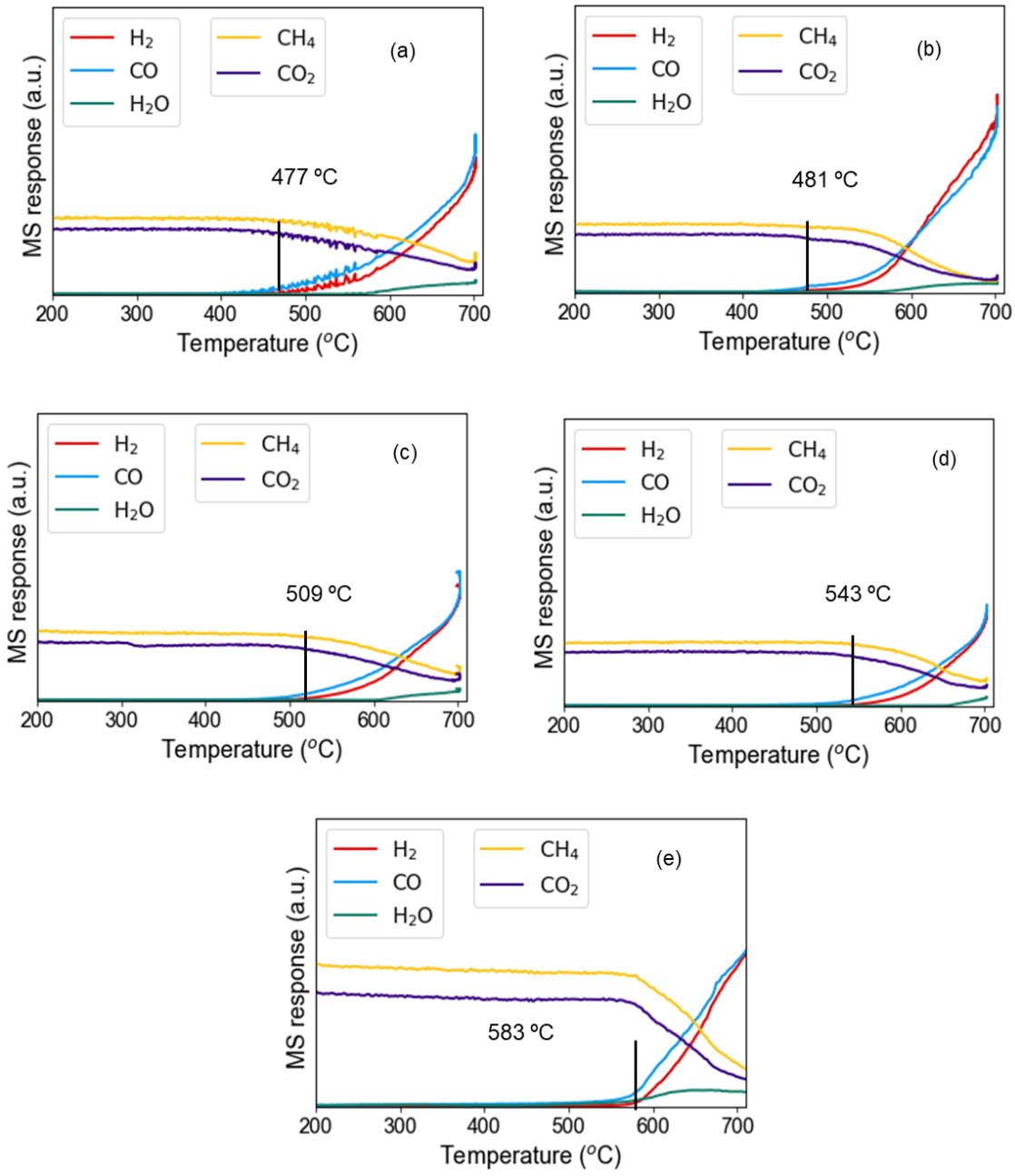

Figure S5.15. Temperature Programmed Surface Reaction profiles and associated light-off temperatures of $LaFe_{0.7}Ni_{0.1}Co_{0.1}Cu_{0.05}Pd_{0.05}O_3$ reduced at 700 ºC for dwell times (a) 0 min (b) 10 min (c) 30 min (d) 60 min (e) 120 min.

Table S5.1. Rates of reaction of methane and carbon dioxide consumption and H_2/CO product ratios at 700°C for various catalyst samples

Catalyst	CH_4 rate @ 700°C (μmol/s.g. cat.)	CO_2 rate @ 700°C (μmol/s.g. cat.)	H_2/CO @ 700°C
$LaFe_{0.7}Ni_{0.1}Co_{0.1}Cu_{0.05}Pd_{0.05}O_3$ 700 °C 0 min reduced	4.90	5.16	0.87
$LaFe_{0.7}Ni_{0.1}Co_{0.1}Cu_{0.05}Pd_{0.05}O_3$ 700 °C 10 min reduced	5.96	5.74	1.03
$LaFe_{0.7}Ni_{0.1}Co_{0.1}Cu_{0.05}Pd_{0.05}O_3$ 700 °C 30 min reduced	4.87	5.12	0.93
$LaFe_{0.7}Ni_{0.1}Co_{0.1}Cu_{0.05}Pd_{0.05}O_3$ 700 °C 60 min reduced	4.83	5.14	0.95
$LaFe_{0.7}Ni_{0.1}Co_{0.1}Cu_{0.05}Pd_{0.05}O_3$ 700 °C 2hr reduced	4.53	4.95	0.90
$LaFe_{0.7}Ni_{0.1}Co_{0.1}Cu_{0.05}Pd_{0.05}O_3$ 900 °C (2hr) reduced	2.06	3.26	0.53

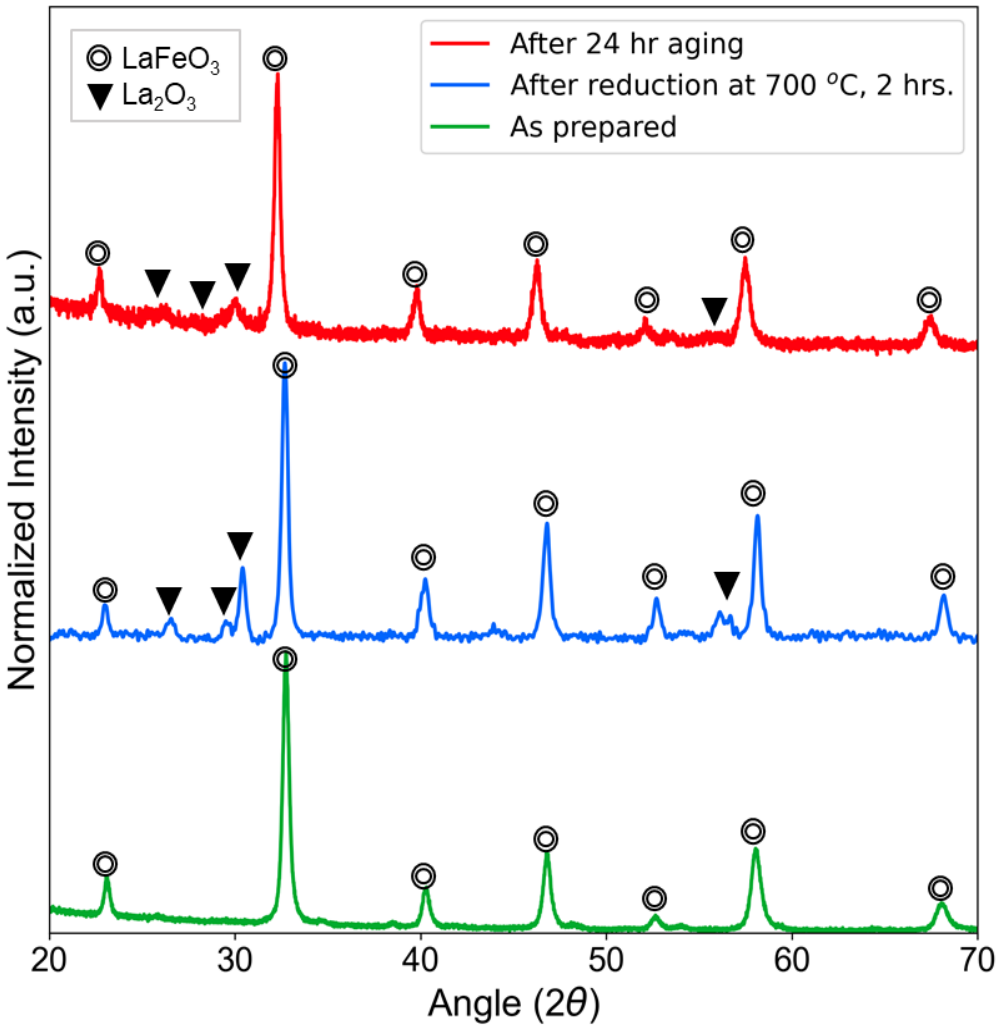

Figure S5.16. XRD of LaFeNiCoCuPdO3 perovskite type material in as prepared state, after reduction for 2 hours at 700°C and, aged for 24 hours in DRM conditions following 2-hour reduction at 700°C.

5.9 References

(1) Yao, Y.; Huang, Z.; Xie, P.; Lacey, S. D.; Jacob, R. J.; Xie, H.; Chen, F.; Nie, A.; Pu, T.; Rehwoldt, M.; Yu, D.; Zachariah, M. R.; Wang, C.; Shahbazian-Yassar, R.; Li, J.; Hu, L. Carbothermal Shock Synthesis of High-Entropy-Alloy Nanoparticles. *Science (80-.).* **2018**, *359* (6383), 1489–1494. https://doi.org/10.1126/science.aan5412.

(2) Sun, Y.; Dai, S. High-Entropy Materials for Catalysis: A New Frontier. *Sci. Adv.* **2021**, *7* (20). https://doi.org/10.1126/sciadv.abg1600.

(3) Yang, T.; Zhao, Y. L.; Tong, Y.; Jiao, Z. B.; Wei, J.; Cai, J. X.; Han, X. D.; Chen, D.; Hu, A.; Kai, J. J.; Lu, K.; Liu, Y.; Liu, C. T. Multicomponent Intermetallic Nanoparticles and Superb Mechanical Behaviors of Complex Alloys. *Science (80-.).* **2018**, *362* (6417), 933–937. https://doi.org/10.1126/science.aas8815.

(4) Li, H.; Han, Y.; Zhao, H.; Qi, W.; Zhang, D.; Yu, Y.; Cai, W.; Li, S.; Lai, J.; Huang, B.; Wang, L. Fast Site-to-Site Electron Transfer of High-Entropy Alloy Nanocatalyst Driving Redox Electrocatalysis. *Nat. Commun.* **2020**, *11*, 5437. https://doi.org/10.1038/s41467-020-19277-9.

(5) Xin, Y.; Li, S.; Qian, Y.; Zhu, W.; Yuan, H.; Jiang, P.; Guo, R.; Wang, L. High-Entropy Alloys as a Platform for Catalysis: Progress, Challenges, and Opportunities. *ACS Catal.* **2020**, *10* (19), 11280–11306. https://doi.org/10.1021/acscatal.0c03617.

(6) Li, M.; Wang, X.; Cheng, Y.; Su, L.; Xu, P.; Li, X. High-Entropy Alloy Nanoparticles As Catalyst For Nanomolar-Level Detection Of Neurotransmitter Serotonin In Serum. In *2021 IEEE 34th International Conference on Micro Electro Mechanical Systems (MEMS)*; IEEE, 2021; pp 314–317. https://doi.org/10.1109/MEMS51782.2021.9375269.

(7) Braic, V.; Balaceanu, M.; Braic, M.; Vladescu, A.; Panseri, S.; Russo, A. Characterization of Multi-Principal-Element (TiZrNbHfTa)N and (TiZrNbHfTa)C Coatings for Biomedical Applications. *J. Mech. Behav. Biomed. Mater.* **2012**, *10*, 197–205. https://doi.org/10.1016/j.jmbbm.2012.02.020.

(8) Batchelor, T. A. A.; Pedersen, J. K.; Winther, S. H.; Castelli, I. E.; Jacobsen, K. W.; Rossmeisl, J. High-Entropy Alloys as a Discovery Platform for Electrocatalysis. *Joule* **2019**, *3* (3), 834–845. https://doi.org/10.1016/j.joule.2018.12.015.

(9) Löffler, T.; Savan, A.; Garzón-Manjón, A.; Meischein, M.; Scheu, C.; Ludwig, A.; Schuhmann, W. Toward a Paradigm Shift in Electrocatalysis Using Complex Solid Solution Nanoparticles. *ACS Energy Lett.* **2019**, *4* (5), 1206–1214. https://doi.org/10.1021/acsenergylett.9b00531.

(10) Pedersen, J. K.; Batchelor, T. A. A.; Yan, D.; Skjegstad, L. E. J.; Rossmeisl, J. Surface Electrocatalysis on High-Entropy Alloys. *Curr. Opin. Electrochem.* **2021**, *26*, 100651. https://doi.org/10.1016/j.coelec.2020.100651.

(11) Tomboc, G. M.; Kwon, T.; Joo, J.; Lee, K. High Entropy Alloy Electrocatalysts: A Critical Assessment of Fabrication and Performance. *J. Mater. Chem. A* **2020**, *8* (30), 14844–14862. https://doi.org/10.1039/D0TA05176D.

(12) Zheng, H.; Luo, G.; Zhang, A.; Lu, X.; He, L. The Synthesis and Catalytic Applications of Nanosized High-Entropy Alloys. *ChemCatChem* **2021**, *13* (3), 806–817. https://doi.org/10.1002/cctc.202001163.

(13) Yao, Y.; Liu, Z.; Xie, P.; Huang, Z.; Li, T.; Morris, D.; Finfrock, Z.; Zhou, J.; Jiao, M.; Gao, J.; Mao, Y.; Miao, J.; Zhang, P.; Shahbazian-Yassar, R.; Wang, C.; Wang, G.; Hu, L. Computationally Aided, Entropy-Driven Synthesis of Highly Efficient and Durable Multi-Elemental Alloy Catalysts. *Sci. Adv.* **2020**, *6* (11). https://doi.org/10.1126/sciadv.aaz0510.

(14) Xie, P.; Yao, Y.; Huang, Z.; Liu, Z.; Zhang, J.; Li, T.; Wang, G.; Shahbazian-Yassar, R.; Hu, L.; Wang, C. Highly Efficient Decomposition of Ammonia Using High-Entropy Alloy Catalysts. *Nat. Commun.* **2019**, *10* (1), 1–12. https://doi.org/10.1038/s41467-019-11848-9.

(15) Shah, S.; Sayono, S.; Ynzunza, J.; Pan, R.; Xu, M.; Pan, X.; Gilliard-Abdulaziz, K. L. The Effects of Stoichiometry on the Properties of Exsolved Ni-Fe Alloy Nanoparticles for Dry Methane Reforming. *AIChE J.* **2020**, *66* (12), e17078. https://doi.org/https://doi.org/10.1002/aic.17078.

(16) Shah, S.; Xu, M.; Pan, X.; Gilliard-Abdulaziz, K. L. Exsolution of Embedded Ni–Fe–Co Nanoparticles: Implications for Dry Reforming of Methane. *ACS Appl. Nano Mater.* **2021**, *4* (8), 8626–8636. https://doi.org/10.1021/acsanm.1c02268.

(17) Buck, M. R.; Bondi, J. F.; Schaak, R. E. A Total-Synthesis Framework for the Construction of High-Order Colloidal Hybrid Nanoparticles. *Nat. Chem.* **2012**, *4* (1), 37–44. https://doi.org/10.1038/nchem.1195.

(18) Nie, Z.; Li, W.; Seo, M.; Xu, S.; Kumacheva, E. Janus and Ternary Particles Generated by Microfluidic Synthesis: Design, Synthesis, and Self-Assembly. *J. Am. Chem. Soc.* **2006**, *128* (29), 9408–9412. https://doi.org/10.1021/ja060882n.

(19) Yang, Y.; Song, B.; Ke, X.; Xu, F.; Bozhilov, K. N.; Hu, L.; Shahbazian-Yassar, R.; Zachariah, M. R. Aerosol Synthesis of High Entropy Alloy Nanoparticles. *Langmuir* **2020**, *36* (8), 1985–1992. https://doi.org/10.1021/acs.langmuir.9b03392.

(20) Ganguli, A. K.; Ganguly, A.; Vaidya, S. Microemulsion-Based Synthesis of Nanocrystalline Materials. *Chem. Soc. Rev.* **2010**, *39* (2), 474–485. https://doi.org/10.1039/B814613F.

(21) Schneider, C. A.; Rasband, W. S.; Eliceiri, K. W. NIH Image to ImageJ: 25 Years of Image Analysis. *Nat. Methods* **2012**, *9* (7), 671–675. https://doi.org/10.1038/nmeth.2089.

(22) Karemore, A. L.; Sinha, R.; Chugh, P.; Vaidya, P. D. Parametric and Reaction Kinetic Study of Syngas Production from Dry Methane Reforming over Improved Nickel Catalysts. *Energy and Fuels* **2021**, *35* (7), 6179–6189. https://doi.org/10.1021/acs.energyfuels.0c04037.

(23) Karemore, A. L.; Sinha, R.; Chugh, P.; Vaidya, P. D. Syngas Production by Dry Methane Reforming over Alumina-Supported Noble Metals and Kinetic Studies. *Chem. Eng. Technol.* **2022**, *45* (5), 907–917. https://doi.org/10.1002/ceat.202000382.

(24) Theofanidis, S. A.; Galvita, V. V.; Poelman, H.; Marin, G. B. Enhanced Carbon-Resistant Dry Reforming Fe-Ni Catalyst: Role of Fe. *ACS Catal.* **2015**, *5* (5), 3028–3039. https://doi.org/10.1021/acscatal.5b00357.

(25) Wang, L.; Li, D.; Koike, M.; Koso, S.; Nakagawa, Y.; Xu, Y.; Tomishige, K. Catalytic Performance and Characterization of Ni-Fe Catalysts for the Steam Reforming of Tar from Biomass Pyrolysis to Synthesis Gas. *Appl. Catal. A Gen.* **2011**, *392* (1–2), 248–255. https://doi.org/10.1016/j.apcata.2010.11.013.

CHAPTER 6: DEVELOPMENT OF DUAL FUNCTIONAL MATERIALS FOR SORPTION ENHANCED CATALYTIC UTILIZATION OF CO_2.

6.1 Abstract

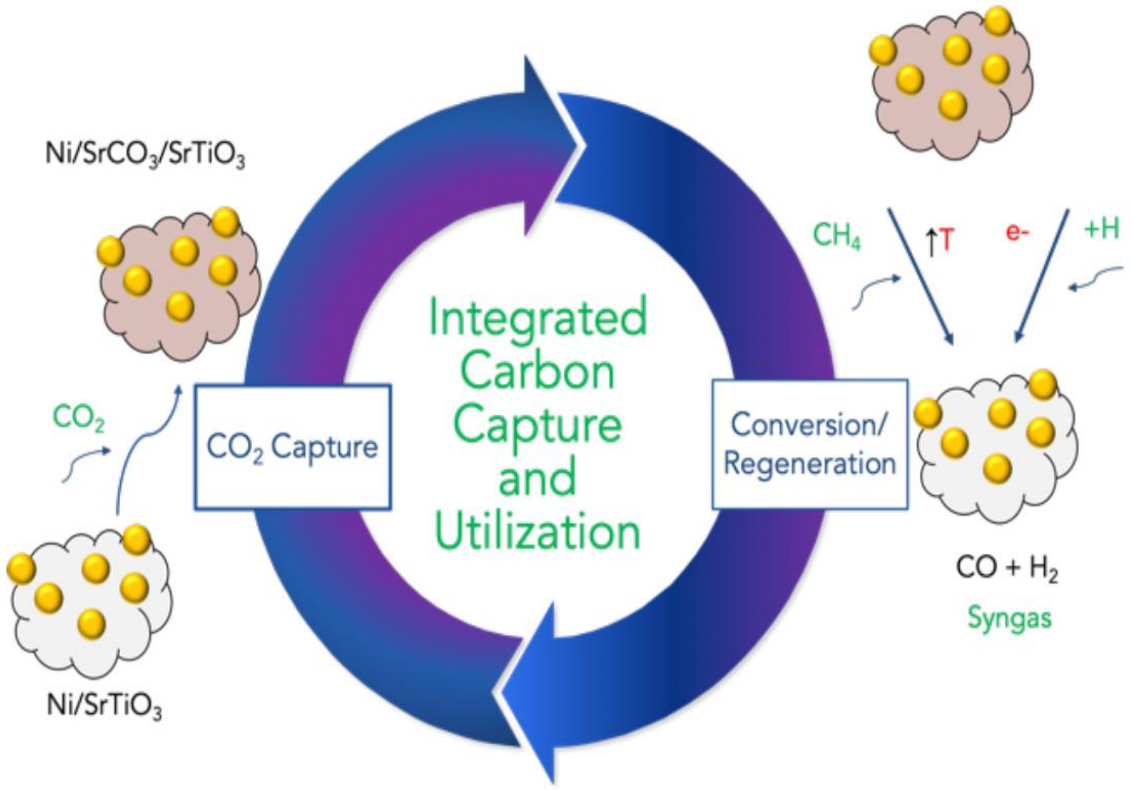

Figure 6.1. A visualization of the cyclic use of perovskite-based Dual Functional Materials for the integrated capture and conversion of CO_2.

The recycling of carbon dioxide by conversion to hydrocarbon fuel and higher value chemicals is a strategy being explored for net reduction in anthropogenic CO_2 emissions. The dilution of CO_2 in flue gas streams containing post-combustion air and impurities such as SO_x and NO_x is a pose a barrier in CO_2 capture and utilization. Heterogenous catalysts supported on sorbent supports can combine adsorption and activation functions for CO_2 capture and conversion processes. Carbon dioxide can be removed from flue gas

or other CO_2 rich gas streams. Subsequently, the catalyst can activate CO_2 for reduction to products such as methane and other hydrocarbons. In this research we explored sorbent support catalysts based on the perovskite materials platform. Alkaline earth materials on the A site of the perovskite afford a basic support facilitating CO_2 adsorption. A Nickel substituent on the B site of the perovskite catalyzes reduction by CH_4, a mild reducing agent or H_2 a stronger reducing agent via dry methane reforming and hydrogenation reactions respectively. The activity, stability and cyclability of these materials are investigated by studying reactions in a packed bed reactor and observing evolution of CO in the product stream. Finally, future work for the further development of these materials is discussed.

6.2 Introduction

Presently, the industrial utilization of carbon dioxide (~200MT/y ca.) is an insignificant fraction (of the total anthropogenic emission of CO_2 (~36,000MT/y)[1,2]. Development of Carbon Capture and Utilization (CCU) technology can catalyze the conversion of CO_2 to valuable commodity chemicals. CO_2 is a highly chemically stable molecule and the activation of the molecule requires overcoming a substantial energy barrier. Moreover, SO_x and NO_x that also typically constitute flue gas streams can poison or considerably degrade catalyst performance and reduce catalyst lifespans. Sintering and coking can also occur at the elevated temperatures required for these reactions, which also inhibit catalytic activity significantly. Thus, the challenge is to develop catalysts that are highly stable in the presence of poisons while operating at high temperature and resisting deactivation. The dilute concentration of CO_2 in flue gas streams also requires

separation or otherwise concentration of CO_2 that can be effectively utilized. Thus, integrated carbon capture and utilization (ICCU) with sorption enhanced catalysts offer lower costs while simplifying the process by combining gas separation and reactive consumption of CO_2.

Solid sorbents typically separated CO_2 from gas streams via physisorption or chemisorption. Physisorption, however, often offers limited capacity for sorption especially at low CO_2 partial pressures or high temperatures. Sorbents with basic sites that interact chemically with acidic CO_2 can offer high selectivity and allowing operation at high temperatures. Materials that combine sorbent and catalytic materials, referred to as Dual Functional Materials are a proposed solution for ICCU[3,4]. The sorbent part is typically alkali or alkaline-earth metals that reversibly form carbonates or oxycarbonates. Catalysts such as Ni, Fe, Co, Cu, Ru and Rh have been explored for upgrading CO_2 to CO, CH_4 or other hydrocarbons. DFMs can potentially eliminate separation, transportation and storage of CO_2 by combining separation and conversion processes.

Perovskites have been used for CO_2 utilizing reactions such as dry methane reforming and CO_2 hydrogenation[5–10] . The tunable exsolution of nanoparticles allows for catalysts that are resistant to deactivation by sintering and coking which is often a limitation for CO_2 conversion reactions that occur at high temperatures[11,12]. The Boudouard reaction (1) can cause the formation of carbonaceous species on the surface of the catalyst that leads to fouling of the catalyst or rendering it inaccessible to reactive species.

$$2CO_2(g) \leftrightarrow CO(g) + C(s) \qquad (1)$$

High temperatures can also lead to agglomeration of catalytic nanoparticles leading to a decline in active surface area. Perovskites have demonstrated resilience to deactivation by sintering and coking when applied to reactions involving CO_2 utilization.[13–18]. In our previous work we demonstrated how perovskites can be tuned on their A and B sites by the introduction of stoichiometric defects and co-dopants that in turn influence catalytic activity and stability[19,20]. Under dry methane reforming conditions $LaFeO_3$ type perovskites demonstrated high stability and activity. The basic sites of La also aid in adsorption of CO_2 while Fe or co-dopants such as Co can activate CO_2 for conversion to CO.

Perovskites with alkaline earth metals as primary or co-doped A-site elements, can also be synthesized feasibly for applications in CO_2 utilizing reactions[21–26]. The presence of these metals can provide basic sites that allow for adsorption of CO_2 via formation of surface carbonate and oxycarbonate species[27]. Meanwhile the B-site of the can host reducible catalytic metals that can activate CO_2 and reducing agents such as H_2 or CH_4 and other hydrocarbons. This allows perovskites to be rationally designed for integrating CO_2 capture on basic A-sites and activation by catalytic B-site making them ideal Dual Functional Material candidates. Khazaal et al. synthesized (5 wt. % Ni) Ni-Fe doped $SrZrO_3$ for methane dry reforming and biogas reforming[28]. Their catalyst showed similar activity as compared to 10%Ni/Al2O3 but with better coking resistance and lower catalyst loading. Dama et al. synthesized Ni doped zirconates of Ca, Sr and Ba. Changing the A-site metal changed reducibility of perovskite[29]. The redox properties of the perovskite played a crucial role in coke removal during DRM, as was revealed by pulse

experiments. Accordingly, $CaZr_{0.8}Ni_{0.2}O_3$ was the best performing catalyst compared to similar zirconates of Sr and Ba.

In this chapter, preliminary data of methane reforming reaction over Ni-$SrZrO_3$ type perovskites are discussed. Their feasibility as dual functional materials is exposed through a looping reaction strategy where the perovskite is cycled between carbonation and reduction cycles.

6.3 Experimental Details

$Sr_{0.9}ZrNi_{0.1}O_3$ (A-SZNO), $SrZr_{0.9}Ni_{0.1}O_3$ (B-SZNO), were synthesized as perovskite based dual functional materials for looping capture and conversion of CO_2 via reduction by CH_4 or H_2. A modified version of the citrate-nitrate sol-gel method was used as the synthesis route[15]. The precursors for Sr, Zr and Ni were their respective nitrate-hydrate salts. The nitrate salts were first dissolved in water, in stoichiometrically appropriate quantities on a hot-plate stirrer with a magnetic stir bar. Citric acid monohydrate (3 mols/mol perovskite) and ethylene glycol (1mol/mol perovskite) were added to the mixture at 60°C.. The solution was then dried overnight in a drying oven and then calcined at 900°C in a muffle furnace to form a mixed-oxide. The sample was further annealed in N_2 at 900°C to remove carbonates and hydroxides. The resulting sample was a mixture of $SrZrO_3$, SrO and ZrO_2 in the case of the zirconate DFM.

Surface area of the perovskite type materials were determined from N2 adsorption isotherm. Pore volumes were determined by the Barett-Joyner-Halenda (BJH) adsorption method. Catalyst testing for the looping reaction and Temperature Programmed Reduction (TPR) of the catalyst was conducted in a quartz tube microreactor (Hiden

Analytical CATLAB). A PANalytical Empyrean Series 2 X-ray Diffractometer was used to collect X-ray Diffraction (XRD) patterns to determine the crystalline nature of the samples. Diffractograms were collected with a step size of 0.026° and dwell time of 30 seconds. Samples were heated to 700^{o}C at in the 5% H_2/He with a 10^{o}C/min ramp rate and then held for another two hours. For the looping reaction, the catalyst was carbonated in 10% CO2/He mixture at 60 ml/min flow rate at 650°C for 30 minutes. After purging He for 10 minutes, the catalyst was reduced by 10% CH4/He also at 60ml/min at 650°C for another 30 minutes. Scanning Transmission Electron Microscopy (STEM) images were collected on a JEOL Grand ARM300CF TEM/STEM with double spherical aberration-correctors operated at 300kV STEM High-angle annular dark-field (HAADF) imaging mode. Energy-dispersive X-ray spectroscopy (EDS) was collected by the large angle dual dry solid-state 100 mm^2 detectors simultaneously with the STEM imaging to observe distribution of the elements on the material surface. Analysis of the STEM images for particle size distribution was done using the ImageJ software[30].

6.4 Results and Discussion

Table 6.1. BET Surface Area and BJH Pore Volumes of A-SZNO and B-SZNO catalysts

Sample	BET Surface Area (m^2/g)	BJH Pore Volume (cm^3/g)
A-SZNO	0.914	0.081
B-SZNO	0.720	0.075

A drawback of using perovskite-based materials is the high calcination temperatures required for their calcination that results in sintering of the material surface. Thus perovskites typically have very low surface areas[31]. The same is observed for the SZNO perovskite-based DFMs where their surface areas are <1 m^2/g (**Table 1**).

XRD patterns revealed that the material was a mixture of $SrZrO_3$, $SrCO_3$ and SrO (**Figure 6.2**). The high absorptivity of CO_2 on Sr-oxides implies that the formation of a single phase $SrZrO_3$ is difficult. The method for synthesizing such alkaline-earth based perovskites likely needs revisiting in future work. Area under peaks were calculated for estimating the ratio of various phases present in the material. For Sr deficient material (A-SZNO) the ratio of phases $SrO:SrZrO_3:SrCO_3$ was 1.06:1:0.48, for Zr deficient material (B-SZNO) the ratio was 1.16:1:0.46. Note the higher SrO content of B-SZNO which is likely due to lower Zr:Sr ratio.

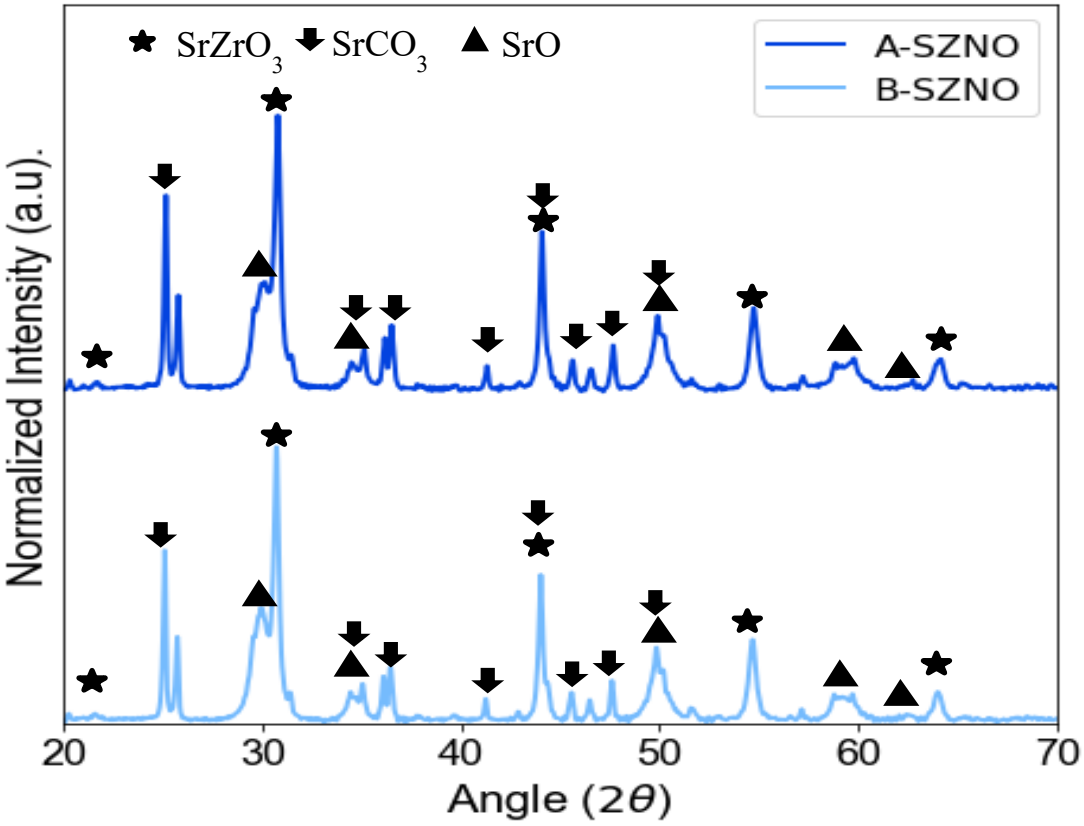

Figure 6.2. X-ray diffractograms of as prepared A-SZNO and B-SZNO perovskite-based DFMs indicating identified peaks of SrO, $SrZrO_3$ and $SrCO_3$ phases.

STEM-HAADF images of the SZNO perovskite-based DFMs were collected after reduction in 5% H_2/He at 600°C for 2 hours to reduce Ni to metallic state and observe exsolution of Ni incorporated in the perovskite phase of the material (**Figure 6.3**). Distinct phases that are rich in Sr and Zr are visible in the EDS mapping, confirming the non-homogeneity of the material. Nickel is present in clusters similar to post-exsolution nanoparticles formed in Ni-doped $LaFeO_3$ type perovskites discussed previously[4,20,32]. Notably, most of the Ni is observed to be in the vicinity of SrZr clusters rather than Sr rich clusters. This is further evidence that despite the non-homogeneity of the material

prepared by the synthesis material, Ni is for the most part incorporated in the perovskite phase of the DFM.

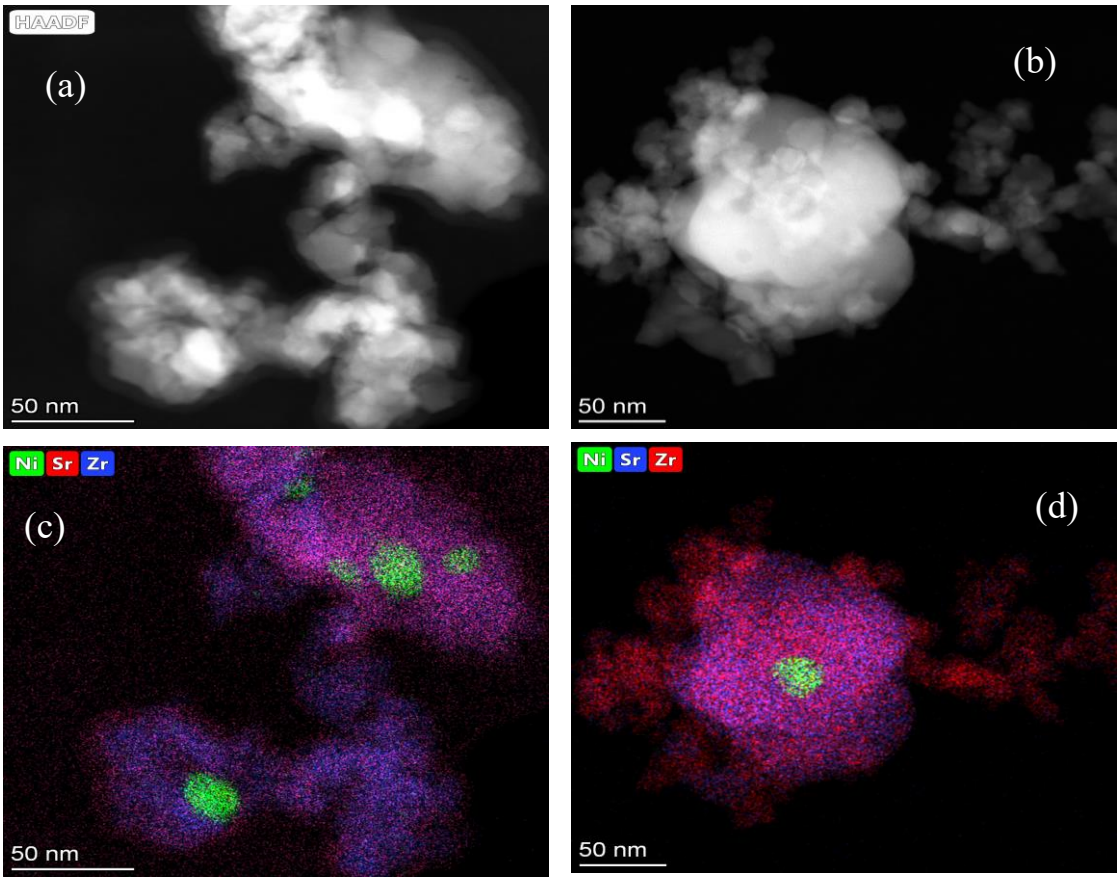

Figure 6.3. STEM-HAADF micrographs of (a) A-SZNO and (b) B-SZNO and respective EDS mapping images (c, d) after reduction in 5% H_2/He at 600°C for 2 hours.

The size distribution of Ni clusters was estimated by measuring sizes of sampled nanoparticles in the STEM-EDS images with the ImageJ software[30]. The mean particle size of Ni clusters in A-SZNO is 12 nm whereas in B-SZNO it is 8 nm (**Figure 6.4**). This is consistent with the trend that A-site stoichiometric deficiencies promote exsolution and result in larger exsolved nanoparticles[19,33]. However, the non-homogeneity of the materials means that those systems are not a like-for-like comparison.

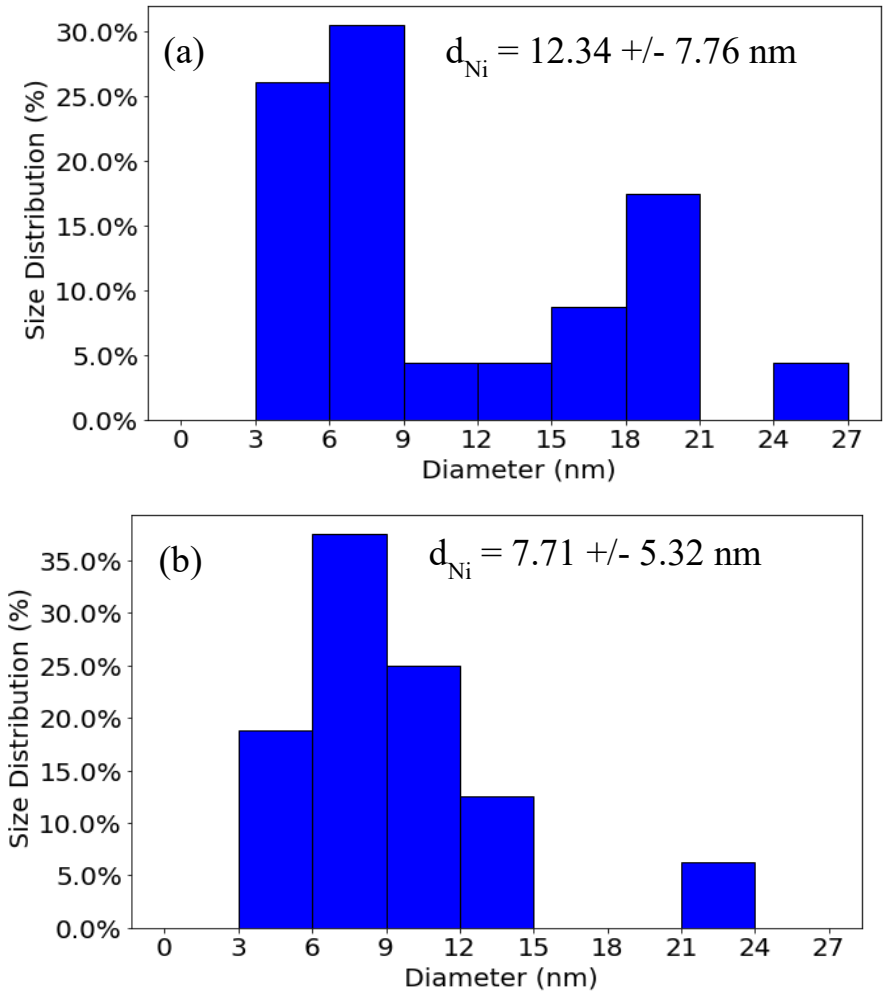

Figure 6.4. Histograms of Ni nanoparticle size distribution in (a) A-SZNO and (b) B-SZNO as seen in STEM-HAADF and EDS images after reduction in 5% H_2/He at 600°C for 2 hours.

Perovskite-based DFMs were first reduced at 600°C in 5% H_2/He for 2 hours and then carbonated in 10% CO2/He at 100°C for 1 hour. The amount of CO_2 adsorbed over 100 mg of A-SZNO was calculated to be 3.49 mmol while, 3.93 mmol of CO_2 were adsorbed over B-SZNO (**Figure 6.5**). Note that B-SZNO has a lower surface area than A-SZNO, implying that B-SZNO likely has a greater number of basic sites per unit area over which CO_2 is adsorbed.

Temperature programmed surface reactions are useful experiments to identify the

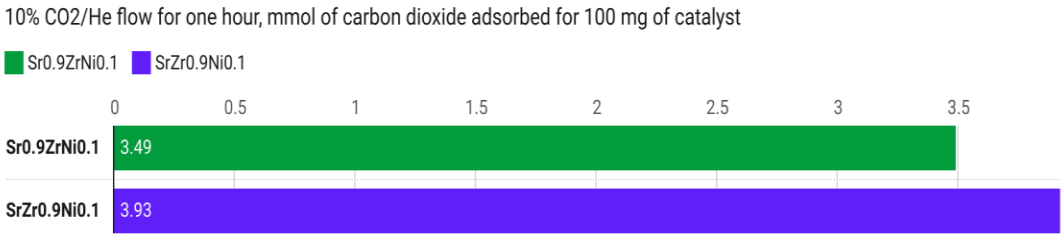

Figure 6.5. Quantities of CO_2 adsorbed over A-SZNO ($Sr_{0.9}ZrNi_{0.1}O_3$) and B-SZNO ($SrZr_{0.9}Ni_{0.1}O_3$)

onset temperature of reactions at which reacting species cross the threshold of activation. The SZNO DFMs were first carbonated under 10% CO_2/He at 100°C for 1 hour to saturate surface with carbonate species. Subsequently, after purging in He for 10 minutes, 10% CH_4/He was introduced to the quartz tube reactor and the temperature was ramped to 700°C at 10°C/min. A-SZNO shows an onset of both CO and H_2 formation ~460°C while B-SZNO shows onset of H_2 production at ~490°C (**Figure 6.6**). In the case of B-SZNO, a continuous presence of CO is seen throughout the TPSR profile with a sharp rise in CO formation seen at 490°C when H_2 formation also begins. Pending further studies, we surmise that CO_2 adsorbs on weaker sites for B-SZNO and the release of CO corresponds to oxidation of the reduced perovskite by adsorbed CO_2. The earlier onset of

CH4 reduction on A-SZNO implies a greater availability of Ni sites on the catalysts either due to a greater degree of exsolution or the higher perovskite content in the mixture as seen in the XRD.

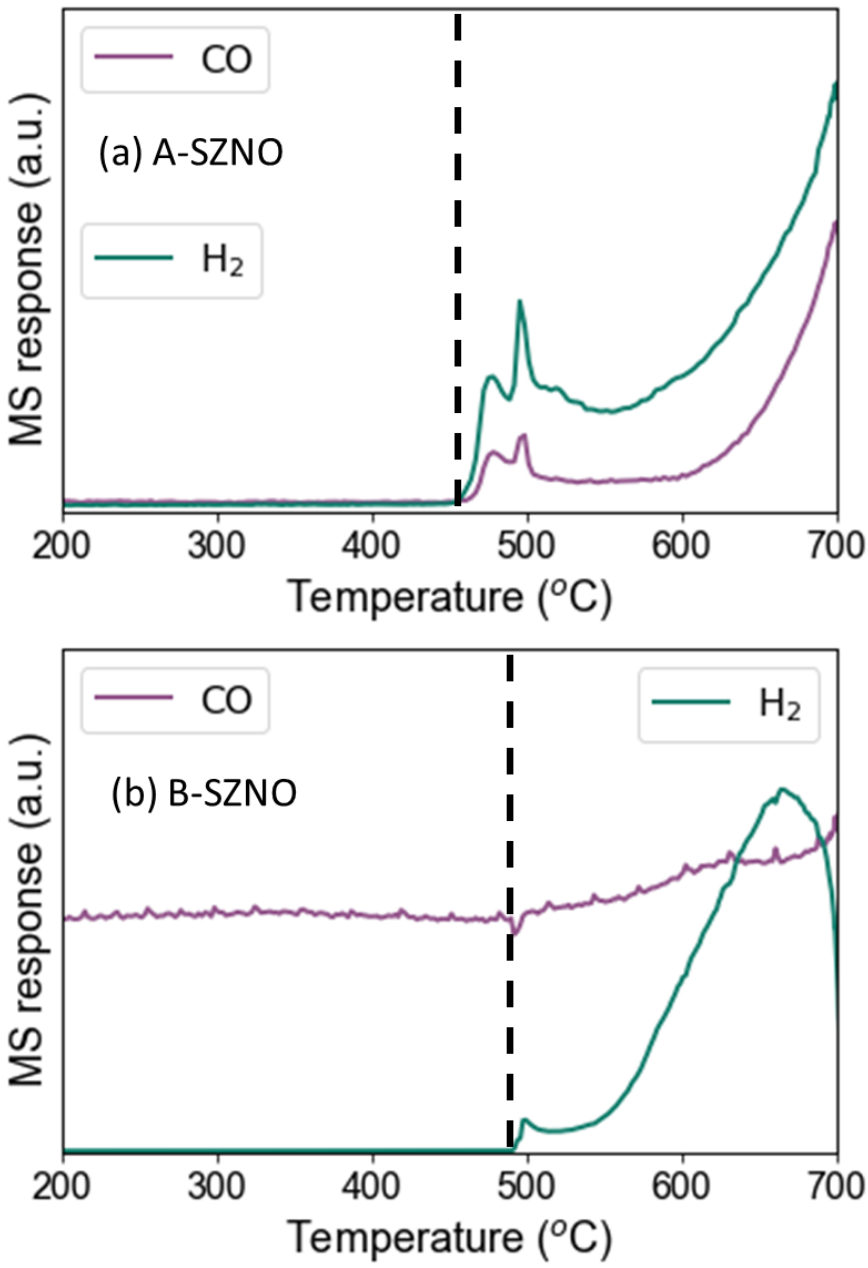

Figure 6.6. Temperature programmed surface reaction profiles of perovskite based DFMs (a) A-SZNO and (b) B-SZNO after carbonation, under 10% CH_4/He.

A cyclic looping test was conducted over the DFM materials with alternating streams of 10% CO_2 (capture step) and 10% CH_4 (utilization step) flowing for 30 minutes each for 5 cycles. A purging stream of helium was also flown in between the carbonation and utilization steps. Both the capture and utilization steps were done at 650°C.

Interestingly, the amount of CO_2 adsorbed in the first cycle was lower than subsequent cycles, but this difference was starker for A-SZNO (1.4 mmol in carbonation step 1, v/s 2.8 mmol in capture step 2) compared to B-SZNO (2.8 mmol in step 1 v/s 3.2 mmol in step 2) (**Figure 6.7**). Methane conversion remained steady for B-SZNO but show a step-up for A-SZNO between step 1 and step 2. The conversion of CH_4 was higher for B-SZNO than A-SZNO throughout the 5 cycles. Despite that, the amount of syngas product formed was higher for A-SZNO (**Figure 6.8**). B-SZNO showed a higher degree of water formation and pending further analysis, we surmise formed greater coking products.

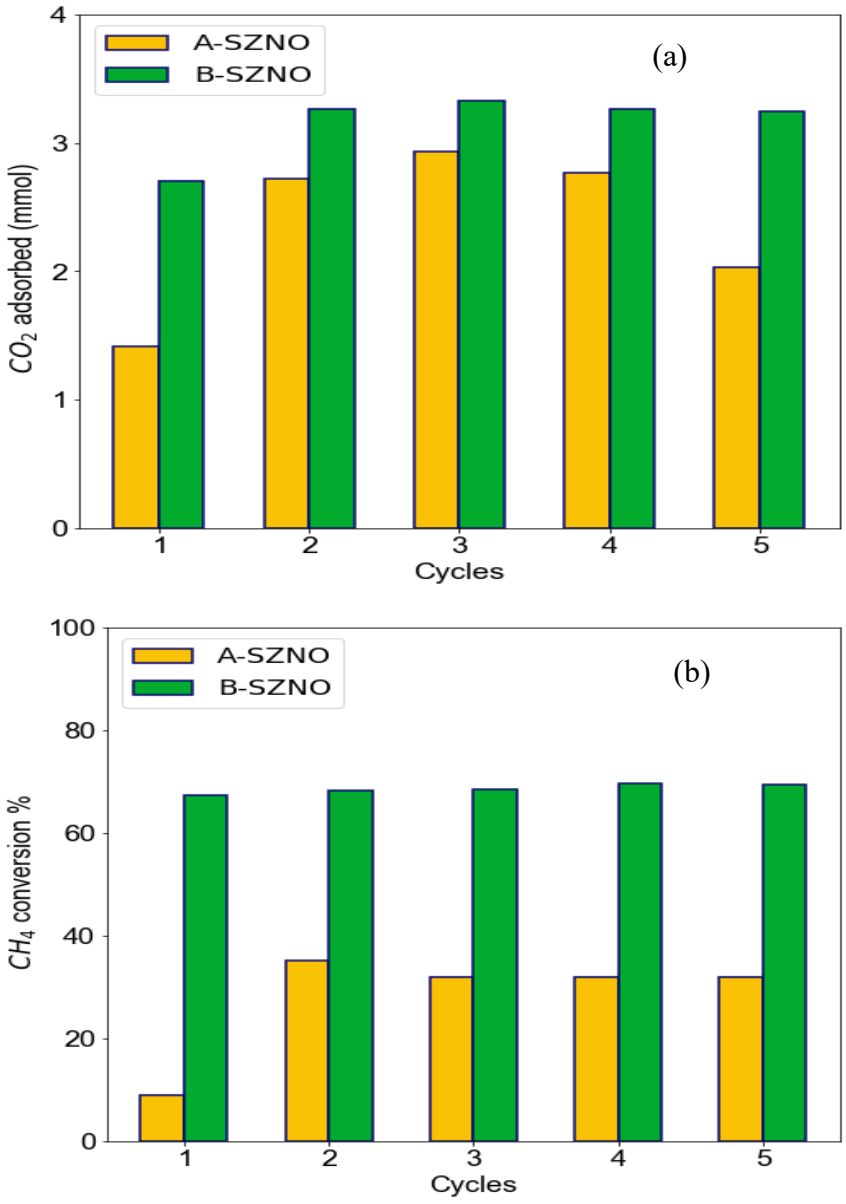

Figure 6.7. (a) CO_2 adsorbed and (b) CH_4 converted during cyclic looping test for CO_2 capture and utilization over A-SZNO and B-SZNO DFMs.

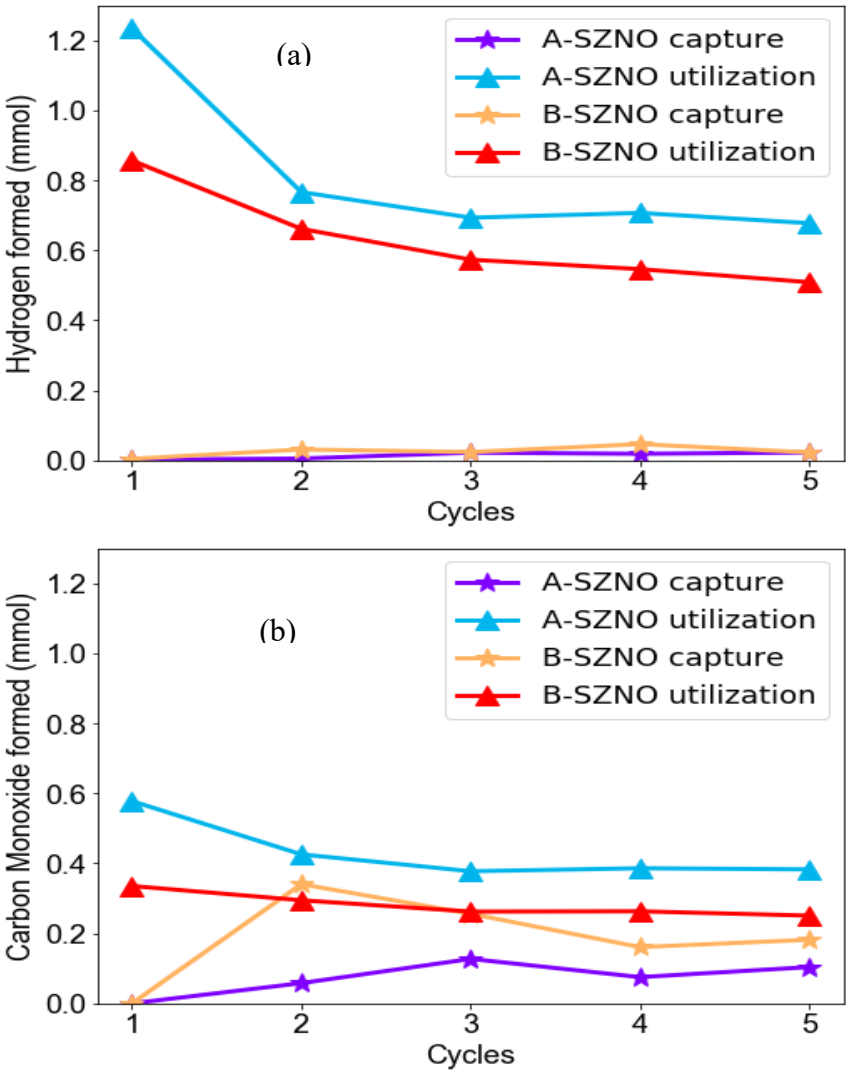

Figure 6.8. (a) H_2 and (b) CO product formed during capture and utilization steps of cyclic looping CO_2 capture and utilization over SZNO DFMs.

6.5 Future Work

From the BET surface area analysis, it is evident that the SZNO perovskites have very low surface area even for perovskite-based materials. A significant improvement could be done by identifying perovskite based DFMs that calcine at temperatures lower than 900°C. Alternatively, silica-based mesoporous templates that provide higher surface

area could be employed that increase surface areas by orders of magnitude[34,35]. Metal organic frameworks (MOFs) can also be used as templates for increasing surface area of catalysts[35]. Geng et al. synthesized $LaMnO_3$ and $LaCoO_3$ catalysts derived from MOFs that had surface areas of 40 m^2/g and 64 m^2/g[36]. Methods to alter sol-gel chemistry to increase surface area such as addition of polymer templates[37,38] or surfactants[39,40], changing pH[41] and addition of co-solvents such as ethanol or glycol[42].

As seen in our previous work, composition, co-dopants, stoichiometric defects can govern exsolution behavior of perovskites. Moreover, synthesis conditions and process parameters such as reduction temperature and duration can affect size and composition of exsolved nanoparticles. The optimization of exsolved nanoparticles can thus maximize both the activity of catalyst towards CO_2 and the reducing gas as well as durability of material. The defect engineering framework we have developed can be a platform for the rational design of catalysts for the specific application of CO_2 capture step and utilization step.

The utilization step in the looping test described earlier used CH_4 as the fuel molecule. This was in part because of our previous work with Dry Methane Reforming with perovskite catalyst. H_2 is a stronger reducing agent and comparing the different redox environments between CH_4-reduction and H_2-reduction of the carbonated catalyst. This can be a useful experiment in understanding the bidirectional exsolution of reducible metals in redox environments.

6.6 Acknowledgement

I would like to acknowledge the contributions of Jacob Graves to this preliminary study. Jacob helped with catalyst synthesis and characterization of the perovskite-based materials.

6.7 References

(1) Aresta, M.; Dibenedetto, A.; Angelini, A. The Changing Paradigm in CO2 Utilization. *J. CO2 Util.* **2013**, *3–4*, 65–73. https://doi.org/10.1016/j.jcou.2013.08.001.

(2) Hepburn, C.; Adlen, E.; Beddington, J.; Carter, E. A.; Fuss, S.; Mac Dowell, N.; Minx, J. C.; Smith, P.; Williams, C. K. The Technological and Economic Prospects for CO2 Utilization and Removal. *Nature* **2019**, *575* (7781), 87–97. https://doi.org/10.1038/s41586-019-1681-6.

(3) Omodolor, I. S.; Otor, H. O.; Andonegui, J. A.; Allen, B. J.; Alba-Rubio, A. C. Dual-Function Materials for CO2Capture and Conversion: A Review. *Ind. Eng. Chem. Res.* **2020**, *59* (40), 17612–17631. https://doi.org/10.1021/acs.iecr.0c02218.

(4) Jo, S.; Cruz, L.; Shah, S.; Wasantwisut, S.; Phan, A.; Gilliard-Abdulaziz, K. L. Perspective on Sorption Enhanced Bifunctional Catalysts to Produce Hydrocarbons. *ACS Catal.* **2022**, *12* (13), 7486–7510. https://doi.org/10.1021/acscatal.2c01646.

(5) Gallego, G. S.; Marín, J. G.; Batiot-Dupeyrat, C.; Barrault, J.; Mondragón, F. Influence of Pr and Ce in Dry Methane Reforming Catalysts Produced from La1-XAxNiO3-δ Perovskites. *Appl. Catal. A Gen.* **2009**, *369* (1–2), 97–103. https://doi.org/10.1016/j.apcata.2009.09.004.

(6) Sankar, M.; Dimitratos, N.; Miedziak, P. J.; Wells, P. P.; Kiely, C. J.; Hutchings, G. J. Designing Bimetallic Catalysts for a Green and Sustainable Future. *Chem. Soc. Rev.* **2012**, *41* (24), 8099–8139. https://doi.org/10.1039/c2cs35296f.

(7) Oemar, U.; Ang, P. S.; Hidajat, K.; Kawi, S. Promotional Effect of Fe on Perovskite LaNixFe 1-XO3 Catalyst for Hydrogen Production via Steam Reforming of Toluene. *Int. J. Hydrogen Energy* **2013**, *38* (14), 5525–5534. https://doi.org/10.1016/j.ijhydene.2013.02.083.

(8) Steiger, P.; Delmelle, R.; Foppiano, D.; Holzer, L.; Heel, A.; Nachtegaal, M.; Kröcher, O.; Ferri, D. Structural Reversibility and Nickel Particle Stability in Lanthanum Iron Nickel Perovskite-Type Catalysts. *ChemSusChem* **2017**, *10* (11), 2505–2517. https://doi.org/10.1002/cssc.201700358.

(9) Lim, H. S.; Lee, M.; Kim, Y.; Kang, D.; Lee, J. W. Low-Temperature CO2 Hydrogenation to CO on Ni-Incorporated LaCoO3 Perovskite Catalysts. *Int. J. Hydrogen Energy* **2021**, No. xxxx, 1–10. https://doi.org/10.1016/j.ijhydene.2021.02.085.

(10) Zhao, Baohuai; Yan, B.; Jiang, Z.; Yao, S.; Liu, Z.; Wu, Qiyuan; Ran, R.; Senanayake, S. D.; Weng, D.; Chen, J. G. High Selectivity of CO2 Hydrogenation to CO by Controlling the Valence State of Nickel Using Perovskite. *Chem. Commun.* **2018**, *54*, 7354–7357. https://doi.org/doi:10.1039/C8CC03829E.

(11) Gao, X.; Ashok, J.; Kawi, S. Smart Designs of Anti-Coking and Anti-Sintering Ni-Based Catalysts for Dry Reforming of Methane: A Recent Review. *Reactions* **2020**, *1* (2), 162–194. https://doi.org/10.3390/reactions1020013.

(12) Fan, W. K.; Tahir, M. Recent Trends in Developments of Active Metals and Heterogenous Materials for Catalytic CO2hydrogenation to Renewable Methane: A Review. *J. Environ. Chem. Eng.* **2021**, *9* (4), 105460. https://doi.org/10.1016/j.jece.2021.105460.

(13) Neagu, D.; Oh, T. S.; Miller, D. N.; Ménard, H.; Bukhari, S. M.; Gamble, S. R.; Gorte, R. J.; Vohs, J. M.; Irvine, J. T. S. Nano-Socketed Nickel Particles with Enhanced Coking Resistance Grown in Situ by Redox Exsolution. *Nat. Commun.* **2015**, *6* (8120). https://doi.org/10.1038/ncomms9120.

(14) Lai, K. Y.; Manthiram, A. Self-Regenerating Co-Fe Nanoparticles on Perovskite Oxides as a Hydrocarbon Fuel Oxidation Catalyst in Solid Oxide Fuel Cells. *Chem. Mater.* **2018**, *30* (8), 2515–2525. https://doi.org/10.1021/acs.chemmater.7b04569.

(15) Labhasetwar, N.; Saravanan, G.; Kumar Megarajan, S.; Manwar, N.; Khobragade, R.; Doggali, P.; Grasset, F. Perovskite-Type Catalytic Materials for Environmental Applications. *Sci. Technol. Adv. Mater.* **2015**, *16* (3), 1–13. https://doi.org/10.1088/1468-6996/16/3/036002.

(16) Lindenthal, L.; Popovic, J.; Rameshan, R.; Huber, J.; Schrenk, F.; Ruh, T.; Nenning, A.; Löffler, S.; Opitz, A. K.; Rameshan, C. Novel Perovskite Catalysts for CO2 Utilization - Exsolution Enhanced Reverse Water-Gas Shift Activity. *Appl. Catal. B Environ.* **2021**, *292* (January), 120183. https://doi.org/10.1016/j.apcatb.2021.120183.

(17) Zheng, Y.; Li, K.; Wang, H.; Tian, D.; Wang, Y.; Zhu, X.; Wei, Y.; Zheng, M.; Luo, Y. Designed Oxygen Carriers from Macroporous LaFeO3 Supported CeO2 for Chemical-Looping Reforming of Methane. *Appl. Catal. B Environ.* **2017**, *202*, 51–63. https://doi.org/10.1016/j.apcatb.2016.08.024.

(18) Zhu, K.; Wu, T.; Li, M.; Lu, R.; Zhu, X.; Yang, W. Perovskites Decorated with Oxygen Vacancies and Fe-Ni Alloy Nanoparticles as High-Efficiency Electrocatalysts for the Oxygen Evolution Reaction. *J. Mater. Chem. A* **2017**, *5* (37), 19836–19845. https://doi.org/10.1039/c7ta05404a.

(19) Shah, S.; Sayono, S.; Ynzunza, J.; Pan, R.; Xu, M.; Pan, X.; Gilliard-Abdulaziz, K. L. The Effects of Stoichiometry on the Properties of Exsolved Ni-Fe Alloy Nanoparticles for Dry Methane Reforming. *AIChE J.* **2020**, *66* (12), e17078. https://doi.org/https://doi.org/10.1002/aic.17078.

(20) Shah, S.; Xu, M.; Pan, X.; Gilliard-Abdulaziz, K. L. Exsolution of Embedded Ni–Fe–Co Nanoparticles: Implications for Dry Reforming of Methane. *ACS Appl. Nano Mater.* **2021**, *4* (8), 8626–8636. https://doi.org/10.1021/acsanm.1c02268.

(21) Li, J.; Singh, U. G.; Bennett, J. W.; Page, K.; Weaver, J. C.; Zhang, J. P.; Proffen, T.; Rappe, A. M.; Scott, S.; Seshadri, R. BaCe1-XPdxO3-δ($0 \leq x \leq 0.1$): Redox Controlled Ingress and Egress of Palladium in a Perovskite. *Chem. Mater.* **2007**, *19* (6), 1418–1426. https://doi.org/10.1021/cm062500i.

(22) Neagu, D.; Papaioannou, E. I.; Ramli, W. K. W.; Miller, D. N.; Murdoch, B. J.; Ménard, H.; Umar, A.; Barlow, A. J.; Cumpson, P. J.; Irvine, J. T. S.; Metcalfe, I. S. Demonstration of Chemistry at a Point through Restructuring and Catalytic Activation at Anchored Nanoparticles. *Nat. Commun.* **2017**, *8* (1). https://doi.org/10.1038/s41467-017-01880-y.

(23) Dai, S.; Zhang, S.; Katz, M. B.; Graham, G. W.; Pan, X. In Situ Observation of Rh-CaTiO3Catalysts during Reduction and Oxidation Treatments by Transmission Electron Microscopy. *ACS Catal.* **2017**, *7* (3), 1579–1582. https://doi.org/10.1021/acscatal.6b03604.

(24) Li, B.; Katz, M. B.; Duan, Y.; Du, X.; Zhang, K.; Chen, L.; Van Der Ven, A.; Graham, G. W.; Pan, X. A Joint Theoretical and Experimental Study of Phase Equilibria and Evolution in Pt-Doped Calcium Titanate under Redox Conditions. *Chem. Mater.* **2015**, *27* (1), 18–28. https://doi.org/10.1021/cm5022239.

(25) Lin, C.; Jang, J. B.; Zhang, L.; Stach, E. A.; Gorte, R. J. Improved Coking Resistance of "Intelligent" Ni Catalysts Prepared by Atomic Layer Deposition. *ACS Catal.* **2018**, *8* (8), 7679–7687. https://doi.org/10.1021/acscatal.8b01598.

(26) Lin, C.; Foucher, A. C.; Ji, Y.; Curran, C. D.; Stach, E. A.; McIntosh, S.; Gorte, R. J. "Intelligent" Pt Catalysts Studied on High-Surface-Area $CaTiO_3$ Films. *ACS Catal.* **2019**, 7318–7327. https://doi.org/10.1021/acscatal.9b01278.

(27) Sutthiumporn, K.; Maneerung, T.; Kathiraser, Y.; Kawi, S. CO2 Dry-Reforming of Methane over La0.8Sr 0.2Ni0.8M0.2O3 Perovskite (M = Bi, Co, Cr, Cu, Fe): Roles of Lattice Oxygen on C-H Activation and Carbon Suppression. *Int. J. Hydrogen Energy* **2012**, *37* (15), 11195–11207. https://doi.org/10.1016/j.ijhydene.2012.04.059.

(28) Khazaal, M. H.; Staniforth, J. Z.; Alfatlawi, Z. A.; Ormerod, R. M.; Darton, R. J. Enhanced Methane Reforming Activity of a Hydrothermally Synthesized Codoped Perovskite Catalyst. *Energy and Fuels* **2018**, *32* (12), 12826–12832. https://doi.org/10.1021/acs.energyfuels.8b02848.

(29) Dama, S.; Ghodke, S. R.; Bobade, R.; Gurav, H. R.; Chilukuri, S. Active and Durable Alkaline Earth Metal Substituted Perovskite Catalysts for Dry Reforming of Methane. *Appl. Catal. B Environ.* **2018**, *224* (October 2017), 146–158.

(30) Schneider, C. A.; Rasband, W. S.; Eliceiri, K. W. NIH Image to ImageJ: 25 Years of Image Analysis. *Nat. Methods* **2012**, *9* (7), 671–675.

(31) Choudhary, V. R.; Banerjee, S.; Uphade, B. S. Activation by Hydrothermal Treatment of Low Surface Area ABO3-Type Perovskite Oxide Catalysts. *Appl. Catal. A Gen.* **2000**, *197* (2), 183–186. https://doi.org/10.1016/S0926-860X(99)00485-8.

(32) Shah, S.; Sayono, S.; Ynzunza, J.; Pan, R.; Xu, M.; Pan, X. Tuning the Activity, Selectivity and Stability of Ni-Fe Bimetallic Nanoparticles for Dry Methane Reforming. *AIChE J.* **2020**, modifications after review.

(33) Neagu, D.; Tsekouras, G.; Miller, D. N.; Ménard, H.; Irvine, J. T. S. In Situ Growth of Nanoparticles through Control of Non-Stoichiometry. *Nat. Chem.* **2013**, *5* (11), 916–923. https://doi.org/10.1038/nchem.1773.

(34) Nguyen, S. V.; Szabo, V.; Trong On, D.; Kaliaguine, S. Mesoporous Silica Supported LaCoO3 Perovskites as Catalysts for Methane Oxidation. *Microporous Mesoporous Mater.* **2002**, *54* (1–2), 51–61. https://doi.org/10.1016/S1387-1811(02)00340-2.

(35) Samanta, A.; Zhao, A.; Shimizu, G. K. H.; Sarkar, P.; Gupta, R. Post-Combustion CO 2 Capture Using Solid Sorbents: A Review. *Ind. Eng. Chem. Res.* **2012**, *51* (4), 1438–1463. https://doi.org/10.1021/ie200686q.

(36) Geng, G.; Cai, M.; Fang, R.; Luan, Q.; Zhang, Z.; Song, J.; Zhang, J. Metal-Organic Frameworks-Derived Perovskite Catalysts for Efficient Degradation of 2, 4-Dichlorophenol via Peroxymonosulfate Activation. *Appl. Surf. Sci.* **2020**, *534* (August), 147467. https://doi.org/10.1016/j.apsusc.2020.147467.

(37) Melezhyk, O. V.; Prudius, S. V.; Brei, V. V. Sol-Gel Polymer-Template Synthesis of Mesoporous WO3/ZrO2. *Microporous Mesoporous Mater.* **2001**, *49* (1–3), 39–44. https://doi.org/10.1016/S1387-1811(01)00397-3.

(38) Feng, J.; Liu, T.; Xu, Y.; Zhao, J.; He, Y. Effects of PVA Content on the Synthesis of LaFeO3 via Sol-Gel Route. *Ceram. Int.* **2011**, *37* (4), 1203–1207. https://doi.org/10.1016/j.ceramint.2010.11.045.

(39) Zhang, S.; Jiang, F.; Qu, G.; Lin, C. Synthesis of Single-Crystalline Perovskite Barium Titanate Nanorods by a Combined Route Based on Sol-Gel and Surfactant-Templated Methods. *Mater. Lett.* **2008**, *62* (15), 2225–2228. https://doi.org/10.1016/j.matlet.2007.11.055.

(40) Carreon, M. A.; Guliants, V. V.; Olga Guerrero-Perez, M.; Bañares, M. A. Mesostructured Mixed Mo-V-Nb Oxides for Propane Ammoxidation. *Catal. Commun.* **2009**, *10* (4), 416–420. https://doi.org/10.1016/j.catcom.2008.10.008.

(41) Lopez, T.; Garcia-Cruz, I.; Gomez, R. Synthesis of Magnesium Oxide by the Sol-Gel Method: Effect of the PH on the Surface Hydroxylation. *J. Catal.* **1991**, *127* (1), 75–85. https://doi.org/10.1016/0021-9517(91)90210-U.

(42) Abbasi, B.; Guo, H.; Wu, H.; Tailor, H. N.; Ye, Z. G. An Ethylene Glycol-Based New Sol-Gel Route to Multiferroic (1-x)LaCrO3-x BiCrO3 Solid Solution. *Can. J. Chem.* **2018**, *96* (2), 255–259. https://doi.org/10.1139/cjc-2017-0512.

CHAPTER 7. CONCLUSION AND FUTURE OUTLOOK

7.1 Conclusions

This study began with uncovering the factors that govern the dynamics of exsolution while also exploring and optimizing nanoparticles synthesized in-situ via exsolution for application in catalysis of the dry methane reforming reaction. There was precedent of manipulating exsolution through the introduction of stoichiometric defects[1]. We took that work forward by exploiting defect engineering to drive exsolution forward in Ni-doped $LaFeO_3$-type perovskites as discussed in Chapter 2. We uncovered the implications of stoichiometrically driven exsolution in the context of catalysis by studying activity and stability towards dry methane reforming[2]. A-site deficient perovskite displayed a significantly greater degree of exsolution of Ni-Fe nanoparticles. The nanoparticles thus formed were larger in size and also richer in Fe composition. Consequently, the catalytic activity was much lower than samples with La present in stoichiometric quantities. The larger nanoparticles also bind to the parent-perovskite support less strongly which renders them susceptible to particle growth, through sintering or additional exsolution, as well as coking. Additionally, the sample showed a lower H_2/CO ratio due to reverse water gas shift as well as CO_2 consumption by the reduced perovskite. The La-deficient perovskite also showed a more drastic decline in activity than the La-stoichiometric sample, with a much lower activity seen at a higher onset temperature.

The concept of defect engineering perovskite precursors was extended further by introducing Co as a co-dopant along with Ni in $LaFeO_3$-type perovskites[3]. The underlying idea was that Co having lower reducibility than Ni would have an effect on the dynamics of exsolution. Furthermore, we also wanted to observe the synergistic effect of having Ni-Fe-Co trimetallic alloys supported over the parent-perovskite support in catalyzing dry methane reforming. Indeed, lower reducibility resulted in nanoparticles that were smaller and well-dispersed than the Ni-Fe nanoparticles. In fact, the La-deficient sample in this case was the best performing catalyst despite their larger initial size. Changing the Ni:Co ratio had an effect on the long-term activity of the catalyst due to changing composition of the nanoparticles in the redox environment of the reaction. We also explored the effect of reduction temperature on the size and composition of exsolved nanoparticles and thus catalyst performance. Catalysts reduced at 800°C showed higher initial activity towards DRM at 900°C than catalysts reduced at 950°C which we posit is due to smaller nanoparticles[4] that are also relatively rich in Ni. However, over time at 900°C, their activity declined to a level very similar to the high-temperature reduced perovskites. We suggest that exsolution continues in the reductive environment of DRM and the nanoparticle characteristics evolve according to redox conditions to which the perovskite-based material is exposed. These results are discussed in chapter 3. This study allowed us to outline additional factors that can be optimized for the in-situ synthesis of nanoparticles by controlling exsolution with the levers of perovskite composition, the presence of defects and the reduction conditions. This study

also showed that exsolution is a dynamic process and that controlling the kinetics of the process would be crucial to the goal of optimized synthesis of nanoparticles.

Having seen the control of kinetics of exsolution on nanoparticle characteristics in chapter 2 and chapter 3, we set out to determine the growth and evolution of the nanoparticles during reduction (discussed further in chapter 4). Furthermore, nanoparticles evolve in the redox environment of reaction or regress in the perovskite upon exsolution. Interactions between Ni and Fe in bimetallic catalysts for dry methane reforming has been discussed before[5,6]. CO_2 oxidized Fe partially forming a Fe/FeO_x redox couple which oxidized surface carbon products thus improving long-term activity of the catalyst. The bidirectional exsolution however adds a layer of complexity to these interactions. The goal to observe the changing states of Ni, Fe, parent perovskite in reduction, reaction and oxidation conditions, justified the need to use X-ray Absorption Spectroscopy (XAS). X-ray Absorption Near Edge Spectroscopy (XANES) allowed the in-situ observation of bulk average chemical oxidation states of Ni and Fe as they changed over time during each treatment. Extended X-ray Absorption Fine Structure (EXAFS) analysis shed light on the local neighborhoods of the Ni and Fe atoms.

We observed that Ni, being more predisposed to reduction, reduces earlier than Fe, with a transition in the Ni XANES observed at 270°C. The transition in the oxidation state of Fe occurs at 700°C. Thus, Fe follows Ni in reduction and gradually enters the nanoparticles, which become richer in Fe composition over time. Upon introduction to DRM reaction gases, Fe is oxidized immediately and returns to the perovskite phase, leaving Ni-rich metallic nanoparticles supported by La_2O_3-$LaFeO_3$. The oxidation of the

perovskite-based material indeed causes the nanoparticles to regress, but this process is gradual. The trend is opposite to that of reduction, with Fe oxidizing earlier, forming a γ-Fe_2O_3 intermediate phase, and reentering the perovskite phase. The oxidation of Ni is slower, its reentry into the perovskite phase is gradual and an NiO intermediate phase is also formed. Ex-situ observations with Scanning Tunneling Electron Microscopy High-Angle Annular Dark Field (STEM-HAADF) and Energy Dispersive X-ray Spectroscopy (EDS) provided supporting evidence for these observations. As the duration for which the perovskite was reduced in H_2/He increased, the nanoparticles increased in size and also became richer in Fe composition. Ni-rich metallic particles, and NiO nanoparticles were seen after DRM and oxidation testing respectively. Tracking the state of exsolution allows a firmer control on the characteristics of the exsolved nanoparticles which is a big step forward in the tunable synthesis of catalytic materials.

Complex concentrated alloys are interesting candidates for catalytic materials due to the synergistic interactions between the metals that provide high activity and the entropic stabilization that make them more durable for challenging reaction conditions[7–11]. The variety of adsorption sites also aid the activity towards catalyzing reactive molecules[12]. There were few studies on their application in thermocatalytic reactions. Moreover, the controlled nucleating nanoparticles consisting of multiple metals on a support remained a challenge. As discussed in chapter 5, we proposed in-situ exsolution in perovskites as a facile method for the synthesis of CCA nanoparticles. Nanoparticles consisting of Fe, Ni, Co, Cu and Pd were exsolved by introducing these metals as substituents in a $LaFeO_3$-type perovskite and reducing them in 5% H_2/He. The

composition of the nanoparticles was also tuned by changing the temperature of reduction or the duration for which the perovskite precursor was reduced. Higher reduction times and longer reduction durations also caused phase-separations of nanoparticles as heterostructures such as core-shell and Janus nanoparticles were observed. The perovskite-based CCA catalysts showed excellent activity and stability towards dry methane reforming, compared to Ni-Fe and Ni-Fe-Co nanoparticles discussed earlier. This was attributed to synergistic contributions such as higher oxygen mobility because of Cu, and enhanced reducibility of Ni due the addition of Pd.

In chapter 6, the use of the perovskite platform for the development of dual functional materials is discussed. Perovskites containing alkaline earth metals such as Sr can be used for enhanced sorption of CO_2. The adsorbed CO_2 can then be reacted with fuel gases such as CH_4 or H_2 over catalysts exsolved from the perovskite precursor. The perovskite can be oxidized and regenerated by reintroducing CO_2 and the process can continue cyclically. Preliminary data from the testing of $Sr(ZrNi)O_3$ type perovskites are discussed and future work in the project are outlined. The low surface area of the perovskites due to the requirement of high temperature calcination for their synthesis remains a barrier in the development of these materials.

The research conducted in the writing of this dissertation can be summarized as the exploration of perovskites as a platform for novel catalyst materials. The purported stabilization of nanoparticles anchored to the parent-perovskite support and the tunability of composition and size can be used for earth-abundant metals to be used sustainably for long durations in catalytic applications. This can in-turn reduce the need for mining of

catalytic metals while being competitive in activity compared to more expensive metals such as platinum and palladium. We also discussed applications of particular interest to solving the climate crisis, by converting greenhouse gases such as CO_2 and CH_4 into high-value petrochemical precursors such as syngas.

7.2 Future Outlook

Future efforts should focus on increasing the surface area of perovskite materials. The surface areas of the materials discussed here, at ~1-10 m^2/g are orders of magnitude less than commercially applicable materials. Strategies to modify sol-gel chemistry to increase surface area include raising the pH of the initial sol[13,14] and the addition of different co-solvents such as ethanol[15] or ethylene glycol[16]. The addition of surfactants, polymers such as PEG or PVA, biopolymers such as cellulose can also increase surface area of the materials synthesized via sol-gel method[17]. Mesoporous silica templates such as MCM-41 or SBA-15 have also been used to increase surface area and their effect on catalyst activity and stability should be explored[18,19]. Perovskite composites with MOFs[20] and zeolites[21] can also be explored for enhanced adsorption of specific molecules along with high catalyst surface areas.

As is evident that the redox environment has a very notable effect on characteristics of nanoparticles. Thus, the conditions in which perovskites are reduced, oxidized or subjected to reactions can be controlled and the nanoparticle evolution can be examined. For example, the perovskite can be reduced in methane, a milder reducing agent than H_2 or oxidized in CO_2. Exsolution can also be modulated by electrochemical switching by reducing or oxidizing the perovskite by an applied voltage[22,23] in a similar

manner to chemical reduction. This route could allow greater control on the exsolution process and thus the nanoparticle size and composition. Calcination temperatures for the annealing of the xerogel into the perovskite oxide changes the grain sizes which in-turn affects the nucleation of nanoparticles[24,25].

The reducibility of the perovskite could be altered by changing or partially substituting either A or B site. For example, changing the metal on the B-site affects reducibility of the perovskite which may result in exsolution of doped catalytic metals such as Ni into smaller particles[26]. The introduction of A-site dopants such as Ca, Sr or Ce could alter surface properties of the support and also introduce O-vacancies that control exsolution[27–31]. Lastly, the tailor-ability of perovskites as catalysts would require demonstration in newer applications in reactions with commercial significance. Thermal-catalytic reactions such as CO_2 hydrogenation to methanol, CH_4 partial oxidation to methanol or higher hydrocarbons or electro-catalytic reactions such as oxygen evolution or CO_2 reduction are reactions that require novel catalytic solutions. The perovskite platform can be explored for potential candidate materials for these reactions.

A lot of progress has been made in the synthesis of nanoparticle catalysts from perovskites since they were first described for their self-regenerative properties[32–34]. The progress in this research area has served as a guide for this research and is discussed with due credit given. This research hopes to inform future conversations about the perovskite materials and their application as sustainable catalytic materials.

7.3 References:

(1) Neagu, D.; Tsekouras, G.; Miller, D. N.; Ménard, H.; Irvine, J. T. S. In Situ Growth of Nanoparticles through Control of Non-Stoichiometry. *Nat. Chem.* **2013**, *5* (11), 916–923. https://doi.org/10.1038/nchem.1773.

(2) Shah, S.; Sayono, S.; Ynzunza, J.; Pan, R.; Xu, M.; Pan, X.; Gilliard-Abdulaziz, K. L. The Effects of Stoichiometry on the Properties of Exsolved Ni-Fe Alloy Nanoparticles for Dry Methane Reforming. *AIChE J.* **2020**, *66* (12), e17078. https://doi.org/https://doi.org/10.1002/aic.17078.

(3) Shah, S.; Xu, M.; Pan, X.; Gilliard-Abdulaziz, K. L. Exsolution of Embedded Ni–Fe–Co Nanoparticles: Implications for Dry Reforming of Methane. *ACS Appl. Nano Mater.* **2021**, *4* (8), 8626–8636. https://doi.org/10.1021/acsanm.1c02268.

(4) Lai, K. Y.; Manthiram, A. Evolution of Exsolved Nanoparticles on a Perovskite Oxide Surface during a Redox Process. *Chem. Mater.* **2018**, *30* (8), 2838–2847. https://doi.org/10.1021/acs.chemmater.8b01029.

(5) Theofanidis, S. A.; Galvita, V. V.; Poelman, H.; Marin, G. B. Enhanced Carbon-Resistant Dry Reforming Fe-Ni Catalyst: Role of Fe. *ACS Catal.* **2015**, *5* (5), 3028–3039. https://doi.org/10.1021/acscatal.5b00357.

(6) Theofanidis, S. A.; Galvita, V. V.; Sabbe, M.; Poelman, H.; Detavernier, C.; Marin, G. B. Controlling the Stability of a Fe–Ni Reforming Catalyst: Structural Organization of the Active Components. *Appl. Catal. B Environ.* **2017**, *209*, 405–416. https://doi.org/10.1016/j.apcatb.2017.03.025.

(7) Sun, Y.; Dai, S. High-Entropy Materials for Catalysis: A New Frontier. *Sci. Adv.* **2021**, *7* (20). https://doi.org/10.1126/sciadv.abg1600.

(8) Batchelor, T. A. A.; Pedersen, J. K.; Winther, S. H.; Castelli, I. E.; Jacobsen, K. W.; Rossmeisl, J. High-Entropy Alloys as a Discovery Platform for Electrocatalysis. *Joule* **2019**, *3* (3), 834–845. https://doi.org/10.1016/j.joule.2018.12.015.

(9) Löffler, T.; Savan, A.; Garzón-Manjón, A.; Meischein, M.; Scheu, C.; Ludwig, A.; Schuhmann, W. Toward a Paradigm Shift in Electrocatalysis Using Complex Solid Solution Nanoparticles. *ACS Energy Lett.* **2019**, *4* (5), 1206–1214. https://doi.org/10.1021/acsenergylett.9b00531.

(10) Zheng, H.; Luo, G.; Zhang, A.; Lu, X.; He, L. The Synthesis and Catalytic Applications of Nanosized High-Entropy Alloys. *ChemCatChem* **2021**, *13* (3), 806–817. https://doi.org/10.1002/cctc.202001163.

(11) Tomboc, G. M.; Kwon, T.; Joo, J.; Lee, K. High Entropy Alloy Electrocatalysts: A Critical Assessment of Fabrication and Performance. *J. Mater. Chem. A* **2020**, *8* (30), 14844–14862. https://doi.org/10.1039/D0TA05176D.

(12) Li, H.; Han, Y.; Zhao, H.; Qi, W.; Zhang, D.; Yu, Y.; Cai, W.; Li, S.; Lai, J.; Huang, B.; Wang, L. Fast Site-to-Site Electron Transfer of High-Entropy Alloy Nanocatalyst Driving Redox Electrocatalysis. *Nat. Commun.* **2020**, *11*, 5437. https://doi.org/10.1038/s41467-020-19277-9.

(13) Lopez, T.; Garcia-Cruz, I.; Gomez, R. Synthesis of Magnesium Oxide by the Sol-Gel Method: Effect of the PH on the Surface Hydroxylation. *J. Catal.* **1991**, *127* (1), 75–85. https://doi.org/10.1016/0021-9517(91)90210-U.

(14) Job, N.; Pirard, R.; Marien, J.; Pirard, J. P. Porous Carbon Xerogels with Texture Tailored by PH Control during Sol-Gel Process. *Carbon N. Y.* **2004**, *42* (3), 619–628. https://doi.org/10.1016/j.carbon.2003.12.072.

(15) Habibi, N.; Wang, Y.; Arandiyan, H.; Rezaei, M. Low-Temperature Synthesis of Mesoporous Nanocrystalline Magnesium Aluminate (MgAl2O4) Spinel with High Surface Area Using a Novel Modified Sol-Gel Method. *Adv. Powder Technol.* **2017**, *28* (4), 1249–1257. https://doi.org/10.1016/j.apt.2017.02.012.

(16) Abbasi, B.; Guo, H.; Wu, H.; Tailor, H. N.; Ye, Z. G. An Ethylene Glycol-Based New Sol-Gel Route to Multiferroic (1-x)LaCrO3-x BiCrO3 Solid Solution. *Can. J. Chem.* **2018**, *96* (2), 255–259. https://doi.org/10.1139/cjc-2017-0512.

(17) Danks, A. E.; Hall, S. R.; Schnepp, Z. The Evolution of "sol-Gel" Chemistry as a Technique for Materials Synthesis. *Mater. Horizons* **2016**, *3* (2), 91–112. https://doi.org/10.1039/c5mh00260e.

(18) Rivas, I.; Alvarez, J.; Pietri, E.; Pérez-Zurita, M. J.; Goldwasser, M. R. Perovskite-Type Oxides in Methane Dry Reforming: Effect of Their Incorporation into a Mesoporous SBA-15 Silica-Host. *Catal. Today* **2010**, *149* (3–4), 388–393. https://doi.org/10.1016/j.cattod.2009.05.028.

(19) Wang, N.; Yu, X.; Wang, Y.; Chu, W.; Liu, M. A Comparison Study on Methane Dry Reforming with Carbon Dioxide over LaNiO3perovskite Catalysts Supported on Mesoporous SBA-15, MCM-41 and Silica Carrier. *Catal. Today* **2013**, *212*, 98–107. https://doi.org/10.1016/j.cattod.2012.07.022.

(20) Geng, G.; Cai, M.; Fang, R.; Luan, Q.; Zhang, Z.; Song, J.; Zhang, J. Metal-Organic Frameworks-Derived Perovskite Catalysts for Efficient Degradation of 2, 4-Dichlorophenol via Peroxymonosulfate Activation. *Appl. Surf. Sci.* **2020**, *534* (August), 147467. https://doi.org/10.1016/j.apsusc.2020.147467.

(21) Wang, P.; Wang, B.; Liu, Y.; Li, L.; Zhao, H.; Chen, Y.; Li, J.; Liu, S. (Frank); Zhao, K. Ultrastable Perovskite–Zeolite Composite Enabled by Encapsulation and In Situ Passivation. *Angew. Chemie* **2020**, *132* (51), 23300–23306. https://doi.org/10.1002/ange.202011203.

(22) Opitz, A. K.; Nenning, A.; Vonk, V.; Volkov, S.; Bertram, F.; Summerer, H.; Schwarz, S.; Steiger-Thirsfeld, A.; Bernardi, J.; Stierle, A.; Fleig, J. Understanding Electrochemical Switchability of Perovskite-Type Exsolution Catalysts. *Nat. Commun.* **2020**, *11* (1), 1–10. https://doi.org/10.1038/s41467-020-18563-w.

(23) Fan, W.; Sun, Z.; Bai, Y. Manipulating Electrocatalytic Activity of Perovskite Oxide Through Electrochemical Treatment. *Small* **2022**, *18* (12).

(24) Jo, Y. R.; Koo, B.; Seo, M. J.; Kim, J. K.; Lee, S.; Kim, K.; Han, J. W.; Jung, W. C.; Kim, B. J. Growth Kinetics of Individual Co Particles Ex-Solved on SrTi0.75Co0.25O3-? Polycrystalline Perovskite Thin Films. *J. Am. Chem. Soc.* **2019**, *141* (16), 6690–6697. https://doi.org/10.1021/jacs.9b01882.

(25) Kousi, K.; Tang, C.; Metcalfe, I. S.; Neagu, D. Emergence and Future of Exsolved Materials. *Small* **2021**, *17* (21). https://doi.org/10.1002/smll.202006479.

(26) Kwon, O.; Sengodan, S.; Kim, K.; Kim, G.; Jeong, H. Y.; Shin, J.; Ju, Y.; Han, J. W.; Kim, G. Exsolution Trends and Co-Segregation Aspects of Self-Grown Catalyst Nanoparticles in Perovskites. *Nat. Commun.* **2017**, *8* (May), 1–7.

(27) Hui, J.; Neagu, D.; Miller, D. N.; Yue, X.; Ni, C.; Irvine, J. T. S. Metal-Oxide Interactions for Infiltrated Ni Nanoparticles on A-Site Deficient LaxSr1 − 3x/2TiO3. *Solid State Ionics* **2018**, *315* (September 2017), 126–130.

(28) Thalinger, R.; Gocyla, M.; Heggen, M.; Klötzer, B.; Penner, S. Exsolution of Fe and SrO Nanorods and Nanoparticles from Lanthanum Strontium Ferrite La0.6Sr0.4FeO3-δ Materials by Hydrogen Reduction. *J. Phys. Chem. C* **2015**, *119* (38), 22050–22056. https://doi.org/10.1021/acs.jpcc.5b06014.

(29) Li, J.; Singh, U. G.; Bennett, J. W.; Page, K.; Weaver, J. C.; Zhang, J. P.; Proffen, T.; Rappe, A. M.; Scott, S.; Seshadri, R. BaCe1-XPdxO3-δ($0 \leq x \leq 0.1$): Redox Controlled Ingress and Egress of Palladium in a Perovskite. *Chem. Mater.* **2007**, *19* (6), 1418–1426. https://doi.org/10.1021/cm062500i.

(30) Zhu, K.; Wu, T.; Li, M.; Lu, R.; Zhu, X.; Yang, W. Perovskites Decorated with Oxygen Vacancies and Fe-Ni Alloy Nanoparticles as High-Efficiency Electrocatalysts for the Oxygen Evolution Reaction. *J. Mater. Chem. A* **2017**, *5* (37), 19836–19845. https://doi.org/10.1039/c7ta05404a.

(31) Sun, W.; Wei, H.; yang An, L.; Jin, C.; Wu, H.; Xiong, Z. ang; Pu, C.; Sun, C. Oxygen Vacancy Mediated La1-XCexFeO3-Δ Perovskite Oxides as Efficient Catalysts for CWAO of Acrylic Acid by A-Site Ce Doping. *Appl. Catal. B Environ.* **2019**, *245* (September 2018), 20–28. https://doi.org/10.1016/j.apcatb.2018.12.024.

(32) Tanaka, H.; Tan, I.; Uenishi, M.; Taniguchi, M.; Kimura, M.; Nishihata, Y. LaFePdO 3 Perovskite Automotive Catalyst Having a Self-Regenerative Function. *J. Alloys Compd.* **2006**, *412*, 1071–1077. https://doi.org/10.1016/j.jallcom.2004.12.138.

(33) Nishihata, Y.; Mizuki, J. Self-Regeneration of a Pd-Perovskite Catalyst for Automotive Emissions Control. *Nature* **2002**, *418* (x), 164–167. https://doi.org/10.1038/nature00875.1.

(34) Peña, M. A.; Fierro, J. L. G. Chemical Structures and Performance of Perovskite Oxides. *Chem. Rev.* **2001**, *101* (7), 1981–2017. https://doi.org/10.1021/cr980129f.

CHAPTER 8. APPENDICES

8.1 Modelling and Analysis of X-ray Diffractograms by Rietveld refinement on the FullProf software package – step-by-step guide[1,2]

1. Copy and paste XRD data (2θ, Intensity) from CSV or XLSX files onto a new excel sheet and save that as CSV file with two columns.
2. Open the CSV file in Notepad and "Save As" with a .DAT file extension. This is the type of file readable by WinPlotr on the FullProf pacakage.
3. Under "Points selection" use "Select Background Points" and manually select points to determine the background on the diffractogram. Manual selection of about 50-100 points is recommended for best results.
4. Move to the ED-PCR software in the FullProf suite. Select new file and give the file a name under "General Information" and select "Refinement/Calculation of a Powder Diffraction Profile"
5. Under "Patterns", add the first pattern and click on "Data file/Peak shape". The commonly occurring data for diffraction patterns discussed in this research are XY data. For such datasets select "XY Sigma" under "Data File/Format", "Pattern Calculation (X-Ray)" under "Refinement/Simulation" and lastly "Pseudo-Voigt" under peak shape. Select appropriate values for "Theta Min" (starting value of 2θ) and "Theta Max" (ending value of 2θ) and step-size (Δ2θ). Under "Background Type" select "Linear Interpolation between a set background with refinable heights" if a background file has been made. (Recommended).

6. Under “Phases”, give a name to the phase, set weight percentage of the phase to “Calculated automatically”. Under “Contribution to Pattern” select “Current phase contributes to pattern” and “Peak Shape” as “Pseudo-Voigt”. Under “Symmetry” enter the space group corresponding to the model crystal structure.
7. Select “Load CIF files” to load a Crystallographic Information File (CIF) corresponding to the crystal structure serving as the initial guess for the Rietveld refinement model.
8. Select “Refinement”. For the “Cycles of Refinement” select 15-25 (Recommended). Under “Background” upload background file (.BGR file) prepared in WinPlotr. Under “Atoms” the atoms from the crystal structure of the phase from the CIF file should be automatically updated. The lattice parameters should be visible under “Profile”.
9. Save the PCR file and select “Run FullProf program”.
10. Select atomic positions under “Refinement>Atoms” for refinement and reiterate the refinement by running FullProf.
11. Deselect atomic positions and select coefficients under “Refinement>Profile” and reiterate refinement.
12. Repeat steps 10 and 11 until residuals are minimized. Use good judgement and model with other crystal structures for comparison.

8.2 Modelling and Analysis of Extended X-ray Absorption Fine Structures on the Demeter software package – step-by-step guide[3]

1. Begin with the analysis of metal foil sample or other standard sample to calculate S_0^2 (amplitude reduction factor) which would then be used for analysis of custom samples.
2. Load trajectory files on the Athena software. At least 4 independently collected trajectory files. Ensure Athena has identified the correct metal and edge or correct manually. Normalize the spectra by selecting the appropriate pre-edge and post-edge normalization range and adjusting background. (This is subjective to some degree.)
3. Merge normalized files. The merged file will be exported to Artemis for analysis.
4. Open Artemis and click “Add” under “Data Sets” and import the merged project file prepared in Athena and plot in k-space or R-space.
5. Under Feff calculations click “Add” and select appropriate Crystallographic Information File (CIF) for the EXAFS model.
6. Under “Atoms” ensure the correct central atom is selected and adjust “Longest Path” to select the upper limit of scattering path length. Run “Atoms” and then run “Feff”.
7. From the “Atoms” window import paths into path list in the “Data” window. Ensure R-window for the model calculations exceeds that of the longest path selected in the path list. Ensure k-window is large enough to provide enough independent points for the number of variables to be modeled.

8. For the foil/standard fitting guess S_0^2, ΔE_0, ΔR and σ^2. Ensure k-window is large enough to provide enough independent points for the number of variables to be modeled. S_0^2 and ΔE_0 are model specific parameters and repeat across each path while ΔR and σ^2 are path specific parameters that need a new variable to be defined for each path ($\Delta R1$, $\Delta R2$, $\Delta R3$…. and σ_1^2, σ_2^2, σ_3^2….) Ensure k-window is large enough to provide enough independent points for the number of variables to be modeled. (A smaller k-window can help minimize residuals especially because of noisy data seen typically at high k values)
9. Repeat steps 7-8 to include paths within the desired R-window. Single scattering paths generally have a higher contribution to EXAFS models and should be considered over path types. Guess (or fix) model parameters for each path.
10. Once S_0^2 has been determined for a given element and edge, use the same value S_0^2 value in constructing model for the same element and edge for custom samples. Repeat the steps above.

8.3 Additional Resources

https://www.ill.eu/sites/fullprof/php/tutorials.html

https://bruceravel.github.io/demeter/documents/Athena/index.html

https://bruceravel.github.io/demeter/documents/Artemis/index.html

8.4 References

(1) Rodriguez-Carvajal, J. Recent Advances in Magnetic Structure Determination by Neutron Powder Diffraction. *Phys. B* **1993**, *192* (1–2), 55–69.

(2) Roisnel, T.; Rodriguez-Carvajal, J. WinPLOTR: A Windows Tool for Powder Diffraction Patterns Analysis. *Proc. Seventh Eur. Powder Diffr. Conf. (EPDIC 7)* **2000**, 118–123.

(3) Ravel, B.; Newville, M. ATHENA, ARTEMIS, HEPHAESTUS: Data Analysis for X-Ray Absorption Spectroscopy Using IFEFFIT. *J. Synchrotron Radiat.* **2005**, *12* (4), 537–541. https://doi.org/10.1107/S0909049505012719.